Electrocaloric applications based on multilayer capacitors of $PbSc_{0.5}Ta_{0.5}O_3$

Bhaskaran Padmakumar Nair

Trinity College, University of Cambridge

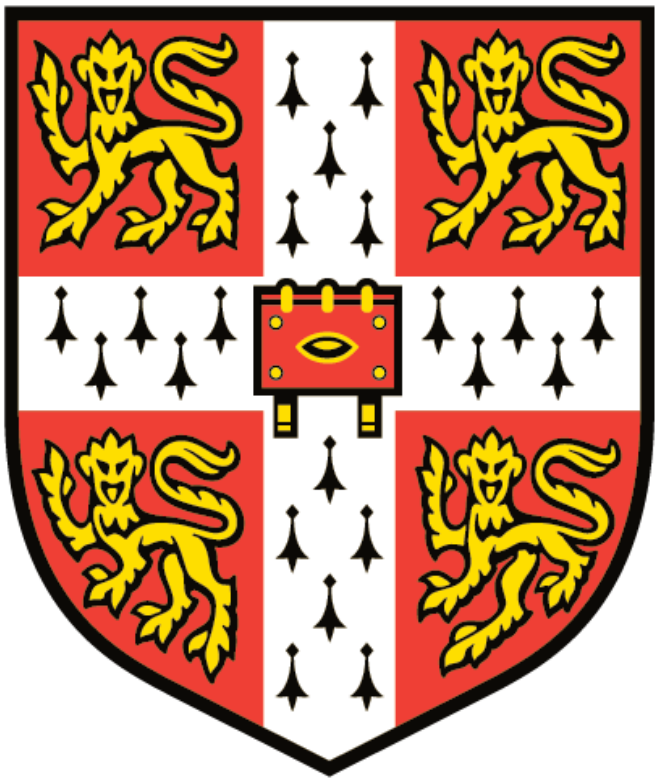

A dissertation submitted for the degree of Doctor of Philosophy at the University of Cambridge

August 2020

അപ്പൂപ്പന്

To my late grandfather, Bhaskaran Nair (*Sr.*),
who passed during the course of my doctoral studies.

In his honour, each chapter of this dissertation
is preceded by an idiomatic saying in Malayalam.

AND

To Prof. A. J. Burggraaf, my parents' PhD supervisor,
who also passed during the course of my doctoral studies.
This work stands on the shoulders of
his early work on lead scandium tantalate.

Declaration

I hereby declare that this thesis is the result of my own work carried out as part of the Device Materials Group (Department of Materials Science & Metallurgy, University of Cambridge) under the supervision of Professor Neil Mathur. This work includes nothing that is the outcome of work done in collaboration except as specified below and in the text.

It is not substantially the same as any work that has been submitted for a degree, diploma or other qualification at the University of Cambridge or any other University or similar institution.

It does not exceed the prescribed word limit of 60,000 words, as prescribed by the Degree Committee.

Bhaskaran P Nair

Chapter 3 is based closely on the following publication:

[1] **B. Nair**, T. Usui, S. Crossley, S. Kurdi, G. G. Guzmán-Verri, X. Moya, S. Hirose and N. D. Mathur, "Large electrocaloric effects in oxide multilayer capacitors over a wide temperature range," *Nature,* vol. 575, p. 468, 2019.

Acknowledgements

First and foremost, I am deeply indebted to my PhD supervisor, Neil Mathur, whose guidance, wisdom, and generosity have been invaluable to this work. From when I was his Part III student till now, I have learned much from him and I truly cherish the many discussions we have had over the years. The quality of this dissertation has no doubt been greatly enhanced by his feedback and rigorous proofreading. Thank you, Neil – working with you has been a true pleasure.

Second, I offer my sincerest thanks to Xavier Moya for his mentorship and kindness throughout. Thank you also for your guidance in the lab, starting from when you demonstrated pulsed laser deposition all those years ago. I remember those night shifts at the Synchrotron very fondly. Lastly, I am extremely grateful for the opportunity to work with you as your Research Assistant during the final stretch of my PhD.

I am eternally indebted to Sam Crossley, who was the demonstrator for my Part III project and my mentor in the lab during the beginning of my doctoral studies. Almost everything I know about lab work is thanks to Sam, and everything I have done in the lab is a pale imitation of the ease and dexterity with which he performed experiments. On top of that, Sam was so wonderfully generous with his time, and always willing to lend a helping hand. From what I understand, he credits his laboratory skills to the mentorship of Sohini Kar-Narayan, whom I also thank for several tips over the years.

I thank all of the collaborators I have worked with, especially those who enabled the work here. It is the painstaking work of Sakyo Hirose and Tomoyasu Usui at Murata Manufacturing that produced the multilayer capacitors of $PbSc_{0.5}Ta_{0.5}O_3$. For this, I express my deepest gratitude. **心からお礼申しあげます**。I thank Gian Guzmán-Verri, who fitted Landau theory to the experimental data presented in Chapter 3. This contribution from him is supplemented by the many insightful conversations we have had, from which I have learned much. I thank Samer Kurdi for performing and analyzing the X-ray diffraction experiments in Chapter 3, and for taking the close-up photograph of an MLC that also appears in Chapter 3.

I thank my sponsors which include Gates Cambridge, the Winton Programme for the Physics of Sustainability, and Trinity College. I am deeply indebted to my college tutor, Richard Serjeantson, whose kindness and support were crucial to my getting through some difficult times.

I thank everyone in the Device Materials Group for various forms of help with equipment as well as their friendship and support. In particular, I thank Nadia Stelmashenko for being the anchor of our lab, and for always being available for any troubleshooting. I thank Massimo Ghidini, who sat behind me in the office and with whom I have had many inspired conversations about politics and shared many laughs. I thank Anke Husmann for all the warmth and kindness with which she listened so patiently over many coffee breaks. I also thank the various colleagues turned friends – Enric, Guillaume, Tommaso, Piotr, Jonathan, Nikos (to name a few) – for the conversations and jokes that turned many frustrating days in the lab into enjoyable ones.

To describe in detail how each of my friends has enriched my time in Cambridge would require a dissertation of its own, but in particular, I would like to highlight four individuals whose encouragement was crucial to the completion of this dissertation:

Arif, who beyond anyone else insisted and pushed me to get this dissertation done. You have been there since the very beginning. Thank you, Kaka.

Samer, who as the rapper Jonwayne said, was “counting on me when I [couldn’t] even count on myself” and was “sure of me when I [wasn’t] so sure of myself.” Thank you, my brother.

Amandla, with whom I spent many a night in DarBar. Our conversations over a double Jaeger or a *Delirium Tremens* were sustenance for the soul. Thank you, habibi.

Edward, it was your encouragement from across the Atlantic that gave me the motivation to make the final push. You were my first friend in Cambridge, and perhaps there was no way more fitting. Thank you, my man.

Sagar, Rohun, Ananya, Greg, Jon, Othman, Stuart, Vince, and so many others – thank you so much for your love and support. I feel truly lucky to call you all my friends.

Ninamme, I have no words to express my gratitude for your love, patience, and grace throughout this process. Managing my anxiety is no easy task, and I do not think I could have put up with what you put up with. Thank you does not cut it, but thank you nonetheless.

I thank my family, to whom I essentially owe everything else. Chetta, we have not always gotten along, but I thank you for all the ways in which you have made me the person I am today. Amme, Acha, you have been nothing short of wonderful parents, and I am so lucky to have your love and support every day. This dissertation would have simply not been possible without you.

Abbreviations and Notation

The following abbreviations are used throughout this dissertation (and are duly introduced at the start of each chapter):

EC	-	electrocaloric
MLC	-	multilayer capacitor
PST	-	$PbSc_{0.5}Ta_{0.5}O_3$

The most frequently used notation in this dissertation are summarized below:

E	-	electric field
P	-	polarization
D	-	electric displacement

In the study of EC materials, the capacitor geometries employed permit the electrostatic vector fields **E**, **P**, and **D** to be represented by scalar fields E, P, and D that correspond to the component that is out-of-plane with respect to the capacitor electrodes.

T	-	temperature − certain temperatures are denoted by subscripts, including:
T_C	-	the Curie temperature (note the subscript 'C' is upper-case)
T_s	-	the starting temperature of a given measurement
T_h	-	the sink temperature of a heat pump ('h' denotes 'hot')
T_c	-	the load temperature of a heat pump (lower-case 'c' denotes 'cold')

S	-	entropy
Q	-	heat
W	-	work
đ	-	inexact differential. Used when considering path-dependent variables, which include heat, work, and hysteretic polarization.

ΔT	-	adiabatic temperature change
ΔT_j	-	non-adiabatic temperature change ('j' refers to the jumps in temperature that are experimentally observed)
ΔS	-	isothermal entropy change
$\Delta T_\#$	-	time-dependent temperature change
$\Delta S_\#$	-	time-dependent entropy change
$E_\#$	-	time-dependent electric field

The hash subscript has been deployed in order to distinguish time-dependent variables from their peak values. For example, $\Delta T_\#(t)$ denotes the time-dependent temperature change whose peak values correspond to ΔT_j (or ΔT in the adiabatic limit). Similarly, EC effects are driven by a time-dependent electric field $E_\#(t)$ whose maximum value is denoted E, as per convention.

q	-	charge
V	-	voltage
I	-	current
P	-	power

P_c	-	cooling power
COP	-	coefficient of performance

Other notation are defined where they appear in the text.

Abstract

Solid-state refrigerants that exhibit electrically driven reversible thermal changes, known as electrocaloric (EC) effects, represent a potentially eco-friendly alternative to the greenhouse gases currently used as refrigerants in refrigerators and heat pumps.

The phenomenology of EC effects is first briefly discussed, and EC materials and prototypes are then reviewed. Methods for parameterizing EC effects are summarized and critically analyzed with the goal of guiding experimental design and cautioning against potential pitfalls.

Multilayer capacitors (MLCs) of $PbSc_{0.5}Ta_{0.5}O_3$ (PST) are demonstrated to be well-suited for cooling applications. The embodiment of highly ordered PST in the MLC geometry yielded a very high breakdown strength in this macroscopic EC working body, allowing the first-order ferroelectric transition to be driven supercritically via fields of up to E = 29.0 V um^{-1}. The resultant EC effects in the large central area of the capacitor were found to peak at 5.5 K near room temperature, and exceed 3 K for starting temperatures that span 176 K. These EC effects compare favourably to magnetocaloric (MC) effects in gadolinium working bodies, suggesting that MC heat-pump design could be repurposed to achieve better performance.

Efficiency values for cooling cycles based on MLCs of PST are computed and analyzed by assuming a hypothetical fluid regenerator that is ideal. The refrigerant efficiency γ is defined as the factor by which the coefficient of performance (COP) for any given cycle is reduced due to losses in the working body. For balanced regenerative cycles with large temperature spans near room temperature (e.g. $T_h - T_c$ = 50 K), the MLCs of PST are found to attain refrigerant efficiencies of up to $\gamma \sim 97\%$.

MLCs of PST are exploited as the EC working body in a device where Peltier elements that separate it from a load and sink are synchronously driven at constant current and voltage. This protocol is found to increase the efficiency of Peltier cooling, but device optimization is required to evaluate meaningful improvements in efficiency.

Contents

List of Figures

List of Tables

“കാലം പോലൊരു ഗുരുവില്ല.”

“There is no teacher like the past.”

Chapter 1

Background

This dissertation focuses on the characterization and application of electrocaloric (EC) effects: nominally reversible thermal changes driven in materials by changes of applied electric field. These thermal changes are large when driving phase transitions, notably ferroelectric-paraelectric transitions. The bulk of the electrocalorics literature is therefore focused on ferroelectric materials that represent candidate working bodies for heat pumps. The work presented here advances the field of EC measurements, working bodies and prototypes.

This dissertation is composed of six chapters. The present chapter provides background information and context for the work. In Chapter 2, a critical overview of EC measurements is presented, providing guidance for tailoring experiments and avoiding potential pitfalls. In Chapter 3, superlative EC effects are demonstrated in multilayer capacitors (MLCs) of the oxide ferroelectric $PbSc_{0.5}Ta_{0.5}O_3$ (PST), establishing them as promising working bodies for EC cooling applications. In Chapter 4, experimental data from Chapter 3 are used to establish the efficiency of cooling cycles with MLCs of PST in an idealized hypothetical prototype. In Chapter 5, MLCs of PST are exploited in a Peltier-EC-Peltier cooling device, and a protocol for achieving efficiency gains in Peltier cooling is demonstrated. Finally, in Chapter 6, conclusions and prospects for future work are discussed.

Chapters 2-5 begin with an abstract that summarizes the chapter. Chapter 3 closely matches my first-author paper “Large electrocaloric effects in oxide multilayer capacitors over a wide temperature range” [1], with methods and supplementary information presented here in the last two sections in order to maintain the flow of the first sections. Chapter 5 follows the same structure. The middle results chapter (Chapter 4) does not require a methods section, but has a section dedicated to supplementary information.

The present chapter begins with phenomenological and microscopic descriptions of the EC effect (Section 1.1), followed by a review of the literature on EC materials and prototypes (Section 1.2). A comprehensive knowledge of undergraduate physics, particularly electrostatics and thermodynamics, is assumed throughout.

The work presented here represents a subset of the projects pursued during the course of my doctoral studies. This dissertation does not contain unpublished work on attempts to detect EC effects in liquid crystals and ionic liquids. EC effects have not been observed in ionic liquids, and initially promising experimental evidence did not culminate in successful direct measurements. The key problem is that the bulk of the conducting liquid phase can only develop a current-induced non-equilibrium polarization that cannot be achieved without concomitant Joule heating. Electrolytic solutions represent a similar, yet simpler system compared to ionic liquids, and a theoretical treatment of non-equilibrium EC effects in electrolytic solutions is currently being developed based on the work of Lars Onsager.

The contents of the following co-authored publications in the field of electrocalorics do not appear in this dissertation:

[2] S. Crossley, **B. Nair**, R. W. Whatmore, X. Moya and N. D. Mathur, "Electrocaloric Cooling Cycles in Lead Scandium Tantalate with True Regeneration via Field Variation," *PRX*, vol. 9, p. 041002, 2019.

[3] S. Crossley, T. Usui, **B. Nair**, S. Kar-Narayan, X. Moya, S. Hirose, A. Ando and N. D. Mathur, "Direct electrocaloric measurement of $0.9Pb(Mg_{1/3}Nb_{2/3})O_3$-$0.1PbTiO_3$ films using scanning thermal microscopy," *Appl. Phys. Lett.*, vol. 108, p. 032902, 2016.

[4] T. Usui, S. Hirose, A. Ando, S. Crossley, **B. Nair**, X. Moya and N. D. Mathur, "Effect of inactive volume on thermocouple measurements of electrocaloric temperature change in multilayer capacitors of $0.9Pb(Mg_{1/3}Nb_{2/3})O_3$–$0.1PbTiO_3$," *J. Phys. D: Appl. Phys.*, vol. 50, p. 424002, 2017.

[5] S. Hirose, T. Usui, S. Crossley, **B. Nair**, A. Ando, X. Moya and N. D. Mathur, "Progress on electrocaloric multilayer ceramic capacitor development," *APL Mater.*, vol. 4, p. 064105, 2016.

For [2], I performed differential scanning calorimetry and independently implemented the analysis of cycle efficiency to verify the findings of the first author. Refs [3-5] were part of a larger collaboration with Murata Manufacturing on electrocalorics. For [3], I performed the polarization measurements and analysis required for indirect characterization of EC effects.

The contents of the following co-authored publications in the field of magnetoelectrics do not appear in this dissertation:

[6] M. Ghidini, R. Mansell, R. Pellicelli, D. Pesquera, **B. Nair**, X. Moya, S. Farokhipoor, F. Maccherozzi, C. H. W. Barnes, R. P. Cowburn, S. S. Dhesi and N. D. Mathur, "Voltage-driven annihilation and creation of magnetic vortices in Ni discs," *Nanoscale,* vol. 12, pp. 5652-5657, 2020.

[7] M. Ghidini, R. Pellicelli, R. Mansell, D. Pesquera, **B. Nair**, X. Moya, S. Farokhipoor, F. Maccherozzi, C. H. W Barnes, R. P. Cowburn, S. S. Dhesi and N. D. Mathur, "Voltage-driven displacement of magnetic vortex cores," *J. Phys. D: Appl. Phys.*, vol. 53, p. 434003, 2020.

[8] M. Ghidini, B. Zhu, R. Mansell, R. Pellicelli, A. Lesaine, X. Moya, S. Crossley, **B. Nair**, F. Maccherozzi, C. H. W. Barnes, R. P. Cowburn, S. S. Dhesi and N. D. Mathur, "Voltage control of magnetic single domains in Ni discs on ferroelectric $BaTiO_3$," *J. Phys. D: Appl. Phys.*, vol. 51, p. 224007, 2018.

In these studies, photoemission electron microscopy (PEEM) using synchrotron radiation permitted the imaging of magnetic and electrical structures via contrast from X-ray magnetic circular dichroism (XMCD) and X-ray linear dichroism (XLD). I was part of the team that performed these measurements and analyzed the data.

The contents of the following co-authored publications in miscellaneous fields (optoelectronics, magnetism, and solid mechanics) do not appear in this dissertation:

[9] S. P. Senanayak, B. Yang, T. H. Thomas, N. Giesbrecht, W. Huang, E. Gann, **B. Nair**, K. Goedel, S. Guha, X. Moya, C. R. McNeill, P. Docampo, A. Sadhanala, R. H. Friend, and H. Sirringhaus, "Understanding charge transport in lead iodide perovskite thin-film field-effect transistors," *Sci. Adv.*, vol. 3, p. e1601935, 2017.

[10] S. Kurdi, M. Ghidini, G. Divitini, **B. Nair**, A. Kursumovic, P. Tiberto, S. S. Dhesi and Z. H. Barber, "Exchange-bias via nanosegregation in novel $Fe_{2-x}Mn_{1+x}Al$ (x = −0.25, 0, 0.25) Heusler films," *Nanoscale Adv.*, vol. 2, pp. 2602-2609, 2020.

[11] J. A. Schiemer, I. Lascu, R. J. Harrison, A. Kumar, R. S. Katiyar, D. A. Sanchez, N. Ortega, C. Salazar Mejia, W. Schnelle, H. Shinohara, A. J. F. Heap, R. Nagaratnam, S. E. Dutton, J. F. Scott, **B. Nair**, N. D. Mathur and M. A. Carpenter, "Elastic and anelastic relaxation behaviour of perovskite multiferroics II: $PbZr_{0.53}Ti_{0.47}O_3$(PZT)–$PbFe_{0.5}Ta_{0.5}O_3$(PFT)," *J. Mater. Sci.*, vol. 52, pp. 285-304, 2017.

For [9], I performed polarization measurements. For [10], I wrote bespoke code to analyze data from XMCD and superconducting quantum interference device (SQUID) measurements. For [11], I performed dielectric spectroscopy.

1.1 An overview of electrocaloric effects

Caloric effects are nominally reversible thermal changes in a material driven by changes in a generalized force that result in changes of the conjugate (generalized) displacement. By conventional definition, caloric effects are restricted to solid-state materials, but the wider principle is most famously exemplified by the vapour-compression technology exploited in domestic refrigeration and air conditioning: thermal changes in fluid refrigerants are driven by changes in pressure (the generalized force) that induce changes in volume (the conjugate variable). Specifically, changes of pressure drive a liquid-gas phase transition in the refrigerant, associated with a substantial change in volume. Similarly, caloric effects are largest when driving solid-state phase transitions via changes in one of several generalized forces [12] (Table 1).

Table 1.1 | **Caloric effects.**

Caloric effects can be driven by different generalized forces that drive phase transitions marked by large changes in the conjugate displacement. The different caloric effects and their corresponding generalized force, conjugate displacement, and associated phase transitions are given below.

Caloric effect		**Generalized force**	**Conjugate variable**	**Phase transitions**
Magnetocaloric (MC)		Applied magnetic field $\mu_0 H$	Magnetization M	Ferromagnetic-paramagnetic, ferromagnetic-antiferromagnetic
Electrocaloric (EC)		Electric field E	Polarization P	Ferroelectric-paraelectric, ferroelectric-antiferroelectric, isotropic-nematic, etc.
Mechanocaloric (mC)	Elastocaloric (eC)	Uniaxial stress σ	Uniaxial strain ε	Ferroelastic-paraelastic, martensite-austenite, etc.
	Barocaloric (BC)	Pressure P	Volume V	Structural transitions, plastic crystal-to-crystal

Changes of applied electric field E that result in changes of electrical polarization can produce sizeable electrocaloric (EC) effects in the vicinity of ferroelectric-paraelectric transitions. Ferroelectrics are marked by a spontaneous polarization that arises in the absence of applied electric field ($E = 0$) from a broken symmetry below the Curie temperature T_C. This spontaneous polarization is thermodynamically stable and can be switched between energetically equivalent orientations via an applied electric field. This second feature is exploited below T_C in ferroelectric random access memory (FRAM), where two stable states at $E = 0$ permit non-volatile data storage [13]. EC applications on the other hand generally operate above T_C, where the ferroelectric-paraelectric transition can be driven with applied electric field.

If the transition is driven isothermally then the EC effect can be observed via a net heat Q leaving or entering the material, corresponding to an entropy change $\Delta S = Q/T$. On the other hand, if the transition is driven adiabatically then the EC effect is instead observed as a temperature change ΔT. Field application and removal necessarily produce EC effects of opposite sign, and the sign of ΔS is opposite to the sign of ΔT for a given EC effect. The absolute signs of ΔT and ΔS depend on the specific details of a given EC material. Conventional EC effects, such as those that exploit a ferroelectric-paraelectric transition, arise when field application promotes the low-temperature phase, in which case $\Delta S < 0$ and $\Delta T > 0$ for field application. Inverse EC effects, on the other hand, arise when field application promotes the high-temperature phase, in which case $\Delta S > 0$ and $\Delta T < 0$ for field application.

In a conventional EC material above its Curie temperature T_C, applying an electric field causes the paraelectric to polarize by suppressing polarization fluctuations whose energy cost is raised by the electric field (field-induced ‘hardening’). In the limit of a displacive transition, the electric field suppresses optical phonons [14], leading to the growth of microscopic dipoles. For the well-known ABO_3 perovskites, these dipoles arise from displacements of the B-cations from the centres of the BO_6 octahedra [15]. In the limit of an order-disorder transition, the electric field suppresses disorder in dipole orientation, leading to better alignment. Examples include the tunnelling of a proton between two stable positions in KH_2PO_4 (KDP) [16] and the reorientation of hydroxyl ions doped into KCl [17].

If the electric field is applied isothermally, the entropy of the paraelectric reduces when excess thermal energy associated with polarization fluctuations is released in the form of heat ($\Delta S < 0$; Fig. 1.1a). If the application of electric field is instead adiabatic, the excess thermal energy associated with polarization fluctuations is redistributed among the non-polar normal modes of the lattice, raising the temperature of the material ($\Delta T > 0$; Fig. 1.1a). If heat is then permitted to flow between the material and its environment, the raised temperature causes heat to flow out of the material until it thermalizes, leading to a reduction in entropy equivalent to the isothermal entropy change. The released EC heat is slightly greater than the isothermal EC heat due to the irreversibility of heat exchange across a finite temperature difference.

Given that the EC effect is nominally reversible, isothermal field removal results in an increase of the entropy, i.e. fluctuations of polarization are promoted as they 'soften' with decreasing field magnitude ($\Delta S > 0$; Fig. 1.1b). Of particular interest to cooling, adiabatic field removal causes the temperature to drop as polarization fluctuations draw energy from the non-polar normal modes of the lattice ($\Delta T < 0$; Fig. 1.1b). If heat is then permitted to flow between the material and its environment, the lowered temperature causes heat to flow into the material until it thermalizes, leading to an increase in entropy equivalent to the isothermal entropy change. The absorbed EC heat is slightly less than the isothermal EC heat due to the irreversibility of heat exchange across a finite temperature difference.

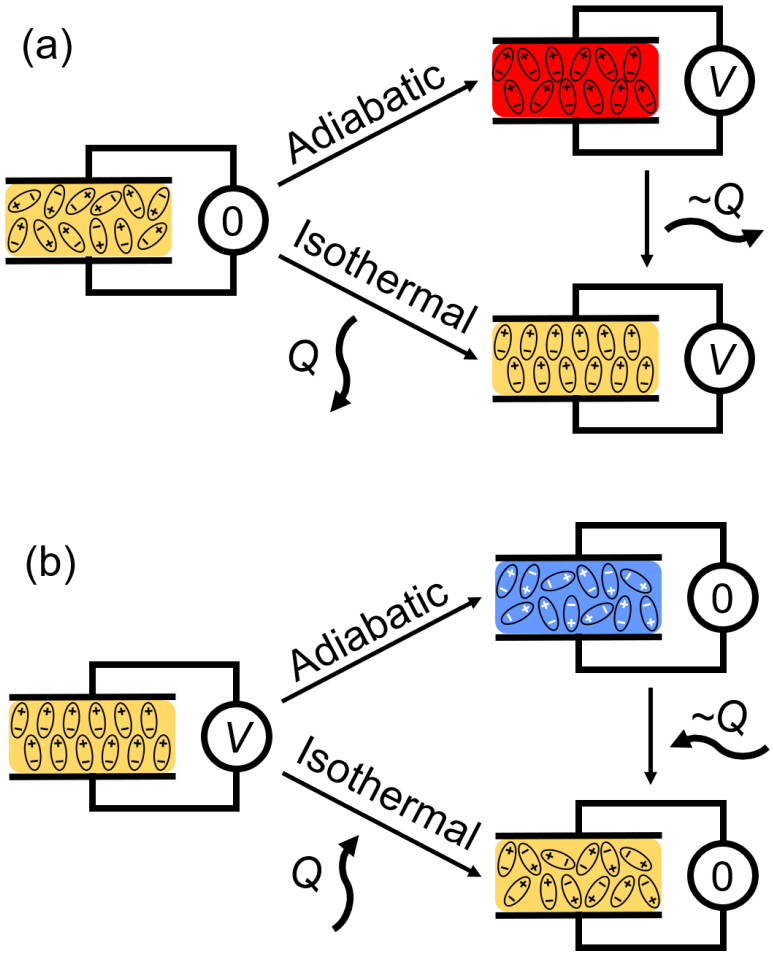

Fig. 1.1 | **Isothermal and adiabatic EC effects in conventional EC materials.**

(a) Application of electric field under adiabatic conditions results in an increase in temperature as dipoles align ($\Delta T > 0$, top) and under isothermal conditions results in the release of EC heat Q as dipole alignment reduces entropy ($\Delta S < 0$, bottom). If the EC material is put into thermal contact with its surroundings after adiabatic field application, the dipoles further align as the hot EC material thermalizes with the environment, releasing slightly more EC heat than the isothermal process. (b) Removal of electric field under adiabatic conditions results in a decrease in temperature ($\Delta T < 0$, top) as dipoles misalign, and under isothermal conditions results in the absorption of EC heat Q as dipole alignment increases entropy ($\Delta S > 0$, bottom). If the EC material is put into thermal contact with its surroundings after adiabatic field removal, thermalization results in EC heat being absorbed from the environment, absorbing slightly less EC heat than the isothermal process. Note that the schematics represent an order-disorder transition based on dipole reorientation, and not a displacive transition in which the electric field grows dipoles.

1.2 A brief history of EC materials and prototypes

In keeping with the conventions of the larger ferroelectrics literature, electric field values are given here in units of kV cm^{-1}, as opposed to the units V μm^{-1} used elsewhere in this dissertation. The conversion is 10 kV cm^{-1} = 1 V μm^{-1} = 1 MV m^{-1} = 10^6 V m^{-1}.

1.2.1 The early period, 314 BCE to 2006 CE

The ancient Greek philosopher Theophrastus noted in his writings that tourmaline when heated attracts sawdust and scraps of hay [18], marking the first recorded observation of what would later be known as pyroelectricity: a change in temperature producing a change in bulk polarization, manifested as static electricity on the surface. The inverse effect, i.e. the EC effect, was not detected for another two millennia. The discovery of its elastic analogue in the nineteenth century [19] gave way for a theoretical description by Lord Kelvin [20] based on the emerging formalism of thermodynamics, and he later generalized this in 1878 to predict EC (and MC) effects [21].

The discovery of ferroelectricity in Rochelle salt by Vallasek in 1920 [22] proved to be a key step in the experimental realization of Lord Kelvin's prediction: EC effects were first observed incidentally as part of a larger study of Rochelle salt by Kobeko and Kurtschatov ten years later [23]. They neglected to parameterize the EC effect quantitatively, suggesting the magnitude of the effect to be very small: a later study of Rochelle salt confirms this, reporting direct measurements of just $|\Delta T| \sim 4$ mK for $E \sim 1.4$ kV cm^{-1} [24]. The second ferroelectric to be discovered [25], potassium dihydrogen phosphate (KDP), proved to be far superior to Rochelle salt, exhibiting indirectly determined EC effects of $|\Delta T| \sim 1$ K for $E = 10$ kV cm^{-1} near $T_C \sim 123$ K [26]. This ~300-fold improvement in the state-of-the-art EC effect reported in 1950 is particularly noteworthy, given the 'giant' EC effects reported in 2006 represented only a five-fold improvement over the state-of-the-art [27].

The majority of electrocalorics research in the second half of the 20th century focused on bulk ceramic perovskites, in which ferroelectricity was first observed in $BaTiO_3$ in 1946 [28]. EC effects in perovskites away from cryogenic temperatures were first observed in the 1960s in

both $BaTiO_3$ [29] and chemically modified $Pb(Zr,Ti)O_3$ ceramics [30]. The latter system proved to be fertile ground for optimizing EC effects [30-33]: directly measured EC effects of $|\Delta T| \sim 2.6$ K in $Pb_{0.99}Nb_{0.02}(Zr_{0.75}Sn_{0.20}Ti_{0.05})_{0.98}O_3$ ceramics (for $E = 30$ kV cm^{-1} near starting temperature $T_s \sim 434$ K) [32], reported in 1981, would remain state-of-the-art for 25 years [27] (or 29 years if direct measurements are the required standard of proof [34]). One of these systems (antiferroelectric $PbZrO_3$) also yielded the first observation of inverse EC effects, reported near liquid helium temperatures in 1993 [35].

The 1950s, 60s, and 70s saw great interest in EC effects at cryogenic temperatures [36-44]. Cooling by adiabatic depolarization was first suggested [36] for the perovskite quantum paraelectric $SrTiO_3$ in 1956, and low-temperature EC effects were first measured in polycrystalline samples of this material five years later [37]. Though larger effects of up to $|\Delta T| \sim 0.3$ K near $T_s \sim 11$ K for $E = 7$ kV cm^{-1} were later observed in single crystal $SrTiO_3$ [38], later studies went on to reveal that in both $SrTiO_3$ [14] and the perovskite quantum paraelectric $KTaO_3$ [39], the irreversible component of the temperature change dominated at lower temperatures. In 1964, an alternative was suggested for adiabatic depolarization: lightly doped alkali halides like KCl doped with OH^- ions, in which a ferroelectric transition near liquid helium temperatures is tuned by varying the degree of doping [17]. In the following year, EC effects of up to $|\Delta T| \sim 0.9$ K near $T_s \sim 1.3$ K for $E = 75$ kV cm^{-1} were directly measured in hydroxyl-doped KCl single crystals, where the electric field lifted the six-fold degeneracy of the hydroxyl-ion orientations [40]. A similar study on Li^+-doped single crystals of KCl published two issues later in *Physical Review Letters* [41] would be the most cited work in electrocalorics until 2011 [12], and subsequent work on doped alkali halides [42-44] would further explore the use of adiabatic depolarization as an alternative to adiabatic demagnetization for achieving temperatures below 1 K.

The late 1980s saw the birth of EC prototyping in the then Soviet Union, based on derivatives of the perovskite $PbSc_{0.5}Ta_{0.5}O_3$ that are described collectively as PST here [45-47]. The first EC refrigeration prototype was reported by a group at the Moscow Power Engineering Institute in 1989. This prototype exploited ceramic plates of PST that could develop adiabatic temperature changes of ~1 K for $E = 15$ kV cm^{-1} and employed pressurized helium as a heat

exchanger to yield a temperature lift of ~2.5 K [45]. In 1992, the same group reported an improved prototype in which temperature changes of ~0.9 K for E = 60 kV cm^{-1}, measured non-adiabatically during operation, were amplified via a liquid-pentane regenerator to yield a temperature lift of ~5 K [46]. Three years later, the group reported an optimized large-scale prototype with a temperature lift of ~12.7 K using more modest applied fields of E = 18.5 kV cm^{-1} [47]. To date, this remains the largest temperature lift achieved in an EC prototype, but it is barely appreciated because it is buried within the paper.

Concurrent work on PST [48-50] focused on optimizing EC effects by exploring the effects of B-site cation ordering and chemical substitution, yielding EC effects of up to $|\Delta T|$ ~ 2.3 K near room temperature in highly ordered PST ceramics for E = 50 kV cm^{-1} [50]. This stream of research on PST led to the first instance in which the multilayer capacitor (MLC) geometry was exploited for EC applications [51], with the reasoning that larger EC effects can be driven by larger electric fields in thinner dielectric layers without breakdown. However, the difficulty of tailoring heat treatments to achieve high B-site cation ordering of PST in the MLC geometry translated to reduced ordering. As a result, EC effects in MLCs of PST were no better than EC effects in bulk PST ceramics.

A notable absence in the body of electrocalorics research prior to 2006 is the family of ferroelectric polymers, which has been known since the discovery of poly(vinylidene fluoride) (PVDF) in 1969 [52]. A 1993 study of pyroelectric effects in 28 μm-thick films of PVDF identified EC effects as a positive-feedback mechanism that enhanced pyroelectric currents at low frequencies [53]. However, these EC effects were not parameterized in standard terms.

1.2.2 The renaissance of electrocalorics, 2006-present

In 2006, the discovery of 'giant' EC effects in ~350 nm-thick sol-gel films of $PbZr_{0.95}Ti_{0.05}O_3$ (PZT) catalyzed a renaissance in the field of electrocalorics [27]. This work, now the most highly cited report of original research in the field, was the first to exploit the order-of-magnitude-larger electric fields that are accessible without breakdown in the thin-film geometry [13]: the indirect method was used to identify $|\Delta T|$ ~ 12 K for E = 480 kV cm^{-1} near T_s ~ 499 K (direct measurements of sub-micron films are challenging). Two years later, thin

films of polymer ferroelectrics, namely poly(vinylidene fluoride-triflouroethylene) (P(VDF-TrFE)), and a relaxor composition achieved with the addition of chloroflouroethylene (P(VDF-TrFE-CFE)), were found to exhibit indirectly determined values of $|\Delta T| \sim 12.5$ K near $T_s \sim 353$ K for $E = 2090$ kV cm^{-1} (P(VDF-TrFE)) and near $T_s \sim 328$ K for $E = 3070$ kV cm^{-1} (P(VDF-TrFE-CFE)) [54]. This work, currently the second-most cited report of original research in electrocalorics, was the first to demonstrate EC effects in ferroelectric polymers. The thin-film geometry combined with the highly-insulating nature of polymers permitted the application of electric fields that were two-orders-of-magnitude larger than those that could be applied to bulk ceramics [12].

Since 2006, 'giant' EC effects have been observed in various perovskite [55-59] and polymer [60-62] thin films (Table 2 in [12]), mostly via the indirect method [27, 54-60], or in the case of polymers sometimes via a modified form of calorimetry [61, 62] that is coupled with fast changes of electric field that are usually associated with thermometry under near-adiabatic conditions (Section 2.4.1). The indirect method relies on routine electrical measurements at different temperatures, thus obviating the need to record the electrically driven changes using thermometry and calorimetry, which are highly challenging for thin films (Chapter 2). Nevertheless, direct measurements with a small bead thermistor have confirmed indirectly determined values of $|\Delta T| \sim 12$ K for polymer thin films [34, 63].

EC thin films, though able to withstand substantially larger electric fields and as a result support larger EC effects, suffer from (1) a thermal mass that is too small (by several orders of magnitude) to effectively cool any macroscopic object and (2) substantial leakage currents at the high fields required, resulting in Joule heat that undermines cooling. Therefore, the resurgence of electrocalorics has come with a second wave of interest in bulk perovskites (Table 2 in [12]), often thinned down to maximize the breakdown field. Sizeable EC effects have been reported in novel materials systems like (i) $(1-x)Pb(Mg_{1/3}Nb_{2/3})O_3$-$xPbTiO_3$ (PMN-PT) solid solutions [64-67], in which direct measurements of up to $|\Delta T| \sim 3.5$ K near $T_s \sim 400$ K have been reported for $x = 0.10$ with $E = 160$ kV cm^{-1} [66], and (ii) $Ba_{1-x}Sr_xTiO_3$ (BST), in which an indirectly determined value of $|\Delta T| \sim 3.1$ K near $T_s \sim 293$ K has been reported for $x = 0.65$ with $E = 130$ kV cm^{-1} [68].

The MLC geometry for EC devices has recently gained fresh attention because it combines the advantages of thin-film EC materials (enhanced breakdown fields allowing access to much larger EC effects) and bulk EC materials (large thermal mass suitable for cooling macroscopic loads) [69]. Furthermore, the interdigitated electrodes of the MLC were recently identified and modelled as a path by which heat can be rapidly transferred via the terminals [69, 70]. Since commercial MLCs of BTO were reported to have serendipitous EC effects of $|\Delta T| \sim 0.5$ K near room temperature (for $E = 300$ kV cm^{-1}) [71], MLCs of other EC materials have yielded larger EC effects. MLCs of electron-irradiated PVDF-TrFE copolymer were reported to exhibit $|\Delta T| \sim 2.2$ K near room temperature (for $E = 800$ kV cm^{-1}) [72], while MLCs of PMN-PT were reported to exhibit $|\Delta T| \sim 2.7$ K near $T_s \sim 380$ K (for $E = 288$ kV cm^{-1}) [4].

The improvements in bulk and MLC EC systems have translated to the development of an additional ten EC prototypes to date [72- 81]. Some of the key developments are highlighted below:

- In 2013, temperature spans of up to ~6.6 K were achieved by a prototype employing the aforementioned polymer multilayers ($|\Delta T| \sim 2.2$ K) with stainless-steel regenerators rather than fluid [72].
- In 2014, active EC regeneration was first demonstrated in a prototype employing bulk PMN-PT with silicone oil. A regeneration factor of ~3.7 was achieved. [74].
- In 2015, the first prototype employing a heat-switch based mechanism was reported: silicon fingers that align and misalign across a lubricated surface to achieve a thermal conductance contrast ratio of 27 were used to control the heat expelled/absorbed by MLCs of BTO [75].
- In 2017, an ingenious EC cooling device based on a flexible polymer bilayer was reported: the bilayer was composed of an EC layer and a framework that serves as an electrostatic actuator in order to bend the bilayer in contact with the sink or load [79]. However, the cooling of a hot battery is likely due to one-shot passive conduction.
- In 2018, energy recovery was demonstrated in a prototype where MLCs of BTO were charged/discharged in antiphase to improve the COP by a factor of ~2.9 [80].

Despite considerable improvements, EC prototypes lag substantially behind the well-developed magnetocaloric prototypes. Moreover, one can envisage EC cooling without any moving parts (Chapter 5), but this is still yet to be demonstrated.

Since the resurgence, EC effects have been reported in several ferroelectric materials that are neither perovskite oxides nor polymers. In 2010, sol-gel thin films of $SrBi_2Ta_2O_9$ were indirectly shown to exhibit giant EC effects of $|\Delta T| \sim 5$ K near room temperature for $E = 600$ kV cm^{-1} [82]. A 2012 PhD dissertation by my predecessor recognized that the large latent heats of the ferroelectric transitions in inorganic salts like $(NH_4)_2SO_4$, KNO_3, and $NaNO_2$ could yield correspondingly large EC effects [83]. These EC effects were measured via the indirect method, taking care to avoid the spurious effects of hysteresis by resetting [83] (Section 2.2.3). The largest EC effects were found to be in KNO_3, with $|\Delta S| \sim 75$ J K^{-1} kg^{-1} for $E = 31$ kV cm^{-1} near $T \sim 400$ K. The utility of these EC effects is however undermined by (1) the narrow (~1 K) range of starting temperatures over which EC effects are observed and (2) Joule heating due to leakage. Several more families of ferroelectrics were identified in the PhD dissertation as promising EC materials, but to date they remain mostly unexploited [83].

EC effects are not limited to ferroelectric and antiferroelectric materials. In 2013, EC effects were reported in the well-known liquid crystal 5CB near the nematic-isotropic transition [84], exploiting the constituent molecules' dielectric anisotropy to yield indirectly measured temperature changes in the range of $|\Delta T| \sim 3.35$-5.26 K near $T \sim 312$ K for $E = 900$ kV cm^{-1}. This was followed in 2016 by a more convincing report of EC effects near the smectic-A-to-isotropic transition in a liquid crystal mixture of 12CB with CdSe nanoparticles [85]. Direct measurements of temperature change were scaled up to account for the thermal mass of the liquid crystal cell, yielding $|\Delta T| \sim 5.2$ K near $T \sim 331$ K for $E = 30$ kV cm^{-1} [85]. In 2015, inverse EC effects associated with the metal-insulator transition were reported in sintered pellets of VO_2 [86], where temperature/entropy changes deduced via the quasi-direct method suggested an EC strength more than two orders of magnitude larger than in single crystals of $BaTiO_3$, in which the state-of-the-art EC strength of ~225 mK kV^{-1} cm was reported in 2013 [87]. EC effects in VO_2 have not been confirmed, and conclusive evidence for EC effects in the vicinity of conducting-to-insulating transitions is yet to be reported. A 2016

molecular dynamics study nevertheless predicts EC effects in CaF_2 near the superionic transition [88].

“ആറ്റിൽക്കളഞ്ഞാലും അളന്നുകളയണം.”

“Even that which you throw [out] into the river must be measured.”

Chapter 2

Electrocaloric measurements

First it is explained how thermal boundary conditions can be experimentally tailored to achieve near-adiabatic or near-isothermal electrocaloric (EC) measurements. Fundamental principles and potential pitfalls are then discussed for the three main types of measurement: (i) indirect measurements that exploit thermodynamic analysis of electrical data, (ii) direct measurements of EC temperature change, and (iii) direct and quasi-direct measurements of EC heat.

In Section 2.1, heat-transfer time scales are discussed in the context of tailoring experiments to ensure the near-isothermal or near-adiabatic conditions used for parameterizing EC effects. Section 2.2 provides an overview of the indirect methods for determining EC effects, which are widely used and exploit thermodynamic analysis of variable-temperature polarization measurements. This class of techniques is often deployed where direct measurements are not possible, e.g. thin films whose low thermal mass results in a small and rapidly decaying thermal signal. In Section 2.3, direct measurements of EC temperature change are discussed. Both contact and non-contact methods are considered, and artefacts that compromise infrared imaging are highlighted. In Section 2.4, direct and quasi-direct measurements of EC heat using calorimetry are considered with an emphasis on the pitfalls in measurement protocols and calibration. Section 2.5 presents conclusions. Throughout this chapter and elsewhere, the standard practice of referring to a flow of heat will be adopted, even though heat is a flow of thermal energy, such that a flow of heat tautologically describes a flow of a flow.

2.1 The isothermal to adiabatic spectrum

Heat exchange can proceed via conduction, convection, or radiation, and in general, the dynamics of heat exchange depend on both the geometry and properties (e.g. specific heat capacity and thermal conductivity) of the materials and interfaces that make up a system. The thermalization of a body with its surroundings via convection or conduction is well described by Newton's law of cooling, which predicts exponential thermal relaxation characterized by some decay timescale τ_c. In more complex heterogeneous systems, heat exchange is governed by multiple characteristic time scales: for example, an EC sample may exchange heat quickly with its holder, but the sample and holder together may take longer to thermalize with a bath.

Whether changes in applied electric field can be considered adiabatic or isothermal depends on how quickly the electric field is ramped relative to the thermal time scale(s) that govern heat exchange between an EC material and its surroundings. For an EC material at starting temperature T_s, if a change in the applied field is much faster than the characteristic thermal time scale(s), a near-adiabatic temperature change is observed, followed by a slower relaxation back to T_s as the EC material exchanges heat with its surroundings. On the other hand, if the change in applied field is much slower than the characteristic thermal time scale(s), a near-isothermal heat is exchanged across negligibly small temperature gradients between the EC material and its environment. In both limiting cases, the rate of heat transfer with the environment is negligible during the field changes and thus the material is assumed to be internally at equilibrium.

The thermal relaxation of a material is, in general, a complex problem, but under specific experimental conditions, the thermal relaxation is greatly simplified. For the typical parallel-plate capacitor geometry, the intrinsic thermal time scale $\tau_{int} = L_c^2/\alpha$ can be identified by recasting the heat equation into the dimensionless form, where α is the thermal diffusivity of the EC material and L_c is the characteristic length given by the thickness of the EC material [89]. For selected EC materials, order-of-magnitude estimates of τ_{int} are tabulated for a range of capacitor thicknesses (Table 2.1).

Table 2.1 | **Order-of-magnitude estimates of intrinsic thermal time scales in selected EC materials.**

Conductive heat transfer perpendicular to the plane of a parallel plate capacitor depends on the intrinsic thermal time scale $\tau_{int} = L_c^2/\alpha$, where α is the thermal diffusivity of the EC material and L_c is its thickness. Order-of-magnitude estimates of τ_{int} for (i) single-crystal $BaTiO_3$, (ii) polycrystalline $(1\text{-}x)PbMn_{0.5}Nb_{0.5}O_3\text{-}(x)PbTiO_3$ (PMN-PT) and (iii) polyvinylidene fluoride (PVDF) copolymers are based on diffusivity values determined from refs. [90-92].

		τ_{int} (s)		
		single-crystal $BaTiO_3$ $\alpha \sim 2\times10^{-6}$ m^2 s^{-1}	Polycrystalline PMN-PT $\alpha \sim 5\times10^{-7}$ m^2 s^{-1}	PVDF copolymers $\alpha \sim 1\times10^{-7}$ m^2 s^{-1}
L_c (m)	10^{-3}	5×10^{-1}	2×10^{0}	1×10^{1}
	10^{-4}	5×10^{-3}	2×10^{-2}	1×10^{-1}
	10^{-5}	5×10^{-5}	2×10^{-4}	1×10^{-3}
	10^{-6}	5×10^{-7}	2×10^{-6}	1×10^{-5}
	10^{-7}	5×10^{-9}	2×10^{-8}	1×10^{-7}

Consider a parallel-plate EC capacitor whose face makes contact with a metallic heat sink that typically sits on a measurement probe to stabilize variable start temperature T_s. Given that the thermal effusivity $f = (k\rho c)^{1/2}$ of a material determines how well it exchanges thermal energy with its environment, conduction across the capacitor-sink interface depends on the ratio $\mathfrak{C} = f_{sink}/f_{EC}$ of the two thermal effusivities (k is thermal conductivity, ρ is density, and c is specific heat capacity) [89]. An intervening layer of electrical insulation or adhesive can be ignored if its effusivity f_{ins} is large with respect to the EC capacitor ($f_{ins} >> f_{EC}$) or if its thickness l_{ins} is sufficiently low ($l_{ins} \ll L_c f_{ins}/f_{EC}$). It is likely that $\mathfrak{C} >> 1$ given that k_{sink} for the metallic sink should greatly exceed k_{EC} for the EC capacitor (assuming $\rho_{sink} \sim \rho_{EC}$ and $c_{sink} \sim c_{EC}$), such that heat flow is limited by thermal conduction within the capacitor and not the sink. In this limit, thermal relaxation is determined by the intrinsic time scale τ_{int} of the EC capacitor, such that an adiabatic temperature change is followed by a temperature relaxation of the form $\sim e^{-ut/\tau_{int}}$, where u is of order unity [89]. If τ_{int} is too small, then an EC temperature change will decay too quickly to be measured.

Highly adiabatic measurements of temperature are typically made on the exposed face of an EC capacitor, and they are assumed to represent the temperature within the bulk. However, this assumption can be compromised by convective heat transfer between the exposed face

and its surroundings. Convection can be described via the dimensionless Biot number $\mathcal{B} = hL_c/k_{EC}$ that compares the temperature gradient across the EC capacitor with the temperature drop across the convective fluid (h is the heat transfer coefficient for the convective fluid, typically air) [89]. For $\mathcal{B} \leq 0.1$, the convective heat transfer is relatively poor, such that the EC capacitor is internally well thermalized as intended. This scenario can be effected by operating in vacuum, as h is proportional to the pressure of the convective fluid.

An alternative but common experimental 'floating' configuration involves creating a weak link between the parallel-plate EC capacitor of interest and its temperature-controlled surroundings. Care must be taken to minimize the thermal mass and conductivity of any addenda, namely the support that keeps the capacitor 'floating', the electrical leads if these do not themselves constitute the support, and any contact thermometry. Heat leaks through electrical leads can be reduced by minimizing wire thickness and the volume of silver paint/solder. Having thus minimized conductive heat leaks, EC heat is primarily exchanged with the surroundings via convection, which should itself be minimized ($\mathcal{B} \leq 0.1$) to ensure thermal homogeneity in the EC capacitor and a slow temperature relaxation of the form $\sim e^{-\mathcal{B}t/\tau_{int}}$ [89].

The thermal relaxation for the capacitor-on-heat-sink and floating-capacitor configurations can be modelled using the following differential equation:

$$\frac{\dot{Q}}{C} + \frac{dT}{dt} = \frac{dT_0}{dt} \tag{2.1}$$

The first term on the left represents a rate of change in temperature due to the flow of EC heat $\dot{Q}$ between the EC materials and the environment, while the heat capacity C of the EC material is assumed constant. The second term represents the rate of change of the temperature T in the EC material, and in the adiabatic limit ($\dot{Q} = 0$) it is equal to the source term on the right, where $T_0(t)$ describes the temperature of the material due to field $E_\#(t)$. The hash subscript is deployed here and elsewhere to identify time dependence when dropping the argument t.

Using Newton's law of cooling, the EC heat flow can be written as $\dot{Q} = (T - T_s)/R$, where the temperature difference $T - T_s$ between the EC material at $T(t)$ and its environment at (starting) temperature T_s drives the EC heat at rate $\dot{Q}$ through a thermal resistance R that subsumes the thermal resistance of the EC material together with its connection to the environment.
Eq. (2.1) thus becomes:

$$\frac{T - T_s}{RC} + \frac{dT}{dt} = \frac{dT_0}{dt} \tag{2.2}$$

It is useful to make the substitutions $\Delta T_{\#}(t) = T - T_s$ and $\Delta T_0(t) = T_0 - T_s$ in order to compact the notation (the hash subscript permits $\Delta T_{\#}$ to be distinguished from the peak value of the time-dependent adiabatic temperature change—universally denoted ΔT—when dropping the argument t). The extrema in $\Delta T_0(t)$ correspond to this adiabatic temperature change ΔT, while the extrema in $\Delta T_{\#}(t)$ correspond to non-adiabatic temperature change ΔT_j, where j denotes jump. In the adiabatic limit, one has $\Delta T_{\#}(t) = \Delta T_0(t)$ and therefore $\Delta T_j = \Delta T$. In the compacted notation, Eq. (2.2) becomes:

$$\frac{\Delta T_{\#}}{RC} + \frac{d(\Delta T_{\#})}{dt} = \frac{d(\Delta T_0)}{dt} \tag{2.3}$$

Eq. (2.3) is identical in form to the differential equation that would describe a series RC circuit in electronics, with the source term ΔT_0 corresponding to an input voltage and the temperature change $\Delta T_{\#}$ corresponding to a voltage across an electrical resistor. The thermal analogue relevant here is a lumped-element model (Fig. 2.1a) in which the EC material (capacitor C) exchanges heat $\dot{Q}$ across a thermal link (resistor R) to the environment (ground). Writing the characteristic time scale as $\tau_c = RC$ permits Eq. (2.3) to be written as:

$$\frac{\Delta T_{\#}}{\tau_c} + \frac{d(\Delta T_{\#})}{dt} = \frac{d(\Delta T_0)}{dt} \tag{2.4}$$

The Green's function required to solve Eq. (2.4) [93] is given by:

$$G(t) = \delta(t) - (\Theta(t)/\tau_c)e^{-t/\tau_c} \tag{2.5}$$

and shown in Fig. 2.1b. Here, $\delta(t)$ is the Dirac delta function and $\Theta(t)$ is the Heaviside step function.

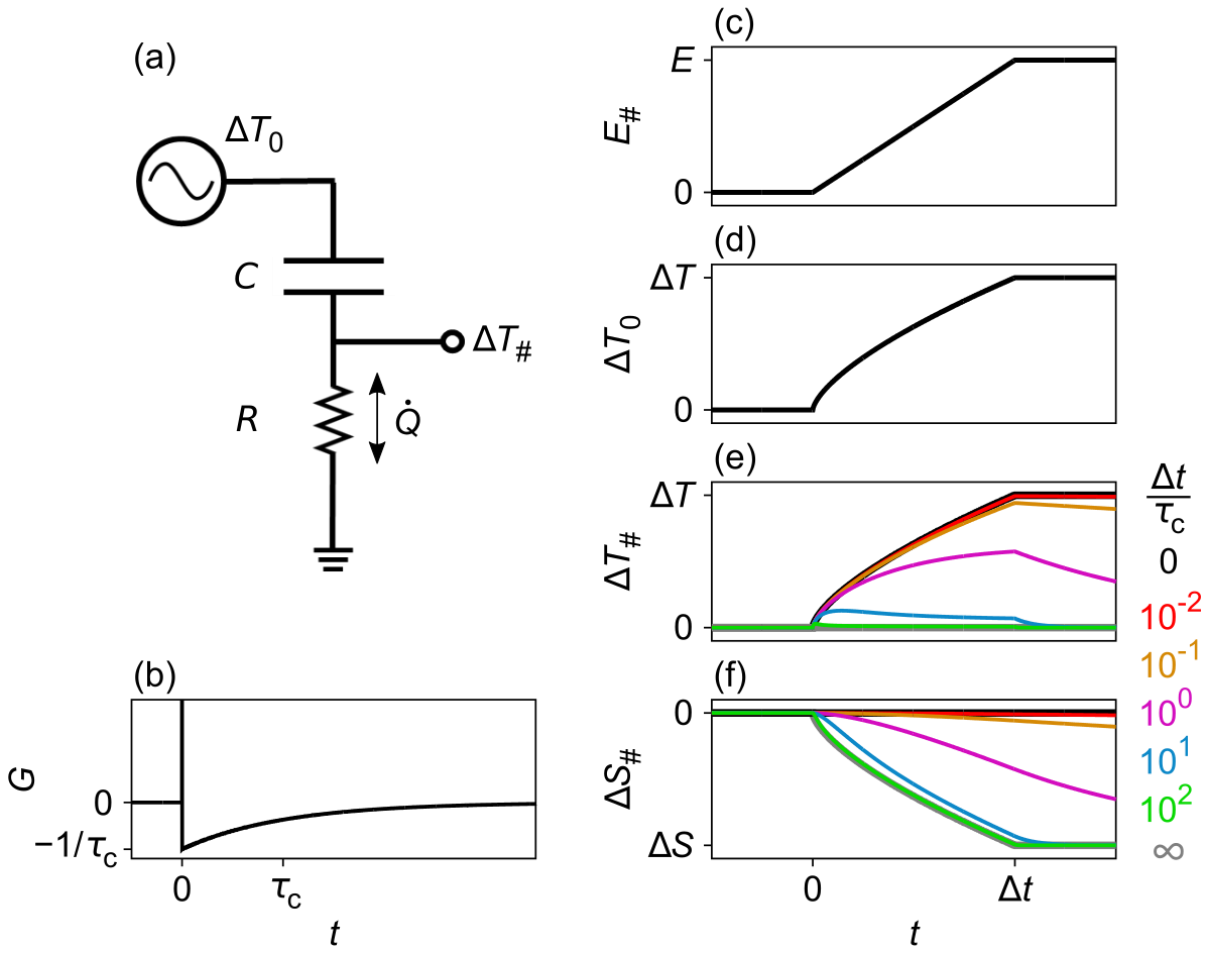

Fig. 2.1 | **Lumped-element thermal model for thermal relaxation describing the cross-over between adiabatic and isothermal field application.**

(a) Lumped-element thermal model for an EC material that can thermalize with its environment, such that the EC temperature change $\Delta T_0(t)$ in the adiabatic limit ($R \to \infty$) is reduced to temperature change $\Delta T_\#(t)$. (b) The Green's function $G(t) = \delta(t) - (\Theta(t)/\tau_c)e^{-t/\tau_c}$ for the RC circuit in (a), where $\tau_c = RC$ is the characteristic time scale for the heat exchange. (c) A linear ramp in electric field $E_\#(t)$ from 0 to E over time Δt generates (d) adiabatic temperature change $\Delta T_0(t)$. (e,f) The corresponding (e) temperature change $\Delta T_\#(t) = \int_{-\infty}^{\infty} G(t')\Delta T_0(t-t')\mathrm{d}t'$ and (f) entropy change $\Delta S_\#(t) = \frac{C}{VT_s}(\Delta T_0 - \Delta T_\#)$ with thermal contact between the EC material and its environment parameterized via τ_c, where $\Delta t/\tau_c \to 0$ corresponds to the adiabatic limit and $\Delta t/\tau_c \to \infty$ corresponds to the isothermal limit.

The time-dependent temperature change is therefore given by:

$$\Delta T_{\#}(t) = \int_{-\infty}^{\infty} G(t')\Delta T_0(t-t')\mathrm{d}t' \tag{2.6}$$

The corresponding time-dependent entropy change is given by:

$$\Delta S_{\#}(t) \sim \frac{1}{T_\mathrm{s}} \int_{-\infty}^{t} \dot{Q}\mathrm{d}t' = \frac{C}{VT_\mathrm{s}} \left(\Delta T_0 - \Delta T_{\#}\right) \tag{2.7}$$

where the factor of T between heat and entropy has been replaced with T_s given that $\Delta T << T_\mathrm{s}$ for EC materials, and where the final expression comes from rearranging and integrating Eq. (2.1) (normalization by volume V ensures that the entropy change is an intensive variable).

Eqs (2.6) and (2.7) permit the time profile of EC effects to be identified from the ratio $\Delta t/\tau_\mathrm{c}$ of the field ramp time to the time scale for thermal relaxation. The adiabatic temperature change $\Delta T_0(t)$ for a given EC material depends on the profile of the electric field $E_{\#}(t)$ via an equation of state $\Delta T(E,S)$ for the material, and this dependence is unique if hysteresis is absent or ignored. Here it will be assumed that $\Delta T_0(t) \propto E_{\#}(t)^{2/3}$ by using $\Delta S(t) \propto E_{\#}(t)^{2/3}$ from the Landau theory of second-order transitions [94] and the extant assumption of constant heat capacity, but the exact form of this relation does not strongly affect the results described below, which may therefore be considered relevant for EC effects more generally.

Assuming a linear ramp of field $E_{\#}(t)$ from 0 to E during time interval Δt (Fig. 2.1c) results in the adiabatic temperature change $\Delta T_0(t)$ shown in Fig. 2.1d. Thermal contact with the environment (parameterized as $\Delta t/\tau_\mathrm{c}$) reduces this temperature change to $\Delta T_{\#}(t)$ (Fig. 2.1e) and the corresponding entropy change is $\Delta S_{\#}(t)$ (Fig. 2.1f). The crossover between the adiabatic limit ($\Delta t/\tau_\mathrm{c} \rightarrow 0$) and the isothermal limit ($\Delta t/\tau_\mathrm{c} \rightarrow \infty$) spans roughly four decades in $\Delta t/\tau_\mathrm{c}$. The field-induced jump in temperature ΔT_j for $\Delta t/\tau_\mathrm{c} \sim 10^{-2}$ (red line in Fig. 2.1e) is 99% of the adiabatic jump ΔT (black line in Fig. 2.1d,e). By contrast, ΔT_j for $\Delta t/\tau_\mathrm{c} \sim 10^{2}$ (green line in Fig. 2.1e) is just 3% of ΔT and the system lies close to the isothermal limit (grey line in Fig. 2.1e). It is therefore reasonable to suggest that changes of field may be

considered highly adiabatic (isothermal) if they proceed faster (slower) than the characteristic time scale of thermal relaxation by roughly two orders of magnitude or more. Field changes at less extreme rates may be considered quasi-adiabatic and quasi-isothermal.

2.2 Indirect Methods

Indirect methods describe a class of techniques that parameterize EC effects by exploiting thermodynamic analysis of electrical measurements obtained over a range of temperatures [12]. These techniques represent an alternative with respect to direct measurements and are often the only way of evaluating EC effects in thin films, whose EC signal cannot be measured directly because it is small and rapidly decaying (due to heat exchange with any substrate). It is becoming ever more apparent that the underlying thermodynamic analysis relies on assumptions that can limit validity. First, analysis based on equilibrium thermodynamics cannot be expected to provide a good description of non-ergodic systems like relaxor ferroelectrics [95], but indirect and direct EC measurements in relaxors have nevertheless yielded reasonable agreement across a range of different materials and embodiments [32, 34, 96]. Second, the assumption of constant stress or constant strain is not always safe. Clamped thin films are assumed to possess an in-plane strain that is fixed by the substrate, but the film is free to deform out-of-plane. It has been suggested that these complex mechanical boundary conditions can modify the EC effect via secondary elastocaloric contributions, which if relatively large would compromise the commonly used Maxwell relation discussed in Section 2.2.1 [97].

Sections 2.2.2 and 2.2.3 cover electrical and thermal hysteresis, respectively, and describe the construction of datasets that are single-valued as required for the thermodynamic analysis described in Section 2.2.1. The pitfalls that can arise in electrical measurements and potential solutions are discussed in Section 2.2.4, and alternative indirect methods are described in Section 2.2.5.

The subsequent discussion assumes that the experimentally measured charge-voltage $q(V)$ characteristics of EC capacitors are geometrically normalized to yield the field-displacement relation $D(E)$, where $D = q/A$, $E = V/d$, A is electrode area and d is capacitor thickness. Note that the displacement D and polarization P can be used interchangeably when using the Maxwell relations of interest because partial derivatives of D and P at constant E are equivalent given that $D = \varepsilon_0 E + P$.

2.2.1 The Maxwell methods

The most common indirect method of measuring EC effects is the Maxwell method [32], which exploits Maxwell relations to compute ΔS or ΔT from variable-temperature electrical polarization measurements. In the standard version of this method, isothermal measurements of polarization $P(E)$ at various temperatures T are used to construct a $P(T,E)$ dataset assumed to be single-valued. The Maxwell relation $\left.\frac{\partial S}{\partial E}\right|_T = \left.\frac{\partial P}{\partial T}\right|_E$ derived from the Gibbs free energy is then used to numerically compute the reversible isothermal entropy change $\Delta S(T,E) = \int_0^E \left.\frac{\partial P}{\partial T}\right|_{E'} \mathrm{d}E'$ for an applied field change of $0 \rightarrow E$.

An alternative Maxwell method [98] was recently implemented in my co-authored paper [2], where isentropic measurements of $P(E)$ at nearby starting temperatures T_s were used to construct a $P(T_s,E)$ dataset assumed to be single-valued (the measurements are described as adiabatic in [2], but this fails to specify the need to avoid dissipation from Joule heating, and the correct description is isentropic). Measurements of the zero-field heat capacity $c(T)$ permit the zero-field entropy $S'(T) = S(T) - S(T_0) = \int_{T_0}^{T} \frac{c(T')}{T'} \mathrm{d}T'$ to be determined with respect to the absolute entropy S at base temperature T_0, permitting the $P(T_s,E)$ dataset to be reparameterized as $P(S',E)$. The Maxwell relation $\left.\frac{\partial T}{\partial E}\right|_S = -\left.\frac{\partial P}{\partial S}\right|_E$ derived from enthalpy is then used to numerically compute the reversible adiabatic temperature change $\Delta T(S',E) = -\int_0^E \left.\frac{\partial P}{\partial S}\right|_{E'} \mathrm{d}E'$ for an applied field change of $0 \rightarrow E$. The inverted zero-field relation $T(S')$ can then be used to reparameterize $\Delta T(S',E)$ as $\Delta T(T_s,E)$.

In the bulk of the EC literature, the interconversion of ΔS and ΔT is achieved via $\Delta T \sim \frac{T\Delta S}{c_{\mathrm{eff}}}$, where the heat capacity $c(T,E)$ is replaced by an effective value c_{eff} instead of performing an evaluation that takes into account the field and temperature dependence [12]. A better method of converting ΔS to ΔT is presented in Chapter 3 and [1], and outlined in Fig. 2.2. Maps of isothermal entropy change $\Delta S(T,E) = \int_0^E \left.\frac{\partial P}{\partial T}\right|_{E'} \mathrm{d}E'$ (Fig. 2.2a) derived from dense isothermal $P(T,E)$ data is combined with $S'(T,0)$ derived from zero-field heat capacity data to construct

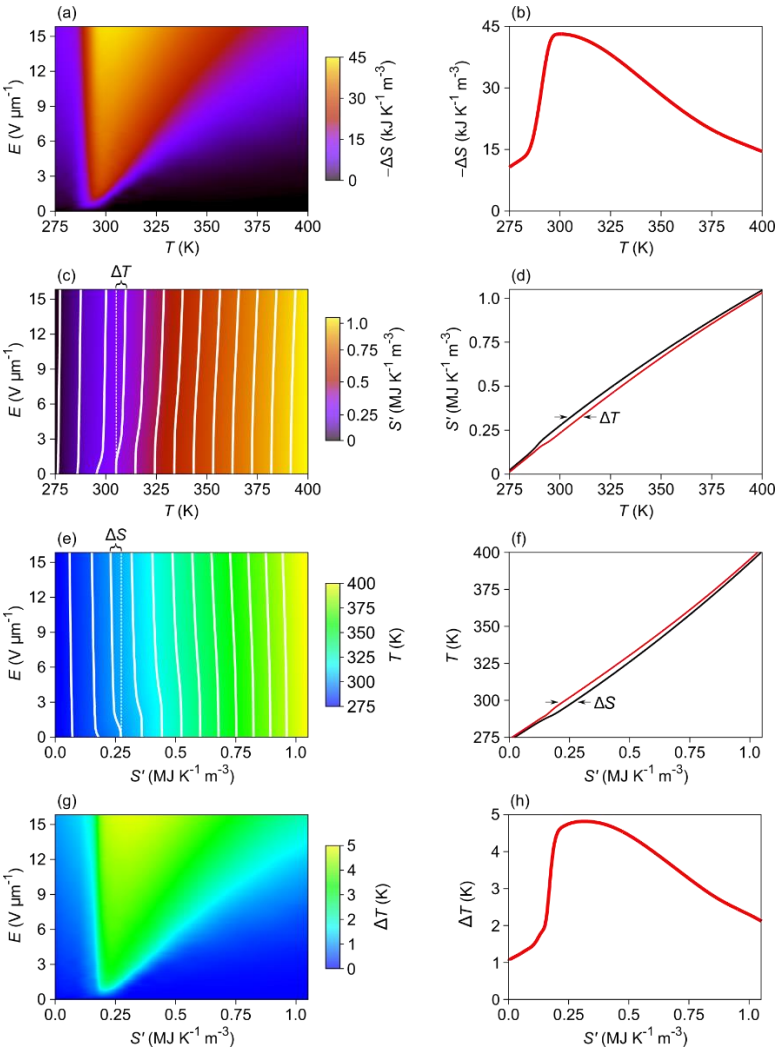

Fig. 2.2 | **Interconversion of Δ*S* and Δ*T*.**

Starting with (a) isothermal entropy change $\Delta S(T,E)$, adding the zero-field entropy $S'(T,0)$ yields (c) entropy map $S'(T,E)$. Adiabatic temperature change ΔT is identified as the T-axis displacement along isentropic contours (solid white lines) in (c). This procedure is equivalent to adding $S'(T,0)$ to (b) any cross-section $\Delta S(T)$ to yield (d) isofield entropy $S'(T)$, shown for both zero field (black) and field applied (red). The adiabatic temperature change ΔT is identified as the T-axis separation between the two isofields. The identification of isentropic contours in (c) represents a transpose that yields (e) the temperature map $T(S',E)$ and subtracting the inverted relation $T(S',0)$ yields (g) adiabatic temperature change $\Delta T(S',E)$. If instead starting with (g) adiabatic temperature change $\Delta T(S',E)$, adding $T(S',0)$ yields (e) temperature map $T(S',E)$. Isothermal entropy change ΔS is identified as the S'-axis displacement along isothermal contours (solid white lines) in (e). This procedure is equivalent to adding $T(S',0)$ to (h) any cross-section $\Delta T(S')$ to yield (f) isofield temperature $T(S')$, shown for both zero field (black) and field applied (red). The isothermal entropy change ΔS is identified as the S'-axis separation between the two isofields. The identification of isothermal contours in (e) represents a transpose that yields (c) the entropy map $S'(T,E)$ and subtracting $S'(T,0)$ yields (a) the isothermal entropy change $\Delta S(T,E)$.

an entropy map $S'(T,E) = S'(T,0) + \Delta S(T,E)$ [Fig. 2.2c]. The reversible adiabatic temperature change ΔT can be read from this map by following isentropic contours for a given change of E and reading the change in contour projection on the T-axis (Fig. 2.2c). Performing this process for the whole $S'(T,E)$ map represents a transpose that yields $T(S',E)$ [Fig. 2.2e], subtracting $T(S',0)$ yields $\Delta T(S',E) = T(S',E) - T(S',0)$ [Fig. 2.2g] and using $T(S',0)$ once more to reparameterize the abscissa yields a map of adiabatic temperature change $\Delta T(T_s,E)$.

The above conversion of $\Delta S(T,E)$ to $\Delta T(T_s,E)$ was pioneered via the reverse process in my co-authored paper [2], where $\Delta T(S',E) = -\int_0^E \left.\frac{\partial P}{\partial S}\right|_{E'} dE'$ (Fig. 2.2g) derived from dense isentropic $P(T_s,E)$ data [after using $S'(T,0)$ to reparameterize as $P(S',E)$] is combined with $T(S',0)$ derived from zero-field heat capacity data to construct a temperature map $T(S',E) = T(S',0) + \Delta T(S',E)$ [Fig. 2.2e]. The reversible entropy change ΔS can be read from this map by following isothermal contours for a given change of E and reading the change in contour projection on the S'-axis (Fig. 2.2e). Performing this process for the whole $T(S',E)$ map represents a transpose that yields $S'(T,E)$ [Fig. 2.2c], and subtracting $S'(T,0)$ yields a map of isothermal entropy change $\Delta S(T,E) = S'(T,E) - S'(T,0)$ [Fig. 2.2a].

2.2.2 Electrical hysteresis

The single-valued datasets $P(T,E)$ obtained from isothermal measurements and $P(T_S,E)$ obtained from isentropic measurements should represent equilibrium states that are accessible via reversible processes, and the measured global polarization P should represent the average magnitude of the local polarization, i.e. as for a single domain state. EC effects arising from paraelectric-to-ferroelectric transitions [2, 99] and antiferroelectric-to-ferroelectric transitions [30] both suffer field hysteresis, such that the outer and inner branches of bipolar or unipolar loops access metastable states [98]. Either the equilibrium polarization can be approximated by averaging inner and outer branches, or EC effects deduced from outer branches can be compared with EC effects deduced from inner branches and hopefully found to be similar [2]. Below T_C, (misoriented) ferroelectric domains compromise both the assumption of equilibrium/reversibility and the correspondence between global and local polarization. Domains are therefore minimized by employing the outer branches of major bipolar loops, whose reversibility can be verified by measuring unipolar loops that are similar [1, 2].

Measurements of $P(E)$ can be frequency-dependent due to the kinetics of nucleation and growth that affect the formation of new phases [100] and ferroelectric domains below T_C [101]. In the Hz-to-MHz range that is typical for indirect EC measurements, the frequency dependence typically arises due to defects that nucleate phases or pin domains. If the EC material is not leaky then one should vary the applied field as slowly as possible to improve reversibility, as evidenced by a convergence of branches that reduces the irrecoverable work $W = \oint E\mathrm{d}P$ [100]. Nevertheless, in the Hz and sub-Hz ranges associated with EC service conditions, reversibility is more likely to be compromised by leakage than defects.

2.2.3 Thermal hysteresis

EC effects associated with phase transitions can be associated with second-order transitions that do not exhibit thermal hysteresis, as seen for a few bulk ferroelectric materials such as triglycine sulphate (TGS) [102], and thin films if strain has driven a first-order transition second order [103]. However, EC effects are commonly associated with first-order phase transitions whose thermal hysteresis can compromise the reversibility of EC effects as discussed below. When measuring indirect (or direct) EC effects associated with first-order phase transitions, it is important to ensure that reversibility is not compromised by thermal hysteresis, as discussed below for conventional EC materials.

On cooling, a thermally hysteretic transition starts at temperature $T_{c1}(E)$ and finishes at temperature $T_{c2}(E)$, while on warming the transition starts at temperature $T_{h1}(E)$ and finishes at temperature $T_{h2}(E)$. For a conventional EC material ($\Delta S < 0$ on field application), these temperatures shift to higher temperatures in an applied field, and it is the relative magnitudes of $T_{c2}(E)$ and $T_{h2}(0)$ that determine whether the transition can be driven reversibly.

As shown in Fig. 2.3a, weakly hysteretic transitions can be readily shifted by an applied field E beyond the temperatures at which there is zero-field hysteresis, such that $T_{c2}(E) > T_{h2}(0)$. Measurements of $P(E)$ should be obtained on warming through the transition in zero field to ensure that field-driven changes are fully reversible (double-headed arrows in Fig. 2.3a). This protocol ensures that field changes either start or finish at a fully transformed single-phase state (green dots in Fig. 2.3a), thereby avoiding irreversibility associated with metastable mixed-phase states that are sensitive to electrical and thermal history. By contrast, on cooling through the transition in zero field, field-driven changes are irreversible (single-headed arrow in Fig. 2.3a) because field removal can cause the system to become trapped in an intermediate metastable state (white dot in Fig. 2.3a).

As shown in Fig. 2.3b, strongly hysteretic transitions cannot be readily shifted by an applied field E beyond the temperatures at which there is zero-field hysteresis, such that $T_{c2}(E) < T_{h2}(0)$. Measurements of $P(E)$ on warming through the transition in zero field are irreversible because the field can take the system between start and end states that are both partially transformed (grey dots in Fig. 2.3b). EC effects are therefore suppressed by strong

thermal hysteresis, as the transition cannot be driven in full electrically. Furthermore, the sensitivity of metastable mixed-phase states to electrical and thermal history can lead to spuriously large indirect measurements of the EC effect [83]. The resultant artefacts in $P(T,E)$ have been hitherto mitigated by using thermal excursions away from the hysteretic regime to reset the sample history between $P(E)$ measurements at different temperatures [83, 104]. This protocol is applicable not just for strong thermal hysteresis but also when cooling through a weakly hysteretic transition.

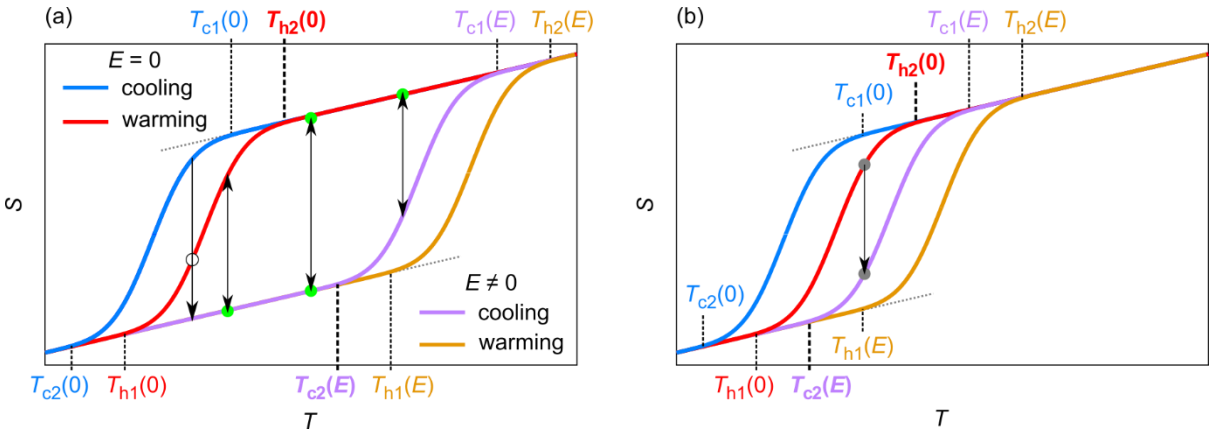

Fig. 2.3 | **EC reversibility with weak and strong thermal hysteresis.**

(a,b) A hysteretic first-order ferroelectric transition at zero field starts on cooling (blue curve) at temperature $T_{c1}(0)$ and finishes at temperature $T_{c2}(0)$, while on warming (red curve) the transition starts at temperature $T_{h1}(0)$ and finishes at temperature $T_{h2}(0)$. For a conventional EC material ($\Delta S < 0$ on field application), all of these temperatures shift to higher temperatures in an applied field E (purple curve represents field cooling; brown curve represent field warming). (a) For a transition that displays weak thermal hysteresis, applied field E shifts $S(T)$ beyond the temperature range in which there is zero-field hysteresis [$T_{c2}(E) > T_{h2}(0)$]. On warming through the transition in zero field, isothermal EC effects can be driven reversibly (double-headed arrows) between two states, of which at least one is a fully transformed single-phase state (green dots). On cooling through the transition in zero field, there are temperatures at which isothermal EC effects are irreversible (single-headed arrow) because field removal causes the system to become trapped in an intermediate metastable state (white dot). (b) For a transition that displays strong thermal hysteresis, applied field E cannot shift $S(T)$ beyond the temperature range in which there is zero-field hysteresis [$T_{c2}(E) < T_{h2}(0)$]. On warming through the transition in zero field, there are temperatures at which isothermal EC effects are irreversible (single-headed arrow) because the start and end points are both partially transformed states (grey dots). (a,b) describe a conventional EC material, such that $\Delta S < 0$ for field application.

2.2.4 Pitfalls and strategies in electrical measurements

Measurements of $q(V)$ are made by circuits that concurrently identify the charge on an EC capacitor and the voltage across it. First, consider a Sawyer-Tower circuit [105] (Fig. 2.4a). The charge drawn by an EC capacitor C_{EC} in response to an input voltage signal accumulates in equal measure on a grounded series shunt capacitor (C_s), and this charge is evaluated by measuring the voltage across the shunt. The voltage across the EC capacitor can be approximated by the input voltage signal across both capacitors because the shunt capacitor is large ($C_s >> C_{EC}$). Second, a virtual ground circuit based on operational amplifiers (Fig. 2.4b) can be used to avoid the shunt capacitor that divides the input voltage. A charge amplifier or a current-to-voltage amplifier can be used to measure the charge or current drawn by the EC capacitor in response to the input voltage [106, 107]. Both circuits are schematized together in Fig. 2.4b: switch down corresponds to the charge-amplifier circuit and switch up corresponds to the current-to-voltage amplifier. Third, a power supply acting as a current source can be used to charge and discharge the EC capacitor to a pre-programmed maximum voltage while the voltage across the capacitor is monitored with a voltmeter [1] (Fig. 2.4c).

The input impedance of any oscilloscope/amplifier/voltmeter can distort low-frequency components of the measured voltage signal, while open or asymmetric $q(V)$ plots can arise from instrumental factors that include leakage through a sense capacitor, DC offsets on the amplified voltage, and electrometer drift [107]. Separately, it is perhaps not well appreciated that the properties of a measurement circuit determine whether EC capacitors are shorted between successive electrical measurements, which affects $P(E)$ characteristics in materials that are sensitive to electrical history, most notably non-ergodic dipolar systems or those with strong thermal hysteresis (Section 2.2.3). Lastly, cabling can contribute stray capacitance that lies electrically in parallel to the EC capacitor, and if the two capacitances are comparable (on the order of pF), stray contributions to the current must be subtracted by measuring the capacitance of the cables.

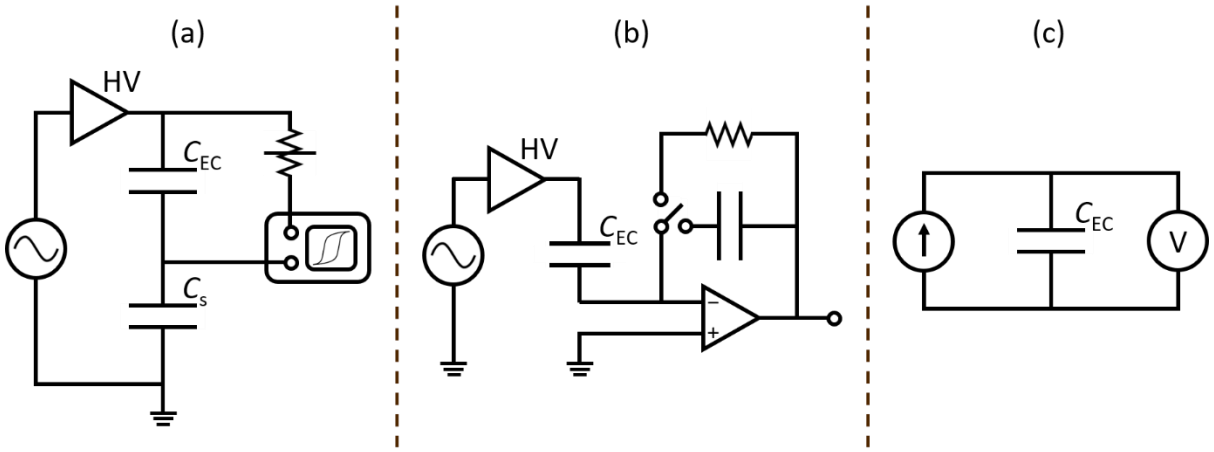

Fig. 2.4 | **Circuits for *P*(*E*) measurements.**

(a) The Sawyer-Tower circuit employs a capacitor shunt to ground in order to convert the charge drawn by the EC capacitor into a voltage that can be traced by an oscilloscope against the input voltage, which is mainly dropped across the EC capacitor ($C_s >> C_{EC}$). (b) Operational amplifiers are exploited in virtual ground circuits to convert the charge or the current associated with the EC capacitor into a voltage at the output, using capacitive (switch down) or resistive (switch up) feedback, respectively. (c) A voltmeter reads the voltage across an EC capacitor while it is charged and discharged by a current source whose maximum voltage is pre-programmed.

Highly insulating samples are required to ensure that the charge $q = \int I \, dt$ on capacitor plates is correctly determined by integrating the current I that flows when EC effects are driven. Ohmic leakage will produce spurious electrical hysteresis [108], as the phase offset between resistive and capacitive current inflates (suppresses) the apparent polarization along outer (inner) branches of $P(E)$ plots; the resulting spurious contribution to $\partial P/\partial T$ would depend on the temperature dependence of the leakage current. Correct values of polarization can however be identified by using a variable resistor in parallel with a Sawyer-Tower shunt capacitor to compensate the leakage current [109]. Alternatively, impedance spectroscopy can be used to determine a parallel RC circuit model for leaky EC capacitors, allowing the leakage current to be removed during data processing. One might instead render leakage currents negligibly small by increasing the drive frequency well beyond the $1/RC$ cut-off, but this can compromise polarization measurements as discussed in Section 2.2.2. However, the concave $P(E)$ loop signature of ferroelectric hysteresis [108] can be produced by spurious effects such as non-linear conduction through Schottky contacts [110] and electret behaviour arising from mobile charge (impurities/defects/dopants) [111]. These artefacts and all of the

aforementioned problems can be difficult to remove satisfactorily, so it is best to have highly insulating samples for EC measurements, especially because Joule heat cannot be tolerated while dumping heat in any application.

When changing the measurement temperature to obtain successive plots of $P(E)$, the pyrocurrent drawn by the EC capacitor is typically not measured, such that the initial (remanent) charge is unknown. However, this does not matter because $P(E)$ plots should be centred along the P-axis, which requires high-quality samples whose hysteresis loops are saturated, symmetric, and closed (no polarization gaps). Internal biasing fields that compromise symmetric hysteresis in ferroelectrics can arise from asymmetries in capacitor geometry as well as ageing, fatigue and imprint [112]. Biasing due to ageing is caused by microstructural defects that explicitly break symmetry over time in response to a sustained state of polarization/strain [113], and can to some extent be reversed [112] by electrical or thermal cycling. Fatigue due to DC poling or unipolar field cycling can generate biasing via space charge accumulation at interfaces (such as grain boundaries or dead layers near the electrodes) in response to depolarizing fields that are not fully screened by free charges and/or the local domain structure [114]. A polarization state may be inadvertently imprinted in films via process-induced oxygen vacancy accumulation at one of the interfaces [115], the presence of dead layers near the electrodes [116], and/or strain gradients [117]. However, imprint in thin films can potentially be undone via UV exposure or annealing [115].

2.2.5 Alternative indirect methods

Maxwell method with pyroelectric measurements

The Maxwell method can be used to evaluate $\Delta S(T,E)$ by constructing a $\frac{\partial P(T,E)}{\partial T} = \frac{I_{\text{pyro}}}{A} \Big/ \frac{\mathrm{d}T}{\mathrm{d}t}$ dataset via constant-electric-field measurements of the closed-circuit pyrocurrent I_{pyro} while sweeping the temperature at rate $\frac{\mathrm{d}T}{\mathrm{d}t}$ [118]. This technique is likely to be time-consuming because it requires multiple temperature sweeps, and it may be necessary to separate pyrocurrents from leakage (Section 2.2.4); but the single-domain assumption of the Maxwell method is likely to be strengthened by the fixed field that is applied during these sweeps, and by any poling that is performed prior to upsweeps through the Curie temperature.

Thermal hysteresis in the pyrocurrent implies the existence of two major $\frac{\partial P(T,E)}{\partial T}$ branches near the transition, each of which should be combined with the corresponding branch of the zero-field heat capacity $c(T)$ to construct two separate $S'(T,E)$ datasets. This method was pioneered for analogous (quasi-direct) measurements of heat in [119], and in Section 2.4.2 it is discussed along with the use of the two $S'(T,E)$ datasets.

One might also consider whether one can replace pyrocurrent measurements that yield $\frac{\partial P(T,E)}{\partial T}$ with pyrovoltage measurements that yield $\frac{\partial E(T,D)}{\partial T}$. This would imply using a Maxwell relation $\left.\frac{\partial E}{\partial T}\right|_D = -\left.\frac{\partial S}{\partial D}\right|_T$ that is derived from the Helmholtz free energy instead of the Gibbs free energy or the enthalpy (Section 2.2.1), such that one would evaluate the isothermal entropy change $\Delta S(T,D) = -\int_0^D \left.\frac{\partial E}{\partial T}\right|_{D'} \mathrm{d}D'$ for a change in electrical displacement $0 \rightarrow D$. However, values of D do not necessarily extend down to zero for single-domain states at equilibrium, which are required for the Maxwell relation to be valid. The practical manifestation of this problem is that the requisite fixed-charge (constant D) measurements of the open-circuit pyrovoltage V_{pyro} would below the Curie temperature somewhat inevitably involve the formation of ferroelectric domains at all but the highest values of D. This domain formation can be rationalized from an isothermal plot of $D(E)$ below T_{C}, whose many sub-remanent values of D necessarily fail to describe single-domain states at equilibrium (by contrast, all values of E

can be accessed on outer branches). Note that D cannot be replaced with P, as it can when using the Maxwell relations derived from the Gibbs free energy or the enthalpy (Section 2.2.1), and here it is E that could be replaced with $-P$ because their partial derivatives at constant D are equal given that $D = \varepsilon_0 E + P$.

Clausius-Clapeyron method

Near a first-order phase transition, the caloric effect in each phase itself can be negligible with respect to the contribution from the transition itself. If so, the EC effect can be estimated by replacing the Maxwell relations with the Clausius Clapeyron relation $\Delta S = \Delta P \frac{dE}{dT}$ [12], where $\frac{dE}{dT}$ is the slope of the phase boundary in the E-T phase diagram, ΔP is the jump in polarization across the transition, and both ΔS and ΔP are assumed constant along the phase boundary as per standard practice. Experimentally, the values of $\frac{dE}{dT}$ and ΔP are most simply obtained from the same $P(E)$ plots that are used for the Maxwell method.

Quasi-indirect method

This method was pioneered to measure magnetocaloric effects [120] and has been recently implemented to measure EC effects in bulk PST [121]. Values of ΔT and ΔS can be determined by comparing isentropic and isothermal measurements of $P(E)$ at nearby starting temperatures. The adiabatic temperature change ΔT that arises when following some segment of an isentropic $P(E)$ plot is identified as the temperature difference between the isothermal $P(E)$ plots that intersect the start and end points: if the start point on the isentropic $P(E)$ segment intersects an isothermal $P(E)$ plot at $E = 0$ and starting temperature T_s, and if the end point on the isentropic $P(E)$ segment intersects an isothermal $P(E)$ plot at finite E and finish temperature T_f, then the adiabatic temperature change due to the application of field E is identified as $\Delta T(T_s,E) = T_f - T_s$.

Evaluating ΔT by comparing isentropic and isothermal $P(E)$ confers two advantages over the standard Maxwell method. First, the crossing points can be identified from unnormalized values of q and V, so the sample geometry does not need to be known, and no errors result from geometrical data. Second, knowledge of the zero-field heat capacity is not required.

However, if the zero-field heat capacity is known then $P(E)$ can be reparameterized by converting values of temperature to values of entropy. An analogous process to the one described above with the roles of isentropic and isothermal $P(E)$ reversed then permits the identification of the isothermal entropy change $\Delta S(T,E) = S'_f - S'_s$ due to the application of field E.

2.3 Measurements of temperature change

EC temperature changes in response to rapid changes of applied field can be measured directly by thermometry. Ambipolar changes of field generate ambipolar jumps in temperature ΔT_j that correspond to extrema in plots of instantaneous temperature change $\Delta T_{\#}(t)$, and the magnitude of the field-on and field-off values can differ even when EC effects are fully reversible (Section 2.3.1). Adiabatic temperature change ΔT is well approximated by temperature jumps ΔT_j measured via contact thermometry (Section 2.3.2) if the field changes (Section 2.1) and the effective response time of the thermometer are both much faster than the characteristic time scale of thermal relaxation. If these conditions are not met, then assumptions about thermalization or models of heat transfer can be used to quantify EC heat leaks and thus determine a factor that converts non-adiabatic measured values of ΔT_j to adiabatic temperature change ΔT. However, such conversions can ultimately be unsatisfactory where they are unfalsifiable. Adiabatic conditions can often be better approximated, especially in smaller/thin samples, by instead exploiting non-contact thermometry (Sections 2.3.3 and 2.3.4), which avoids the inactive thermal mass of a contact thermometer.

Both contact [122, 123] and non-contact thermometry [97] have been exploited to measure EC effects in thin films on substrates despite rapid thermalization. However, these EC effects were driven cyclically under quasi-isothermal conditions and were therefore determined using a method that is best described as a modified form of AC calorimetry: measured temperature oscillations and a 1D heat-transfer model are used to evaluate EC heat. These techniques are therefore discussed in greater detail along with direct measurements of heat (Section 2.4.1).

2.3.1 Asymmetries in adiabatic temperature changes

Highly adiabatic measurements of EC temperature changes are typically made via a four-step process that corresponds to a Brayton cycle on an entropy-temperature diagram (Fig. 2.5 and inset). Fast field application results in a temperature jump $\Delta T_j > 0$ that is followed by relaxation back to the starting temperature, and subsequent fast field removal results in a jump of temperature $\Delta T_j < 0$ that is likewise followed by relaxation back to the starting temperature. The two jumps are liable to differ in magnitude because the zero-field isofield and the finite-field isofield converge at high and low temperatures. The asymmetry in $|\Delta T_j|$ is intrinsic to the material and does not evidence irreversibility [1, 124] (see Section 3.7.9).

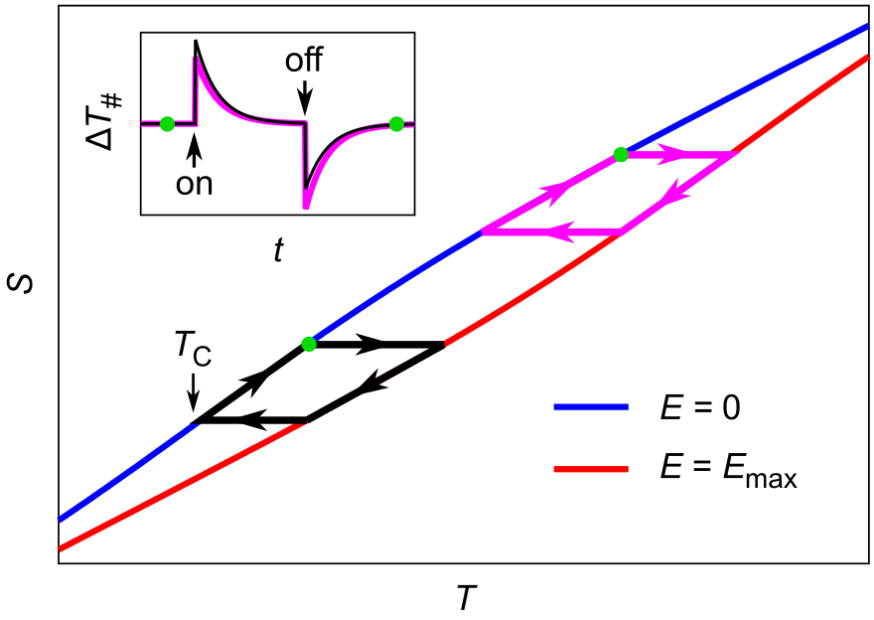

Fig. 2.5 | **Asymmetric Brayton cycles when measuring ΔT.**

A ferroelectric transition is represented by a zero-field $S(T)$ isofield (blue) in the vicinity of the transition temperature T_C. At maximum field E_{max}, the transition is shifted to a different $S(T)$ isofield (red), as shown for a conventional EC material. The black and pink Brayton cycles each involve two temperature jumps ΔT_j that are assumed to be rapid and perfectly isentropic, such that $\Delta T_j = \Delta T$. The other two legs in each cycle coincide with the two isofields. These isofields converge away from the (field-dependent) phase transition, such that the two adiabatic legs in each cycle yield different values of $|\Delta T_j|$, as reported for both first [1] and second-order [124] caloric materials. These different values are also seen when plotting the instantaneous temperature change $\Delta T_{\#}(t)$ for the same cycles (inset) and should not be mistaken for extrinsic differences associated with irreversibility or measurement. Green dots denote start and finish points in the measurement cycle.

The intrinsic asymmetry in jump magnitude described above should not be confused with jump-magnitude asymmetries that arise when hysteretic phase transitions are driven irreversibly [61] (Section 2.2.3). Note that Joule heating in electrically leaky EC materials does not create asymmetries in jump magnitudes because highly adiabatic EC changes of temperature occur very quickly with respect to the time it takes to switch on and off the net temperature lift from Joule heating. Field-off and field-on jump magnitudes should therefore be read directly with respect to the baseline from which each follows. The common practice of erroneously correcting both baselines for Joule heating leads somewhat refreshingly to an unduly conservative interpretation.

2.3.2 Contact thermometry

Contact thermometry of bulk samples [24, 30, 32], multilayer capacitors (MLCs) [4, 51], and free-standing polymer films [34, 63] typically exploit either a thermocouple or a thermistor that is in good thermal contact with the EC capacitor. The thermometer should be electrically isolated from the electrodes to avoid electrical crosstalk, and if the thermometer is situated near one of the electrodes then that electrode should be grounded to minimize electrical crosstalk. Moreover, the heat capacity of the thermometer should be as small as possible to minimize the reduction in the adiabaticity of the EC capacitor. Strategies such as measuring in vacuum and using thin wires to make electrical contact (Section 2.1) can also be exploited to minimize heat leaks between the thermometer and the environment to ensure accurate measurement.

When a contact thermometer thermalizes with an EC capacitor, the response of the thermometer depends on the heat capacities and thermal conductances of the thermometer, the EC capacitor, and any inactive material that separates the two. Two complications arise as follows. First, the inactive material separating the thermometer from the active EC material can lie external to (e.g. adhesive or insulation) or within (e.g. electrodes or inactive dielectric) the EC capacitor, but for simplicity the distinction between the EC capacitor and active EC material will be ignored here. Second, it will be assumed that the thermometer itself does not affect the time scale τ_c that governs thermalization of the EC material with the environment, which is reasonable for a relatively small thermometer. Thermalization of the contact thermometer with the EC capacitor after rapid changes of applied field can therefore be modelled by a differential equation of the same form as Eq. (2.1):

$$\frac{\dot{Q}}{C} + \frac{\mathrm{d}T}{\mathrm{d}t} = \frac{\mathrm{d}T_0}{\mathrm{d}t} \tag{2.8}$$

Here, the first term on the left represents a rate of change in temperature due to the flow of EC heat $\dot{Q}$ between the EC capacitor and the thermometer with heat capacity C. The second term represents the rate of change of the temperature T of the thermometer, which in the limit of perfect thermalization between the thermometer and EC capacitor (i.e. $\dot{Q} = 0$; cf. ideal voltmeter) is equal to the source term on the right: $T_0(t)$ describes the temperature of the EC

capacitor due to a ramp in field $E_{\#}(t)$ over time interval Δt and (subsequent) thermal relaxation with the environment on a characteristic time scale τ_c, such that a rapid field change is represented by the limit $\Delta t/\tau_c \rightarrow 0$ (Section 2.1).

Using Newton's law of cooling, the heat flow to/from the thermometer can be written as $\dot{Q} = (T_0 - T)/R$, where the temperature difference $T_0 - T$ between the EC material at $T_0(t)$ and the thermometer at $T(t)$ drives heat at rate $\dot{Q}$ through a thermal resistance R that subsumes the thermal resistances of the thermometer, EC capacitor, and any inactive material separating the two. Using the notation $\Delta T_{\#}(t) = T - T_s$ and $\Delta T_0(t) = T_0 - T_s$ introduced in Section 2.1, where T_s is the (starting) temperature of the environment, Eq. (2.8) thus becomes:

$$\frac{\Delta T_0 - \Delta T_{\#}}{RC} + \frac{\mathrm{d}(\Delta T_{\#})}{\mathrm{d}t} = \frac{\mathrm{d}(\Delta T_0)}{\mathrm{d}t} \tag{2.9}$$

Eq. (2.9) is identical in form to the differential equation that would describe a series RC circuit in electronics, where the source term ΔT_0 corresponds to an input voltage, but unlike Eq. (2.3), the temperature change $\Delta T_{\#}$ corresponds to a voltage across an electrical capacitor. The thermal analogue relevant here is a lumped-element model (Fig. 2.6a) in which the thermometer (capacitor C) exchanges heat $\dot{Q}$ across a thermal link (resistor R) to the EC capacitor (input).

A small thermometer that does not affect the time scale τ_c (which governs thermalization of the EC capacitor) but nevertheless has finite response time τ_r corresponds to the limits $C \rightarrow 0$ and $R \rightarrow \infty$, such that $\tau_r = RC$ is finite. The Green's function required to solve Eq. (2.9) [93] is given by:

$$G(t) = (\Theta(t)/\tau_r)e^{-t/\tau_r} \tag{2.10}$$

and shown in Fig. 2.6b. The time-dependent temperature change in the thermometer is then given by:

$$\Delta T_{\#}(t) = \int_{-\infty}^{\infty} G(t')\Delta T_0(t - t')\mathrm{d}t' \tag{2.11}$$

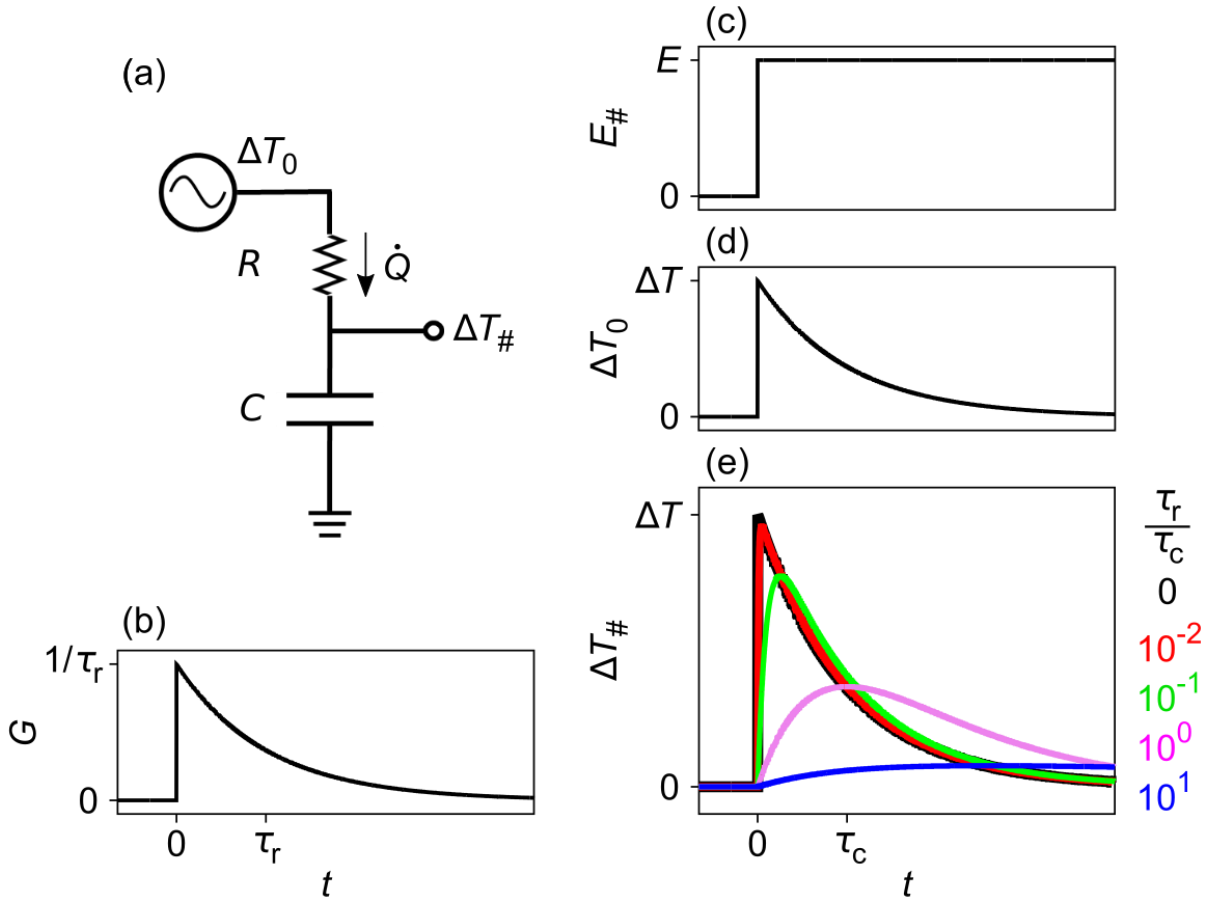

Fig. 2.6 | **Lumped-element thermal model describing the effect of thermometer response time on contact thermometry.**

(a) Lumped-element thermal model for a contact thermometer that thermalizes with an EC capacitor, such that EC temperature change $\Delta T_0(t)$ differs from measured temperature change $\Delta T_\#(t)$ due to finite thermometer response time $\tau_r = RC$. (b) The Green's function $G(t) = (\Theta(t)/\tau_r)e^{-t/\tau_r}$ for the RC circuit in (a). (c) Field $E_\#(t)$ switched on (instantaneously) from 0 to E at time $t = 0$ generates (d) EC temperature change $\Delta T_0(t) = |\Delta T|\Theta(t)e^{-t/\tau_c}$ that relaxes on a characteristic time scale τ_c ($\Theta(t)$ is the Heaviside step function). (e) The resulting temperature change $\Delta T_\#(t) = \int_{-\infty}^{\infty} G(t')\Delta T_0(t - t')dt'$ recorded by the thermometer is parameterized via the ratio τ_r/τ_c.

Eq. (2.11) permits the time profile of measured temperature changes to be identified from the ratio τ_r/τ_c of the thermometer response time to the time scale for thermal relaxation. An electric field $E_{\#}(t)$ (Fig. 2.6c) switched on at $t = 0$ instantaneously (i.e. $\Delta t = 0$) generates in the EC capacitor a temperature change $\Delta T_0(t) = |\Delta T|\Theta(t)e^{-t/\tau_c}$ (Fig. 2.6d), corresponding to the limit $\Delta t/\tau_c \to 0$ in Section 2.1. The resulting measured temperature change $\Delta T_{\#}(t)$ depends on thermometer response time, as shown for selected ratios τ_r/τ_c in Fig. 2.6e.

The jump in temperature ΔT_j recorded by the thermometer for $\Delta t/\tau_c \sim 10^{-2}$ (red line in Fig. 2.6e) is 95% of the adiabatic jump ΔT (black line in Fig. 2.6d,e), while ΔT_j for $\tau_r/\tau_c \sim 10^{-1}$ (green line in Fig. 2.6e) is reduced to 77% of ΔT. It is therefore reasonable to regard contact thermometry to be highly adiabatic if the response time of the thermometer is roughly two or more orders of magnitude faster than the characteristic time scale on which the EC capacitor undergoes thermal relaxation. Note that the effective response time of the thermometer will be increased if there is noise due to longer integration times or the need to calculate rolling averages.

The fastest contact thermometers typically have response times on the order of milliseconds, which is too large to measure samples thinner than 10-100 μm (see Table 2.1). This is especially true when substrates are present, such that thermal relaxation times can be as fast as nanoseconds and microseconds (Table 2.1). The use of heat transfer models to scale any measured temperature jumps into the adiabatic limit is challenging, particularly for heterogeneous systems that thermalize via conduction and convection in three dimensions. Sometimes this scaling is instead performed using the heat capacity of the active EC material divided by the heat capacity of the entire system [51, 64, 85, 125-127] (active EC material, any inactive EC material, electrodes, thermometer, and any glue, sample holder, etc.). The underlying assumption is that the thermometer thermalizes with the rest of the system after the rest of the system has thermalized with itself rather than the environment [1] (see Section 3.6.13). If this assumption is false then $|\Delta T|$ will be overestimated, as explained in my co-authored paper for the case of MLCs [5].

2.3.3 Infrared thermometry

Infrared (IR) thermometry is very attractive because it is non-contact and can be performed with either an inexpensive sensor [2, 128] or a camera [1, 129, 130] that generates images at some frame rate. The resulting movie can be particularly important for optimizing MLC geometry and thus the cooling power that it can deliver [131]. IR thermometry exploits the temperature dependence of grey-body radiation to infer absolute temperature from photon counts at infrared detectors, e.g. InSb photodiodes. Given that radiative heat transfer proceeds at the speed of light, thermometer response time depends on the imaging frame rate and/or the related but independently adjustable integration time, which is reduced at high temperature to prevent detector saturation. For fast measurements near room temperature, cameras operating at long IR wavelengths are preferable to those operating at medium or short IR wavelengths, as the higher photon flux at long wavelengths permits shorter integration times. Acquisition rates of up to ~10^5 Hz make infrared thermometry suitable for directly measured temperature change in substrate-bound EC layers as thin as 1-10 μm (Table 2.1).

In order to use an IR camera to map the temperature of an object, IR emissions that come directly from the focal plane must be distinguished from any other IR radiation. If the object—or rather its surface—displays high emissivity, negligible reflectivity, and negligible transmission then the camera receives emissions somewhat exclusively from this surface, and thus the object alone, as intended. This scenario can be enforced by coating materials and electrodes with a thin layer of high-emissivity material (e.g. black paint in Chapter 3 [1]), and the focal plane of the camera should be set at the surface (Fig. 2.7a). One might instead attempt to image an object for which reflections are not negligible, e.g. the bare top electrode of an EC capacitor, or the uppermost inner electrode of an MLC. As shown in Fig. 2.7b under the assumption of surface reflectivity, the camera is then liable to receive emissions from itself (Narcissus effect) and other ambient sources in addition to emissions from the object itself, just as an optical camera can form images of a surface at which light is reflected or generated.

If an object displays non-negligible IR transmission then the resulting images are liable to include radiation that originates below the surface, at depths whose scale is set by the penetration depth [89] if one assumes a monolithic material. One may then set the focal plane below the surface (Fig. 2.7c), e.g. in order to image the uppermost inner electrode of an MLC, but one would detect emissions from above and below the focal plane if studying a monolithic material. If the material displays non-negligible scattering in addition to non-negligible transmission then it is translucent, and sub-surface emissions will originate from points that are laterally displaced with respect to the points in the focal plane from which they appear to come (Fig. 2.7d). The apparent location of EC effects in translucent materials is therefore prone to corruption, most notably when studying a complex device geometry (see Fig. 2.8).

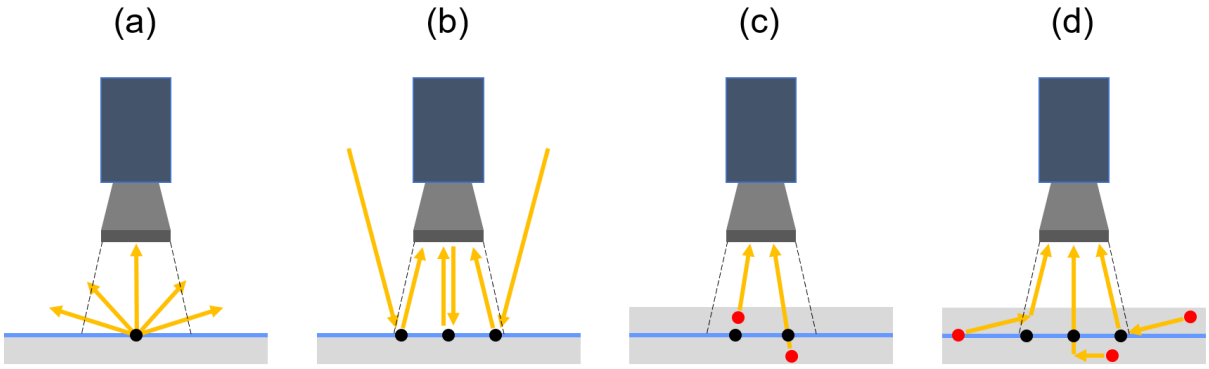

Fig. 2.7 | **Sources of IR radiation detected by a camera.**

(a-d) For a potentially complex object (light grey) in which any given region might or might not display EC effects, the focal plane of the camera (blue line) should be (a,b) set at the surface if IR transmission is negligible at the surface, and (c,d) may be set near or at the surface if IR transmission is appreciable near the surface. Emissions either (a) originate as intended or (b-d) undesirably appear to originate from points (black dots) that lie both on the focal plane and within the field of view (between dotted lines). Orange arrows represent IR rays. (a) Surface emissions dominate the image. (b) If surface reflectivity is appreciable then emissions from the camera and ambient are liable to contribute to the image. (c) If near-surface transmission is appreciable then emissions from a sub-surface focal plane (that are not shown) are accompanied by emissions from points (red dots) that lie above and below. (d) If near-surface scattering is appreciable then the scenario shown in (c) is augmented by emissions from points (red dots) that are laterally displaced with respect to their apparent point of origin. This lateral displacement is not restricted to the field of view.

Raw IR images of surfaces that appear uniform by eye may in fact require pixel-by-pixel correction for spatially varying emissivity, reflectivity, and transmissivity. Furthermore, these three parameters can depend on the frequency of the IR radiation. If the imaged surface has any dispersion [132] in these parameters over the spectral range of the detector then the photon count-to-temperature conversion would be further complicated, but this issue is typically ignored.

In order to determine the temperature of an imaged surface, it is necessary to isolate the emissive contribution (Fig. 2.7a) to the IR radiation received by the camera. Narcissus effects can be minimized by imaging surfaces at a small non-zero angle of incidence [132] such that incident rays originating from the detector array cannot be reflected back to the detector array. Ambient radiation that is reflected by the imaged object can be considered to arise from a uniform background temperature T_R if both camera and sample stage are covered with a thermal shield of high-emissivity material that blocks (heterogeneous) thermal radiation from the environment.

It is challenging to image surfaces of low emissivity and high reflectivity, such as the large metallic electrode of a parallel-plate EC capacitor. Little radiation is emitted, and heterogeneous reflectivity due to surface imperfections [132] (e.g. roughness, cleanliness, etc.) can produce spurious inhomogeneities in apparent temperature. One can instead image an EC capacitor from its side if its thickness exceeds the pixel pitch of the camera, but this requires electrodes that extend near to the edge, which can increase the probability of flashover breakdown at high fields.

Spurious effects can be especially pronounced when imaging the complex geometry of an MLC, in which interdigitated electrodes address an active volume of EC material that is surrounded by inactive regions of EC material and perhaps casing. An IR image (from a movie) of the inactive surface that lies above and around the uppermost interdigitated electrode is shown (Fig. 2.8a) for an MLC of PST (Chapter 3), just after a voltage has been rapidly applied across MLC terminals in order to drive EC effects in the active volume. Regions of the inactive margins lying up to ~1 mm away from the active volume implausibly appear to have reached a higher temperature than the ~38 μm-thick inactive layer that lies directly over the active volume (within the black box). The higher apparent temperature in

the margins is attributed to an artefact caused by the translucency of the EC material: photons that are electrocalorically generated in the active region can be scattered by the inactive margins such that they arrive at the camera as if originating from these margins (Fig. 2.7d). This scattering may arise primarily at grain boundaries given that the grain size of ~2-3 µm (Section 3.6.3) falls within the range of wavelengths detected by the camera. By contrast, photons from the active volume cannot appear as if coming from the top inactive layer, as they are reflected (and absorbed) by the intervening metallic electrode.

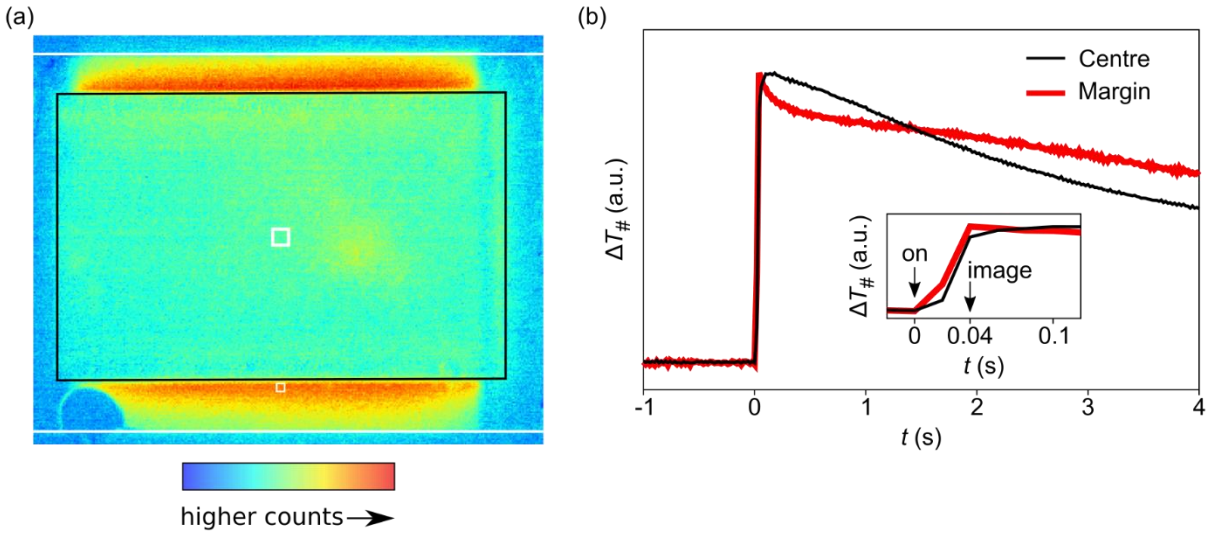

Fig. 2.8 | **Artefacts in IR imaging of EC temperature change in the MLC geometry.**

(a) Raw IR difference image for the bare face of an MLC of PST. The difference was taken between images acquired before and immediately after a rapid field ramp that took place between $t = 0$ and $t \sim 0.04$ s. The image spuriously implies that parts of the inactive margins on either side of the active region (black rectangle) undergo a temperature change that exceeds the temperature change in the (inactive) layer of PST that lies above the active region. (b) The apparent changes of temperature $\Delta T_{\#}$ were averaged within the white boxes in (a) that lie at the centre of the active region (black data) and at a margin (red data). Inset shows detail of main panel. Temperature change is presented in arbitrary units because counts were converted to temperature by assuming the unknown emissivity of PST to be unity, which by default neglects reflection and transmission. The type of MLC imaged here is described in Chapter 3.

Values of temperature change were extracted from the IR movie of the inactive surface without the benefit of absolute units because the unknown emissivity of PST was assumed to be unity, which by default (wrongly) neglects any transmission or reflection. The instantaneous temperature change $\Delta T_{\#}$ soon becomes larger in the centre than at a

representative location in the inactive margins (Fig. 2.8b and inset), as conductive heat transfer causes the top inactive layer to thermalize with the underlying active volume. The inactive margins later thermalize with the active volume via conduction, resulting in a crossover at ~1.5 s into the thermal relaxation that is likely to again be an artefact. Though the temperature at the centre of the top inactive layer is likely to be higher (in reality) as it lies closer to the active volume, the apparent temperature is suppressed due to radiation from ambient reflected by the metallic electrode (Fig. 2.7b). By contrast, the apparent temperature (at the surface) of the inactive margins is inflated due to transmitted radiation originating from underlying regions (Fig. 2.7c) and the nearby active volume (Fig. 2.7d).

Coating the surface to be imaged with a thin (e.g. $\lesssim 20\,\mu m$) layer of high-emissivity paint can avoid the aforementioned artefacts, at the minimal expense of adding inactive thermal mass [1]. The relationship between the temperature T and photon counts x for the new surface can be determined via independent calibration, e.g. using a thermocouple. By fitting $T(x)$ to a modified form of Planck's law, e.g. the Sakuma-Hattori equation(s) [133, 134], one can account for the spectral range of the infrared detector. A semi-empirical form of Planck's law $x = \frac{\beta}{e^{\alpha/T} - \gamma} + \delta$ [135] is used in Chapter 3 (Section 3.7.15), where α is the effective temperature of the photons lying in the spectral range of the detector, $\beta = \varepsilon\beta_0$ is a constant of proportionality in which the black-body value β_0 is scaled down by emissivity ε, γ is a free parameter that differs from unity to account for the spectral width of the detector(s), and δ is the contribution to photon counts that arises from both the detector background as well as reflected ambient radiation (Fig. 2.7b). For a homogeneous surface, the first three parameters should be constant, while the last parameter can vary from pixel-to-pixel. The detector contribution to δ is typically corrected for non-uniformity by camera software [132]. Measuring ΔT over a wide range of temperatures requires changes of integration time in order to avoid detector saturation (Section 3.7.15). In principle, both β and δ are proportional to the integration time, but changes of integration time often require non-uniformity corrections that cause δ to deviate slightly from scaling linearly with integration time. Values of δ for each pixel can be identified by comparing and matching frames taken at the same temperature before and after the change of integration time and non-uniformity correction.

2.3.4 Scanning thermal microscopy

Scanning thermal microscopy (SThM) is a form of non-contact thermometry, where a resistance thermometer is embedded in a modified AFM tip to measure the local temperature at surfaces. SThM offers spatial resolution, but unlike IR imaging it is necessary to repeat EC cycles at each location to produce a map of $\Delta T_{\#}$. SThM tips with an estimated heat capacity of ~1 nJ K^{-1} [130] have been used to measure EC effects in bulk samples [2], MLCs [130], and tens-of-micron-thick films on substrates [3]. SThM is typically performed with 5-20 µm lift heights that separate the tip from a grounded top electrode, thus minimizing the possibility of electrical crosstalk [83, 130]. Given that heat from an EC film can be exchanged with its substrate on time scales that are similar to those governing convective and radiative heat transfer, any temperature change measured by SThM can be substantially suppressed with respect to its adiabatic counterpart ΔT. A suitable model for establishing the adiabatic value would likely be non-trivial considering the need to account for conductive, convective, and (possibly) radiative heat transfer.

2.4 Measurements of heat

The heat measured by calorimetry is denoted Q whether or not it corresponds to an EC heat in the isothermal limit, thus contrasting the practice of using ΔT to exclusively denote adiabatic temperature change. Isothermal EC heat can be measured directly while varying electric field E at a fixed temperature T, and the corresponding (unmeasurable) isothermal entropy change ΔS can then be identified via $Q = T\Delta S$. Quasi-direct measurements of isothermal EC heat involve varying the temperature at fixed values of electric field and integrating the resulting heat capacity $c(T,E)$ to identify the isothermal EC heat and entropy change.

Direct and quasi-direct measurements of Q have been made using different types of calorimeter. The most common is a modified form of differential scanning calorimeter (DSC) in which electrical feedthroughs permit the EC material to be electrically addressed [87, 136]. The EC capacitor and reference sample make equivalent thermal contact to a common heat sink, and one measures the difference between the heat that each exchanges with the sink. The measured heat flow is typically calibrated against a well-known first-order phase transition, e.g. using the enthalpy of fusion for indium.

The term calorimetry does not exclusively refer to measurements of heat flow and can also refer to measurements of temperature change from which changes in enthalpy are deduced (e.g. adiabatic calorimetry [137]). Calorimeters in this sense have been exploited to set start temperatures when making direct measurements of temperature change while driving EC effects quasi-adiabatically [64, 125-127] (in which case measured ΔT_j are scaled up as discussed in Section 2.3.2) or quasi-isothermally through a sharp first-order transition in order to deduce the latent heat [138].

2.4.1 Direct measurements of Q

For direct measurements of Q [87], slow isothermal changes in applied field at rate $\frac{\mathrm{d}E}{\mathrm{d}t}$ yield EC heat flow $\frac{đQ}{\mathrm{d}t}$, where $đQ$ denotes an inexact differential because Q is not a state function. One integrates the resulting $\frac{đQ}{\mathrm{d}E} = \frac{đQ}{\mathrm{d}t} \Big/ \frac{\mathrm{d}E}{\mathrm{d}t}$ to obtain the isothermal EC heat $Q = \int_0^E \frac{đQ}{\mathrm{d}E'}\Big|_T \mathrm{d}E'$, and hence $\Delta S = Q/T$. In the absence of hysteresis, any difference between $\frac{đQ}{\mathrm{d}E}$ for field application and field removal can distinguish the reversible EC heat of interest from Joule heating [139]. However, substantial Joule heating will likely compromise the isothermal conditions.

Heat leaks via the electrical contacts can be corrected by measuring the shortfall with geometrically analogous resistors that continuously dissipate a known power [140, 141]. As discussed below, the comparison of continuously dissipated power in a resistor with EC heat has also been used to calibrate direct measurements that do not employ a reference sample. The EC heat flow is measured using either a heat flux sensor that is typically composed of thermoelectric modules [61, 142] or a thermometer [128], where the heat flux is proportional to the measured temperature difference between sample and bath.

Fast (quasi-adiabatic) changes of field are often employed in the aforementioned reference-free method and in differential scanning calorimetry. The quasi-adiabatic EC heat Q is converted to an adiabatic temperature change $\Delta T = Q/c_{\mathrm{eff}}$ by assuming an effective heat capacity c_{eff}, but this is not a direct measurement of ΔT as typically stated [96, 140-143]. Fortuitously, the quasi-adiabatic EC heat should only differ from the isothermal heat of interest by less than $\Delta T/2T \sim 1\%$ in most EC materials that operate anywhere near room temperature, as seen by comparing the EC heat $Q = \int T\mathrm{d}S$ exchanged with the sink/load in Brayton and Ericsson cycles (Fig. 4.2). Moreover, the large heat flux associated with a fast field change permits the measurement of thin films, whose thermal time scales are much faster than the response time of the sensor. However, there are two matters arising. First, the transient response of the sensor and/or any inactive thermal mass (such as adhesive) may render the calibration frequency-dependent, such that it may be inappropriate to calibrate against steady-state dissipation. Second, the calibration will be compromised by dissimilar heat leaks if the calibration resistor and sample are not analogously situated with respect to

the thermometer or do not make analogous thermal contact with the heat-flux sensor. These two issues should be explicitly ruled out in order to confirm the reports of the largest temperature changes (tens of kelvin).

Direct measurements of *Q* have been made in nanometre-thick films on substrates via a modified form of AC calorimetry. Standard AC calorimetry yields measurements of heat capacity by measuring the oscillatory temperature response to a known oscillatory heat flux [144]. The modified calorimetry involves cyclically driving EC films under quasi-isothermal conditions to generate temperature oscillations in a proximal layer, and these temperature oscillations are used to deduce EC heat flux via a 1D heat-transfer model that is based on known heat capacities and thermal conductivities [97, 122, 123]. The temperature oscillations in the proximal layer have been measured using a thermistor track that was either deposited on an electrically insulating overlayer [123] or deposited before the film such that it doubled as the bottom electrode [122]. Temperature oscillations in a proximal layer have also been measured using laser-based thermometry after depositing a proximal layer of vanadium on the top electrode of an EC film [97].

2.4.2 Quasi-direct measurements of *Q*

For quasi-direct measurements of *Q* [87], isofield temperature sweeps at temperature ramp rate $\frac{\mathrm{d}T}{\mathrm{d}t}$ yield heat flow $\frac{đQ}{\mathrm{d}t}$, and the resulting $\frac{đQ}{\mathrm{d}T} = \frac{đQ}{\mathrm{d}t} \Big/ \frac{\mathrm{d}T}{\mathrm{d}t}$ should be equivalent to the specific heat capacity $c(T,E)$ after normalizing by mass. For a given applied field, one then has the entropy $S'(T,E) = \int_{T_0}^{T} \frac{c(T',E)}{T'} \mathrm{d}T'$ with respect to the absolute entropy at base temperature T_0, which should lie properly below the transition in order to correctly parameterize the transition [12]. The $S'(T,E)$ dataset then permits one to determine the isothermal entropy change ΔS, and by following isentropic contours (Section 2.2.1) one can evaluate the adiabatic temperature change ΔT.

The equivalence between $\frac{đQ}{\mathrm{d}T}$ and $c(T,E)$ can be compromised by heat leaks, Joule heating, asymmetries between sample and reference stages, and miscalibration. Heat leaks can be minimized by ensuring that the EC capacitor has a good thermal link to nothing but the heat sink, e.g. by using thin wires to drive the EC effect. If Joule heating is small then the heat flow can be corrected by subtracting the dissipated power $P = IV$, where I is the measured current that flows through the EC capacitor and V is the voltage used to drive the EC effect. Asymmetries between sample and reference stages can be corrected by removing a baseline that is measured while sweeping temperature with no EC sample and no reference. The temperature-dependent calibration constant for converting $\frac{đQ}{\mathrm{d}T}$ to $c(T,E)$ can be determined by measuring a standard sample of known heat capacity [145].

Thermal hysteresis in the heat capacity can arise near the transition and produce an ambiguity regarding the branch of $c(T,E)$ from which to produce $S'(T,E)$. If the thermal hysteresis is weak then EC effects can be correctly evaluated by choosing the correct branches [119]. For a conventional EC material, adiabatic temperature change ΔT (isothermal entropy change ΔS) should be determined by constructing isentropes (isotherms) that connect the zero-field entropy $S(T,0)$ obtained from warming data with the field-on entropy $S(T,E)$ obtained from cooling data (Fig. 2.3). For inverse EC materials, one should instead use $S(T,0)$ obtained from cooling data and $S(T,E)$ obtained from warming data.

2.5 Conclusions

The metrology of electrocalorics should continue to evolve as novel device geometries and novel materials impose new measurement challenges. Indirect methods dominate the EC literature [146] as they are based on electrical measurements that can be implemented on readily available equipment. However, indirect methods are prone to produce ‘false positives’ in the form of large EC effects that might not be verified by direct measurements. This is because spurious effects that compromise measurements of $P(E)$ are plenty, and often difficult to resolve. It is therefore essential to measure EC effects directly using thermometry and calorimetry, but it remains challenging to implement these techniques in order to verify large EC effects in thin films. Moreover, direct EC measurements are themselves prone to error because techniques are often implemented in unsuitable experimental regimes, e.g. thermometry with slow field changes, or calorimetry with fast field changes. This chapter has drawn attention to the potential pitfalls when making various types of EC measurement, and will hopefully serve as a useful guide to the reader wishing to measure EC effects properly.

“ആയിരംകണ്ണുപൊട്ടിച്ചെ അര വൈദ്യനാകു.”

“One must blind a thousand patients to become even half a doctor.”

Chapter 3

Characterizing electrocaloric effects in multilayer capacitors of $PbSc_{0.5}Ta_{0.5}O_3$

Heat pumps based on magnetocaloric (MC) and electrocaloric (EC) working bodies—in which entropic phase transitions are driven by changes of magnetic and electric field, respectively—use displaceable fluids to establish relatively large temperature spans between loads to be cooled and heat sinks [12, 147]. However, the performance of prototypes is limited because practical MC working bodies driven by permanent magnets [148-150] and EC working bodies driven by voltage [45-47, 72-81] display temperature changes of less than 3 K. Reported here are high-quality multilayer capacitors (MLCs) of $PbSc_{0.5}Ta_{0.5}O_3$ (PST) that display large EC effects over a wide range of starting temperatures when the first-order ferroelectric phase transition is driven supercritically (as verified by Landau theory) above the Curie temperature of 290 K by electric fields of 29.0 V μm^{-1}. Changes of temperature in the large central area of the MLC peak at 5.5 K near room temperature and exceed 3 K for starting temperatures that span 176 K (complete thermalization would reduce these values from 5.5 to 3.3 K and from 176 to 73 K). If MC working bodies were to be replaced with MLCs of PST, then the established design principles behind MC heat pumps could be repurposed for better performance without bulky and expensive permanent magnets.

This chapter details the characterization of EC effects in MLCs of PST. The text of this chapter is adapted from the text of my first-author publication “Large electrocaloric effects in oxide multilayer capacitors over a wide temperature range” [1]. Modifications to the text have been made to avoid the use of the first-person plural “we”, “us”, and “our” that is standard in scientific publishing. The work presented here was performed by me, except for the following:

(i) MLCs were fabricated and optimized by Tomoyasu Usui and Sakyo Hirose at Murata Manufacturing. Density measurements and determination of grain size via scanning electron microscopy were also conducted at Murata Manufacturing.
(ii) X-ray diffraction and analysis were performed by Samer Kurdi. The photograph of an MLC in Fig. 3.2 was also taken by Samer Kurdi.
(iii) The Landau theory was performed by Gian Guzmán-Verri.

The structure of this chapter mirrors that of the publication. The context for this work is set in Section 3.1 by briefly discussing the current state of EC cooling and the performance gap that separates magnetocaloric cooling from EC cooling. Section 3.2 describes the high-quality MLCs of PST used in this work. Section 3.3 presents the characterization of these MLCs via some of the techniques described in Chapter 2, including infrared imaging and the indirect method. In Section 3.4, the superlative performance of the MLCs of PST is compared to Gd working bodies in state-of-the-art MC prototypes, and figures of merit for applications are discussed. Section 3.5 provides a summary of the work and conclusions. Section 3.6 details methods for this chapter, while Section 3.7 contains the information that was published as supplementary information. This information is cited in Sections 3.1-3.6.

3.1 The performance of EC working bodies

The development of EC cooling devices in past [45-47] and recent [72-81] times continues to lag the highly developed activity on near-room-temperature MC cooling devices [147, 148]. In parallel, the recent development of devices [151] in which uniaxial stress drives elastocaloric materials [12] is complemented by the nascent development of devices in which isotropic stress drives barocaloric materials [12]. Thermal changes are particularly large in these two types of mechanocaloric material [12, 152], but it is difficult to adapt the highly evolved MC prototypes to use mechanocaloric materials instead.

MC prototypes [148] typically use permanent magnets to address beds of commercial-grade Gd spheres, whose adiabatic temperature change of $|\Delta T| \sim 2.5$ K [149] drives heat exchange with a fluid, permitting heat to be pumped over much larger temperature spans. These temperature spans are established either along the fluid alone (passive regeneration) [147] or along the bed and the fluid together (active regeneration) [148], such that heat is absorbed from the load at the cold end, and dumped to the sink at the hot end. MC effects larger than 2.5 K can be achieved in Gd by increasing the magnetic field and reducing the demagnetizing factor, but these modifications would be challenging to use in practical applications (see Section 3.7.1). EC effects larger than 2.5 K have not previously been demonstrated in macroscopic bodies (bulk samples and MLCs) near room temperature if one requires unambiguous evidence in the form of directly measured temperature change (see Section 3.7.2).

Bulk EC ceramics such as those used in EC cooling devices [45-47, 74] are no thicker than 0.1-0.5 mm, to avoid unduly compromising the breakdown field [12], but the largest applied fields yield at best a directly measured value of $|\Delta T| \sim 2.2$ K near room temperature (in PST) [2, 45-47]. A larger temperature change may be achieved in order-of-magnitude thinner EC films [3], but there is insufficient active material for applications (and therefore an innovative device [79] based on the electrostatic actuation of a flexible polymer bilayer would struggle to continuously cool a macroscopic object). However, an assembly of EC films in the form of an MLC represents a viable working body that is macroscopic [69]. Although MLCs have now been exploited in several EC cooling devices [72, 73, 75-78, 80, 81], directly measured

temperature jumps $|\Delta T_j|$ have been limited to 2.2 K near room temperature (in MLCs based on a polymer) [72] and 2.7 K near 380 K (in MLCs of $0.9Pb(Mg_{1/3}Nb_{2/3})O_3$-$0.1PbTiO_3$) [4]. These highly adiabatic temperature jumps arise within the active area (where interdigitated electrodes overlap) following rapid thermalization between active and inactive layers and are typically measured at the face centres of MLCs.

3.2 High-quality MLCs of PST

Described here are high-quality MLCs based on the well-known EC material PST [45-51], which is paraelectric near and above room temperature. On cooling, there is a broad transition to a relaxor state (with glassy ferroelectric order) if the B-site cation order is low, and there is a sharp first-order phase transition to a ferroelectric state if the B-site cation order is high. Highly ordered PST was used to access large EC effects associated with the latent heat of the first-order transition, which increases with increasing B-site cation order [153, 154] as expected for a first-order transition when varying the degree of disorder [155]. Driving this transition supercritically allowed access to about 1.5 times the entropy associated with this latent heat. To do this while avoiding electrical breakdown and leakage-induced Joule heating required fine grains of similar size, a low density of physical and chemical defects, and no discernible impurity phases. Sintering and annealing conditions were optimized to yield all of these properties, as well as high B-site cation order.

The MLC geometry was copied from previous work that I co-authored on MLCs of $0.9Pb(Mg_{1/3}Nb_{2/3})O_3$-$0.1PbTiO_3$, where 19 active layers yielded a larger value of $|\Delta T_j|$ than 14 layers [4] or 49 layers [5], and where the layer thickness of about 40 μm falls in a broad range for which the breakdown field is maximized. However, the active area was increased at the expense of the surrounding inactive area to generate more EC heat and reduce internal thermalization, while retaining sufficient inactive area to suppress cracking by suppressing piezoelectricity. The inactive area also hinders breakdown by suppressing electrical discharge between the inner electrodes.

MLC fabrication, characterization and measurement are described in Section 3.6; the challenges of fabrication are discussed in Section 3.7.3; and the set-ups for direct EC measurements are shown in Fig. 3.1. A plan-view optical image (Fig. 3.2a) and schematic (Fig. 3.2b) accompany a cross-sectional schematic (Fig. 3.2c) showing six rather than all 21 layers of PST. The 19 active layers, of average thickness 37.9 μm, were electrically addressed by interdigitated inner electrodes of Pt (about 2 μm thick), the active area was approximately 49 mm^2, and the active volume occupied 54% of the total MLC volume (10.45 mm × 7.43 mm × 0.84 mm).

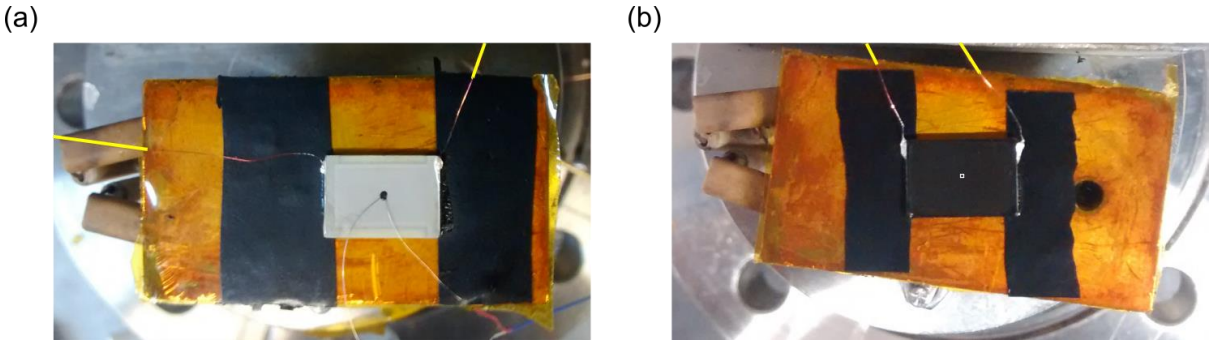

Fig. 3.1 | **The thermocouple and IR measurement set-ups.**

(a) The thermocouple was secured to the MLC face centre using a drop of black paint. (b) For measurements with the IR camera, the MLC face was spin-coated with black paint. White square overlay denotes the MLC face centre (300 μm × 300 μm). For both set-ups, black insulating tape was used below each end of the MLC to suspend it approximately 0.9 mm above the Kapton tape insulation (orange) that covered the bespoke heater block. Yellow overlays near image edges identify MLC terminal wiring. Both images show MLC1. Its appearance in (a) differs with respect to Fig. 3.2a because here image contrast was not optimized to distinguish each region.

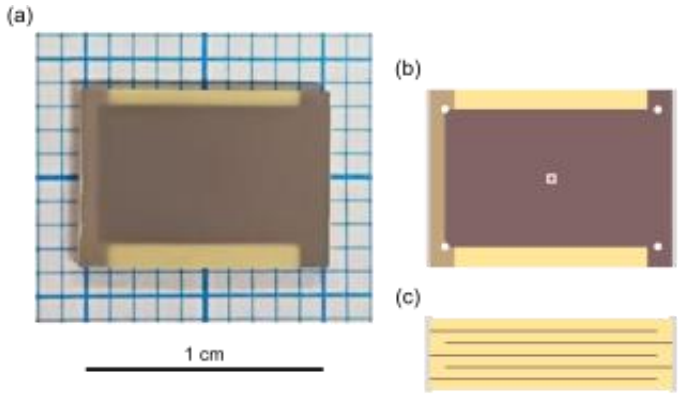

Fig. 3.2 | **MLC structure**.

(a) Optical image, and (b) schematic illustration, showing the uppermost inner electrode (dark brown), part of the next inner electrode (light brown), the two outer electrodes (grey) and through-thickness PST (yellow). Image contrast was optimized to distinguish each region. The MLC shown here is equivalent to MLC1. In (b), the white square denotes the face centre (300 μm × 300 μm), and the four white dots define the corners of a rectangle that represents the active area in which the inner electrodes overlap. (c) Cross-sectional schematic, showing six rather than all 21 layers of PST. Optical image in (a) taken by Samer Kurdi.

EC effects were directly measured with an infrared camera whose field of view covered most of the MLC face (Section 3.3). The resulting values of $|\Delta T_j|$ describe the face centre and were corroborated by using a thermocouple. As a result of driving the first-order ferroelectric phase transition supercritically without electrical breakdown, large EC effects were achieved over starting temperatures whose wide range would traditionally be associated with smaller EC effects in relaxors [12]. Specifically, the measured changes of temperature peaked at $|\Delta T_j| \sim 5.5$ K near room temperature and exceeded $|\Delta T_j| \sim 3$ K for starting temperatures that spanned 176 K in the range 294-470 K. The height and width of this peak compare favourably with respect to the MC effects [149] that can be driven in a macroscopic volume of commercial-grade Gd using bulky and expensive permanent magnets, even in the limit of complete internal MLC thermalization (Section 3.4). These EC capacitors should therefore permit MC prototype design principles [148] to be repurposed for improved performance, without permanent magnets.

3.3 Characterization of MLCs of PST

3.3.1 Ordering and the transition

X-ray diffraction revealed a high degree of B-site cation order (order parameter S_{111} ~ 0.96; see Section 3.7.4). This represents a substantial improvement with respect to MLCs of PST (S_{111} ~ 0.6-0.7), for which $|\Delta T|$ ~ 2.4 K in the active volume [51] was identified via a type of correction that can be prone to overestimation [4] (Section 2.3.2). Zero-field calorimetry (Fig. 3.3a) revealed a Curie temperature and latent heat (inset of Fig. 3.3a) that differ only slightly from the corresponding values for bulk PST with similar B-site cation order [153] (T_C ~ 298 K and $|Q_0|$ ~ 10.0 MJ m^{-3}, assuming a similar density of 8750 g cm^{-3}). Dielectric measurements (Fig. 3.3c) recorded a Curie temperature of T_C ~ 292 K, a small loss tangent of 0.05 just below T_C, and a much smaller loss tangent of $<10^{-3}$ above T_C, where the large EC effects reported here are found.

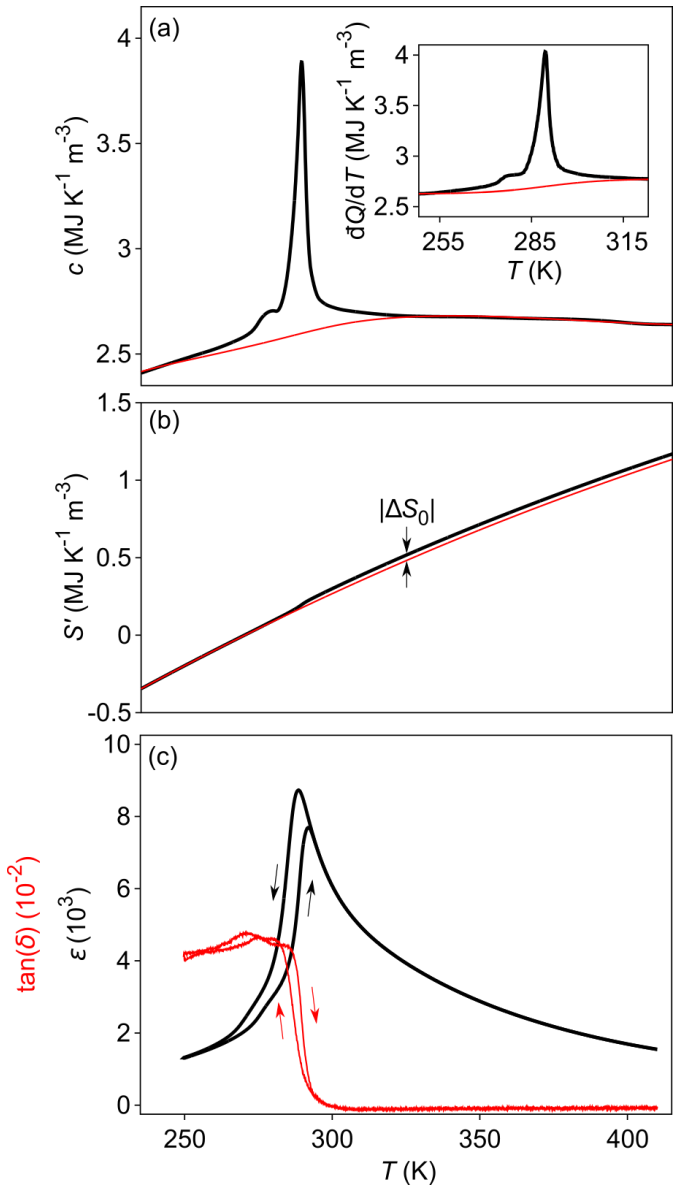

Fig. 3.3 | **The zero-field phase transition.**

(a) Volumetric heat capacity c versus increasing temperature T, showing the zero-field phase transition at Curie temperature T_C ~ 290 K. Inset: the đQ/dT precursor used to identify $c(T)$ (see Section 3.6) was integrated after subtracting a sigmoidal baseline (red) to yield latent heat $|Q_0|$ ~ 10.2 MJ m^{-3}. The baseline in the main panel (red) was identified via the sigmoidal baseline of the inset at the intermediate temperatures of the inset, and via least-squares linear regression at higher and lower temperatures (intersections between these different regimes of temperature were smoothed). (b) Black data represent entropy $S'(T) = \int_{270\,\mathrm{K}}^{T} c(T')/T'\,\mathrm{d}T' = S(T) - S(270\,\mathrm{K})$, red data neglect the transition and correspond to the baseline in (a), $|\Delta S_0| = |Q_0|/T_C$ ~ 35 kJ K^{-1} m^{-3}. (c) Relative permittivity ε (black) and loss tangent tan(δ) (red) measured at 100 Hz on cooling and subsequent warming at ±1 K min^{-1}. The peak measured on warming occurred at T_C ~ 292 K, and the thermal hysteresis for the transition was 4 K. All data for MLC1.

3.3.2 Indirect Method

EC effects were first evaluated for the active volume (Fig. 3.4) using the well-known indirect method (see Section 2.2.1) while implementing three improvements (see Section 3.6.10) introduced in a paper that I co-authored [2]. Isothermal electrical polarization $P(E)$ was measured every 0.35 K at 385 values of increasing temperature T, and field-removal branches obtained under unipolar conditions ($0 \leq E \leq 15.8$ V μm^{-1}) were used to plot $P(T,E)$ (Fig. 3.4a). Inflection points in these field-removal branches were used to identify the phase boundary $E(T)$ and critical endpoint. Combining the gradient $\mathrm{d}E/\mathrm{d}T = 0.15$ V μm^{-1} K^{-1} of this boundary near T_C with a field-driven polarization change of $|\Delta P| \sim 24.0$ μC cm^{-2} (Section 3.7.7) implies, via the Clausius–Clapeyron equation $|\mathrm{d}E/\mathrm{d}T| = |\Delta S_0|/|\Delta P|$, an isothermal entropy change of $|\Delta S_0| \sim 36$ kJ K^{-1} m^{-3}, in good agreement with the thermally driven entropy change of $|\Delta S_0| \sim 35$ kJ K^{-1} m^{-3} (from $|Q_0| \sim 10.2$ MJ m^{-3} and $T_C \sim 290$ K; inset of Fig. 3.3a).

The dense $P(T,E)$ data (Fig. 3.4a) were used to evaluate the reversible isothermal entropy change $\Delta S(T, E) = \int_E^0 (\partial P/\partial T)_{E'} \mathrm{d}E' > 0$ (Fig. 3.4b) for field removal ($E \rightarrow 0$) at temperature T, using the Maxwell relation $(\partial S/\partial E)_T = (\partial P/\partial T)_E$. The largest field used in the indirect measurements ($E = 15.8$ V μm^{-1}) yields an entropy change whose magnitude reaches a peak of $|\Delta S| \sim 43$ kJ K^{-1} m^{-3} near 300 K, while the corresponding refrigerant capacity is $\int_{T_1}^{T_2} |\Delta S(T)| \mathrm{d}T \sim 2.8$ MJ m^{-3} (T_1 and T_2 define the FWHM of $|\Delta S(T)|$ for $E = 15.8$ V μm^{-1}). Subtracting the entropy change on field removal $\Delta S(T,E) > 0$ from the zero-field entropy $S'(T,0) = S(T,0) - S(270\ \mathrm{K},0)$ (Fig. 3.3b) yields entropy map $S'(T,E)$ (Fig. 3.4c; adiabatic contours are white). Following an adiabatic contour identifies the reversible adiabatic temperature change for the active regions (Section 2.2.1), yielding $\Delta T(T_s,E) < 0$ (Fig. 3.4d) for the removal of field E at starting temperature T_s. For $E = 15.8$ V μm^{-1}, the peak temperature change identified using the indirect method is $|\Delta T| \sim 4.8$ K near 309 K.

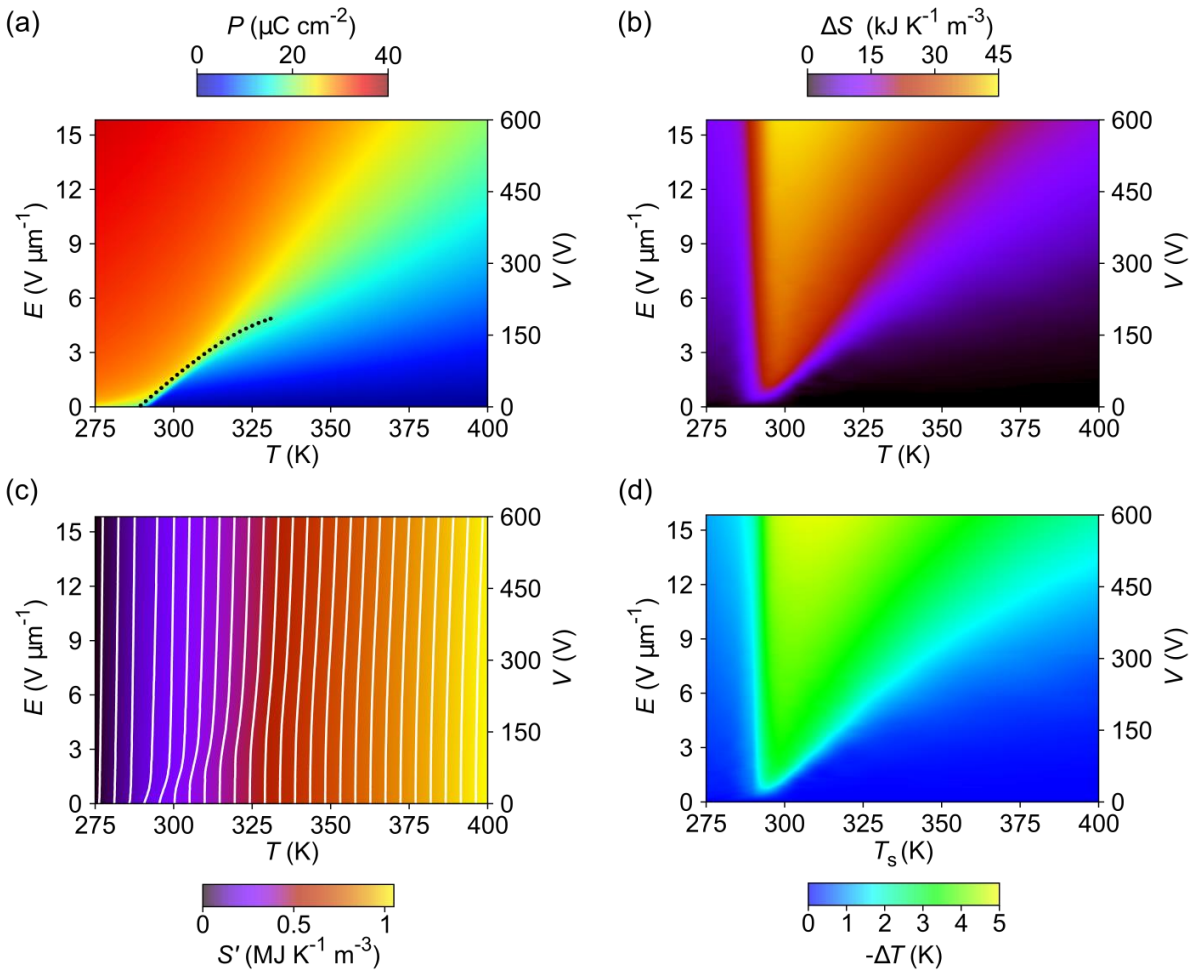

Fig. 3.4 | **Indirect EC measurements.**

(a) Polarization $P(T,E)$ constructed from upper branches of 385 unipolar P(E) plots measured isothermally every 0.35 K on warming (dotted line shows phase boundary with critical endpoint). (b) The reversible isothermal entropy change $\Delta S(T,E) > 0$ due to the removal of field E, as determined from (a). (c) Entropy $S'(T,E)$ obtained by subtracting EC entropy change $\Delta S(T,E) > 0$ from zero-field entropy $S'(T) = S(T) - S(270\ \mathrm{K})$ (Fig. 3.3b), white adiabatic contour separation is about 4.8 K. (d) Reversible adiabatic temperature change $\Delta T(T_s,E) < 0$ due to the removal of field E at starting temperature Ts, as determined from (c). Data for MLC1. Selected $P(E)$ plots in Section 3.7.5. Selected constant-field cross-sections in Section 3.7.6. Abscissae exclude both extremes of the 270-405 K measurement temperature range, for reliable evaluation of $(\partial P/\partial T)_E$.

3.3.3 Direct measurements

Thermocouple measurements of temperature change $\Delta T_{\#}$ versus time t recorded temperature jumps of $|\Delta T_j| \sim 4.0$ K at the MLC face centre, when driving a four-step Brayton cycle for which $E = 15.8$ V μm^{-1}and $T_s \sim 315$ K (left inset, Fig. 3.5a). This well-known cycle comprised (1) a highly adiabatic field-on temperature jump $\Delta T_j > 0$, (2) a slow isofield return to T_s, (3) a highly adiabatic field-off temperature jump $\Delta T_j < 0$ and (4) a slow zero-field return to T_s. The absence of Joule heating, while dumping EC heat in step (2), is important for applications.

Infrared camera measurements at the MLC face centre (300 μm × 300 μm) recorded a slightly larger value of $|\Delta T_j| \sim 4.3$ K (main panel, Fig. 3.5a), reflecting improved adiabaticity (owing to faster data acquisition by a factor of 11) and reduced thermal mass (approximately 6 μm-thick black paint with relatively low volumetric heat capacity versus the thermocouple affixed with a <0.05 mm^3 drop of black paint). The inactive layers in the active area render this value 10% smaller than the indirectly measured value of $|\Delta T| \sim 4.8$ K for the active volume (Fig. 3.4d), yielding $|\Delta T_j| \sim 0.90|\Delta T|$ as roughly expected (see Section 3.6.13). By contrast, inactive thermal mass outside the active area only diminished the magnitude of the temperature change near the periphery of the active area (right inset, Fig. 3.5a).

Infrared camera measurements at different starting temperatures recorded similar values of $|\Delta T_j|$ for field application/removal (red and blue data, Fig. 3.5b). The crossover in the magnitude of these field application/removal values (seen previously for Gd) [124] was also observed when varying field (Section 3.7.8) and is explained in Section 3.7.9. For the intermediate field of $E = 15.8$ V μm^{-1}, values of $|\Delta T_j|$ (red and blue circles, Fig. 3.5b) match well with values of $0.90|\Delta T|$ from the indirect method (black line, Fig. 3.5b), and slightly exceed values of $|\Delta T_j|$ from thermocouple measurements (brown and black circles, Fig. 3.5b) due to the improved adiabaticity and reduced thermal mass explained earlier. For T_s near 330 K, the maximum field of $E = 29.0$ V μm^{-1} yielded the highest value of $|\Delta T_j| \sim 5.5$ K (Fig. 3.5b). Similar results for five similar MLCs appear in Section 3.7.10.

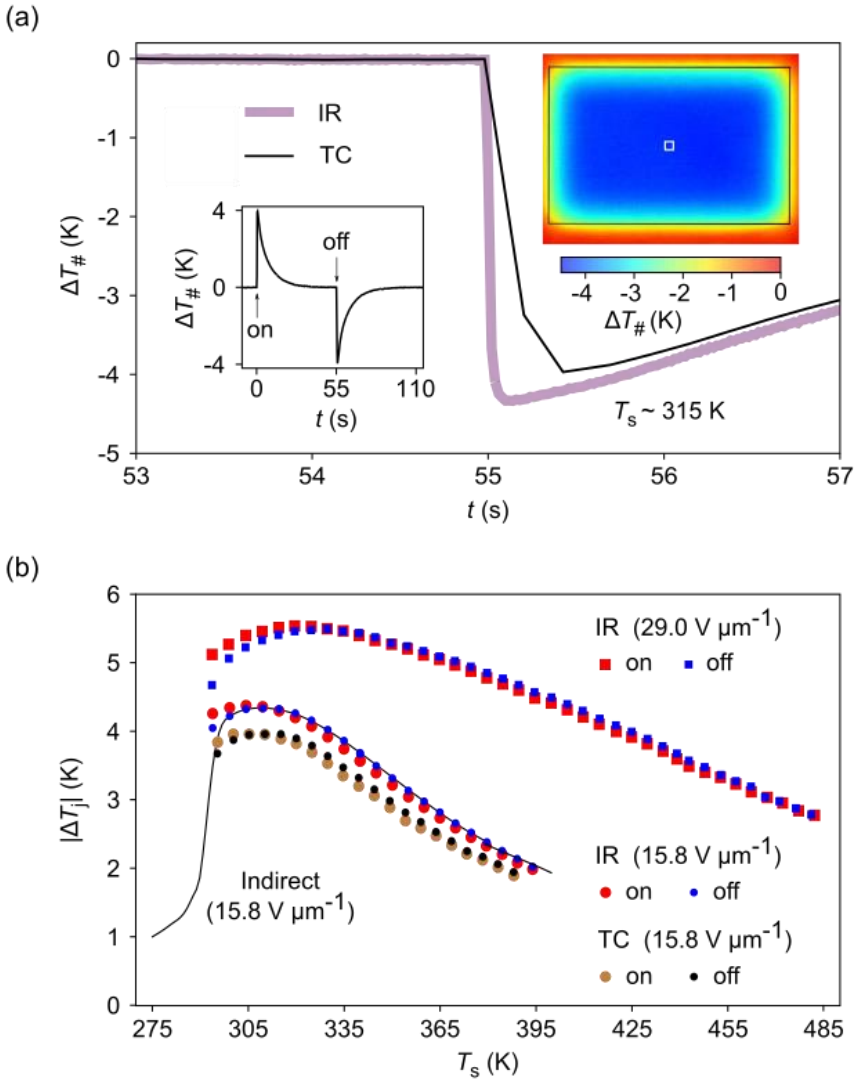

Fig. 3.5 | **Direct EC measurements.**

(a) Left inset shows temperature change $\Delta T_{\#}$ versus time t when a field of 15.8 V μm^{-1} was switched on and off. Data were measured at the MLC face centre with the thermocouple, starting at temperature T_s ~ 315 K. The main panel shows a detail of this inset (black data), as well as the corresponding infrared camera measurements for the 300 μm × 300 μm face centre (purple data). Right inset shows an infrared image of the MLC face at t ~ 55.1 s, when the face centre (white square overlay) and surrounding area were coldest (dark blue). The black rectangular overlay outlines the active area. IR, infrared; TC, thermocouple. (b) For different values of T_s, temperature jump magnitude $|\Delta T_j|$ are plotted for when a field of 15.8 V μm^{-1} or 29.0 V μm^{-1} was switched on and later off. Data were measured at the MLC face centre using the infrared camera or thermocouple. Black line shows $0.90|\Delta T|$ versus T_s for 15.8 V μm^{-1}, identified using $|\Delta T|$ from the indirect method (Fig. 3.4d) after scaling by 0.90 to achieve a least-squares fit with field-off values of $|\Delta T_j|$ (blue circles). All data for MLC1. Similar data for five similar MLCs appear in Fig. 3.12.

3.4 Comparing MLCs of PST to Gd for applications

The directly measured value of $|\Delta T_j| \sim 5.5$ K exceeds the MC benchmark of $|\Delta T| \sim 2.5$ K for Gd in prototypes (Section 3.7.1). Moreover, it represents an improvement over other macroscopic EC bodies at any starting temperature, including those for which temperature changes of $|\Delta T_j| \approx 2.2$ K have been directly measured near room temperature (Section 3.7.2). For the active volume alone, the maximum field of 29.0 V μm^{-1} yields peak values of $|\Delta T| \sim |\Delta T_j|/0.90 \sim 6.1$ K near 330 K, $|\Delta S| \sim 53$ kJ K^{-1} m^{-3} near 308 K (Section 3.7.11), and $|Q| = T|\Delta S| \sim 16.6$ MJ m^{-3} near 330 K. The corresponding electrical work $|W| \sim 2.5$ MJ m^{-3} near 330 K (Section 3.7.12) implies an isothermal materials efficiency $|Q|/|W| \sim 7$ that is similar to the values identified for other EC or elastocaloric materials, and slightly smaller than the values identified for MC materials driven by permanent magnets [156].

The large EC effects observed here are predicated on the large latent heat associated with high B-site cation order [153, 154], such that reducing the B-site cation order reduces the EC effects (Section 3.7.13), as seen for bulk PST [50]. However, the entropy change ($|\Delta S_0| \sim 35$ kJ K^{-1} m^{-3}) that corresponds to the zero-field latent heat ($|Q_0| \sim 10.2$ MJ m^{-3}) accounts for only about 2/3 of the largest value of $|\Delta S| \sim 53$ kJ K^{-1} m^{-3}, revealing that there are also substantial EC effects associated with the enhancement of polarization in the transformed phase (see $|\Delta T_j|$ versus E, Section 3.7.8). Substantial caloric effects associated with a single phase away from absolute zero are well known in mechanocaloric materials (near and away from phase transitions) [157] and in MC materials (near phase transitions) [158], but not in EC materials.

The effective temperature change exploited in applications $|\Delta T_{eff}|$ lies somewhere between two bounds that define the shaded regions in Fig. 3.6a. The upper bound assumes that the active area thermalizes and then exchanges heat with its intended target before exchanging any heat with the inactive area, such that $|\Delta T_{eff}| \approx |\Delta T_j|$. The lower bound assumes that the active volume completely thermalizes with the inactive volume, such that $|\Delta T_{eff}| \sim 0.54|\Delta T| \sim 0.6|\Delta T_j|$ given an active volume of 54% for which $|\Delta T| \sim |\Delta T_j|/0.90$. Upper and lower bounds for the five similar MLCs are presented in Section 3.7.10.

When considering MLC performance with the maximum field (E = 29.0 V μm^{-1}) it is important to bear in mind that complete thermalization may be unduly pessimistic because the large, thin active area would make intimate contact with its intended target, for example heat-exchange fluid. Values of $|\Delta T_{\mathrm{eff}}|$ peak at 5.5 K if thermalization of the active area alone is assumed (3.3 K for complete thermalization). Moreover, values of $|\Delta T_{\mathrm{eff}}|$ remain large over a wide range of starting temperatures (Fig. 3.6b), exceeding 3 K for starting temperatures that span 176 K if thermalization of the active area alone is assumed (73 K for complete thermalization). Large temperature spans have been hitherto accessed through the broad transitions associated with smaller EC effects in relaxors [12], but here a large temperature span is accessed by driving a first-order transition using supercritical fields (Fig. 3.4a), as verified for the MLCs by using Landau theory to model the active volume (Section 3.7.14).

Fig. 3.6 and Table 3.1 compare $|\Delta T_{\mathrm{eff}}|$ with temperature jumps $|\Delta T_{\mathrm{eff}}| = |\Delta T_{\mathrm{j}}| = |\Delta T|$ for a bed of commercial-grade Gd spheres [149]. The bed was addressed by fields that could be achieved with permanent magnets [149, 150], such that it represents the archetypal MC working body in prototype devices. The peak upper bound of $|\Delta T_{\mathrm{eff}}| \sim 5.5$ K for the MLCs is roughly double the peak value of $|\Delta T_{\mathrm{eff}}| \sim 2.5$ K for Gd in prototypes, and the values of $|\Delta T_{\mathrm{eff}}|$ for the MLCs fall considerably more slowly when the starting temperature is varied. Even considering the conservative case of both the lower field (E = 15.8 V μm^{-1}) and complete internal thermalization, the peak value of $|\Delta T_{\mathrm{eff}}| \sim 2.6$ K is similar to the peak value for Gd.

Table 3.1 | **Performance summary.**

For an MLC of PST driven using electric field E, peak upper and lower bounds on effective temperature change $|\Delta T_{eff}|$ are presented (Fig. 3.6a), along with peak entropy change $|\Delta S|$ normalized by active volume (Section 3.7.11). EC data are for MLC1. Presented for comparison are the corresponding data near 291 K for a bed of commercial-grade Gd spheres driven with permanent magnets [149]. The internal magnetic field of $\mu_0 H_{int} \sim 1.0$ T corresponds to an applied magnetic field of $\mu_0 H_{app} \sim 1.4$ T (where μ_0 is the permeability of free space).

	MLC of PST		Gd in prototypes
Driving field	E = 15.8 V μm^{-1}	E = 29.0 V μm^{-1}	$\mu_0 H_{app} \sim 1.4$ T
$\|\Delta T_{eff}\|$	2.6-4.3 K	3.3-5.5 K	2.5 K
$\|\Delta S\|$	43 kJ K^{-1} m^{-3}	53 kJ K^{-1} m^{-3}	21 kJ K^{-1} m^{-3}

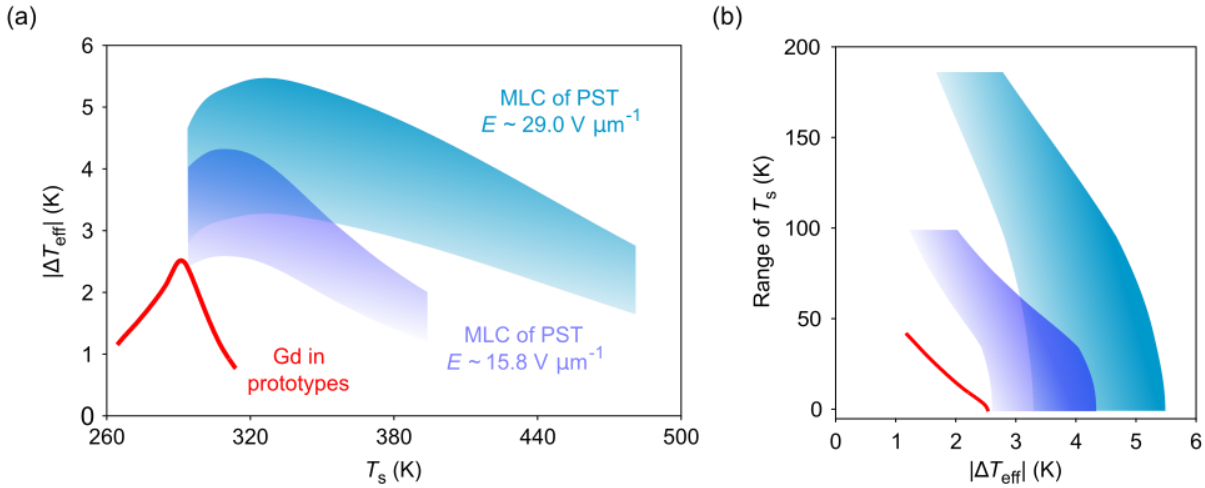

Fig. 3.6 | **Large EC effects over a wide range of operating temperatures.**

(a) Effective EC temperature change $|\Delta T_{eff}|$ as a function of starting temperature T_s, for fields of E = 15.8 V μm^{-1} and 29.0 V μm^{-1}. Upper bounds from highly adiabatic infrared measurements of $|\Delta T_j|$ (field-off data, Fig. 3.5b) assume thermalization in the active area alone before useful heat transfer. Lower bounds of $0.60|\Delta T_j|$ assume complete internal thermalization before useful heat transfer. Data are for MLC1. Similar data for five similar MLCs appear in Fig. 3.13. For comparison, $|\Delta T_{eff}|$ versus T_s is plotted for a bed of commercial-grade Gd spheres driven with permanent magnets [149], where the internal magnetic field of $\mu_0 H_{int} \sim 1.0$ T corresponds to an applied magnetic field of $\mu_0 H_{app} \sim 1.4$ T (and where μ_0 is the permeability of free space). (b) The range of T_s for which a given value of $|\Delta T_{eff}|$ is exceeded, with upper and lower bounds shaded as for (a). This description of peak width provides more information than a single value of refrigerant capacity.

3.5 Conclusions

In summary, large EC effects were demonstrated in high-quality MLCs of PST. These effects remain large over a wide range of starting temperatures, such that they could be used for active or passive regeneration in which a large temperature span would be accessed with just a single type of MLC. If MLCs of PST were to replace Gd in MC prototypes, then the impressive developments of recent decades [147, 148] could be exploited by using larger caloric effects over a wider range of temperatures. There would be no need for bulky and expensive permanent magnets [149, 150], and the dynamic field profile in an active regenerator [148] could be tailored at will because the constituent MLCs would be individually addressable. The operating temperatures of the MLCs are relevant for cooling consumer electronics and solar cells, and can be reduced below room temperature by using doped PST [50, 159]. MLCs of PST could be further developed by increasing the breakdown field through process optimization, reducing the inactive volume by automated mass production, increasing the active area, and tuning the number of layers to match thermal conductance with system design.

3.6 Methods

3.6.1 Samples

All data were obtained using MLC1, except when verifying reproducibility (MLCs 2–6, Section 3.7.10), evaluating electrical work (MLC7, Section 3.7.12) and investigating the effect of reduced B-site cation order (MLC8, Section 3.7.13). The X-ray diffraction and heat capacity data were obtained after MLCs had been crushed to form a powder. The optical image in Fig. 3.2a was obtained using an MLC that was similar to MLC1.

3.6.2 MLC Fabrication

MLCs of PST were fabricated by Tomoyasu Usui and Sakyo Hirose at Murata Manufacturing Co. MLCs of PST were prepared by solid-state reaction and tape casting. Stoichiometrically weighed powders of Pb_3O_4, Sc_2O_3 and Ta_2O_5 were ball-milled in distilled water for 17 h with balls of partially stabilized zirconia. The resulting slurry was dried and calcined at 850 °C for 4 h to obtain PST powder. This powder was ball-milled for 24 h in an organic solvent with a binder, and the resulting slurry was used to form green sheets of PST with a 300-μm-gap doctor blade. After screen-printing inner electrodes of Pt paste, the green sheets were stacked, pressed, and cut to obtain green chips. Next, the binder was burned off at 500 °C for 4 h. Proto-MLCs were then sintered at 1400 °C for 4 h and subsequently annealed at 1000 °C for 100-1000 h, while surrounded with a mixture of Pb_3O_4 and ZrO_2 powders whose Pb:Zr ratio was 1:1 (the resulting $PbZrO_3$ reaction product prevented lead loss). However, MLC8 with reduced B-site cation order (Section 3.7.13) did not undergo the anneal at 1000 °C. Outer electrodes were fabricated with silver paste. The challenges of MLC fabrication are discussed in Section 3.7.3.

3.6.3 PST grain size and density

Determination of grain size and density measurements were conducted at Murata Manufacturing. An average grain size of 2-3 μm was identified by scanning electron microscopy. An average value of density $\rho \sim 8750$ kg m^{-3} was calculated by using Archimedes' principle to identify $\rho = (w\rho_{water})/(w - v)$ for three samples (5 mm × 5 mm × 0.3 mm) fabricated from thick green sheets without electrodes. Here, w denotes the sample

weight in air, v denotes the apparent sample weight in purified water, and ρ_{water} is the density of water.

3.6.4 Temperature control for isothermal measurements of dielectric constant and electrical polarization

A bespoke cryogenic probe [83] was used for temperature control, with good thermal contact ensured between the probe and the MLC under study. To establish an appropriate timescale for isothermal measurements, the thermal relaxation time (approximately ~2.2 s for 1/e decay) was identified at room temperature from infrared measurements of quasi-adiabatic temperature change in air (not shown). The use of vacuum had nominally no effect on thermal relaxation time.

3.6.5 Temperature control for highly adiabatic EC measurements with the thermocouple and infrared camera

The MLC was suspended approximately 0.9 mm above the heater block of a bespoke heating stage [83] that was open to air (Fig. 3.1). The thermal relaxation time (about ~7 s for 1/e decay) was identified from thermocouple measurements of temperature change (left inset of Fig. 3.5a).

3.6.6 Dielectric measurements

These were performed with an Agilent 4294A Precision Impedance Analyzer, by sweeping the frequency from 100 Hz to 100 kHz. Data were collected approximately every 0.12 K while cooling and subsequently warming at the slow rate of ±1 K min^{-1} in the cryogenic probe [83].

3.6.7 X-ray diffraction measurements

These were performed by Samer Kurdi with Cu-Kα radiation using a Bruker D8 Advance diffractometer equipped with a LYNXEYE EX detector. The intensities of the 111 and 200 reflections were determined by fitting a pseudo-Voigt function using HighScore Plus software.

3.6.8 Differential scanning calorimetry

This was performed using a TA Instruments Q2000 DSC that was calibrated via the melting transition of an indium reference sample. Data were obtained on increasing the temperature at 10 K min^{-1}. Following standard practice [160], heat flow đQ/dt was normalized by temperature ramp rate dT/dt to yield đQ/dT. Integration of đQ/dT yielded latent heat $|Q_0| \sim 10.2$ MJ m^{-3} after subtracting a sigmoidal baseline (inset, Fig. 3.3a). Calibration with a sapphire reference permitted đQ/dT to be recast as zero-field heat capacity $c(T)$ (Fig. 3.3a). From $c(T)$, the zero-field entropy $S'(T) = S(T) - S(270\ \mathrm{K}) = \int_{270\ \mathrm{K}}^{T} c(T')/T'\ \mathrm{d}T'$ (Fig. 3.3b) was obtained, defined with respect to the entropy S at 270 K.

3.6.9 Indirect EC measurements

Using a Keithley 2410 SourceMeter, highly isothermal measurements of electrical polarization were obtained at constant current (10 μA above T_C, 5 μA below T_C) on warming from 270 K to 405 K in the cryogenic probe [83], such that approximately every 0.35 K one bipolar cycle in ±600 V, two unipolar cycles out to +600 V, and two unipolar cycles out to −600 V were measured. Bipolar cycles were used to centre unipolar cycles on the polarization axis, and $P(T,E)$ data for indirect EC measurements were harvested from the second positive unipolar cycle (examples of bipolar and unipolar cycles appear in Fig. 3.8). The small constant current limited the instantaneous speed of the field-driven transition to yield approximately isothermal conditions (the duration of ≥ 20 s for each cycle branch was ≥9 times as large as the thermal relaxation time of approximately 2.2 s for 1/e decay).

3.6.10 Improvements to the indirect method

Three improvements introduced in my co-authored paper [2] permit excellent agreement between the indirect EC measurements and the direct measurements (comparisons appear in Fig. 3.5b and Fig. 3.14). First, $P(E)$ was measured approximately every 0.35 K, in contrast with the standard practice of using 10 K increments, resulting in a dense map of $P(T,E)$ (Fig. 3.4a) that was used to construct a dense map of $\Delta S(T,E)$ (Fig. 3.4b). Second, unipolar not bipolar $P(E)$ measurements (Section 3.7.5) were used, thus minimizing field hysteresis to strengthen the single-valued assumption on $P(T,E)$. Third, $\Delta T(T_s,E)$ (Fig. 3.4d) was evaluated

by following adiabatic contours on the entropy map $S'(T,E)$ (Fig. 3.4c) that were created by subtracting $\Delta S(T,E)$ (Fig. 3.4b) from $S'(T,0)$ (Fig. 3.3b), thus improving on the standard practice of identifying $\Delta T \sim -T\Delta S/c$ under the assumption of some single effective value for the specific heat capacity c.

3.6.11 Direct thermocouple measurements of temperature change

The measurement set-up appears in Fig. 3.1a. A bespoke K-type thermocouple was monitored at approximately 4.5 Hz to record EC cycles roughly every 5 K on warming from 295 K to 388 K. These cycles were driven using a current of magnitude 10 mA from a Keithley 2410 SourceMeter. The insulation of the 40-μm-diameter thermocouple wires was removed within about 2 cm of the weld to reduce thermal mass. The weld was pressed onto the centre of the MLC face and attached with a drop of matt black paint (PNM400, Electrolube) for good thermal contact. To prepare the MLC for subsequent infrared measurements, the thermocouple and black paint were removed from the MLC by using acetone and then isopropyl alcohol.

3.6.12 Direct infrared measurements of temperature change

The measurement set-up appears in Fig. 3.1b. The infrared camera (SC7500, FLIR) was operated at 50 Hz to image EC cycles approximately every 5-10 K on warming in air. These cycles were driven using a current of magnitude 1-10 mA from a Keithley 2410 SourceMeter. To increase emissivity, two layers of matt black paint (PNM400, Electrolube) were spin-coated on the MLC face, resulting in a total thickness of approximately 6 μm. All infrared data represent an average within the 300 μm × 300 μm face centre (white square, Fig. 3.2b), with the exception of the infrared image that is presented in the right inset of Fig. 3.5a. Section 3.7.15 explains how good calibration across starting temperatures that spanned 188 K was achieved, and how emissivity of 0.84-0.87 for the black paint was identified.

3.6.13 Accounting for inactive thermal mass in the active area

Inside and not near the periphery of the active area, complete thermalization between the 19 active layers of PST and the inactive layers (two outer layers of PST, 20 inner electrodes of Pt) implies $|\Delta T_j| \sim 0.86|\Delta T|$, assuming an off-peak volumetric heat capacity of

$c \sim 2.7$ MJ K^{-1} m^{-3} for PST (Fig. 3.3a), and $c \sim 2.8$ MJ K^{-1} m^{-3} for Pt. The prediction of $|\Delta T_j| \sim 0.86|\Delta T|$ is similar to the empirical finding of $|\Delta T_j| \sim 0.90|\Delta T|$.

3.7 Supplementary Information

3.7.1 Larger magnetocaloric effects in Gd

The strategies for attaining adiabatic temperature changes in Gd that exceed 2.5 K include:

- increasing the applied magnetic field beyond $\mu_0 H_{app}$ ~ 1.4 T, but this is considered too expensive for widespread applications [149, 150].
- reducing the demagnetizing factor, but by doing so failing to exploit well the finite volume addressed by the applied magnetic field. Consequently, thin Gd sheets with a low demagnetizing factor are deployed in prototypes [147] as dense arrays with a relatively large demagnetizing factor [124, 161].

For example, [162] describes a 10 mm × 4 mm × 4 mm bar of high-purity Gd (99.99 wt.%), whose relatively low demagnetizing factor would permit the $\mu_0 H_{app}$ ~ 1.4 T available from permanent magnets [149, 150] to generate a peak temperature change of ~4.0 K. Increasing the applied field to $\mu_0 H_{app}$ ~ 2.0 T would increase the peak temperature change to ~5.4 K. For this larger field, [162] shows that $|\Delta T_{eff}| \geq 3$ K for starting temperatures that span ~30 K.

3.7.2 Previous work on macroscopic EC bodies

From the summary on macroscopic EC bodies presented below, it is apparent that the 2.5 K benchmark for Gd in prototypes (Fig. 3.6) has not been hitherto exceeded by directly measured values of temperature near room temperature (RT), and that the 5.5 K reported here for MLCs of PST has not been hitherto exceeded at any starting temperature.

Key

PST = $PbSc_{0.5}Ta_{0.5}O_3$

PMN-PT = $(1\text{-}x)Pb(Mg_{1/3}Nb_{2/3})O_3\text{-}xPbTiO_3$

PZST = $Pb_{0.99}Nb_{0.02}[(Zr_{0.73}Sn_{0.27})_{0.93}Ti_{0.07}]_{0.98}O_3$

BST = $Ba_{0.65}Sr_{0.35}Ti_{0.997}Mn_{0.003}O_3$

BZT-BST = $0.8BaZr_{0.18}Ti_{0.82}O_3\text{-}0.2BaSn_{0.11}Ti_{0.89}O_3$

BZT = $Ba_{0.2}Zr_{0.8}TiO_3$; BTO = $BaTiO_3$

1) Bulk ceramics. These are parameterized in terms of adiabatic temperature change $|\Delta T|$:

a. **Directly measured peak values of $|\Delta T|$ near RT.** The 200-500 μm thick plates of PST and PMN-PT that were used in three EC prototypes displayed [45, 46, 74] $|\Delta T| \sim 0.9\text{-}1.8$ K, while 400 μm-thick samples of PST displayed [2] $|\Delta T| \sim 2.2$ K.

b. **Directly measured peak values of $|\Delta T|$ above 100 °C.** PZST displayed [32] $|\Delta T| \sim 2.6$ K, and PMN-PT displayed [64-67] $|\Delta T| \sim 1.2\text{-}3.5$ K.

c. **Indirectly measured peak values of $|\Delta T|$ near RT.** BST was reported to display [68] $|\Delta T| \sim 3.1$ K as determined via the well-known indirect method that employs a Maxwell relation [12].

d. **Calorimetrically measured peak values of $|\Delta T|$ near RT.** BZT-BST was reported to display [163] $|\Delta T| \sim 3.5$ K, and BZT was reported to display [164] $|\Delta T| \sim 4.5$ K. However, the technique assumes that the thermal resistance between sample and sensor has been correctly evaluated, and that rapidly driven EC effects result in the flow of isothermal heat. Corroborative reports of directly measured temperature change have not been forthcoming.

2) **Ceramic and polymer MLCs.** These have been parameterized in terms of highly adiabatic temperature jumps $|\Delta T_j|$ that were directly measured within the active area following rapid thermalization between the active and inactive layers:

   a. **Directly measured peak values of $|\Delta T_j|$ near RT.** Commercially available MLCs of BTO displayed [71] $|\Delta T_j| \sim 0.5$ K. Polymer MLCs displayed [72] $|\Delta T_j| \sim 2.2$ K.

   b. **Directly measured peak values of $|\Delta T_j|$ at high temperature.** MLCs of PMN-PT displayed [4] $|\Delta T_j| \sim 2.7$ K near 380 K.

MLCs have also been parameterized by scaling up values of $|\Delta T_j|$ to identify the adiabatic temperature change $|\Delta T|$ for the active material, but values were overestimated by assuming complete internal thermalization prior to measurement [4]:

   c. **Directly measured peak values of $|\Delta T|$ near RT after scale up.** For MLCs of PST, an unspecified experimental temperature change $|\Delta T_j|$ was scaled up to yield $|\Delta T| \sim 2.4$ K for the active volume [51].

   d. **Directly measured peak values of $|\Delta T|$ above 100 °C after scale up.** For MLCs of PMN-PT, the experimental temperature change was scaled up by a factor of 2.86 to yield $|\Delta T| \sim 2.3$ K for the active volume [67].

3.7.3 Challenges of MLC fabrication

MLCs of PST were fabricated and optimized by Tomoyasu Usui and Sakyo Hirose at Murata Manufacturing. MLCs of PST with high B-site cation order and high breakdown strength have not been hitherto realized. This reflects two non-trivial challenges: the fabrication of high-quality PST, and the co-firing of inner electrodes. Simultaneously overcoming both of these challenges led to the selection of Pt for the inner electrodes, in order to avoid reaction with PST during the high-temperature sintering that is required.

For bulk PST reported elsewhere (Section 3.7.2), the precursor powder is typically calcinated and ground several times to eliminate parasitic phases, sintered at temperatures that typically exceed 1500 °C, quenched to room temperature in some cases, and annealed for a long time to achieve high B-site cation order. For MLCs of PST, the grinding would destroy the Pt inner electrodes, and sintering at the optimal temperature for bulk PST would result in both delamination and chemical reaction (between the Pt inner electrodes and PbO). Moreover, the Pt inner electrodes may block diffusion during the sintering and annealing steps, thus compromising PST grain growth and B-site cation order.

Considerable optimization was therefore required in order to fabricate high-quality MLCs of PST with just one sintering step (at 1400 °C). For example, to obtain high-quality green sheets that were dense and smooth, it was necessary to carefully optimize particle size (via ball-milling duration), slurry composition (via PST powder, organic solvent, binder, plasticizer), slurry viscosity, tape-casting conditions (via drying temperature, casting speed, air flow) and calcination. Calcination at too low a temperature (800 °C) tended to cause MLCs to crack or delaminate when sintered, while calcination at too high a temperature (900 °C) precluded high B-site cation order after a long anneal of 100-1000 hours.

The use of PST is particularly challenging. This is because the high-temperature sinter is required for high breakdown field (via high density), and the long anneal is required for high B-site cation order, but these very treatments can compromise breakdown field and cation order by promoting lead loss. Overcoming this challenge involved optimizing the porosity of sufficiently fresh ZrO_2 saggars, which had been annealed with $PbZrO_3$ in order to avoid the undue absorption of PbO.

3.7.4 B-site cation order from X-ray diffraction after powdering

X-ray diffraction measurements and analysis were performed by Samer Kurdi. B-site cation order was parameterized via $S_{111} = [(I_{111}/I_{200})_{measured}/(I_{111}/I_{200})_{expected}]^{1/2} \sim 0.96$, using the measured and expected [165] intensities I of the 111 and 200 reflections (Fig. 3.7).

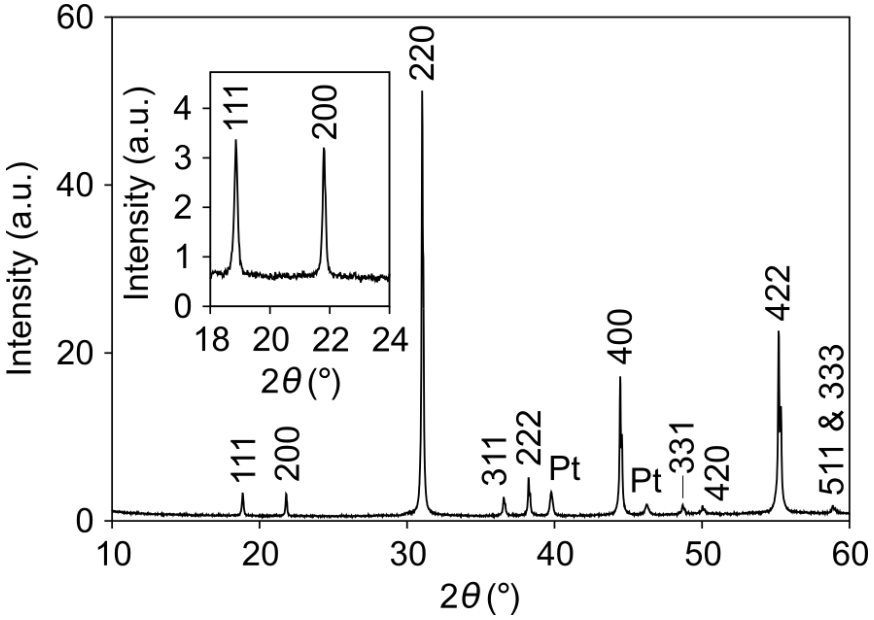

Fig. 3.7 | **X-ray diffraction after powdering.**

XRD 2θ-ω scan with (inset) detail of the 111 and 200 reflections. Data for MLC1 after crushing to form a powder.

3.7.5 Bipolar and unipolar measurements of isothermal electrical polarization

Shown here are examples of isothermal bipolar cycles (Fig. 3.8a) that were used to centre isothermal unipolar cycles (Fig. 3.8b) measured at the same temperature (see Section 3.6.9). The field-removal branches of these unipolar cycles yielded a map of polarization $P(T,E)$ that was presented for positive fields in Fig. 3.4a. Ferroelectric behaviour at low temperature gives way to paraelectric behaviour at high temperature via a regime in which the field-driven transition is characterized by inflection points. These inflection points were used to identify the phase boundary and critical end point in the polarization map (dotted line in Fig. 3.4a).

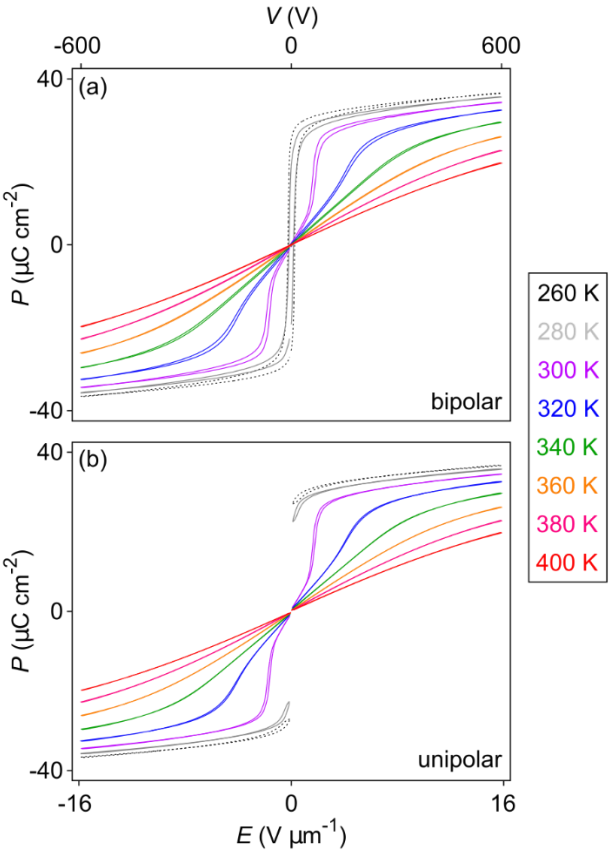

Fig. 3.8 | **Bipolar and unipolar measurements of isothermal electrical polarization.**

(a) Bipolar and (b) unipolar cycles for $P(E)$ at eight of 385 increasing measurement temperatures separated by ~0.35 K. Section 3.6.9 describes the profile of the driving voltage V that was used to collect the bipolar and then the unipolar data at each temperature. Data for MLC1.

3.7.6 Constant-field cross-sections through Fig. 3.4 panels showing indirect EC effects

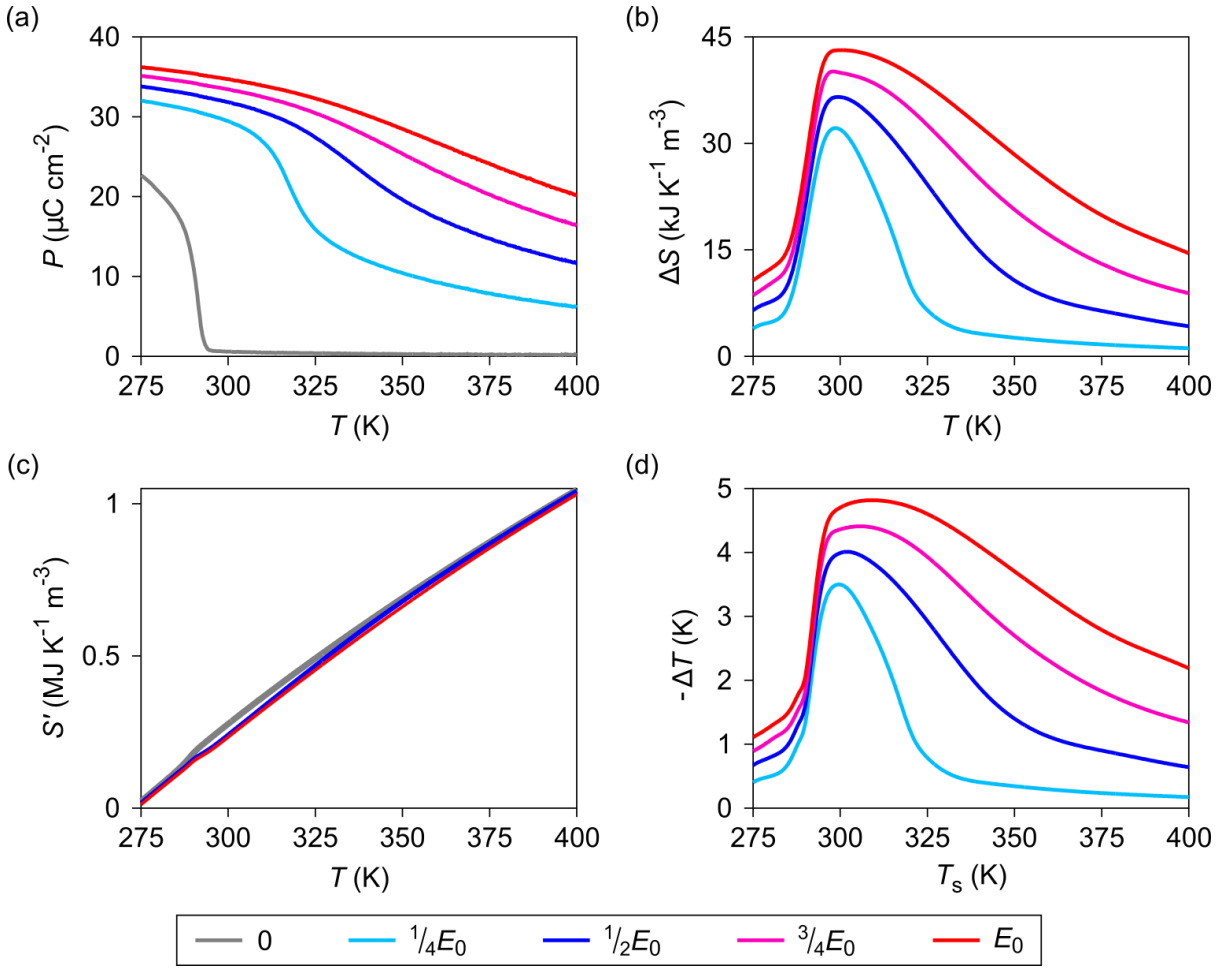

Fig. 3.9 | **Constant field cross-sections through the Fig. 3.4 panels showing indirect EC effects.**

For fractional values of the applied field E_0 = 15.8 V μm^{-1}, shown are (a) $P(T)$, (b) $\Delta S(T)$, (c) $S'(T) > 0$, and (d) $-\Delta T(T_s)$. In (c), the prime indicates the subtraction of the zero-field entropy at 270 K. Data for MLC1.

3.7.7 Polarization jump at the finite-field phase boundary

The Clausius-Clapeyron equation in Section 3.3.2 employs a value of $|\Delta P| \sim 24.0$ μC cm^{-2} that was identified from field-removal $P(E)$ data just above T_C after correcting for the difference in gradient above and below the field-driven transition (Fig. 3.10a). This correction was made by subtracting the paraelectric background that was identified by integrating the sigmoidal baseline identified for $\varepsilon = \frac{1}{\varepsilon_0}\frac{\partial P}{\partial E}$ (Fig. 3.10b) (ε is the relative dielectric constant, ε_0 is the permittivity of free space, and sigmoidal-baseline corrections to heat capacity data (Fig. 3.3a,b) are well established).

Note that $|\Delta P| \sim 24.0$ μC cm^{-2} (Fig. 3.10a) was identified by including the small increase in P that follows the sharp jump, as the peak in $\varepsilon(E)$ (Fig. 3.10b) reveals that the transition extends beyond the jump field.

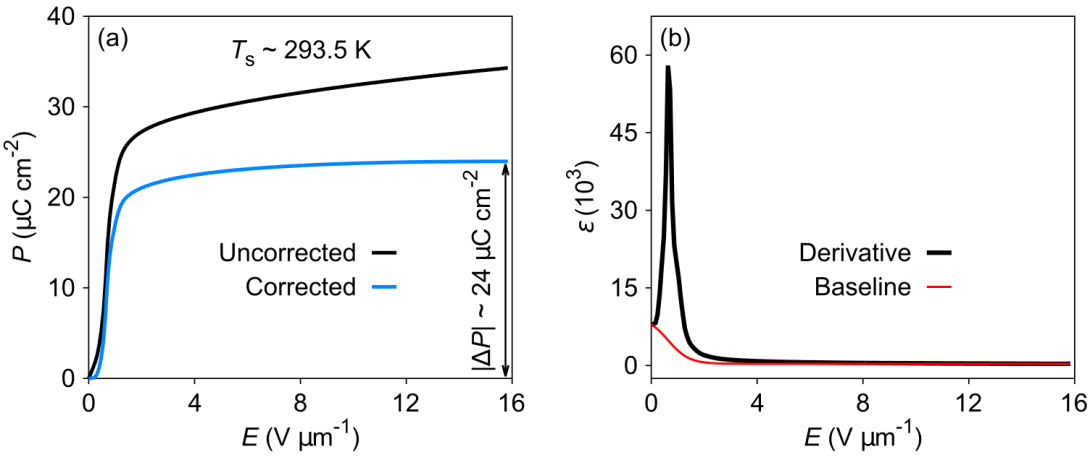

Fig. 3.10 | **Identification of $|\Delta P| \sim 24.0$ μC cm^{-2} at the E(T) phase boundary.**

(a) Upper branch of unipolar field-removal $P(E)$ data at $T_s \sim 293.5$ K (from Fig. 3.4a) before (black) and after (blue) correction. Correction was made by a subtraction that followed integration of (b) the sigmoidal baseline (red) for $\varepsilon = \frac{1}{\varepsilon_0}\frac{\partial P}{\partial E}$ (black). Data for MLC1.

3.7.8 Field dependence of the EC effect

Large high-field EC effects. Direct measurements of $|\Delta T_j|$ versus E for a representative starting temperature of $T_s \sim 315$ K (red and blue squares, Fig. 3.11) show that the jump associated with driving the phase transition is followed by high-field EC effects in the transformed phase. Large EC effects that are not directly associated with the phase transition itself make a significant contribution to the large values of $|\Delta T_j|$, both above and below the critical temperature that was identified in Fig. 3.4a.

Comparison with indirect EC measurements. Directly measured values of $|\Delta T_j|$ match well with indirectly measured values of $0.90|\Delta T|$ when varying both E (Fig. 3.11) and T_s (Fig. 3.5b).

Crossover. The values of $|\Delta T_j|$ obtained for field application/removal experience a crossover when varying field (Fig. 3.11) and T_s (Fig. 3.5b). These crossovers are explained in Section 3.7.9.

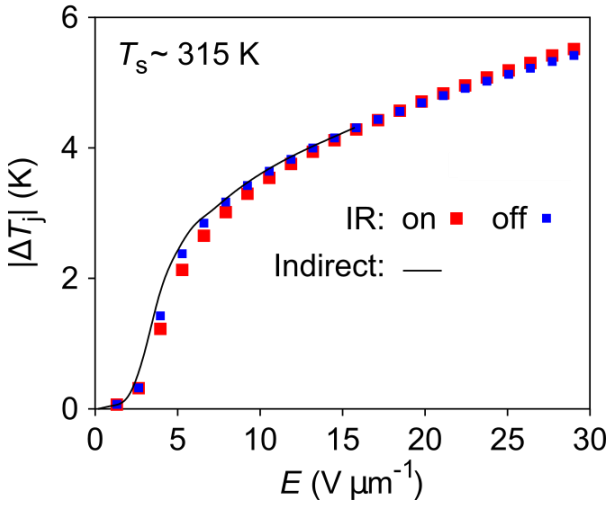

Fig. 3.11 | **Electric-field dependence of the EC effect.**

Temperature jump magnitude $|\Delta T_j|$ versus the electric field E that was switched on and then off, starting each time at temperature $T_s \sim 315$ K. Data were measured at the MLC face centre using the IR camera. The black line showing $0.90|\Delta T|$ for $T_s \sim 315$ K was derived via the indirect method, and corresponds to a constant-temperature cross-section through Fig. 3.4d after scaling by 0.90. Data for MLC1.

3.7.9 Crossover in field application/removal values of $|\Delta T_j|$ when varying T_s or E

Crossover in starting temperature T_s

Directly measured values of $|\Delta T_j|$ were slightly larger on field application (removal) below (above) some crossover starting temperature (Fig. 3.5b).

Crossover in field E

Directly measured values of $|\Delta T_j|$ were slightly larger on field application (removal) above (below) some crossover field (Fig. 3.11).

Reason for crossover

As explained in Section 2.3.1, field application/removal values of $|\Delta T_j|$ represent two legs in a given Brayton cycle. The other two legs are $S(T,0)$ and $S(T,E)$ isofields, which converge at temperatures away from the phase transition in a field-dependent manner (Fig. 2.5). This renders field application/removal values of $|\Delta T_j|$ asymmetric, as observed. The discrepancies in $|\Delta T_j|$ on field application/removal are therefore intrinsic rather than a consequence of any irreversibility, and they are small because the transition is broad.

3.7.10 Large EC effects over a wide range of useful temperatures for six MLCs

Here the IR-based data from Fig. 3.5b and Fig. 3.6a are reproduced along with comparable data for five similar MLCs.

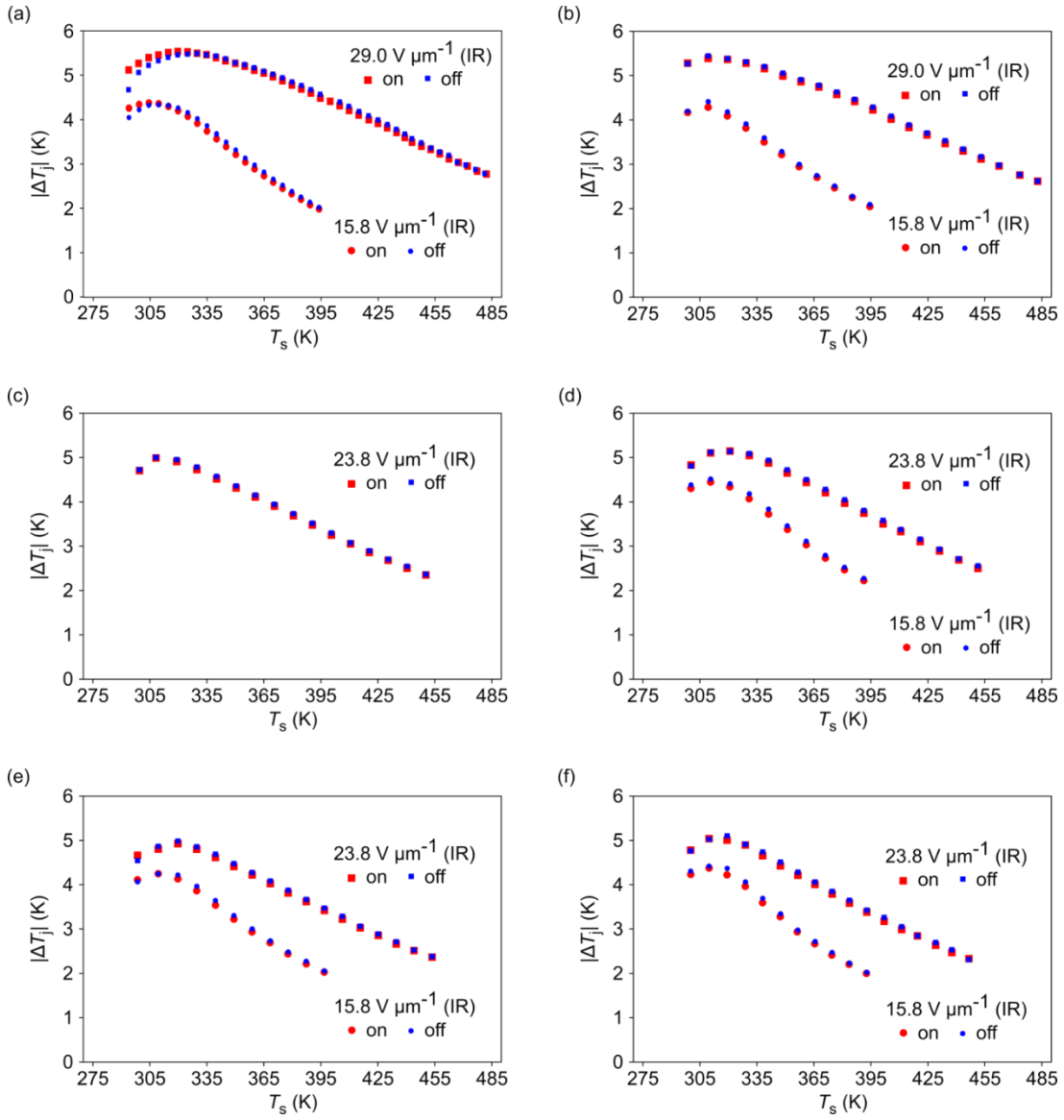

Fig. 3.12 | **Direct EC measurements for six MLCs of PST.**

IR data for (a) MLC1 (S_{111} ~ 0.96) (from Fig. 3.5b), and the corresponding data for (b) MLC2 (S_{111} ~ 0.90), (c) MLC3 (S_{111} ~ 0.91), (d) MLC4 (S_{111} ~ 0.96), (e) MLC5 (S_{111} ~ 0.92) and (f) MLC6 (S_{111} ~ 0.93).

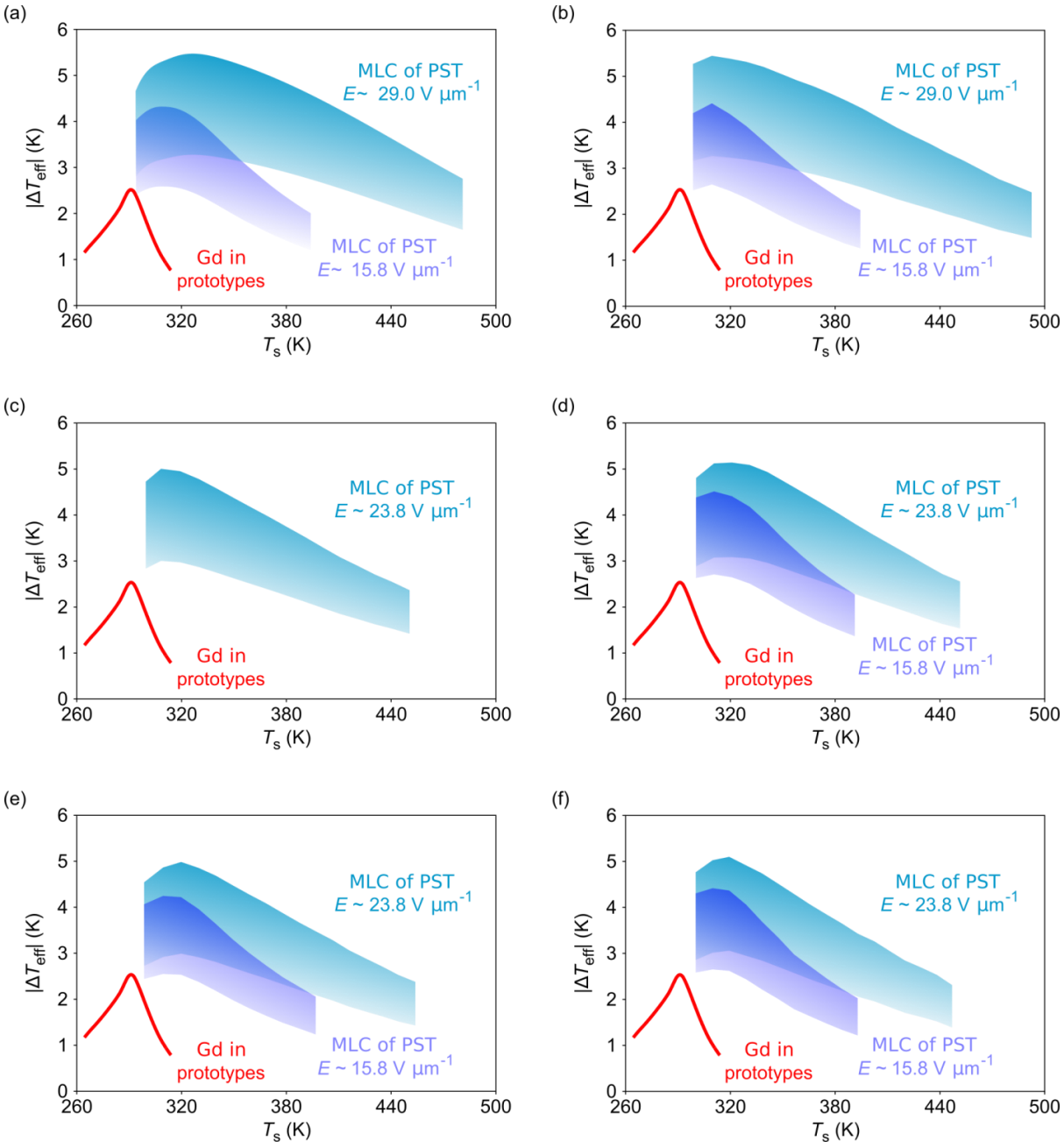

Fig. 3.13 | **Large EC effects over a wide range of operating temperatures for six MLCs of PST.**

Data for (a) MLC1 (S_{111} ~ 0.96) (from Fig. 3.6a), and the corresponding data for (b) MLC2 (S_{111} ~ 0.90), (c) MLC3 (S_{111} ~ 0.91), (d) MLC4 (S_{111} ~ 0.96), (e) MLC5 (S_{111} ~ 0.92) and (f) MLC6 (S_{111} ~ 0.93).

3.7.11 Self-consistent evaluation of $|\Delta S|$ from direct and indirect EC measurements

For E = 15.8 V μm^{-1}, the same changes of entropy were identified via the indirect and direct EC measurements (Fig. 3.14), thus confirming the equivalence of the two methods. For E = 15.8 V μm^{-1}, the peak entropy change identified by both methods was $|\Delta S|$ = 43 kJ K^{-1} m^{-3} at ~300 K. For E = 29.0 V μm^{-1}, the peak entropy change identified via direct EC measurements was $|\Delta S|$ ~ 53 kJ K^{-1} m^{-3} at ~308 K.

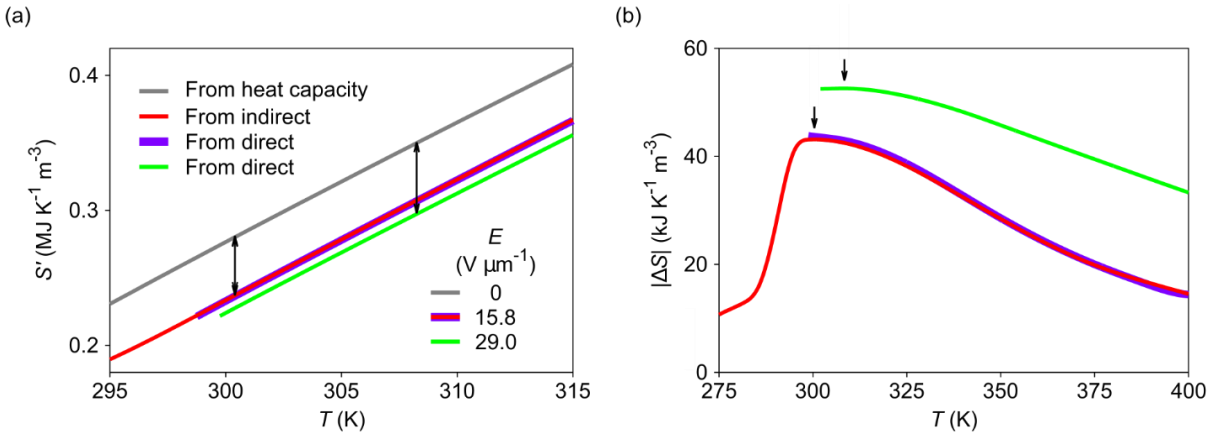

Fig. 3.14 | **Variation of entropy with temperature and field.**

(a) Entropy $S'(T,0)$ (grey) obtained from heat capacity data (Fig. 3.3b). Entropy $S'(T,15.8$ V μm$^{-1})$ (red) obtained from indirect EC measurements (Fig. 3.9c). Entropy $S'(T,15.8$ V μm$^{-1})$ (purple) and $S'(T,29.0$ V μm$^{-1})$ (green) obtained by adding adiabatic temperature change $\Delta T(T_s,E)$ to $S'(T,0)$, where $\Delta T(T_s,E) = \Delta T_j(T_s,E)/0.90$ was identified via the direct measurements of $\Delta T_j(T_s,E)$ on field application (Fig. 3.5b). Prime indicates subtraction of zero-field entropy at 270 K, scaling factor of 0.90 identified in Section 3.6.13, T_s denotes starting temperature, plots interpolate between data points, data points not shown for clarity. Hence (b) isothermal entropy change $|\Delta S(T,E)|$. Vertical arrows at 300 K and 308 K in (a,b) identify the peak in $|\Delta S(T)|$. Data for MLC1.

3.7.12 Electrical work done to drive MLCs of PST

Electrical work of magnitude $|W| \sim 2.5$ MJ m^{-3} is required to isothermally apply the maximum electric field of $E = 29.0$ V μm^{-1} at ~330 K, as deduced from the plot of $P(E)$ in Fig. 3.15. (Electrical work $W = \int E đ D$ was evaluated as $\int E đ P$ using the field application branch.)

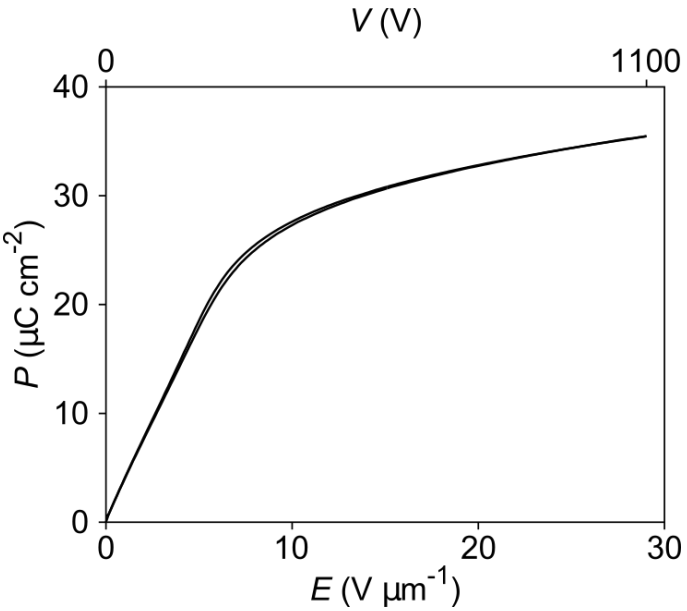

Fig. 3.15 | **Isothermal electrical polarization measured out to the maximum field of 29.0 V μm^{-1}.**

Unipolar polarization P at ~330 K is presented as a function of both electric field E and the corresponding voltage V. Data for MLC7 ($S_{111} \sim 0.94$).

3.7.13 The effect of B-site cation order on EC effects in MLCs of PST

The peak in $|\Delta T_j|$ versus T_s was suppressed when the B-site cation order was reduced from S_{111} ~ 0.96 to S_{111} ~ 0.81 (Fig. 3.16). The small enhancement at the largest values of T_s is a consequence of the broader phase transition.

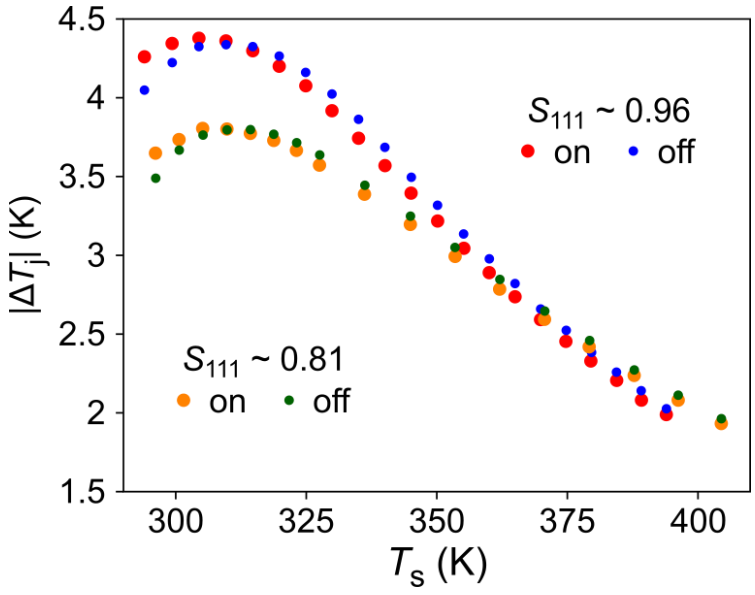

Fig. 3.16 | **Direct EC measurements in MLCs of PST with reduced B-site cation order.**

Temperature jump magnitude $|\Delta T_j|$ versus T_s, when 15.8 V µm^{-1} was switched on and later off, as measured at the face centre using the IR camera. Peak values are $|\Delta T_j|$ ~ 4.3 K and $|\Delta T_j|$ ~ 3.8 K. Data for MLC8 (S_{111} ~ 0.81) is compared with data for MLC1 (S_{111} ~ 0.96) copied from Fig. 3.5b.

3.7.14 Landau model for PST in MLCs

The fitting of experimental data to Landau theory was performed by Gian Guzmán-Verri. Landau theory describes well the experimental behaviour of conventional (non-relaxor) ferroelectric materials like that reported here (Fig. 3.17), most notably when using supercritical fields to access a wide range of operating temperatures, and more generally when identifying its adiabatic temperature change $\Delta T(T_s,E)$, isothermal entropy change $\Delta S(T,E)$, electrical polarization $P(T,E)$ and entropy $S_L(T,E)$ with respect to the unpolarized zero-field state at the same temperature [entropy S_L differs with respect to the total entropy S, and the relative entropy $S'(T) = S(T) - S(270\ \text{K})$ that was employed elsewhere].

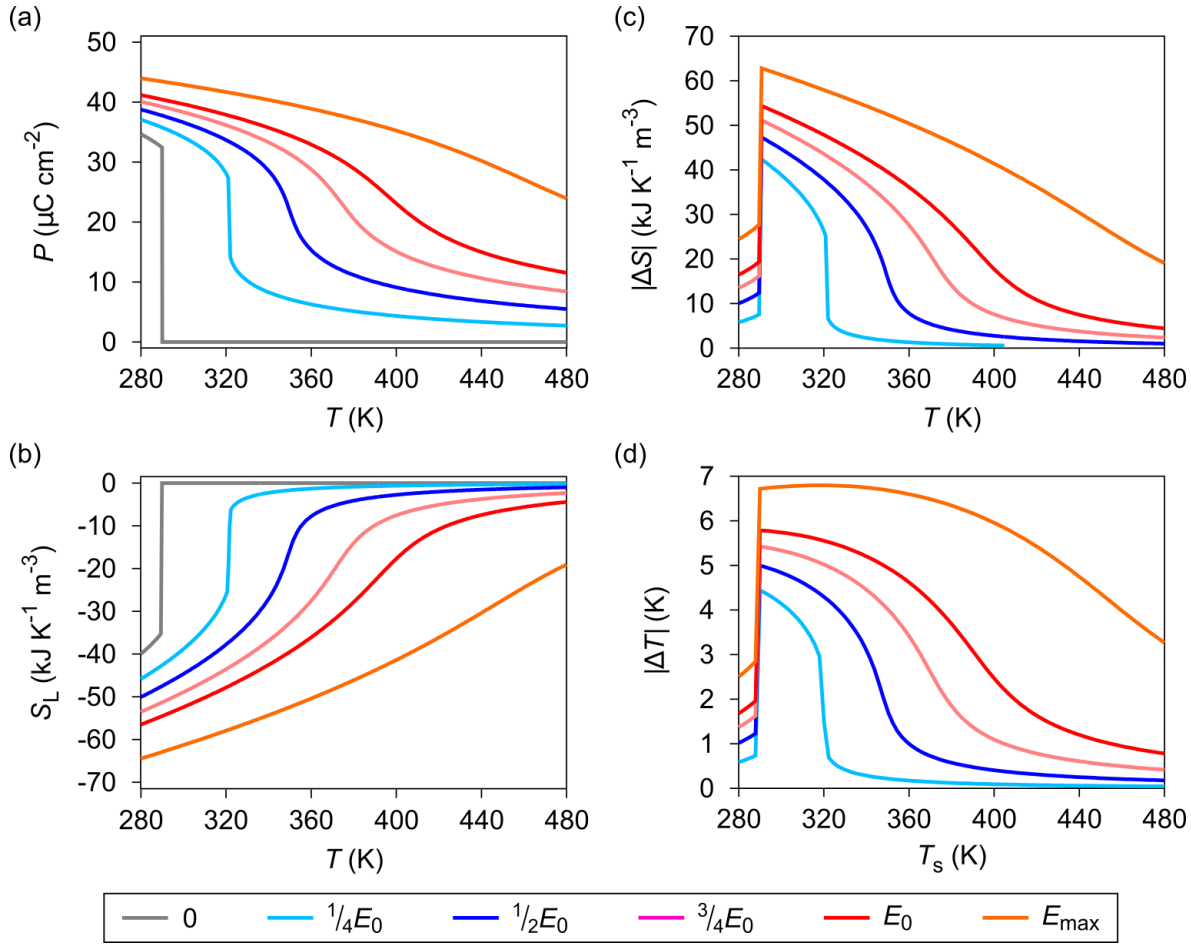

Fig. 3.17 | **Results of the Landau model for PST in MLCs.**

(a) $P(T,E)$, (b) $S_L(T,E)$, (c) $|\Delta S(T,E)|$ and (d) $|\Delta T(T_s,E)|$, with E_0 = 15.8 V μm^{-1} and E_{max} = 29.0 V μm^{-1}.

The Landau model

At temperature T, the free energy density F with respect to the unpolarized zero-field state was expanded out to P^6, yielding:

$$F(T,E) = \frac{\alpha}{2}(T - T_0)P^2 + \frac{b}{4}P^4 + \frac{c}{6}P^6 - EP \tag{3.1}$$

where polarization P and applied electric field E are collinear with respect to the same pseudo-cubic <111> direction, and where α, T_0, b and c are constants to be determined by fitting.

Minimizing free energy with respect to polarization ($\frac{\partial F}{\partial P} = 0$) yields the equation of state:

$$a_0(T - T_0)P + bP^3 + cP^5 = E \tag{3.2}$$

and hence $P(T,E)$. Differentiating free energy with respect to temperature yields entropy:

$$S_L(T,E) = -\frac{\partial F}{\partial T} = -\frac{a_0}{2}P^2(T,E) \tag{3.3}$$

in terms of $P(T,E)$.

Fitting the model

Table 3.2 | **Model parameters for PST in MLCs.**

a_0	0.6676	$10^6\,C^{-2}\,m^2\,N\,K^{-1}$
b	-7.276	$10^8\,C^{-4}\,m^6\,N$
c	5.204	$10^9\,C^{-6}\,m^{10}\,N$
T_0	273	K

The equation of state was used to evaluate $P(T,E)$ (Fig. 3.17a) and hence $S_L(T,E)$ (Fig. 3.17b), with four model parameters (Table 3.2) that were obtained by fitting to four experimental parameters T_C, $|\Delta S_0|$, T_{cp} and E_{cp}:

1) The Curie temperature T_C = 290 K is associated with the development of an absolute minimum in the zero-field free energy via $F(T_C,0)|_{P(T_C,0)} = 0$, where $P(T_C,0)$ is the spontaneous polarization at T_C (to be predicted by the model).
2) The zero-field entropy jump of $|\Delta S_0| \sim 35$ kJ K^{-1} m^{-3} at T_C is identified via Eq. (3.3).
3) The abscissa and ordinate values $(T_{cp}, E_{cp}) = (330\text{ K}, 5\text{ V }\mu\text{m}^{-1})$ of the critical end point (cp), which were determined from inflection points in experimental $P(E)$ data (Fig. 3.4), satisfy the condition:

$$\left.\frac{\partial F}{\partial P}\right|_{cp} = \left.\frac{\partial^2 F}{\partial P^2}\right|_{cp} = \left.\frac{\partial^3 F}{\partial P^3}\right|_{cp} = 0 \qquad (3.4)$$

The predicted value of $P_{cp} = P(T_{cp}, E_{cp}) = 20.5\ \mu\text{C cm}^{-2}$ matches well with the measured value of $P_{cp} = P(T_{cp}, E_{cp}) = 18\ \mu\text{C cm}^{-2}$. However, the polarization jump $|\Delta P|$ at T_C given by $P(T_C,0) \sim 32.4\ \mu\text{C cm}^{-2}$ (Fig. 3.17a) exceeds the effective value of $|\Delta P| \sim 24\ \mu\text{C cm}^{-2}$ (Section 3.7.7) that was used earlier to correctly identify the zero-field entropy change $|\Delta S_0|$ via the Clausius-Clapeyron equation. This discrepancy in $|\Delta P|$ is likely a consequence of inhomogeneity, most notably due to thermal and electrical edge effects, and possibly also due to the use of a polycrystalline material. The inhomogeneity renders evaluation of $|\Delta P|$ at T_C challenging (Section 3.7.7), and justifies not selecting $|\Delta P|$ at T_C as an input parameter.

EC effects predicted by the model

The isothermal entropy change $\Delta S(T,E) = S_L(T,0) - S_L(T,E) = -\frac{a_0}{2}\left[P^2(T,0) - P^2(T,E)\right]$ for the removal of field E (Fig. 3.17c) follows from the earlier expression for entropy $S_L(T,E) = -\frac{a_0}{2}P^2(T,E)$.

The adiabatic temperature change $\Delta T(T_s,E) = T_f - T_s$ for the removal of field E (Fig. 3.17d) follows from the relation [166] $T_f = T_s \exp\left\{\frac{a_0}{2c}\left[P^2(T_f,E) - P^2(T_s,0)\right]\right\}$ between start

temperature T_s and finish temperature T_f, with volumetric heat capacity $c = 2.7$ M J K^{-1} m^{-3} (Fig. 3.3a) evaluated well above the Curie temperature T_C.

High-field EC effects predicted by the model are large over a wide range of temperatures (Fig. 3.17c,d), in fair qualitative and quantitative agreement with the indirect EC measurements of ΔS (Fig. 3.9b) and ΔT (Fig. 3.9d), and the direct EC measurements of temperature jump magnitude $|\Delta T_j| = 0.90|\Delta T|$ (Fig. 3.5b).

$F(P)$ plots on the E-T phase diagram

The phase boundary on an E-T phase diagram (red line, Fig. 3.18) predicted by the Landau model is approximately consistent with experimental observations (dotted line, Fig. 3.4a). Following common practice in the field of thermofluids [167], the phase diagram may be divided at the critical point into four quadrants that are distinguished by qualitatively different $F(P)$ plots (Fig. 3.18).

Note that the two transcritical quadrants are not phases, and instead describe regions where one control parameter is supercritical while the other is subcritical. A transcritical paraelectric cannot be transformed into a ferroelectric by applying an electric field, just as a transcritical gas cannot be compressed into a liquid. A transcritical ferroelectric cannot be transformed into a paraelectric by increasing its temperature, just as a transcritical liquid cannot be heated to form a gas.

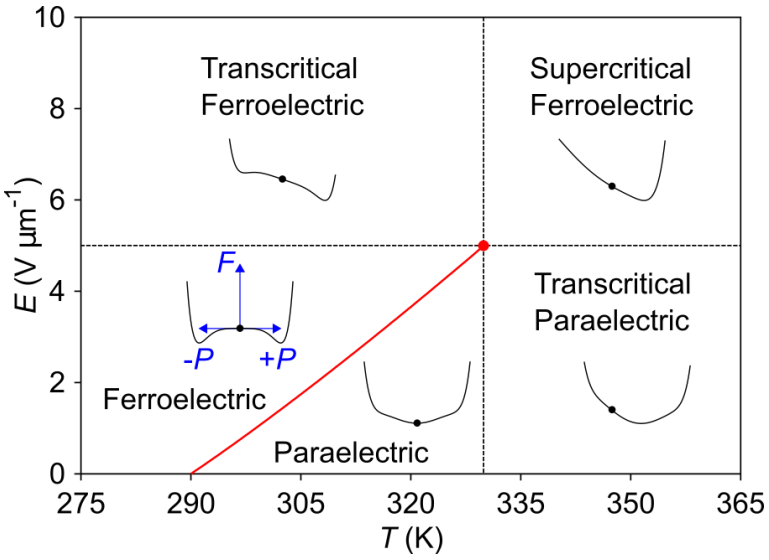

Fig. 3.18 | **Calculated *E*-*T* phase diagram for PST in MLCs.**

The phase boundary (red line) terminates at the critical end point (red dot) that defines the boundaries between quadrants (black dashed lines). Representative plots of free energy density *F* versus polarization *P* are also shown (axes are only shown for the ferroelectric phase, black dot denotes origin).

3.7.15 Calibration of the IR camera and evaluation of emissivity

At a series of increasing measurement set temperatures that ranged from 294 K to 340 K, two parameters were recorded simultaneously, namely (1) the number of counts x for each relevant pixel using an integration time of τ = 637 μs, and (2) the temperature T as measured using a bespoke K-type thermocouple that was attached with Kapton tape near the edge of the MLC face. This procedure yielded calibration curves $x(T)$ for each pixel. On further increasing the measurement set temperature to a maximum measurement temperature of 482 K, the steps described below were taken to avoid saturation and extend the calibration to higher temperatures.

1) Avoiding saturation. Three shorter integration times were used to avoid saturating the pixel detectors, such that a total of four integration times were required to span the 188 K range of starting temperatures (at each temperature of overlap, changes of integration time did not modify the measured values of $|\Delta T_j|$ by more than ~30 mK):

637 μs for 294-340 K

228 μs for 340-395 K

75 μs for 395-465 K

45 μs for 465-488 K

For a given pixel of interest, the number of counts x was proportional to the integration time τ, with just a small discrepancy of <0.5%. This small discrepancy was likely associated with the non-uniformity correction that was performed after each change of integration time, where the use of a shutter may have slightly modified the separation of the camera and MLC (drifts of 1-2 pixels in the image plane were duly corrected).

2) Extending the calibration curves. The $x(T)$ calibration curves for each pixel were extended above 340 K via a semi-empirical form of Planck's law $x = \frac{\beta}{e^{(\alpha/T)} - \gamma} + \delta$ [135], where:

- α is the effective temperature of detectable photons whose wavelengths span 2.0-5.1 μm,
- $\beta = \varepsilon\beta_0$ differs from the black body prefactor β_0 due to emissivity ε.
- γ is a free parameter that differs from unity to account for the spectral width of the detectors in the camera (as specified in the instruction manual).
- δ accounts for radiation $\frac{\beta_0}{e^{(\alpha/T_R)} - \gamma}$ that originates in black-body surroundings at effective temperature T_R before being reflected by the sample with coefficient $(1 - \varepsilon)$, such that T_R may be evaluated from $\delta = (1 - \varepsilon)\frac{\beta_0}{e^{(\alpha/T_R)} - \gamma}$ (assuming the detector background is small).

For each pixel, the four parameters α, β, γ and δ were identified via a least-squares fit to $x(T)$ below 340 K. The values of α and γ were assumed constant for all pixels, whereas the values of β and δ varied from pixel to pixel due to variations in their dependent variables ε and T_R. These variations in ε and T_R were understood to arise because of diffuse emission and reflection arising from non-uniformity in the spin-coated black paint. The fit parameters used are shown in Table 3.3, with ε and T_R presented as a range given the pixel-to-pixel variations.

Table 3.3 | **Fit parameters for the IR camera calibration.**

The emissivity of the painted MLC was found to be $\varepsilon \sim 0.84$-0.87. The parameters β and δ are normalized by the integration time τ with which they varied; δ/τ was slightly different for each integration time due to the <0.5% discrepancy in $x \propto \tau$; and T_R is likely reduced with respect to room temperature due to narcissus from the camera (self-observation via reflected radiation). Data obtained using MLC1.

α	2899 K
β_0/τ	6.71×10^{10} s^{-1}
γ	25
δ/τ	~1.44×10^{6} s^{-1}
ε	0.84-0.87
T_R	274-278 K

“ആന കൊടുത്താലും ആശ കൊടുക്കരുത്."

“You can even gift an elephant, but never give (false) hope.”

Chapter 4

Cooling cycles based on multilayer capacitors of $PbSc_{0.5}Ta_{0.5}O_3$

My co-authored paper describes the efficiency of idealized hypothetical heat pumps that are based on bulk $PbSc_{0.5}Ta_{0.5}O_3$ (PST) operating in Brayton cycles with balanced regeneration via field variation [2]. Here the analysis is repurposed for the multilayer capacitors (MLCs) of PST described in Chapter 3 and extended in three ways. First, the extension includes balanced Ericsson cycles as well as Carnot cycles that are intrinsically balanced. Second, the extension also includes the introduction of a refrigerant efficiency γ that specifies the factor by which the coefficient of performance (COP) for any given cycle is reduced due to losses in the working body. Third, the extension includes a recalculated raw refrigerant efficiency γ_+ that applies if electrical work is dissipated instead of recovered. For the useful temperature spans required by many industrial and domestic applications, regenerative cycles based on MLCs of PST achieve up to $\gamma \sim 97\%$, assuming perfect recovery of electrical work [80]. If electrical work is not recovered, refrigerant efficiency is substantially suppressed, but can nevertheless be as high as $\gamma_+ \sim 87\%$ for a small range of load temperatures near T_C. These findings imply that if electrical work is duly recovered then the losses in an electrocaloric (EC) heat pump will be overwhelmingly due to engineering losses associated with the mechanism around the working body rather than losses within the working body. Corresponding values of γ for bulk PST and a thin clamped companion sample [2] are found to be smaller, possibly due to the sample quality and supercritical EC effects associated with the MLCs.

This chapter details the analysis of idealized EC cooling cycles that employ MLCs of PST. The context for this work is set in Sections 4.1 and 4.2. Section 4.1 contains a brief discussion of caloric heat pumps, and Section 4.2 contains a discussion of literature on intrinsic losses in caloric cooling. Section 4.3 describes the construction of EC cooling cycles for MLCs of PST using data from Chapter 3, and Section 4.4 presents figures of merit for these cooling cycles. In Section 4.5, the refrigerant efficiency is introduced as a novel figure of merit for candidate refrigerants, and in Section 4.6 the raw refrigerant efficiency without energy recovery is examined. In Section 4.7, the refrigerant efficiency is argued to be the appropriate figure of merit for comparisons between different caloric refrigerants, and in Section 4.8, EC cooling cycles employing MLCs of PST are compared to similar cycles employing bulk and thin clamped PST studied in [2]. Section 4.9 provides a summary of the study, and Section 4.10 provides supplementary information cited in earlier sections.

4.1 Caloric heat pumps

Prior to the work presented in Chapter 3, thermal changes in solid-state refrigerants have been typically modest, i.e. $\lesssim$3 K, when driven electrically (Section 3.7.1) or magnetically (Section 3.7.2). Heat pumps based on these materials exploit passive or active regeneration to amplify these temperature changes and achieve large temperature spans across regenerators that separate loads to be cooled from heat sinks. In passive regeneration [147], a caloric refrigerant that undergoes relative motion with respect to a regenerative fluid column cyclically absorbs heat from the cold end of the column (the load) and expels heat at the hot end (the sink), resulting in the development of a large temperature span along the fluid column (Fig. 4.1a). In active regeneration [168, 169], the load and sink are instead separated by a regenerative bed of caloric refrigerant, with which they exchange heat via the motion of a heat transfer fluid, resulting in the development of a large temperature span along the bed (Fig. 4.1b). Discounting lubricant, fluids have recently been avoided in passive regeneration by using a solid-state regenerator [72], and in active regeneration by employing the relative motion of two regenerative arrays of refrigerant that are driven in anti-phase [81].

The most important figures of merit for a heat pump are (i) the temperature span $T_h - T_c$ separating the sink and load at temperatures T_h and T_c, respectively, and (ii) the corresponding coefficient of performance COP = $\frac{Q_c}{W}$, the ratio of the heat Q_c absorbed from the load to the net work W required to pump this heat. State-of-the-art magnetocaloric prototypes are the most developed among the caloric cooling technologies, and they achieve maximum temperature spans of up to ~40 K [148, 170], but only when the cooling power is zero, i.e. COP = 0. In contrast, the best vapour-compression refrigerators [171] achieve temperature spans greater than 60 K while operating at ~60% of the Carnot limit. Vapour compression therefore represents a highly evolved technology that cannot be easily displaced from its mainstream dominance as the industry standard. If caloric cooling were to compete with vapour compression as a truly eco-friendly energy-efficient alternative, the associated losses, as well as cost, must be substantially reduced.

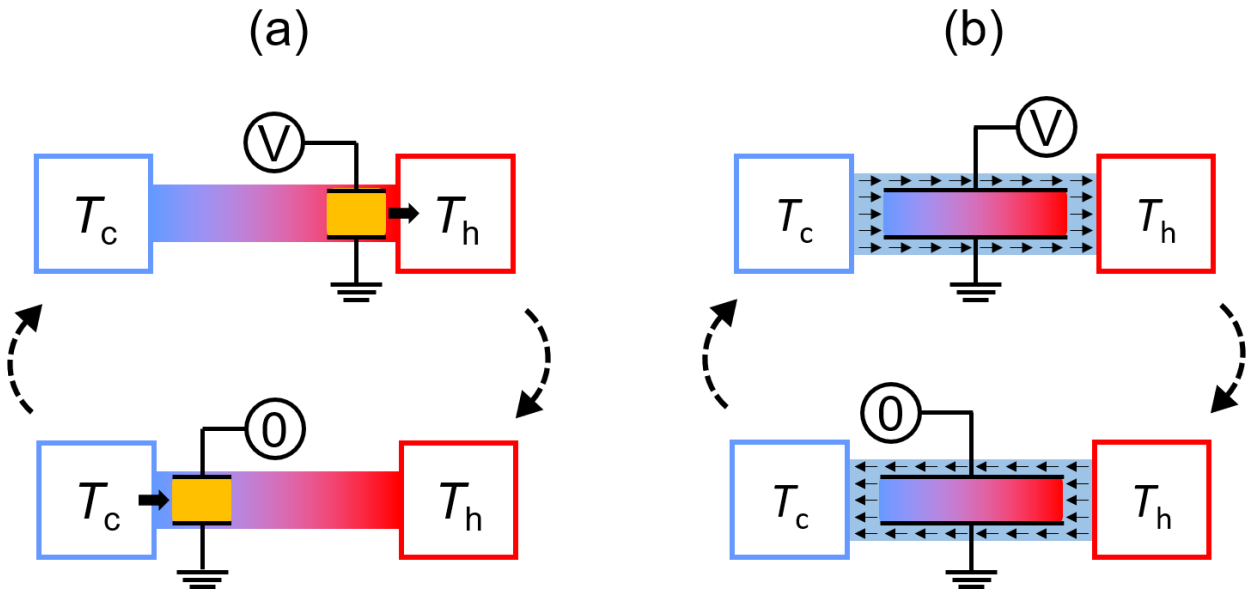

Fig. 4.1 | **Passive and active regeneration.**

(a) Passive regeneration. The EC working body (yellow) moves along a fluid column (blue-to-red gradient) that separates a heat source at temperature T_c (blue) and a heat sink at temperature T_h (red). The direction of heat transfer is denoted by solid arrows. EC heat is dumped to the sink by moving the EC working body to the sink and applying electric field, and EC heat is absorbed from the source by moving the EC working body to the source and removing electric field. A temperature gradient (blue to red) develops as a result and is stored in the fluid column that acts as the regenerator. (b) Active regeneration. A bed of EC refrigerant (blue-to-red gradient) acts as the working body and constitutes the regenerator. Upon field application, EC heat is transferred from the bed to the sink via the motion of heat-transfer fluid (pale blue) towards the sink (solid arrows indicate direction of fluid motion). Upon field removal, EC heat is transferred from the source to the bed via the motion of the fluid towards the source.

4.2 Intrinsic losses in caloric cooling

Losses in caloric cooling can be divided between intrinsic losses arising from the field-cycling and thermal-cycling of the refrigerant, and extrinsic engineering losses arising from the prototype around the refrigerant. The intrinsic efficiency of EC ceramic and polymer materials was first examined in the context of isothermal field cycling, for which Defay *et al.* suggested the dimensionless materials efficiency $\eta = \frac{Q}{W}$ [172], where Q is the isothermal heat generated by maximal field changes and W is the corresponding work. Moya *et al.* later adopted this approach in order to compare materials that show the different types of caloric effect [156] where values of Q were identified from the literature based primarily on the well-known indirect method, and where values of W were calculated from plots of order parameter versus field. The materials efficiency η can equally be interpreted as the COP of an idealized Carnot or Ericsson cycle with zero temperature span [156, 173].

The paper that I co-authored [2] demonstrated a framework by which polarization data dense in temperature and field could be used to calculate the efficiency of idealized EC Brayton cycles with an arbitrary span. The approach differs from previous studies of cycle efficiency in the calorics literature in two key respects.

Firstly, in standard regenerative cycles, the refrigerant absorbs heat while traversing the regenerator at zero-field and expels heat while traversing back at the maximum applied field. As noted in the past [147, 174], heat absorbed from the regenerator need not equal heat expelled to the regenerator, resulting in a net heat transfer between the refrigerant and the regenerator that compromises both cycle efficiency and the parameterization of cycles in terms of well-defined sink and load temperatures. While previous studies either did not address this net-heat transfer issue [175-181] or suggested solutions that would not be useful in practice [182-184], we proposed in [2] that balanced regeneration and hence greater efficiency can be achieved by varying the applied field when the refrigerant dumps heat while traversing the regenerator. Balanced regeneration ensures that net heat transfer occurs only at the extremities of the regenerator (i.e. at the sink and the load) and prevents the possibility of undesirable heat sinks/sources anywhere along the length of the regenerator. Dense

experimental data were key because they permitted the determination of the field-profile that ensures balanced regeneration.

Secondly, by using hysteretic polarization data to calculate per-cycle work W, [2] was able to approximately account for losses intrinsic to the refrigerant and thus provide realistic upper bounds on cycle efficiency.

In what follows, the approach taken in [2] has been adopted to construct balanced Brayton cycles as well as balanced Ericsson cycles and Carnot cycles (which are intrinsically balanced) based on MLCs of PST. The analysis presented in the next section is based on data from Chapter 3, namely the $S'(T, E)$ map (Section 3.3.2) and underlying $P(E)$ data (shown for selected temperatures in Section 3.7.5) out to E = 15.8 V μm^{-1}. The cycles described here are based on a working body that comprises one or more MLCs equivalent to MLC 1 (Section 3.6.1).

4.3 The construction of cooling cycles for MLCs of PST

Permutation of the variables in $S'(T,E)$ (Fig. 3.4c) yields $E(T,S')$, which is shown three times with a superimposed Brayton (Fig. 4.2a), Ericsson (Fig. 4.2d) and Carnot (Fig. 4.2g) cycle (with E_{max} = 15.8 V μm^{-1} as the maximum field).

The Brayton cycle consists of (i) adiabatic field application starting at T_h (1→2), (ii) relaxation back to T_h as heat $Q_h = \int_{S_X}^{S_2} T\mathrm{d}S$ is expelled to the sink (2→X; see right inset of Fig. 4.2a), (iii) cooling down to T_c as the MLC expels heat while traversing the regenerator with the applied field on (X→3), (iv) adiabatic field removal starting at T_c (3→4), (v) relaxation back to T_c as heat $Q_c = \int_{S_4}^{S_Y} T\mathrm{d}S$ is absorbed from the load (4→Y; see left inset of Fig. 4.2a), and (vi) warming up to T_h as the MLC absorbs heat while traversing the regenerator with no field applied (Y→1). The net heat transfer that would result from isofield regenerator legs is avoided by arranging for the field-on regenerator leg (X→3) to be constructed by translating the zero-field regenerator leg (Y→1) down in entropy by ΔS_0, the maximum possible translation while still lying within the accessible parameter space delineated by $E(T,S')$. The irrecoverable work $W_{cyc} = \oint T\mathrm{d}S$ depends only on the geometry of the cycle on (T,S') axes and hence does not reveal losses in the refrigerant.

The field variation during the entire cycle can be determined from the underlying $E(T, S')$ plot by interpolation, yielding the cycle on (T,E) axes (Fig. 4.2b). The field variation in the X→3 regenerator leg need not be monotonic because the electric field E required to maintain fixed ΔS_0 can undergo a minimum at temperatures where peak EC effects occur. My co-authored publication [2] failed to recognize this fact and instead mistakenly attributes non-monotonic field variation in the X→3 regenerator leg to an artefact caused by a “small mismatch in the absolute temperatures underlying electrical and thermal data”.

The polarization in the active MLC volume during the entire cycle can be determined from the field variation in Fig. 4.2b via interpolation to yield the cycle on (E,P) axes (Fig. 4.2c). The polarization branch corresponding to field application (red) is determined by interpolation of the polarization data $P(T,E)$ measured for field application, and the

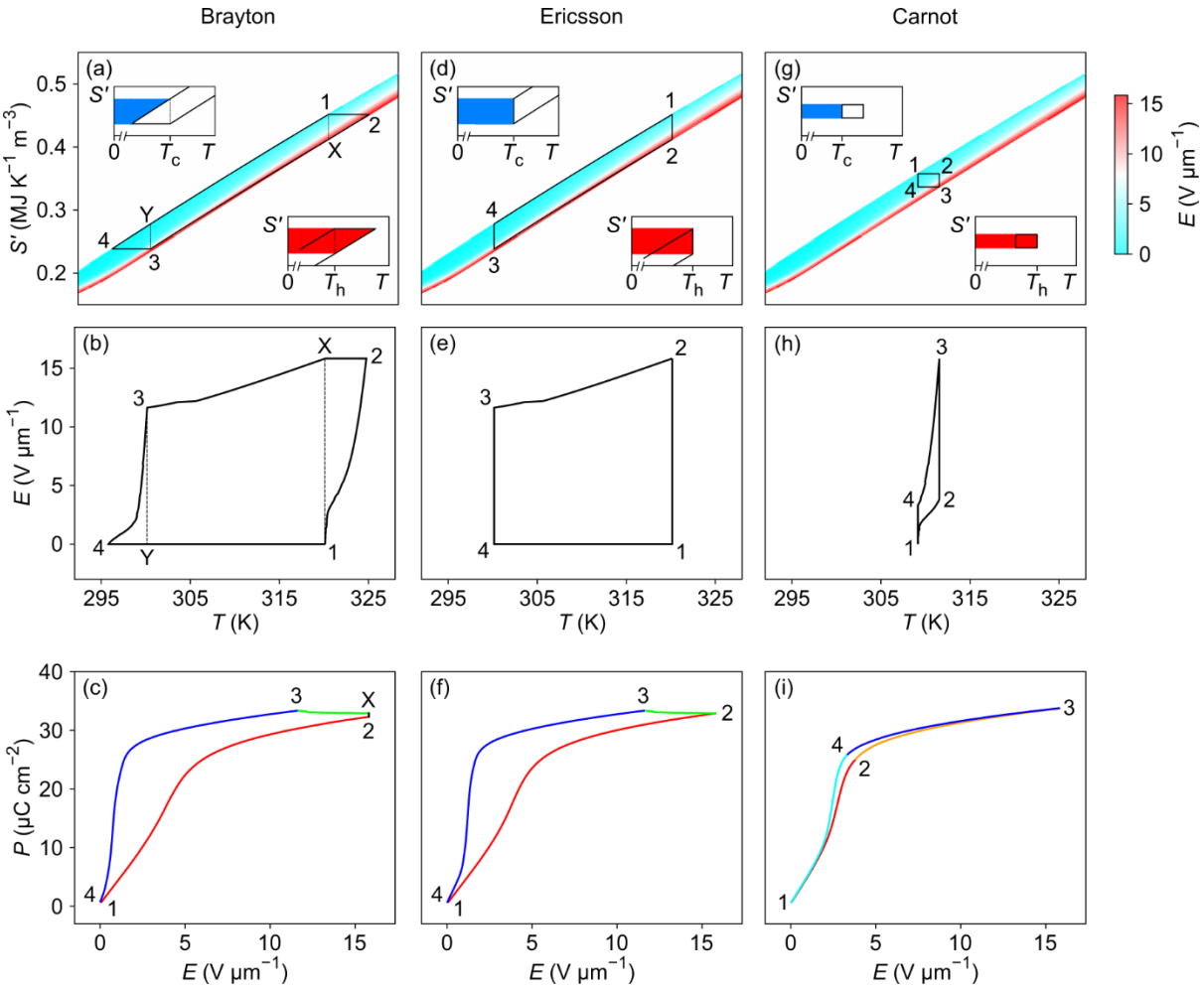

Fig. 4.2 | **Construction of cooling cycles based on an MLC of PST.**

(a-c) An example of a balanced Brayton cycle (T_c = 300 K and T_h - T_c = 20 K) is shown on axes of (a) (T,S'), (b) (T,E) and (c) (E,P). An example of a balanced Ericsson cycle (T_c ~ 300 K and $T_h - T_c$ ~ 20 K) is shown on (T;S'), (T;E), and (E;P) axes in (d)-(f), respectively. An example of a Carnot cycle (T_c ~ 309 K and $T_h - T_c$ ~ 2.4 K) is shown on (T;S'), (T;E), and (E;P) axes in (g)-(i), respectively. Insets in (a), (d), and (g) use shading to represent the heat Q_h expelled to the sink (red) and the heat Q_c absorbed from the load (blue). Balanced regeneration is achieved in the Brayton (Ericsson) cycle by varying the field during X → 3 (during 2 → 3). In (c,f), red data derive from polarization data measured on field application, blue data derive from polarization data measured on field removal, and green data derive from either or both polarization datasets depending on the sign of the applied field change. In (i), red (orange) data represent adiabatic (isothermal) field application and are derived from polarization data measured on field application; blue (cyan) data represent adiabatic (isothermal) field removal and are derived from polarization data measured on field removal. Abscissae in (a,b,d,e,g,h) truncate the temperature range of the polarization data $P(T,E)$, which extends out to 405 K (Section 3.3.2).

polarization branch corresponding to field removal (blue) is determined via interpolation of the polarization data $P(T, E)$ measured for field removal. The X→3 regenerator leg (green) primarily comprises field-removal $P(T, E)$ data for the decrease of field, but for cycles with load temperature $T_c < 298$ K (where ΔS peaks for $E = 15.8$ V μm^{-1}; Section 3.3.2), the small increasing-field fragment was constructed from field-applied $P(T, E)$ data. The very short isofield relaxation leg (2→X) (black) connects the field-application branch (1→2) with the regenerator branch (X→3). As noted in [2], the cycle on (E,P) axes permits the computation of the irrecoverable work $W_{mat} = \oint E đP$ that is done to drive the material, thus accounting in some way for the hysteretic losses that are intrinsic to the MLCs of PST.

A balanced Ericsson cycle is represented on axes of (T,S'), (T,E), and (E,P) (Fig. 4.2d-f). This cycle avoids the points X and Y by changing the 1→2 and 3→4 legs from adiabatic to isothermal (Fig. 4.2d). Heat $Q_h = \int_{S_2}^{S_1} T\mathrm{d}S$ is exchanged with the sink (right inset of Fig. 4.2d) and heat $Q_c = \int_{S_3}^{S_4} T\mathrm{d}S$ is exchanged with the load (left inset of Fig. 4.2d). Note that the regenerator legs are unchanged but relabelled with respect to the Brayton cycle.

A Carnot cycle is represented on axes of (T,S'), (T,E) and (E,P) (Fig. 4.2g-i). Carnot cycles do not employ regeneration and thus the temperature span is relatively modest. The four-step process consists of: (i) adiabatic field application (1→2), (ii) isothermal field application (2→3) and the exchange of heat $Q_h = \int_{S_3}^{S_2} T\mathrm{d}S$ with a sink (right inset of Fig. 4.2g), (iii) adiabatic field removal (3→4), and (iv) isothermal field removal (4→1) and the exchange of heat $Q_c = \int_{S_4}^{S_1} T\mathrm{d}S$ with a load (left inset of Fig. 4.2g). The Carnot cycle span $T_h - T_c$ cannot exceed the maximum adiabatic temperature change of magnitude $|\Delta T|$. The temperature spans of Carnot cycles are therefore described using $\frac{T_h - T_c}{|\Delta T|}$ rather than $T_h - T_c$, which makes the presentation of data simpler in the next section.

4.4 Figures of merit for cooling cycles based on MLCs of PST

The cycles constructed in the previous section can be uniquely parameterized by specifying the load temperature T_c and the temperature span $T_h - T_c$. For each type of cycle, the following figures of merit were computed on axes of (T_c,$T_h - T_c$) as shown in Fig. 4.3: (i) the heat Q_c absorbed from the load, (ii) the irrecoverable work W_{cyc} that assumes the MLC to be anhysteretic and (iii) the resulting efficiency $\frac{\mathrm{COP_{cyc}}}{\mathrm{COP_{Carnot}}} = \frac{Q_c}{W_{cyc}} \Big/ \frac{T_c}{T_h - T_c}$, where $\frac{T_c}{T_h - T_c}$ is the Carnot efficiency, and (iv) the irrecoverable work W_{mat} that accounts for the small hysteresis in the PST and (v) the resulting efficiency $\frac{\mathrm{COP_{mat}}}{\mathrm{COP_{Carnot}}} = \frac{Q_c}{W_{mat}} \Big/ \frac{T_c}{T_h - T_c}$ (non-normalized COPs are presented in Fig. 4.7). Note that T_c exceeds the Curie temperature of T_C = 292 K for all cycles in order to avoid the deleterious effect of field hysteresis associated with the ferroelectric phase.

Balanced Ericsson cycles operate with a cycle efficiency of unity if the material does not display hysteresis [2], as do Carnot cycles, and so two plots of $\frac{\mathrm{COP_{cyc}}}{\mathrm{COP_{Carnot}}}$ are absent from Fig. 4.3. For balanced Brayton cycles (Fig. 4.3a-e), the efficiency increases with increasing $T_h - T_c$ because the triangular areas 12X and 34Y (Fig. 4.2a) represent an ever smaller fraction of the cycle area $\oint T\mathrm{d}S$ on increasing $T_h - T_c$. Therefore, larger values of $T_h - T_c$ lead to a convergence in the performance of balanced Brayton cycles and balanced Ericsson cycles (whether or not the hysteresis of the material is taken into account). The non-regenerative Carnot cycles are relatively small and therefore the irrecoverable work is relatively much larger when the PST is assumed to be hysteretic (Fig. 4.3l) rather than anhysteretic (Fig. 4.3k), resulting in low cycle efficiencies (Fig. 4.3m).

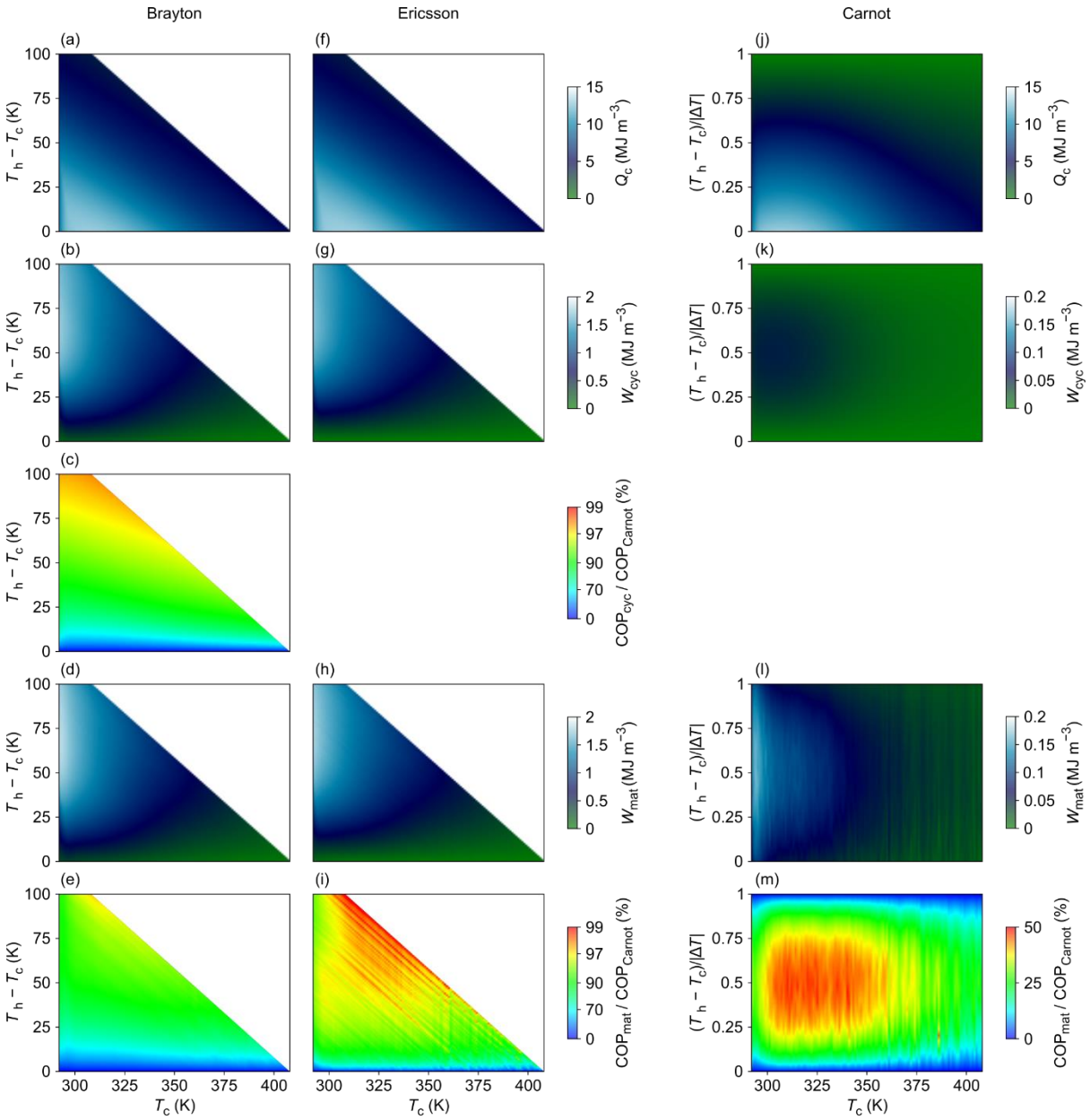

Fig. 4.3 | **Figures of merit for cooling cycles based on MLCs of PST.**

(a-e) For balanced Brayton cycles, axes of load temperature T_c and temperature span $T_h - T_c$ are used to present (a) the heat Q_c pumped from the load, (b) the work $W_{cyc} = \oint T\mathrm{d}S'$ done per cycle assuming the PST to be anhysteretic and (c) the corresponding cycle efficiency COP_{cyc}/COP_{Carnot}, and (d) the work $W_{mat} = \oint E\text{đ}P$ done per cycle that accounts for the small hysteresis in the PST and (e) the corresponding cycle efficiency COP_{mat}/COP_{Carnot}. (f-i) and (j-m) show the corresponding data for balanced Ericsson cycles and Carnot cycles, respectively, where COP_{cyc}/COP_{Carnot} is not shown because it is 100% throughout. The vertical axis for Carnot cycles is presented as $\frac{T_h - T_c}{|\Delta T|}$ rather than $T_h - T_c$ so that colour maps fill the plot area. The colour bar scale for (c,e,i) is logarithmic to highlight efficiency variations near 100%, and it renders unduly visible the noise in (i).

4.5 Refrigerant efficiency for MLCs of PST

The COPs for cooling cycles with a given T_c and T_h are typically parameterized as a fraction of the limiting COP = $\frac{T_c}{T_h - T_c}$ for Carnot cycles in order to yield efficiencies measured in percent. However, some types of cycle intrinsically operate below the Carnot efficiency. For example, Brayton cycles trade cycle efficiency for increased temperature differences that promote faster heat exchange with sinks and loads, thus increasing cooling power. In order to evaluate losses in an EC working body without also considering any losses that are intrinsic to the thermodynamic cycle, refrigerant efficiency $\gamma = \frac{\mathrm{COP_{mat}}}{\mathrm{COP_{cyc}}} = \frac{W_{cyc}}{W_{mat}}$ is introduced here to specify the factor by which the COP for any given cycle is reduced due to losses in the working body. Refrigerant efficiency is thus introduced here to account for the losses in working bodies that undergo Brayton cycles; for balanced Ericsson cycles and Carnot cycles with $\mathrm{COP_{cyc}} = \frac{T_c}{T_h - T_c}$, the cycle efficiency $\frac{\mathrm{COP_{mat}}}{\mathrm{COP_{Carnot}}}$ is trivially equal to the refrigerant efficiency γ.

For balanced Brayton cycles, constant-temperature-span cross-sections through the map of $Q_c(T_c, T_h - T_c)$ (Fig. 4.3a) are presented as $Q_c(T_c)$ (Fig. 4.4a) above the corresponding plots of $\gamma(T_c)$ (Fig. 4.4b) [the corresponding cross-sections of cycle efficiency $\frac{\mathrm{COP_{mat}}}{\mathrm{COP_{Carnot}}}$ are shown in Fig. 4.8]. For balanced Ericsson cycles, constant-temperature-span cross-sections through the map of $Q_c(T_c, T_h - T_c)$ (Fig. 4.3f) are presented as $Q_c(T_c)$ (Fig. 4.4c) above the corresponding plots of $\gamma(T_c)$ (Fig. 4.4d). On increasing the temperature span (by increasing T_h), Q_c is reduced because the two regenerator legs come closer together to fit within the reduced parameter space at large T_h.

In general, smaller cycles are characterized by lower refrigerant efficiencies. Consider a zero-temperature span Ericsson cycle, i.e. with cycle area $W_{cyc} = 0$: field hysteresis associated with the first-order transition yields a finite irrecoverable work W_{mat}, resulting in $\gamma = \frac{W_{cyc}}{W_{mat}} = 0$. For zero-temperature-span Brayton cycles (Fig. 4.4b), the refrigerant efficiency γ exceeds 50% for all values of T_c, but is nevertheless relatively low. For larger cycles, W_{cyc} and W_{mat}

begin to converge as the thermodynamic contribution to the irrecoverable work becomes dominant. Balanced Brayton cycles and balanced Ericsson cycles with finite temperature spans show similar refrigerant efficiencies as expected given that the losses intrinsic to Brayton cycles are factored out, and these refrigerant efficiencies increase to ~97% on increasing the temperature span to $T_h - T_c = 50$ K.

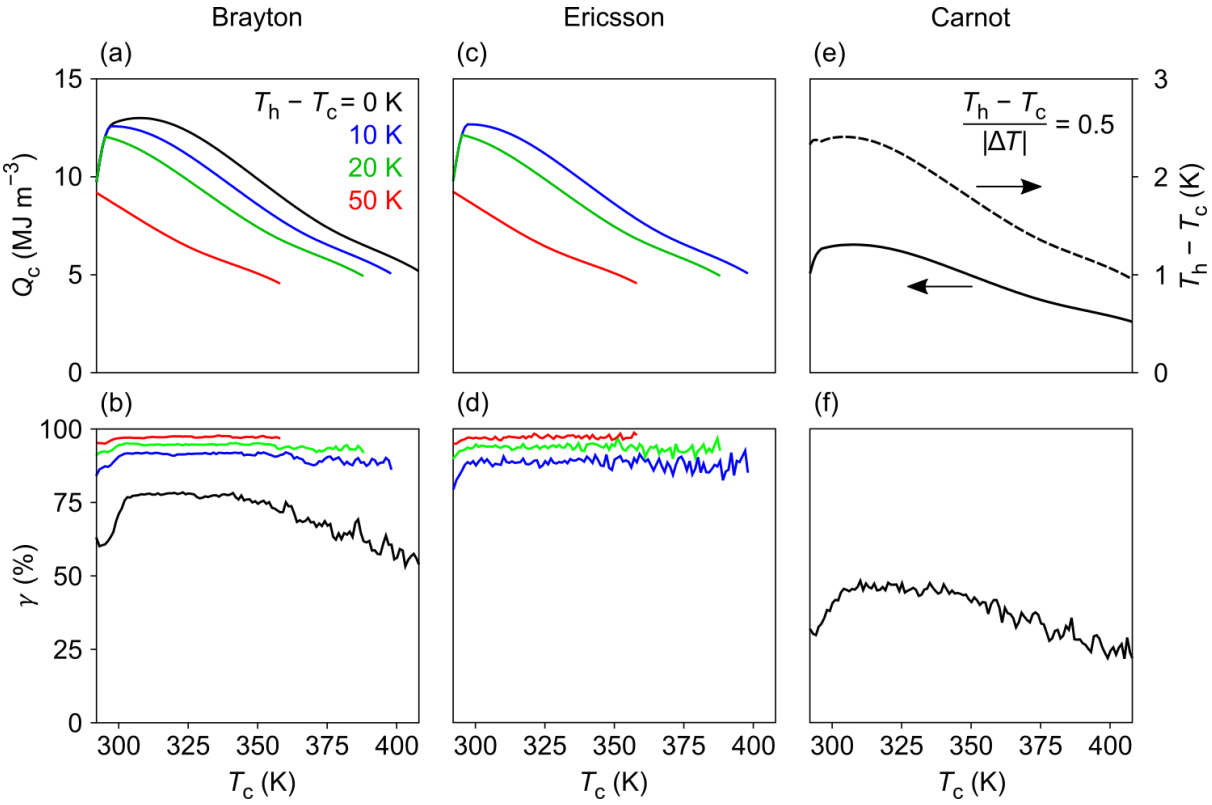

Fig. 4.4 | **Pumped heat and refrigerant efficiency for cycles based on MLCs of PST.**

(a,b) Balanced Brayton cycles are described via (a) cross-sections through $Q_c(T_c, T_h - T_c)$ (Fig. 4.3a) at constant values of $T_h - T_c$ and (b) refrigerant efficiency $\gamma = \frac{\mathrm{COP_{mat}}}{\mathrm{COP_{cyc}}} = \frac{W_{cyc}}{W_{mat}}$ (data from Fig. 4.3b,d). (c,d) Balanced Ericsson cycles are described via (c) cross-sections through $Q_c(T_c, T_h - T_c)$ (Fig. 4.3f) at constant values of $T_h - T_c$ and (d) $\gamma = \frac{\mathrm{COP_{mat}}}{\mathrm{COP_{cyc}}} = \frac{W_{cyc}}{W_{mat}}$ (data from Fig. 4.3g,h). (e,f) Carnot cycles with $\frac{T_h - T_c}{|\Delta T|} = 0.5$ maximize γ and are described via (e) cross-section through $Q_c(T_c, \frac{T_h - T_c}{|\Delta T|})$ (Fig. 4.3j) (solid line), $T_h - T_c$ (dashed line) and (f) $\gamma = \frac{\mathrm{COP_{mat}}}{\mathrm{COP_{cyc}}} = \frac{W_{cyc}}{W_{mat}}$ (data from Fig. 4.3k,l).

For Carnot cycles with a given value of T_c, the value of γ is maximized by maximizing the cycle area (W_{cyc}) in order to minimize the relative contribution of field-hysteresis losses in the working body. This requires the Carnot cycles from Fig. 4.3 with $\frac{T_h - T_c}{\Delta T} \sim 0.5$ (Fig. 4.4e), as derived in Section 4.10.3. The duly maximized refrigerant efficiency $\gamma(T_c)$ (Fig. 4.4f) of these Carnot cycles lies below 50% as their cycle area is only a quarter the cycle area for zero-temperature-span Brayton cycles. Note that Carnot cycles (Fig. 4.4f) and zero-temperature-span Brayton cycles (Fig. 4.4b) both display reduced values of γ at both the lowest values of T_c (due to increased hysteresis associated with the field-driven transition when closer to the Curie temperature) and the highest values of T_c (due to reduced ΔT and ΔS and hence reduced W_{cyc}).

4.6 Refrigerant efficiency without energy recovery

Up to this point in the present chapter, the performance of EC cycles has been evaluated by assuming that the net electrical work done per cooling cycle comprises the work $W_+ = \int_{\mathcal{C}} E đP$ done to charge an MLC ($\frac{đP}{dt} > 0$) in cycle portions now denoted $\mathcal{C}$, less the work $W_- = \int_{\mathcal{D}} E đP$ done by an MLC when it discharges ($\frac{đP}{dt} < 0$) in cycle portions now denoted $\mathcal{D}$. Here, t denotes time, $E \geq 0$, and note that cooling in the regenerator permits P to increase when E is decreased (X→3 in Fig. 4.2c). The net work $W_{\text{mat}} = W_+ - W_-$ done therefore assumes the perfect recovery of electrical work, which would in practice be attempted using circuitry of the type shown in [80].

Here, refrigerant efficiency $\gamma = \frac{W_{\text{cyc}}}{W_{\text{mat}}}$ for the three types of cycles (Fig. 4.4) is recalculated as a raw refrigerant efficiency $\gamma_+ = \frac{W_{\text{cyc}}}{W_+}$ by assuming that the recoverable work of magnitude $|W_-|$ is dissipated and not recovered (Fig. 4.5). Neglecting to recover electrical work suppresses the refrigerant efficiency most substantially in smaller cycles, for which $W_{\text{mat}} << W_- \lesssim W_+$. For example, the refrigerant efficiency for the optimized Carnot cycles is $\gamma_+ \lesssim 6\%$ for all T_c (Fig. 4.5c). Refrigerant efficiency is also suppressed for the Brayton and Ericsson cycles with load temperatures T_c that lie well above the zero-field transition at T_C because the work associated with driving and undriving the transition is large when the transition occurs at high temperature and therefore high field [the $P(T,E)$ phase boundary is shown in Fig. 3.4a].

By the reverse logic, raw refrigerant efficiency peaks for the Brayton and Ericsson cycles with load temperatures T_c that lie slightly above T_C: the work associated with undriving the transition is small in comparison to the work associated with driving the transition because the transition is undriven at low field (Fig. 3.4a). Thus refrigerant efficiencies can approach up to ~87% for the Brayton cycles with $T_h - T_c = 50$ K (red data in Fig. 4.5a), suggesting that applications could be pursued without the complexity required to effect energy recovery, albeit for a limited range of load temperatures. Note that the Brayton cycles show slightly larger values of γ_+ than the corresponding Ericsson cycles (Fig. 4.5) despite showing little difference in γ (Fig. 4.4) because Ericsson cycles benefit slightly more from energy recovery

[W_+ is smaller and W_- is larger for a given Ericsson cycle (Fig. 4.2f) in comparison with a given Brayton cycle (Fig. 4.2c)].

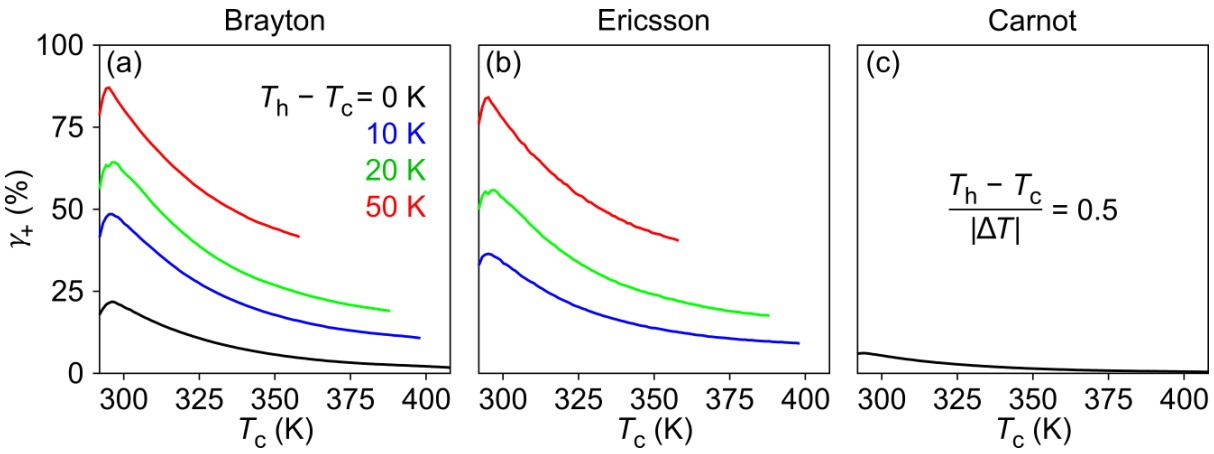

Fig. 4.5 | **Raw refrigerant efficiency for cycles employing MLCs of PST without energy recovery.**

(a-c) Refrigerant efficiency $\gamma = \frac{W_{cyc}}{W_{mat}}$ from Fig. 4.4 (b,d,f) is recalculated as the raw refrigerant efficiency $\gamma_+ = \frac{W_{cyc}}{W_+}$ by replacing the net electrical work $W_{mat} = W_+ - W_-$ done on the MLC in each cycle with the electrical work W_+ that would be done if the recoverable work W_- is not recovered.

4.7 Refrigerant efficiency as a way of comparing refrigerants

For the purpose of comparing caloric refrigerants, refrigerant efficiency $\gamma = \frac{\mathrm{COP_{mat}}}{\mathrm{COP_{cyc}}}$ is preferred to cycle efficiency $\frac{\mathrm{COP_{mat}}}{\mathrm{COP_{Carnot}}}$ for two key reasons.

First, a comparison of refrigerants in terms of cycle efficiency would conflate hysteresis losses in the refrigerant with fundamental losses that can be attributed to the thermodynamic cycle. Refrigerants that support larger values of ΔT will in general possess lower cycle efficiencies even in the absence of hysteresis. The COP for a balanced Brayton cycle assuming no hysteresis is given by the formula $\mathrm{COP_{cyc}} \sim \frac{T_\mathrm{c} - \Delta T/2}{T_\mathrm{h} - T_\mathrm{c} + \Delta T}$ (derived in Section 4.10.4), which approaches the Carnot efficiency as ΔT approaches zero. Reduced (theoretical) cycle efficiency with increasing ΔT reflects the fundamental trade-off that pumping heat faster across larger temperature differences generates increased dissipation, and this trade-off is independent of the refrigerant. A meaningful comparison of refrigerants in terms of cycle efficiency could be made for a fixed cycle geometry, e.g. Brayton cycles employing a given ΔT, but this would mean that some refrigerants are considered at submaximal driving.

Second, for a given choice of cycle (e.g. Brayton, Ericsson, etc), the upper bound on the performance of a prototype is not set by the Carnot COP but rather by $\mathrm{COP_{cyc}}$. In this sense, the cycle efficiency $\mathrm{COP_{cyc}}$ can be understood to be the COP of an idealized prototype operating with an idealized anhysteretic refrigerant such that losses incurred are restricted to the fundamental losses of the thermodynamic cycle itself.

The refrigerant efficiency γ isolates the effect of hysteresis losses on the COP by factoring out the fundamental losses associated with the thermodynamic cycle. Thus, the refrigerant efficiency γ represents a measure of how the performance of a refrigerant for a given cycle compares to the performance of an idealized anhysteretic refrigerant. Caloric refrigerants can therefore be compared using the refrigerant efficiency γ in a manner similar to how the materials efficiency η was used elsewhere [156, 172].

4.8 Comparison with cycles based on monolithic PST

Balanced Brayton cycles for MLCs of PST (E_{max} = 15.8 V μm^{-1}) are compared with balanced Brayton cycles for bulk polycrystalline PST (B-site cation ordering S_{111} ~ 0.80, thickness ~400 μm, E_{max} = 2.6 V μm^{-1}) [2] by plotting both $Q_c(T_c,T_h - T_c)$ (Fig. 4.6a) and the freshly evaluated parameter $\gamma(T_c,T_h - T_c)$ (Fig. 4.6b) for temperature spans of $T_h - T_c$ = 10 K and 20 K in the range 295 K < T_c < 315 K. Fig. 4.6c,d presents the equivalent comparison between the MLCs and a thinner clamped companion sample of PST (S_{111} ~ 0.80, thickness ~95 μm) [2], which operates up to higher temperatures (295 K < T_c < 360 K) than bulk PST because the transition is broader and because the electric field that can be applied is larger (E_{max} = 16.0 V μm^{-1}). Note that MLCs of PST supported applied electric fields as large as E = 29.0 V μm^{-1} (Chapter 3), but in order to avoid breakdown, a safe applied field of E = 15.8 V μm^{-1} was employed when obtaining the dense $P(E)$ data used for the analysis in this chapter.

Significantly larger values of the maximum applied field E_{max} in both the MLCs and the thin clamped PST yield substantial enhancements in the volume-normalized heat $Q_c(T_c,T_h - T_c)$ that can be pumped (Fig. 4.6a,c), thus ratifying the importance of a large breakdown field for applications. The MLCs show larger values of $Q_c(T_c,T_h - T_c)$ compared to the thin clamped PST despite a marginally lower value of the maximum applied field E_{max}: EC effects in the thin clamped PST are probably suppressed by lower ordering, clamping and/or defects introduced by polishing. Remarkably, the MLCs also show the largest refrigerant efficiencies, over a wide range of temperatures. This is because the large electric fields in the MLCs drive supercritical EC effects that exist in a wide range of temperatures and anhysteretically supplement the EC effects associated with the first-order transition. Though the maximum applied field E_{max} = 16.0 V μm^{-1} in the thin clamped PST is probably also supercritical, the refrigerant efficiency is considerably lower in comparison to the MLCs: polarization data for the thin clamped PST indicate significant field hysteresis above T_C, probably due to pinning of phase nuclei caused either by clamping, or by defects introduced during hand polishing.

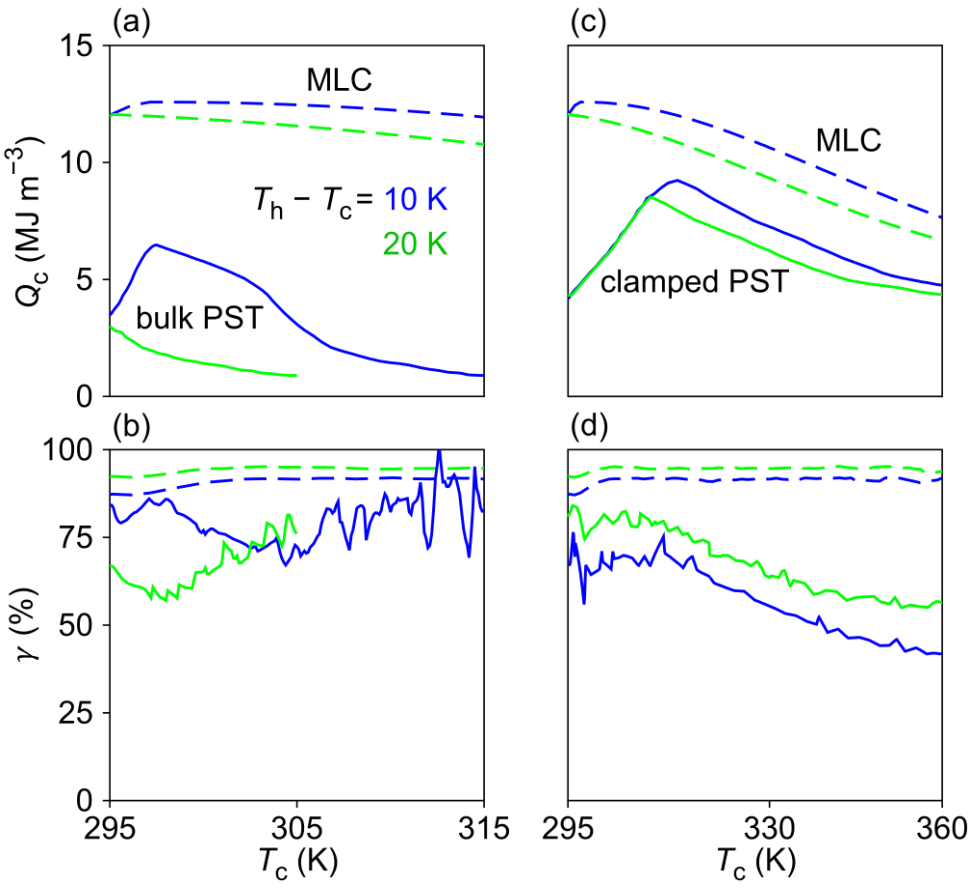

Fig. 4.6 | **Performance comparison for MLCs of PST and monolithic PST.**

MLCs are compared with (a,b) bulk PST and (c,d) thin clamped PST in terms of balanced Brayton cycles by plotting (a,c) the heat pumped $Q_c(T_c,T_h - T_c)$ and (b,d) the refrigerant efficiency $\gamma(T_c,T_h - T_c)$. Data are shown for $T_h - T_c$ = 10 K (blue) and 20 K (green) in (a,b) 295 K < T_c < 315 K and (c,d) 295 K < T_c < 360 K. For the monolithic PST, $Q_c(T_c,T_h - T_c)$ in (a,b) was copied from Fig. 5a,c in [2] and $\gamma(T_c,T_h - T_c)$ in (b,d) was evaluated as $\frac{COP_{mat}}{COP_{cyc}}$ using $\frac{COP_{mat}}{COP_{Carnot}}$ data and $\frac{COP_{cyc}}{COP_{Carnot}}$ data from Fig. 5b,d in [2].

4.9 Conclusions

My co-authored paper describes balanced Brayton cycles based on monolithic samples of polycrystalline PST [2]. In this chapter, the same analysis has been applied to the MLCs of PST studied in Chapter 3 and extended in three ways. First, Ericsson and Carnot cycles have been included. Second, refrigerant efficiency $\gamma = \frac{\mathrm{COP_{mat}}}{\mathrm{COP_{cyc}}} = \frac{W_{\mathrm{cyc}}}{W_{\mathrm{mat}}}$ was introduced to specify the factor by which the coefficient of performance (COP) for any given cycle is reduced due to losses in the working body. The MLCs achieve near theoretical efficiency ($\gamma \sim 97\%$) for the useful temperature span of $T_h - T_c = 50$ K if one assumes that all electrical work is recovered [80] when MLCs discharge during the cycle (this same assumption holds for cycle efficiency $\frac{\mathrm{COP_{mat}}}{\mathrm{COP_{Carnot}}}$ both here and in [2]). Third, refrigerant efficiency is recast without energy recovery as a raw refrigerant efficiency γ_+ that can be as large as ~87%, suggesting that energy recovery may be dispensable for a limited range of load temperatures. The MLCs of PST represent a substantial improvement over monolithic PST [2] in balanced Brayton cycles given the larger heat pumped and greater refrigerant efficiency. The improvement in refrigerant efficiency, like the concomitant improvements in Q_c and $|\Delta T|$ (Chapter 3), can be attributed to supercritical EC effects, which minimize the relative significance of losses associated with the first-order transition. The large breakdown field made accessible here by the MLC geometry may therefore confer an additional advantage of improved efficiency, provided electrical work is duly recovered [80].

4.10 Supplementary Information

4.10.1 Repeat of Fig. 4.3c,e,i,m with COPs instead of cycle efficiency

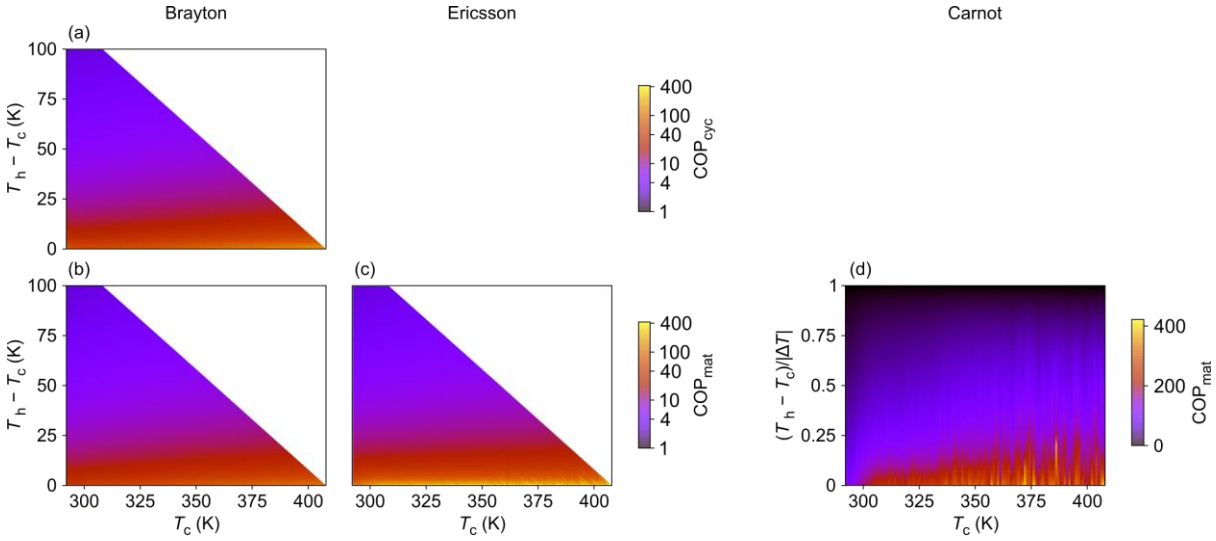

Fig. 4.7 | **COP_{cyc} and COP_{mat} for MLCs of PST.**

(a,b) For balanced Brayton cycles, (a) $COP_{cyc} = Q_c / W_{cyc}$ and (b) $COP_{mat} = Q_c / W_{mat}$ were normalized by the Carnot limit $COP_{Carnot} = \frac{T_c}{T_h - T_c}$ to yield the cycle efficiencies presented in Fig. 4.3c,e respectively. (c,d) COP_{mat} for both (c) balanced Ericsson cycles and (d) Carnot cycles was likewise normalized to yield the cycle efficiencies presented in Fig. 4.3i,m respectively. For balanced Ericsson cycles and Carnot cycles, COP_{cyc} is not presented because $COP_{cyc} = COP_{Carnot}$.

4.10.2 Repeat of Fig. 4.4b with cycle efficiency instead of refrigerant efficiency

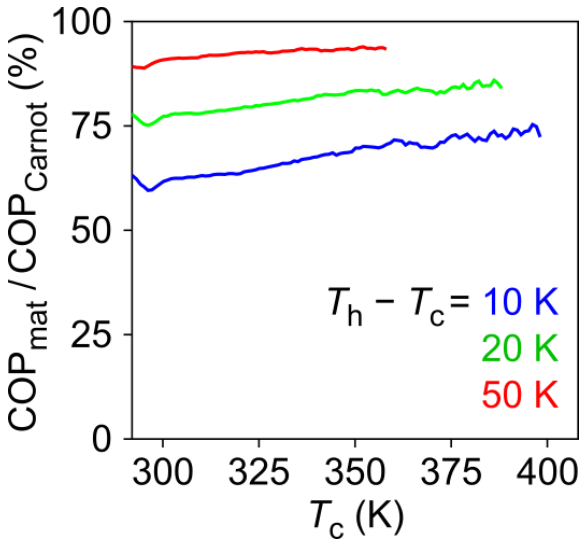

Fig. 4.8 | **Cycle efficiency for balanced Brayton cycles based on MLCs of PST.**

(a,b) Balanced Brayton cycles are described here via cross-sections through the cycle efficiency $\frac{COP_{mat}}{COP_{Carnot}}(T_c, T_h - T_c)$ (Fig. 4.3e) at constant values of $T_h - T_c$. Data for $T_h - T_c = 0$ K are not shown because the cycle efficiency for $T_h - T_c = 0$ K is zero for all load temperatures ($COP_{Carnot} \to \infty$). Data for balanced Ericsson cycles and Carnot cycles are not shown because the cycle efficiency is trivially equivalent to the refrigerant efficiency $\gamma = \frac{COP_{mat}}{COP_{cyc}}$, which is shown in Fig. 4.4d,f respectively.

4.10.3 Maximizing W_{cyc} for Carnot cycles

For a given load temperature T_c, a Carnot cycle must lie within a roughly 'triangular area' whose sides correspond to (i) the adiabatic temperature change $\Delta T(T_c, 0 \to E)$, (ii) the isothermal entropy change $\Delta S(T_c, 0 \to E)$, and (iii) a segment of the isofield $S(T)$ that connects the two (see the 'triangular areas' in the insets of 4.3a). This segment can be taken to be linear because c/T is reasonably constant over the small temperature range spanned by the adiabatic temperature change. Finding the Carnot cycle that maximizes the cycle area W_{cyc} is thus equivalent to finding the largest rectangle that is inscribed by a right triangle. By the calculus of variations, this rectangle must have side-lengths of $|\Delta T|/2$ and $|\Delta S|/2$.

4.10.4 COP_{cyc} for balanced Brayton cycles

The adiabatic temperature changes along the field application leg (1→2) and the field removal leg (3→4) of a balanced Brayton cycle are given by the approximate expressions $|\Delta T(1\rightarrow2)| \sim \frac{T_h \Delta S_0}{c(T_h,E)}$ and $|\Delta T(3\rightarrow4)| \sim \frac{T_c \Delta S_0}{c(T_c,0)}$, respectively. The Dulong-Petit law implies that the factors of c/T can be considered roughly equal if they describe single-phase states, which is the case for $T_c > T_C$ and sufficiently large E. Under this assumption, the simplification $|\Delta T(1\rightarrow2)| \sim |\Delta T(3\rightarrow4)| \sim |\Delta T|$ can be made.

The heat $Q_c = \int_{S_4}^{S_Y} T\mathrm{d}S$ pumped from the load is then given by:

$$Q_c \sim T_c \Delta S_0 - |\Delta T| \Delta S_0/2 \tag{4.1}$$

The first term corresponds to the heat pumped from the load for a balanced Ericsson cycle employing the same regenerator legs (left inset of Fig. 4.2d). The second term corresponds to the 'triangular area' (left inset of Fig. 4.2a) that reduces the heat pumped from the load in a Brayton cycle due to the dissipation associated with pumping heat across finite temperature differences [the zero-field relaxation leg (4→Y) is assumed to be approximately linear by the logic outlined in Section 4.10.3]. The cycle area $W_{cyc} = \oint T\mathrm{d}S$ is given by:

$$W_{cyc} \sim (T_h - T_c)\Delta S_0 + |\Delta T| \Delta S_0 \tag{4.2}$$

The first term corresponds to the work dissipated in the regenerator and corresponds to the cycle area for a balanced Ericsson cycle, which looks identical to the expression for the cycle area for a Carnot cycle because of the parallel regenerator legs ensured by balanced regeneration. The second term corresponds to the two 'triangular areas' (left and right insets of Fig. 4.2a) corresponding to the additional work required to pump heat across finite temperature differences [both isofield relaxation legs (2→X and 4→Y) are assumed to be approximately linear]. The resultant COP_{cyc} is given by:

$$COP_{cyc} \sim \frac{T_c \Delta S_0 - |\Delta T| \Delta S_0/2}{(T_h - T_c)\Delta S_0 + |\Delta T| \Delta S_0} = \frac{T_c - |\Delta T|/2}{T_h - T_c + |\Delta T|} \tag{4.3}$$

“അടിച്ചവഴിയെ പോയില്ലെങ്കിൽ പോയവഴിയെ അടിക്കണം.”

“If [it] didn’t go the way you hit [it], hit [it] the way [it] went.”

Chapter 5

A Peltier-electrocaloric-Peltier cooling device based on multilayer capacitors of $PbSc_{0.5}Ta_{0.5}O_3$

Refrigerant-based cooling currently exploits a flowing refrigerant [171] but it could also exploit a caloric refrigerant that makes relative motion with respect to a heat-transfer fluid [147, 148]. However, neither method is amenable to the miniaturization required for novel applications such as portable cooling of medicine. The suggestion that Peltier coolers can control the flow of heat in caloric prototypes and thus avoid all macroscopic motion [186-188] is tested here using two Peltiers that sandwich an electrocaloric (EC) multilayer capacitor (MLC) of $PbSc_{0.5}Ta_{0.5}O_3$ (PST) (Chapter 3). However, a Peltier element that pumps heat does not constitute a heat switch with variable thermal conductance and so it cannot rectify cyclically generated caloric heat, just as a DC voltage source cannot rectify a series AC voltage source. Experimentally, the measured cooling power was therefore found to be insensitive to whether or not EC effects in the MLC were actually driven. Here it is shown that EC cycling can instead improve the performance of Peltiers that are alternately current-sourced and voltage-sourced. The EC effect reduces the temperature span of each Peltier in the current-sourced half of the operating cycle and so less power is consumed; this gain is not cancelled in the other half cycle by the switch to voltage sourcing. Device architecture was not optimized and so it is not possible to identify meaningful improvements in efficiency. However, the toggled-source method may in future permit EC working bodies to yield demonstrable improvements in Peltier efficiency.

This chapter details the characterization of a Peltier-EC-Peltier cooling device that is based on an MLC of PST (Chapter 3). Section 5.1 discusses solid-state cooling and the habitual misuse of this term to describe solid caloric materials in prototypes with macroscopic motion. Section 5.2 debunks previous proposals in which Peltier elements assist caloric materials in the quest for solid-state cooling with no macroscopic motion. Section 5.3 describes a novel way of using EC working bodies to increase Peltier efficiency, such that Peltier-assisted EC cooling is replaced by EC-assisted Peltier cooling. This is followed by a description of the construction (Section 5.4), characterization (Section 5.5) and performance (Section 5.6) of the Peltier-EC-Peltier device. Section 5.7 summarizes the study, Section 5.8 details the methods, and Section 5.9 provides supplementary information cited earlier in the chapter.

5.1 The search for true solid-state cooling

Caloric prototypes are often referred to as ‘solid-state’, but this term typically only describes the caloric working body itself, and in practice there is macroscopic motion. Macroscopic motion is necessarily required to drive mechanocaloric effects, while magnetocaloric (MC) effects in prototypes are normally driven by relative motion with respect to a permanent magnet, as current-driven solenoids would be prohibitively inefficient [12, 156]. However, EC effects are driven by a voltage rather than mechanical motion given that viable EC fluids are in their infancy [85, 156]. Nevertheless, all thirteen EC prototype coolers reported in the literature exploit motion to pump heat [45-47, 72-81], while six of these employ displaceable fluids to achieve large temperature spans between loads and sinks via regeneration [45-47, 74, 76, 77]. This reliance on motion and fluids precludes the development of a truly solid-state cooling technology for novel applications, especially those involving miniaturization.

Alternative EC prototype designs have been based on heat switches [189] and thermal diodes [190], which are analogous to electrical switches and electrical diodes. Heat switches have been exploited in one prototype to date [75], but the thermal conductance was switched by macroscopic mechanical motion. Diode heat pipes [190] that exploit a liquid-vapour phase transition and gravity can achieve a high conductance contrast between forward and reverse bias [191], but it is difficult to make them small enough to be compatible with EC working bodies, and the reliance on gravity could preclude some mobile applications. Moreover, all-solid-state cooling represents an attractive challenge that plays to the strength of the EC effect. Unfortunately, extant solid-state heat switches and thermal diodes display conductance contrasts on the order of unity [191], implying poor prototype performance.

5.2 Previous work on Peltier-assisted caloric cooling

Peltier coolers are often deployed as solid-state cooling devices, and have been suggested as an alternative to heat switches and thermal diodes in caloric prototypes [185]. Thermal conductance switching can be achieved in Peltiers by toggling between open-circuit and closed-circuit conditions [192], but the resulting on/off ratios are only around as large as the thermoelectric figure of merit *ZT*, such that this rather passive form of operation would yield very low cooling powers.

Most proposals have therefore focused on using Peltier elements to actively pump heat in Brayton cycles that are thus Peltier-assisted [186-188]: one Peltier element pumps heat towards a sink after it has been rejected by a caloric working body following field application, while a similar process on the other side of the caloric working body causes heat to be pumped from the load to this working body after it has been cooled following field removal. However, it is shown here (Section 5.9.1) that the cooling power of such Peltier-assisted Brayton cycles is not affected by whether or not the EC effect is actually driven, thus confirming calculations in which MC gadolinium was taken to represent the caloric working body [193]. Pumping heat fails to generate the conductance contrasts required to rectify caloric heat, which is akin to the failure of a DC voltage source to rectify a series AC voltage source. The electrical analogy applies here because the heat equation is linear in source terms that are themselves highly linear in temperature, said source terms representing the thermoelectric effect, the EC effect, and Joule heating from either (Section 5.9.2).

5.3 An alternative operating protocol

It is proposed here that the operating protocol for Peltier-assisted Brayton cycles in Peltier-EC-Peltier devices can be modified in order to use the EC element to improve the efficiency of the Peltiers. Specifically, the Peltiers operate as quasi-steady-state heat pumps that are toggled between current-sourced and voltage-sourced while synchronously driving cyclical EC effects (Fig. 5.1). By thus changing the electrical boundary conditions on the Peltiers in each half cycle while using the EC effect to change their thermal boundary conditions, it is possible to reduce the power consumed by the Peltiers. This strategy of perpetually driving the Peltiers represents an active version of the more passive strategy in which Peltiers are toggled between open and short circuit [192]. Toggling between open and short circuit switches the thermal conductance according to the thermoelectric figure of merit *ZT*, whereas toggling between current-sourced and voltage-sourced leads to efficiency improvements that depend on the Seebeck coefficient of the Peltier modules and the magnitude of the EC effect (Sections 5.9.3 and 5.9.4). This suggests that the EC effect can usefully be exploited to harness thermoelectric materials even if *ZT* is low, provided that the Seebeck coefficient is large.

In the proposed operating protocol, the EC temperature change in each half cycle is responsible for a change in the voltage across both Peltiers due to the Seebeck effect. In the half cycle when the EC effect reduces the temperature span across a given Peltier, which is the case for the sink-side (load-side) Peltier when driving (undriving) the EC effect (inner two Peltiers in Fig. 5.1), this voltage change has the opposite polarity to the electrical current that flows through the relevant Peltier. Current sourcing the relevant Peltier in this half of the cycle therefore reduces the voltage required to drive the constant current, thus reducing the power consumed by the relevant Peltier without affecting the heat pumped by this constant current.

In the half cycle when the EC effect increases the temperature span across a given Peltier, which is the case for the sink-side (load-side) Peltier when undriving (driving) the EC effect (outer two Peltiers in Fig. 5.1), the resulting change of voltage has the same polarity as the electrical current that flows through the relevant Peltier. Continuing to current-source the

relevant Peltier in this half of the cycle would draw more power and cancel the gain from the other half cycle, whereas a switch to voltage-sourcing forces the EC-induced voltage change to reduce the Peltier current. Voltage-sourcing the relevant Peltier in this half of the cycle therefore leads to a reduction in current, such that the relevant Peltier consumes less power while proportionately pumping less heat. The Peltier that is voltage-sourced therefore enjoys no substantial change of efficiency, but the efficiency gain in its current-sourced counterpart leads to a net increase of efficiency for each half cycle in which the Peltier-EC-Peltier device operates.

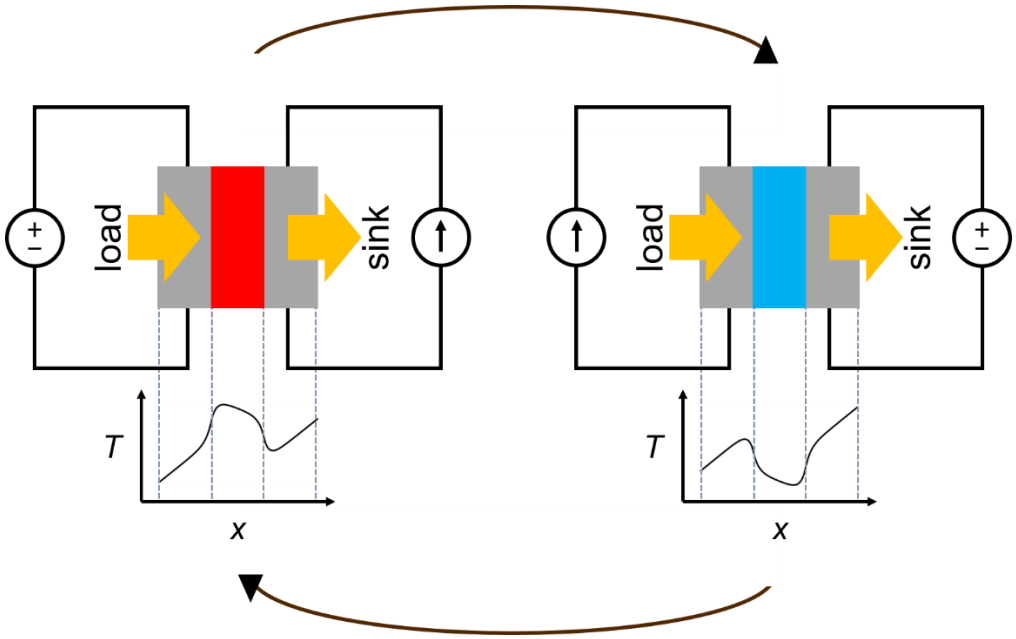

Fig. 5.1 | **EC cycling synchronized with Peltier source-toggling.**

The two-step cycle is performed using an EC working body (red or blue) that is sandwiched between two Peltier elements (grey) that separate it from a load on the left and a sink on the right. Orange arrows represent heat flow. When an applied electric field increases the temperature of the EC working body (red), the load-side Peltier is voltage-sourced, and the sink-side Peltier is current-sourced. When removing the electric field decreases the temperature of the EC working body (blue), the load-side Peltier is current-sourced and the sink-side Peltier is voltage-sourced. Schematic temperature transects $T(x)$ for each half cycle show that current is sourced to the Peltier whose temperature span has been reduced by the EC effect, and that voltage is sourced to the Peltier whose temperature span has been increased by the EC effect.

5.4 Peltier-EC-Peltier device construction

To construct the Peltier-EC-Peltier device (Fig. 5.2), two 3 mm-thick Peltier coolers (Adaptive, ET-011-05-15-RS) sandwiched an 0.84 mm-thick MLC of PST that is equivalent to the MLCs described in Chapter 3, except the B-site cation order was slightly lower (S_{111} ~ 0.7-0.8) such that its performance was slightly suppressed (Section 3.7.13). The two large MLC faces were insulated using Kapton tape (70 μm thick), and silver paint (50 μm thick) was used to achieve good thermal contact between these insulated faces and the faces of the Peltier coolers. To maximize the electrocalorically induced temperature change in the Peltiers, their juxtaposed faces (6 mm × 4 mm) were centred with respect to the slightly larger active area of the MLC (8.8 mm × 5.6 mm).

The Peltier-EC-Peltier device was placed between a copper heat sink block and a Pt-100 thermistor load (Fig. 5.2a), using zirconia-based thermal paste to make good thermal contact. The sink temperature (T_h ~ 335 K) was measured via a K-type thermocouple that was fed through the copper block to meet the Peltier-EC-Peltier device. The current sourced to the Pt-100 determined the power that it dissipated and hence the cooling power P_c of the Peltier-EC-Peltier device, while simultaneous four-point resistance measurements determined the Pt-100 temperature and hence the load temperature T_c. The temperature lift ΔT_{lift} was evaluated with respect to the baseline values of T_h and T_c when the device was not in operation (i.e. before start-up and after switch-off), such that $\Delta T_{lift} = \Delta T_h - \Delta T_c = \Delta(T_h - T_c)$.

Electrical contacts to the MLC, the Peltiers, and the Pt-100 were made via 40 μm-thick copper enamelled wires that were attached using silver paint. Thin wires were used in order to minimize heat leaks to the environment, and silver paint was preferred to solder in order to avoid thermal damage. Further details of temperature stabilization, electrical contacts, electrical sourcing, and measurements are provided in Section 5.8.

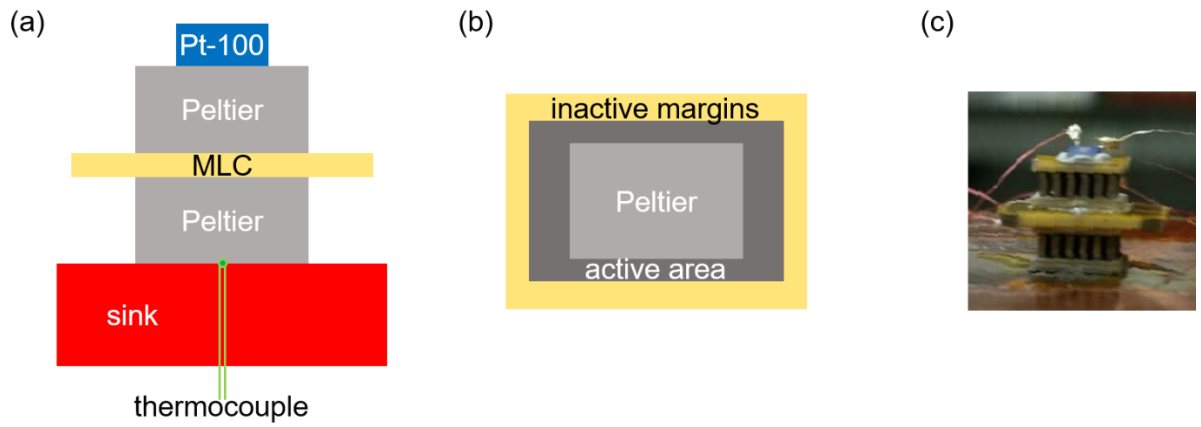

Fig. 5.2 | **Schematic of the Peltier-EC-Peltier device.**

(a) Lateral view of the device, sink not to scale. The heat sink is the copper block whose embedded thermocouple is used to measure sink temperature T_h. The load is the Pt-100 thermistor, whose resistance gives load temperature T_c, and whose power dissipation represents the cooling power P_c of the entire device. (b) Planar view of the device. (a,b) Each Peltier is centred with respect to the MLC active area such that it lies away from the inactive MLC margins shown in (b). (c) Photograph of the device (lateral view).

5.5 Results for the Peltier-EC-Peltier device

Various current and voltage drive levels were determined for steady-state Peltier operation (Section 5.9.5) in order to ensure that the heat transferred to the MLC from the voltage-driven (current-driven) load-side Peltier would be equal to the heat transferred from the MLC to the current-driven (voltage-driven) sink-side Peltier in one (the other) half cycle. While operating each Peltier at a given drive level, the MLC was driven in a four-step Brayton cycle using an electric field of 15.8 V μm^{-1} (600 V), which for a thermally isolated MLC would drive a temperature change of $|\Delta T_j| \sim 3.4$ K (Fig. 3.16) in all parts of the active area contacting the Peltiers. In contrast with Peltier-assisted Brayton cycles, heat exchange between the MLC and each Peltier proceeded by passive thermalization alone, such that the thermoelectric response to the EC effect was independent of drive level and slow to relax (Fig. 5.3a-d).

For the intended cycles with source-toggled Peltiers and synchronized EC cycling, the data in Fig. 5.3a-d were used to model the power consumption, which was found to be minimized when operating with a period of 12 s (Section 5.9.6). When operating the intended cycles on this 12 s period, the measured temperature lift ΔT_{lift} for each Peltier drive level was found to vary linearly with respect to the cooling power P_c that was set by driving the Pt-100, both with the EC effect operative as intended (hollow circles, Fig. 5.3e) and without the EC effect operative for comparison (filled circles, Fig. 5.3e). The gradient of the linear variation implies a normalized device conductance of ~150 W m^{-2} K^{-1}. For $P_c = 0$, switching on the EC cycling reduced the temperature lift by just ~50 mK due to the judicious reduction in current during the voltage-sourced half-cycle in each Peltier, and Eq. (5.31) in Section 5.9.3 predicts this reduction in temperature lift to be independent of drive level, as observed to within the noise of the data (Fig. 5.3e and inset). The corresponding EC-induced change ΔP_{source} in the power drawn from the source (Fig. 5.3f-j) agrees well with the model (Section 5.9.6), and the time-averaged value of the reduction in power consumption varies in an approximately linear fashion with Peltier drive level (dashed black lines, Fig. 5.3f-j). Note that the power P_{source} drawn from the source exceeds the power P_{work} consumed by the Peltiers due to additional series resistance between the source and the Peltiers, as discussed in the next section.

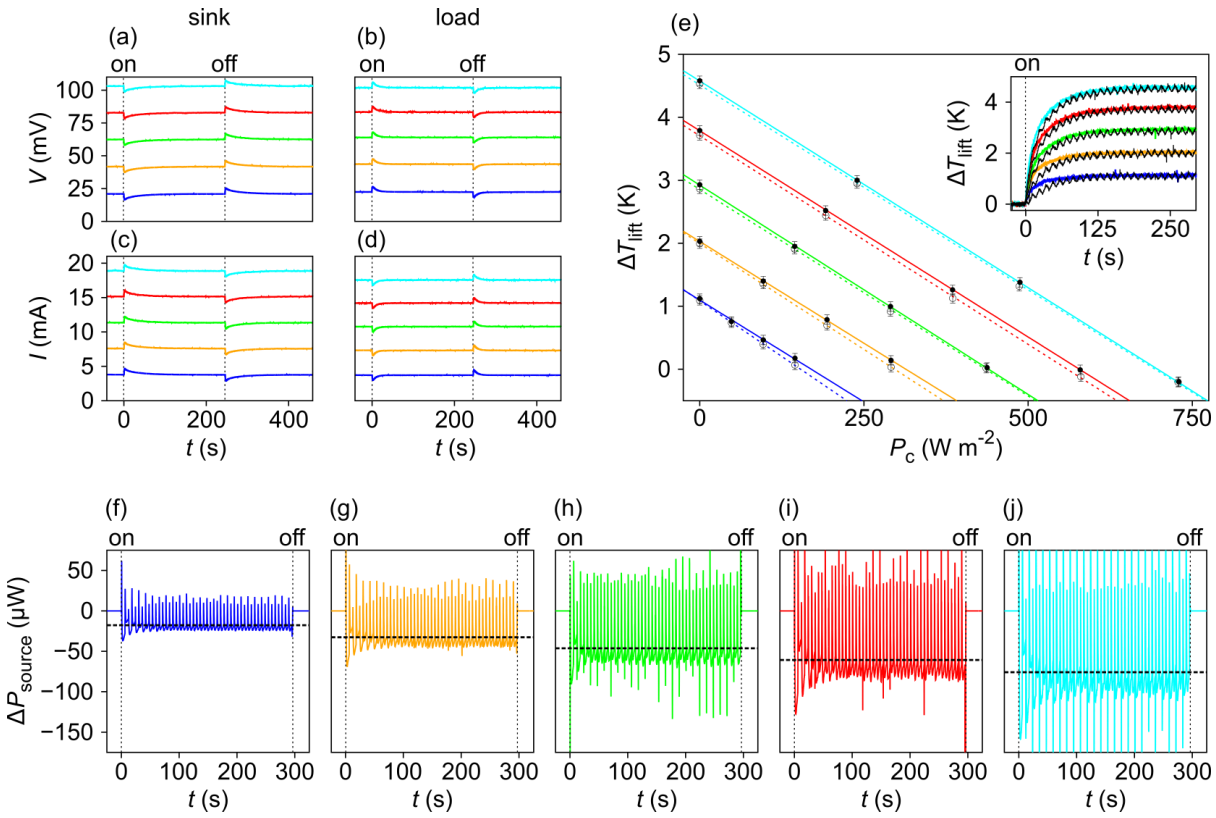

Fig. 5.3 | **Results for the Peltier-EC-Peltier device.**

(a-d) Preliminary measurements prior to intended cycles. While driving the MLC on and off in a Brayton cycle, the (a,b) measured voltage $V(t)$ when current-sourcing the Peltiers at the (a) sink and (b) load, and the (c,d) measured current $I(t)$ when voltage-sourcing the Peltier at the (c) sink and (d) load, are plotted for selected drive levels (coloured) that each yield a given steady-state of Peltier operation. (Note that the voltage across the Peltiers is less than the measured voltage due to series resistance discussed in Section 5.6) (e-j) Device operation with 12 s cycles that minimize power consumption. (e) The measured steady-state temperature lift ΔT_{lift} versus the cooling power P_c that was set by driving the Pt-100 thermistor is plotted when operating at each of the Peltier drive levels, without EC cycling as a reference for comparison (filled circles, solid lines of best fit) and with EC cycling as intended (hollow circles, dashed lines of best fit). Inset: after start-up, the evolution of ΔT_{lift} for $P_c = 0$ at each drive level is similar both without (coloured data) and with (black data) the EC effect operational. (f-j) The power drawn from the source differs with and without EC cycling by an amount ΔP_{source} whose time evolution is shown for each drive level at $P_c = 0$. The time-averaged values of the EC-induced reduction in power consumption are indicated by (horizontal) dashed black lines.

5.6 Performance evaluation

In order to meaningfully evaluate the performance of the Peltier-EC-Peltier device, it was retrospectively found necessary to correct for the series electrical resistance R_s that was identified by comparing two-terminal electrical measurements of each Peltier with subsequent four-terminal electrical measurements. This series resistance is likely to have arisen primarily due to the resistance of the 40 μm-thick copper wires (which were employed in order to minimize heat leaks to the environment) and the contact resistance associated with the silver paint (which was preferred to solder in order to avoid thermal damage). The values of $R_s \sim 4.0\ \Omega$ (sink-side Peltier) and $R_s \sim 4.7\ \Omega$ (load-side Peltier) were found to be large compared to the electrical resistance $R \sim 1.8\ \Omega$ of each Peltier itself, with two consequences. First, the power P_{source} drawn from the source is much larger than the power P_{work} consumed by the Peltiers. Second, the series resistance suppresses the reduction in Peltier current that is achieved when switching to voltage-sourced operation during each half of the cycle, thus suppressing the concomitant reduction in both power consumption and heat pumped.

Corrections for the ideal limit of $R_s = 0$ are derived in Section 5.9.7, and the resultant evaluation is presented in Table 5.1. For $P_c = 0$ and all Peltier drive levels, the percentage reduction in power consumption is roughly double the corresponding percentage reduction in temperature lift, as predicted in Section 5.9.3. The percentage reduction in power consumption was found to be similar for all values along a given load line in Fig. 5.3e, and given that these load lines may be used to convert the percentage reduction in temperature lift at zero cooling power into an equivalent percentage reduction in the cooling power at zero temperature lift, one may calculate the percentage improvement in the COP at zero temperature lift for the two Peltiers (Table 5.1). This percentage improvement in the COP at zero temperature lift was found to be as large as ~24% at the lowest Peltier drive level.

Table 5.1 | **Peltier-EC-Peltier device performance with series-resistance correction.**

For each of the selected Peltier drive levels in Fig. 5.3, the table shows the measured temperature lift ΔT_{lift} at zero cooling power ($P_c = 0$), and the cooling power P_c at zero temperature lift ($\Delta T_{lift} = 0$) that was identified using the Pt-100. On reducing to zero the series electrical resistance R_s (constituted primarily by the 40 μm-thick copper wires and the silver paint contacts), the table shows percentage reductions for the measured temperature lift ΔT_{lift} at zero cooling power ($P_c = 0$), percentage reductions for the Peltier power consumption P_{work} at zero cooling power ($P_c = 0$), and percentage improvements in the coefficient of performance (COP) for the two Peltiers at zero temperature lift ($\Delta T_{lift} = 0$). The corrections for series resistance are derived in Section 5.9.7.

		Measured performance		**Corrected performance**		
Peltier drive level		**ΔT_{lift} at $P_c = 0$ (K)**	**P_c at $\Delta T_{lift} = 0$ (W m^{-2})**	**Reduction in ΔT_{lift} at $P_c = 0$ (%)**	**Reduction in P_{work} at $P_c = 0$ (%)**	**Improvement in two-Peltier COP at $\Delta T_{lift} = 0$ (%)**
sink	**load**					
***I* (mA)**	***I* (mA)**					
3.9	**3.8**	1.1	170	16	32	24
7.7	**7.4**	2.0	310	8	16	9
11.6	**10.9**	2.9	440	6	11	6
15.4	**14.3**	3.8	580	5	8	4
19.2	**17.5**	4.6	700	4	7	3

5.7 Conclusions

A Peltier-EC-Peltier device was reported using an MLC of PST to constitute the EC working body. Previous proposals in which the Peltiers play a supporting role cannot—and did not—lead to the requisite rectification of EC heat. Instead, the Peltiers were promoted to a lead role and their power consumption was reduced due to electrocalorically induced cyclical changes of Peltier temperature span, which are exploited by antiphase current and voltage sourcing. The Peltiers dropped less voltage when current sourced and drew less current when voltage sourced, such that each consumed less power in both halves of the cycle and pumped less heat when voltage sourced, resulting in a net gain in efficiency. The reduction in power consumption therefore outweighed by roughly a factor of two the accompanying reduction in temperature lift (and the concomitant reduction in cooling power at the other end of a given load line, Fig. 5.3e). Series resistances suppressed the expected performance by inflating the total power consumption and suppressing the reduction of current in the voltage-sourced Peltier, and thus it would be attractive in future to reduce the series resistance that has suppressed efficiency here. It would also be attractive to geometrically optimize the MLC in order to reduce the work required to drive the EC cycle (Section 5.9.8), which has not been considered in the calculations presented here. Furthermore, adding an inductor [194] in series with the Peltiers could resist the reduction in current when switching to the voltage-sourced half of the cycle, permitting steady-state Peltier operation by ensuring the same current in both halves of the cycle. Overall, EC effects are attractive in the context presented here because they permit Peltier efficiency to be somewhat decoupled from the thermoelectric figure of merit *ZT*, which has long represented a bottleneck for the development and application of new thermoelectric materials.

5.8 Methods

5.8.1 Temperature stabilization of the Peltier-EC-Peltier device

In order to avoid hysteresis losses in the MLC, the device was characterized well above the critical temperature (T_h ~ 335 K > T_{cp} ~ 330 K; Section 3.3.2) by placing the device/copper-block assembly on a hot plate. A beaker was placed over the device without touching it, followed by a larger cardboard box covering the whole device/copper-block assembly to limit heat leaks via convection.

5.8.2 Electrical contacts to the Peltier-EC-Peltier device

Two separate strategies were employed in order to minimize heat leaks from the Peltier-EC-Peltier device to the environment. First, the electrical leads of the Peltiers and the Pt-100, which inadvertently represent good thermal conductors, were cut to within ~6 mm and ~3 mm of their respective modules. Second, electrical contacts to the Peltiers, the MLC, and the Pt-100 were made via thin wires (40 μm-thick copper enamelled wires of length ~15 cm) that were attached using silver paint to avoid thermal damage caused by solder. Insulation was removed from the ends of each wire by first stripping the thin layer of insulation using a razor blade and then tinning the ends using solder. Wires coming from the Peltier-EC-Peltier device were attached on the opposite end via solder to various sockets that were mounted on a bespoke panel. Standard electrical wires connected the sources to the sockets on the panel, e.g. a banana plug to a banana socket. All the wiring and contacts between the Peltiers and the source constituted a significant series resistance (R_s ~ 4.0 Ω for the sink-side Peltier and R_s ~ 4.7 Ω for the load-side Peltier) that was large in comparison to the Peltier resistance (R ~ 1.8 Ω). The biggest contributions to this series resistance are likely to have been the 40 μm-thick copper wires and the silver paint contacts.

5.8.3 Sourcing and measuring the Peltier-EC-Peltier device

A Keithley 2410 SourceMeter operating with a compliance current of 10 mA was used to drive electrical cycles in the MLC between applied voltages of 0 V and 600 V. Each Peltier

was sourced by its respective Keithley 2440 SourceMeter that toggled between current sourcing and voltage sourcing while measuring both current and voltage. Four-point resistance measurements of the Pt-100 were made using a Keithley 2400 SourceMeter in the 'Manual Ohms' mode, which permitted the current used in the measurements to be varied and thus allowed control of the power dissipated in the Pt-100 load. Each resistance measurement point involved sourcing current for ~86 ms, followed by a gap of ~103 ms to yield a duty cycle of $D \sim 46\%$. The average dissipated power was then calculated using the expression $P_c = DI^2R$. The temperature of the K-type thermocouple embedded in the sink-side copper block was measured using a Keithley 2110 Digital Multimeter (DMM). Operation of the device and concurrent measurements were all coordinated using a bespoke Python script. The 'threading' module in Python enabled source-toggling, EC cycling, and concurrent measurements to be implemented in parallel.

5.8.4 Measurements of Peltier-assisted Brayton cycles

For the test of Peltier-assisted Brayton cycles presented in Section 5.9.1, the voltage across each heat-flux sensor was monitored using a Keithley 2110 DMM. Calibration of each heat-flux sensor was performed against the power dissipated in a Pt-100 thermistor that was attached to the sensor via zirconia-based thermal paste. The temperature of each K-type thermocouple (i.e. one embedded in each copper block) was measured using a Keithley 2110 DMM.

5.8.5 Polarization measurements

Polarization data for the MLC of PST in the Peltier-EC-Peltier device (Section 5.9.8.) were obtained using a Radiant Precision Premier II ferroelectric tester with a Trek 609E-6 High-Voltage Power Amplifier. Measurements were made at $T_h \sim 335$ K with the Peltiers switched off, while implementing two voltage drive forms: (i) a single cycle of a square wave oscillating between 0 V and 600 V with a 12 s period, which corresponds to the EC cycling implemented with Peltier source-toggling, and (ii) a 100 ms monopolar triangular pulse of amplitude 600 V, which is taken to be sufficiently fast to represent the limit in which the active volume of the MLC exchanges minimal EC heat with its surroundings.

5.9 Supplementary Information

5.9.1 Peltier-assisted Brayton cycles

Peltier-assisted Brayton cycles were tested with the Peltier-EC-Peltier device in a modified configuration schematized in Fig. 5.4. The device made contact with copper blocks on either side via heat-flux sensors (greenTEG, gSkin XM 26 9C) used to measure the instantaneous rates of heat flow $\dot{Q}_c$ at the cold end and $\dot{Q}_h$ at the hot end. Replacing the load (Pt-100) at the cold end of the device with a thermal reservoir (i.e. the copper block) acting as a heat source permitted accurate measurements of the heat flow at the cold end. Zirconia-based thermal paste was used to make good thermal contact between the device and the heat-flux sensors, and between the heat-flux sensors and the copper blocks. The heat flux sensors (4 mm × 4 mm in area) were centred with respect to the juxtaposed Peltier faces (6 mm × 4 mm). The source and sink temperatures, T_c and T_h, respectively, were measured via K-type thermocouples that were fed through both copper blocks to meet the heat-flux sensors. The Peltier-EC-Peltier device was characterized in this configuration with $T_c \sim T_h \sim 300$ K.

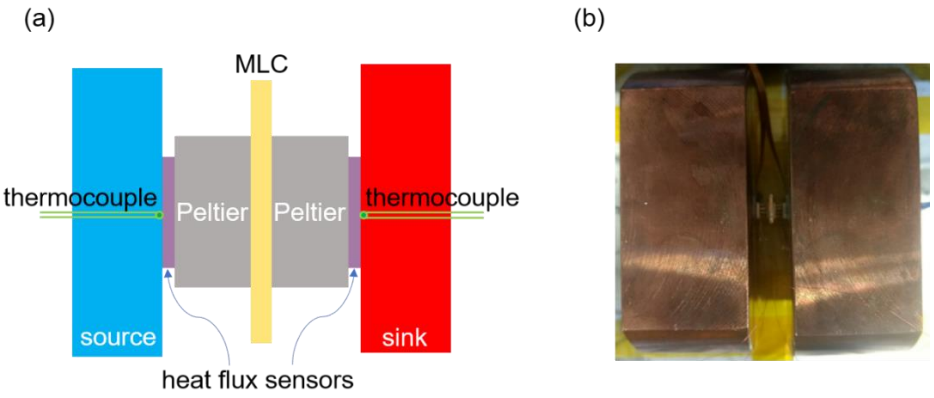

Fig. 5.4 | **Configuration for testing Peltier-assisted Brayton cycles.**

(a) Lateral view of the device, source and sink not to scale. The heat source and heat sink are copper blocks whose embedded thermocouples are used to measure source and sink temperatures, T_c and T_h, respectively. Heat-flux sensors between the source (sink) and the Peltier-EC-Peltier device permit measurement of the heat flow rate $\dot{Q}_c$ ($\dot{Q}_h$) at the cold (hot) end of the device. (b) Photograph of the device (lateral view).

Peltier-assisted Brayton cycles (Fig. 5.5a) consist of four steps: (1) near-adiabatic application of field E starting at temperature T_s generates a (positive) temperature change $\Delta T(T_s,0\rightarrow E)$ in the EC working body, (2) the sink-side Peltier is driven with a current to extract heat from the EC working body, returning it to its starting temperature T_s, (3) near-adiabatic field removal generates a (negative) temperature change $\Delta T(T_s,E\rightarrow 0)$ in the EC working body (4) the source-side Peltier is driven with a current to inject heat into the EC working body, returning it to its initial state at the starting temperature T_s with zero applied field.

EC effects in the MLC were driven by applying and removing E = 6.6 V μm^{-1} (250 V). The corresponding EC heat $|Q|$ ~ 230 mJ was determined by integrating the heat flow through both heat-flux sensors while driving the MLC in a zero-temperature-span Brayton cycle with the Peltiers switched off. Heat exchange between the MLC and the sink/source therefore proceeded by passive thermalization over a half-cycle duration of 250 s.

By contrast, Peltier-assisted Brayton cycles can in principle operate with a substantially reduced half-cycle duration because the Peltiers are used to actively pump heat. A half-cycle duration of 5 s was determined to be sufficient to ensure thermalization of the Peltier face juxtaposed to the active region of the MLC, given that only a ~2 s delay was observed between changes in the MLC electric field and the resultant peaks in the thermoelectric signal of the Peltiers (Fig. 5.3a-d).

Extracting ~230 mJ of heat from the MLC in a 5 s half cycle was found to require a current of 133 mA in the sink-side Peltier; injecting ~230 mJ of heat into the MLC in a 5 s half cycle was found to require a current of 98 mA in the source-side Peltier. These drive currents were identified by operating each Peltier in reverse-bias with 5 s pulses of different currents while the other Peltier was switched off. Operating in reverse-bias allowed the heat-flux sensors to measure the heat that is pumped into/out of the MLC when operating in forward-bias, i.e. the heat entering the sink-side Peltier and the heat exiting the source-side Peltier. This differs from the heat flow measured when operating in forward-bias because the heat exiting a given Peltier is greater than the heat entering the Peltier by an amount that corresponds to the Joule heat generated in the Peltier. This explains the discrepancy between the drive currents for the two Peltiers, as the heat injected into the MLC includes the Joule heat generated in the source-side Peltier.

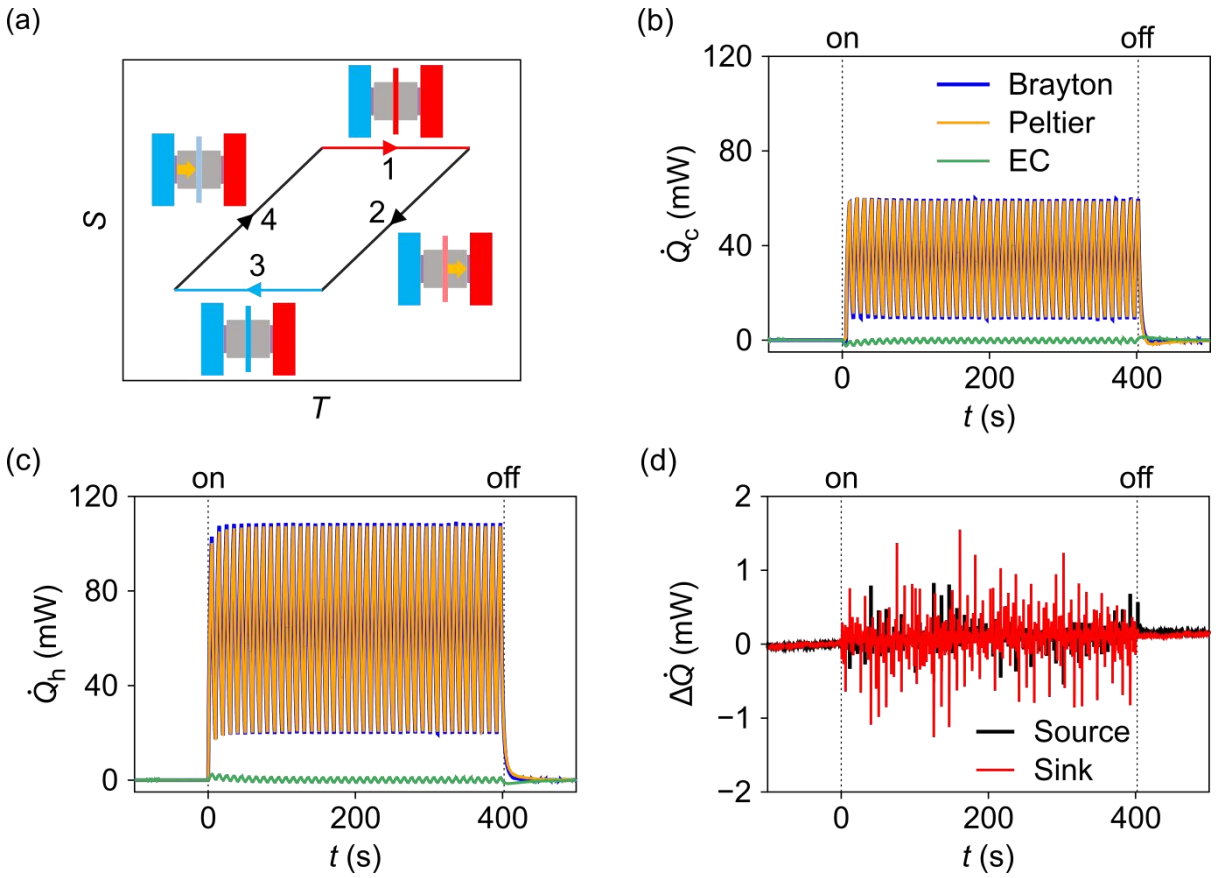

Fig. 5.5 | **Peltier-assisted Brayton cycles in the Peltier-EC-Peltier device.**

(a) Zero-temperature-span Brayton cycles, schematized on (*T*;*S*) axes, were implemented with the assistance of the Peltiers in the Peltier-EC-Peltier device. Modified forms of the schematic in Fig. 5.4 represent the four steps of the cycle: (1) Field application causes the MLC to become hot (red). (2) Heat is pumped (orange arrow) out of the MLC by the sink-side Peltier which causes the MLC to become less hot (pink) as it returns to its starting temperature. Field removal causes the MLC to become cold (blue). (4) Heat is pumped (orange arrow) into the MLC by the source-side Peltier, causing the MLC to become less cold (light blue) as it returns to its starting temperature. (b,c) The instantaneous rates of heat flow at the (b) source $\dot{Q}_c$ and (c) sink $\dot{Q}_h$ were measured under three different operating conditions: (i) Peltier-assisted Brayton cycles, i.e. Peltier driving synchronized with MLC field cycling ($\dot{Q}_{c/h}^{Brayton}$, in blue), (ii) Peltier driving like in the Peltier-assisted Brayton cycles but without MLC field cycling ($\dot{Q}_{c/h}^{Peltier}$, in orange), and (iii) MLC field cycling like in the Peltier-assisted Brayton cycles but without Peltier driving ($\dot{Q}_{c/h}^{EC}$, in green). (d) From (b) and (c) the difference in the rates of heat flow between these different operating conditions, i.e. $\Delta\dot{Q}_{c/h} = \dot{Q}_{c/h}^{Brayton} - \dot{Q}_{c/h}^{Peltier} - \dot{Q}_{c/h}^{EC}$, was calculated for both the source (black) and sink (red). The resulting differences in heat flow evidence the superposition of heat and the failure to rectify EC heat.

The instantaneous rates of heat flow at the source $\dot{Q}_c$ (Fig. 5.5b) and sink $\dot{Q}_h$ (Fig. 5.5c) were measured under three different operating conditions:

(i) Peltier-assisted Brayton cycles, i.e. synchronized driving of the Peltiers with field cycling of the MLC ($\dot{Q}_{c/h}^{Brayton}$),

(ii) driving the Peltiers like in the Peltier-assisted Brayton cycles but without field cycling the MLC ($\dot{Q}_{c/h}^{Peltier}$) and

(iii) field cycling the MLC like in the Peltier-assisted Brayton cycles but without driving the Peltiers ($\dot{Q}_{c/h}^{EC}$).

When the Peltiers are operational, the average rate of heat flow $\dot{Q}_c$ at the source, which is equivalent to the average cooling power P_c, was found to be ~34 mW regardless of whether the EC effect was driven (Fig. 5.5b). Despite using two thermal reservoirs for the heat source and heat sink, a small average temperature lift ΔT_{lift} ~ 0.4 K was observed, but this was likewise found to be insensitive to whether the EC effect was driven. Note that EC cycling with the Peltiers switched off generated a very modest heat flow across the heat-flux sensors (Fig. 5.5b,c). This is because the 5 s half-cycle duration was much faster than the time scale on which EC heat is passively conveyed to the heat-flux sensors.

Taking the difference between the rates of heat flow $\Delta\dot{Q}_{c/h} = \dot{Q}_{c/h}^{Brayton} - \dot{Q}_{c/h}^{Peltier} - \dot{Q}_{c/h}^{EC}$ (Fig. 5.5d) for the different operating conditions indicates that no synergistic gains in cooling power are achieved when operating Peltier-assisted Brayton cycles. Instead, almost perfect superposition of the EC heat and Peltier heat was observed: the difference in heat flow is characterized by only a small drift in the baseline and noise associated with small errors in the synchronization (Fig. 5.5d). These experiments suggest that Peltier-assisted Brayton cycles fail to rectify EC heat, which follows from the linearity of the heat equation, as outlined in Section 5.9.2.

5.9.2 Linearity of the heat equation and superposition of EC/Peltier heat

The heat equation incorporating the EC effect, the thermoelectric effect, and the Joule heat associated with either takes the form [193, 195]:

$$c\rho\frac{\partial T}{\partial t} = \nabla\cdot(k\nabla T) \; - \; \nabla\cdot(ST\mathbf{J}) + \frac{\mathbf{J}^2}{\sigma} \; - \; \rho T\Sigma\frac{\partial E}{\partial t} \tag{5.1}$$

where T is temperature, t is time, c is specific heat capacity, ρ is density, k is thermal conductivity, $\mathbf{J}$ is current density, S is the Seebeck coefficient, σ is electrical conductivity, and Σ is the electrocaloric coefficient, i.e. $\frac{\partial s}{\partial E}$ (where s is specific entropy). The second term on the right contains both the Peltier and Thomson effects ($-T\mathbf{J}\cdot\nabla S$) and an additional term ($-S\mathbf{J}\cdot\nabla T$) that modifies the dissipated work, which is given by the standard Joule heat term ($\mathbf{J}^2/\sigma$) in the absence of thermoelectric effects. The material specificity of the various scalar properties (c, ρ, k, S, σ and Σ) are encoded in their spatial variation, e.g. Σ is non-zero only in the regions of space occupied by EC material.

For small temperature spans, the temperature dependence of the Seebeck coefficient, and hence the Thomson effect, can be neglected. Similarly, the heat capacity, the thermal conductivity and the electrical conductivity can all be considered approximately temperature independent for small temperature spans far from absolute zero. The temperature-dependence of Σ, can likewise be neglected for small temperature spans when considering EC materials with slowly varying EC effects over a wide range of temperatures [1] (Chapter 3). (Note that the electric-field dependence of Σ is often significantly non-linear and therefore cannot be neglected, but this has no impact on linearity with respect to temperature.)

Under these assumptions, the heat equation becomes linear in temperature and its solutions obey the principle of superposition. Driving the Peltiers to pump heat thus fails to rectify the flow of EC heat. Experimental evidence supporting this conclusion is presented in Section 5.9.1.

5.9.3 Theory of EC-synchronized source-toggling of Peltiers

The theoretical treatment below is based on the treatment of Peltier cooling found in [196]. A simplified, one-dimensional model of the Peltier-EC-Peltier device is shown in Fig. 5.6. The Peltier-EC-Peltier device separates a load to be cooled at temperature T_c from a heat sink at temperature T_h. Each Peltier is characterized by an electrical resistance R, a thermal conductance K, and a Seebeck coefficient S equal to the difference between the coefficients for the p and n-type semiconductors that constitute the Peltier. The temperature at the Peltier face in contact with the EC working body is denoted T_x for the load-side Peltier and T_y for the sink-side Peltier. EC cycling modifies the temperatures T_x and T_y by an effective temperature change of magnitude $|\Delta T_{eff}|$, such that they are enhanced with field on and suppressed with field off. The relationship between $|\Delta T_{eff}|$ and the temperature change in the EC working body depends on the heat capacities and thermal conductivities of both the EC working body and the Peltiers, as discussed in Section 5.9.4.

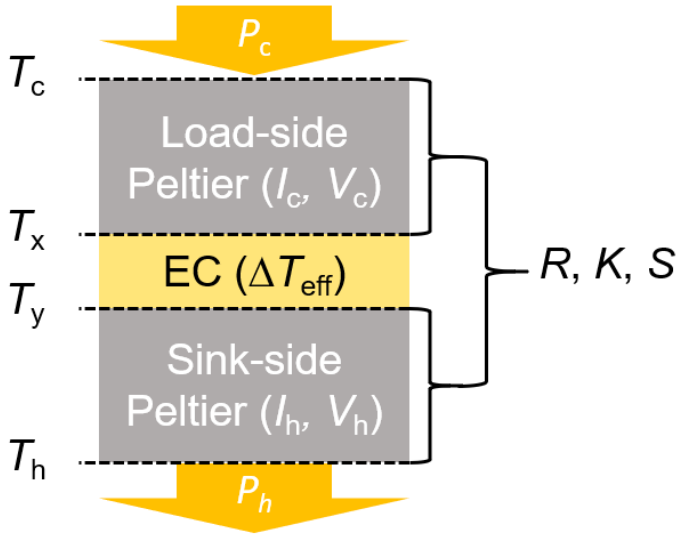

Fig. 5.6 | **Simplified schematic of a Peltier-EC-Peltier device.**

The Peltier-EC-Peltier device separates a load at temperature T_c from a sink at temperature T_h. The Peltiers are characterized by resistance R, thermal conductance K, and Seebeck coefficient S. The cooling power delivered to the load P_c is generated by driving the load-side Peltier with either current I_c or voltage V_c. The heating power rejected at the sink P_h is generated by driving the sink-side Peltier with either current I_h or voltage V_h. The temperature at the Peltier face in contact with the EC working body is denoted T_x for the load-side Peltier and T_y for the sink-side Peltier. EC cycling modifies the temperatures T_x and T_y by an effective temperature change of magnitude $|\Delta T_{eff}|$.

The device in operation is characterized by the cooling power P_c delivered to the load, the heating power P_h rejected at the sink, and the currents I_c and I_h used to drive the load and sink-side Peltiers, respectively. The expressions for P_c, P_h, and the power consumed by each Peltier $P_{c/h}^{work}$ are as follows:

$$P_c = ST_cI_c - I_c^2R/2 - K(T_x - T_c) \tag{5.2}$$

$$P_c^{work} = I_c^2R + S(T_x - T_c)I_c \tag{5.3}$$

$$P_h = ST_hI_h + I_h^2R/2 - K(T_h - T_y) \tag{5.4}$$

$$P_h^{work} = I_h^2R + S(T_h - T_y)I_h \tag{5.5}$$

The three terms in P_c and P_h correspond to the Peltier effect, Joule heat, and the thermal conduction opposing the Peltier effect in the steady state (in that order). To replicate the steady states generated by the currents I_c and I_h, voltages V_c and V_h must be sourced to the load and sink-side Peltiers, respectively. These voltages are given by the expressions:

$$V_c = I_cR + S(T_x - T_c) \tag{5.6}$$

$$V_h = I_hR + S(T_h - T_y) \tag{5.7}$$

Inverting Eqs (5.6) and (5.7) and plugging into Eqs (5.2)-(5.5) yields the corresponding expressions for P_c, P_h, and $P_{c/h}^{work}$ when voltage-sourcing:

$$P_c = ST_x\frac{V_c}{R} - \frac{V_c^2}{2R} - \frac{S^2}{2R}(T_x + T_c)(T_x - T_c) - K(T_x - T_c) \tag{5.8}$$

$$P_c^{work} = \frac{V_c^2}{R} - S(T_x - T_c)\frac{V_c}{R} \tag{5.9}$$

$$P_h = ST_y\frac{V_h}{R} + \frac{V_h^2}{2R} - \frac{S^2}{2R}(T_h + T_y)(T_h - T_y) - K(T_h - T_y) \tag{5.10}$$

$$P_h^{work} = \frac{V_h^2}{R} - S(T_h - T_c)\frac{V_h}{R} \tag{5.11}$$

A new effective thermal conductance can be defined in terms of the thermoelectric figure of merit ZT, i.e. $\widetilde{K} = K + (S^2T/R) = K(1+ZT)$. Given the temperature spans involved are much

smaller than the absolute temperature, i.e. $T_c \sim T_x \sim T_y \sim T_h \sim T$, Eqs (5.8) and (5.10) can be approximated by the equations:

$$P_c \cong ST_x \frac{V_c}{R} - \frac{V_c^2}{2R} - \widetilde{K}(T_x - T_c) \tag{5.12}$$

$$P_h \cong ST_y \frac{V_h}{R} - \frac{V_h^2}{2R} - \widetilde{K}(T_h - T_y) \tag{5.13}$$

To account for the effect of EC cycling, each half cycle of operation can be analyzed separately. When electric field is applied to the EC working body, current is sourced to the sink-side Peltier and voltage is sourced to the load-side Peltier. The new expressions for P_c, P_h, and $P_{c/h}^{work}$ can be written by replacing T_x with $T_x + |\Delta T_{eff}|$ in Eqs (5.8) and (5.9) and likewise replacing T_y with $T_y + |\Delta T_{eff}|$ in Eqs (5.4) and (5.5). Subtracting the original expressions from the new yields the changes in P_c, P_h, and $P_{c/h}^{work}$ due to EC cycling:

$$\Delta P_c \cong S|\Delta T_{eff}| \frac{V_c}{R} - \widetilde{K}|\Delta T_{eff}| \tag{5.14}$$

$$\Delta P_c^{work} = -S|\Delta T_{eff}| \frac{V_c}{R} \tag{5.15}$$

$$\Delta P_h = K|\Delta T_{eff}| \tag{5.16}$$

$$\Delta P_h^{work} = -S|\Delta T_{eff}|I_h \tag{5.17}$$

When electric field is removed from the EC working body, current is sourced to the load-side Peltier and voltage is sourced to the sink-side Peltier. The new expressions for P_c, P_h, and $P_{c/h}^{work}$ can be written by replacing T_x with $T_x - |\Delta T_{eff}|$ in Eqs (5.2) and (5.3) and likewise replacing T_y with $T_y - |\Delta T_{eff}|$ in Eqs (5.10) and (5.11). Subtracting the original expressions from the new yields the changes in P_c, P_h, and $P_{c/h}^{work}$ due to EC cycling:

$$\Delta P_c = K|\Delta T_{eff}| \tag{5.18}$$

$$\Delta P_c^{work} = -S|\Delta T_{eff}|I_c \tag{5.19}$$

$$\Delta P_h \cong -S|\Delta T_{eff}| \frac{V_h}{R} - \widetilde{K}|\Delta T_{eff}| \tag{5.20}$$

$$\Delta P_h^{work} = -S|\Delta T_{eff}| \frac{V_h}{R} \tag{5.21}$$

Averaging across both half cycles yields:

$$\Delta P_{\mathrm{c}} \cong \frac{1}{2}(S|\Delta T_{\mathrm{eff}}|\frac{V_{\mathrm{c}}}{\mathrm{R}} - ZT(K|\Delta T_{\mathrm{eff}}|)) \tag{5.22}$$

$$\Delta P_{\mathrm{c}}^{\mathrm{work}} = -\frac{1}{2}S|\Delta T_{\mathrm{eff}}|(I_{\mathrm{c}}+\frac{V_{\mathrm{c}}}{R}) \tag{5.23}$$

$$\Delta P_{\mathrm{h}} \cong -\frac{1}{2}(S|\Delta T_{\mathrm{eff}}|\frac{V_{\mathrm{h}}}{R} + ZT(K|\Delta T_{\mathrm{eff}}|)) \tag{5.24}$$

$$\Delta P_{\mathrm{h}}^{\mathrm{work}} = -\frac{1}{2}S|\Delta T_{\mathrm{eff}}|(I_{\mathrm{h}} + \frac{V_{\mathrm{h}}}{R}) \tag{5.25}$$

Dividing the change in power consumption by the baseline power consumption without EC cycling [i.e. Eqs (5.3) and (5.5)] yields the fractional change in power consumption:

$$\frac{\Delta P_{\mathrm{c}}^{\mathrm{work}}}{P_{\mathrm{c}}^{\mathrm{work}}} = \frac{-S|\Delta T_{\mathrm{eff}}|(I_{\mathrm{c}} + \frac{V_{\mathrm{c}}}{R})}{2(I_{\mathrm{c}}^2R + S(T_{\mathrm{x}} - T_{\mathrm{c}})I_{\mathrm{c}})} = \frac{-S|\Delta T_{\mathrm{eff}}|(I_{\mathrm{c}} + \frac{S(T_{\mathrm{x}} - T_{\mathrm{c}})}{2R})}{I_{\mathrm{c}}^2R + S(T_{\mathrm{x}} - T_{\mathrm{c}})I_{\mathrm{c}}} \tag{5.26}$$

$$\frac{\Delta P_{\mathrm{h}}^{\mathrm{work}}}{P_{\mathrm{h}}^{\mathrm{work}}} = \frac{-S|\Delta T_{\mathrm{eff}}|(I_{\mathrm{h}} + \frac{V_{\mathrm{h}}}{R})}{2(I_{\mathrm{h}}^2R + S\left(T_{\mathrm{h}} - T_{\mathrm{y}}\right)I_{\mathrm{h}})} = \frac{-S|\Delta T_{\mathrm{eff}}|(I_{\mathrm{h}} + \frac{S(T_{\mathrm{h}} - T_{\mathrm{y}})}{2R})}{I_{\mathrm{h}}^2R + S\left(T_{\mathrm{h}} - T_{\mathrm{y}}\right)I_{\mathrm{h}}} \tag{5.27}$$

Where Eqs (5.6) and (5.7) have been used to rewrite the voltages in terms of currents. In the limit of maximum cooling power, i.e. zero temperature lift, this simplifies to:

$$\frac{\Delta P_{\mathrm{c}}^{\mathrm{work}}}{P_{\mathrm{c}}^{\mathrm{work}}} = \frac{-S|\Delta T_{\mathrm{eff}}|}{I_{\mathrm{c}}R} \tag{5.28}$$

$$\frac{\Delta P_{\mathrm{h}}^{\mathrm{work}}}{P_{\mathrm{h}}^{\mathrm{work}}} = \frac{-S|\Delta T_{\mathrm{eff}}|}{I_{\mathrm{h}}R} \tag{5.29}$$

In the absence of EC cycling, the mean rate of heat transfer across the device, $\overline{P} = (P_{\mathrm{c}} + P_{\mathrm{h}})/2$, is given by either averaging Eqs (5.2) and (5.4) or equivalently Eqs (5.8) and (5.10). For small currents that generate negligible Joule heat, continuity of heat flow requires that the load and sink-side Peltiers be driven roughly equally, i.e. $I \sim I_{\mathrm{c}} \sim I_{\mathrm{h}}$ or equivalently $V \sim V_{\mathrm{c}} \sim V_{\mathrm{h}}$. Small currents will also generate small temperature spans, i.e. $T \sim T_{\mathrm{h}} \sim T_{\mathrm{c}}$, which permits the simplification:

$$\overline{P} \cong STI - K\overline{\Delta T}_{\mathrm{Pelt}} \tag{5.30}$$

where $\overline{\Delta T}_{\mathrm{Pelt}} = ((T_h - T_y) + (T_x - T_c))/2$. The change in the mean rate of heat transfer due to EC cycling is given by averaging Eqs (5.22) and (5.24), which for $V \sim V_c \sim V_h$ simplifies to:

$$\Delta\overline{P} \cong -\frac{ZT}{2}(K|\Delta T_{\mathrm{eff}}|) \tag{5.31}$$

Dividing the change in the mean rate of heat transfer by the base-line rate of heat transfer without EC cycling yields the fractional change in the mean rate of heat transfer:

$$\frac{\Delta\overline{P}}{\overline{P}} \cong -\frac{ZT(K|\Delta T_{\mathrm{eff}}|)}{2(STI - K\overline{\Delta T}_{\mathrm{Pelt}})} \tag{5.32}$$

In the limit of maximum cooling power, i.e. zero temperature lift, this simplifies to:

$$\frac{\Delta\overline{P}}{\overline{P}} \cong -\frac{ZT(K|\Delta T_{\mathrm{eff}}|)}{2STI} = -\frac{S|\Delta T_{\mathrm{eff}}|}{2IR} \tag{5.33}$$

Thus, the percentage reduction in the heat pumped at zero temperature lift is only half the percentage reduction in power consumption. The percentage reduction in temperature lift at zero cooling power is given by the same expression as Eq. (5.33) because of the linear relationship between the temperature lift and the heat pumped (see the load lines in Fig. 5.3e). A figure of merit χ for the EC-induced improvement in Peltier performance can be defined as:

$$\chi = \frac{S|\Delta T_{\mathrm{eff}}|}{IR} \tag{5.34}$$

which depends on the magnitude of the EC effect as well as the Seebeck coefficient and the resistance of the Peltiers.

5.9.4 Effective temperature change at EC-Peltier interface

The effective temperature change ΔT_{eff} at the surface of contact between a Peltier and an EC working body can be modelled for near-adiabatic field cycling by considering the surface of contact between two semi-infinite solids that are initially at different temperatures before coming into contact [89]. This approximation is roughly valid in the limit that the period $\mathcal{T}$ of field cycling is small enough to ensure that the characteristic length over which a temperature gradient develops (proportional to $\mathcal{T}^{1/2}$) is smaller than both the thickness of the EC working body and that of the Peltiers. A monolithic EC working body with adiabatic temperature change ΔT is assumed for simplicity, in which case the magnitude of the temperature change at the surface of contact is given by:

$$|\Delta T_{\text{eff}}| \sim \frac{f_{\text{EC}}|\Delta T|}{2(f_{\text{EC}}+f_{\text{Peltier}})} \tag{5.35}$$

where the effusivity f is related to other physical properties via the relation $f = (k\rho c)^{1/2}$: k is the thermal conductivity, ρ is the density, c is the specific heat capacity. The factor of two in the denominator arises from the fact that when the period $\mathcal{T}$ of field cycling is much smaller than the thermal relaxation time scale τ, the EC component oscillates about a starting temperature T_s between the temperatures $T_s - |\Delta T|/2$ and $T_s + |\Delta T|/2$. Thus, in the limit $f_{\text{EC}} >> f_{\text{Peltier}}$, the effective temperature change at the juxtaposed surface of the Peltiers is given by $|\Delta T_{\text{eff}}| \sim |\Delta T|/2$.

This treatment assumes an ideal interface, but in practice the EC working body and the juxtaposed Peltier face will be separated by thermal resistances which include layers of insulation, adhesive, etc. Nevertheless, taking Eq. (5.35) as an upper bound on the effective temperature change $|\Delta T_{\text{eff}}|$ and plugging it into Eq. (5.34) from Section 5.9.3 yields a new expression for the figure of merit χ:

$$\chi = \frac{f_{\text{EC}} S|\Delta T|}{2(f_{\text{EC}} + f_{\text{Peltier}})IR} \tag{5.36}$$

5.9.5 Determination of Peltier drive levels

To determine drive levels for the sink-side Peltier, currents I_h, ranging from 1 mA to 20 mA in 1 mA increments, were sourced to the sink-side Peltier, while measuring the voltage across both the load-side Peltier and the sink-side Peltier. The steady-state voltage $V_{h.f.}^{load}$ across the load-side Peltier is proportional to the heat flow across the load-side Peltier generated by driving the sink-side Peltier. The steady-state voltage V_h across the sink-side Peltier corresponds to the voltage that if sourced would replicate the steady state generated by sourcing a given current I_h. To determine drive levels for the load-side Peltier, currents I_c (ranging from 1 mA to 20 mA in 1 mA increments) were sourced to the load-side Peltier while measuring the voltage across the sink-side Peltier ($V_{h.f.}^{sink}$) and the load-side Peltier (V_c).

Curves of the form $f(I) = aI + bI^2$ were fitted to the data for both Peltiers correlating the current I to the steady-state voltage V_{hf} across the opposing Peltier (Fig. 5.7). This form accounts for both the Peltier effect (aI) as well as the Joule heat (bI^2). Zero-net-heat transfer to the MLC was enforced by determining the drive currents in each Peltier that yielded the same selected voltages (0.5 mV, 1.0 mV, 1.5 mV, 2.0 mV, and 2.5 mV) across the opposing Peltier, i.e. $V_{hf}^{load}(I_h) = V_{hf}^{sink}(I_c)$. This ensured that the sink-side Peltier draws the same heat that the load-side Peltier rejects, thereby transferring zero net heat to the MLC.

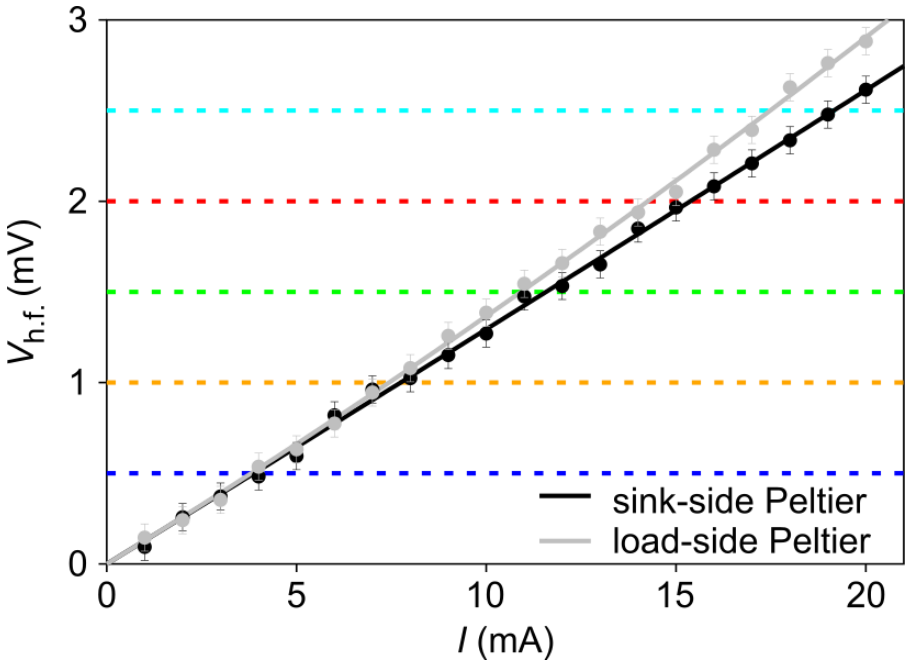

Fig. 5.7 | **Determination of drive levels for Peltiers.**

Current I in each Peltier (black circles for the sink-side Peltier; grey circles for the load-side Peltier) generates a steady-state voltage $V_{h.f.}$ across the opposite Peltier. Curves of the form $f(I) = aI + bI^2$ were fitted for both Peltiers (black line for the sink-side Peltier; grey line for the load-side Peltier). Drive levels were determined by solving for the currents that yielded selected voltages across the opposite Peltier, namely 0.5 mV (blue dashed line), 1.0 V (orange dashed line), 1.5 mV (green dashed line), 2.0 mV (red dashed line), and 2.5 mV (cyan dashed line). The colour coding of drive levels here is the same as that in Fig. 5.3 and Table 5.1.

5.9.6 Modelling of the reduction in power consumption

EC effects in the MLC active volume generate a thermoelectric response in the Peltiers that is, in principle, described by a set of differential equations. These differential equations are both unknown and too complex to be useful, but they are similar in form to Eq. (2.1), which describes an EC working body thermalizing with its environment. In analogy to the lumped-element model in Fig. 2.1, the Peltiers represent a thermal resistance through which the MLC active volume thermalizes with its environment, and the thermoelectric voltage or current is proportional to the temperature span across the Peltier. Differential equations similar in form to Eq. (2.1) are solved by using Green's functions like the one shown in Eq. (2.5). An analytic solution to the thermoelectric response of the Peltiers is not possible given that the differential equations are not known, but a numerical solution is possible by using experimental data to determine the Green's functions. These Green's functions can be used to model the thermoelectric response to arbitrary EC cycling, and thereby determine the optimal cycle period that minimizes power consumption.

When sourcing current to the Peltiers, EC effects in the MLC active volume generate a thermoelectric response in the Peltiers given by:

$$\Delta V(t) = S \int_{-\infty}^{\infty} G_{\mathrm{i}}(t')\Delta T_0(t-t')\mathrm{d}t' \tag{5.37}$$

where $\Delta V(t)$ is the instantaneous change in the voltage across the Peltier, S is the Seebeck coefficient, $G_i(t)$ is a Green's function that represents the thermal relaxation behaviour of the MLC when sourcing current to the Peltiers, and $\Delta T_0(t)$ is the instantaneous change in the temperature of the MLC active volume if it were thermally isolated, i.e. in the absence of thermal relaxation pathways (Section 2.1).

When sourcing voltage to the Peltiers, EC effects in the MLC active volume generate a thermoelectric response in the Peltiers given by:

$$\Delta I(t) = \frac{S}{R+R_{\mathrm{s}}} \int_{-\infty}^{\infty} G_{\mathrm{v}}(t')\Delta T_0(t-t')\mathrm{d}t' \tag{5.38}$$

where $\Delta I(t)$ is the instantaneous change in the current through the Peltier, R is the resistance of the Peltier, R_s is the additional series resistance between the Peltier and the source, and $G_v(t)$ is a Green's function that represents the thermal relaxation behaviour of the MLC when sourcing voltage to the Peltiers. The difference between $G_i(t)$ and $G_v(t)$ arises from the difference in the effective thermal conductance of the Peltiers when sourcing current versus sourcing voltage [192]. For a rapid change of field at time $t = 0$, the form of ΔT_0 is approximated by $\Delta T_0(t) \sim \Delta T\Theta(t)$, where $\Theta(t)$ is the Heaviside step function. Making this substitution, Eqs (5.37) and (5.38) can be respectively written as:

$$\Delta V(t) = A \int_{-\infty}^{\infty} G_i(t')\Theta(t - t')\mathrm{d}t' \tag{5.39}$$

$$\Delta I(t) = B \int_{-\infty}^{\infty} G_v(t')\Theta(t - t')\mathrm{d}t' \tag{5.40}$$

where $A \sim S\Delta T$ and $B \sim A/(R + R_s)$ are constants of proportionality. Deconvolution with a Heaviside step function is equivalent to differentiation, allowing Eqs (5.39) and (5.40) to be rearranged respectively as:

$$G_i(t) = \frac{1}{A}\frac{\mathrm{d}(\Delta V)}{\mathrm{d}t} \tag{5.41}$$

$$G_v(t) = \frac{1}{B}\frac{\mathrm{d}(\Delta I)}{\mathrm{d}t} \tag{5.42}$$

The Green's function $G_i(t)$ and $G_v(t)$ were determined to within the constants of proportionality by computing the numerical derivatives of the thermoelectric signal generated when driving the MLC in a Brayton cycle (Fig. 5.3a-d). Average values for the instantaneous voltage change $\Delta V(t)$ and the instantaneous current change $\Delta I(t)$ were determined for each Peltier by subtracting the baselines and averaging across all drive levels, given that the linearity of the thermoelectric constituent equations ensures that the thermoelectric response is independent of the drive level. The constants of proportionality A and B were not required in subsequent calculations, as they are shown to cancel out in the expressions that describe the reduction in power consumption when EC cycling is synchronized with Peltier source-toggling.

The Green's functions $G_i(t)$ and $G_v(t)$ were used to model the thermoelectric response to EC cycling, for which the form of ΔT_0 is approximated by $\Delta T_0(t) \sim \Delta T \Theta(\sin(2\pi t/\mathcal{T}))$, i.e. a square wave with period $\mathcal{T}$. The resultant thermoelectric response is given by making this substitution in Eqs (5.37) and (5.38), which yields respectively:

$$\Delta V(t) = A \int_{-\infty}^{\infty} G_i(t') \Theta(\sin(2\pi(t-t')/\mathcal{T}))\mathrm{d}t' \tag{5.43}$$

$$\Delta I(t) = B \int_{-\infty}^{\infty} G_v(t') \Theta(\sin(2\pi(t-t')/\mathcal{T}))\mathrm{d}t' \tag{5.44}$$

where the prefactors A and B cancel with the $1/A$ and $1/B$ prefactors in Eqs (5.41) and (5.42), respectively. For fixed current or voltage sourcing, $\Delta V(t)$ and $\Delta I(t)$ oscillates about 0, resulting in no change in the time-averaged power consumption. Peltier source-toggling restricts operation to $\Delta V < 0$ and $\Delta I < 0$, such that only the dips in the power consumption are exploited without the jumps. For the sink-side Peltier, cyclically driving EC effects while toggling between sourcing current I_h and voltage V_h results in a change $\Delta P_h^{source}(t)$ in the power drawn from the source, which is given by:

$$\Delta P_h^{source}(t) = I_h \Delta V_h \Theta(\sin(2\pi t/\mathcal{T})) + V_h \Delta I_h (1 - \Theta(\sin(2\pi t/\mathcal{T}))) \tag{5.45}$$

where $\Theta(\sin(2\pi t/\mathcal{T}))$ and $1 - \Theta(\sin(2\pi t/\mathcal{T}))$ oscillate in value between 0 and 1 in anti-phase. For the load-side Peltier, cyclically driving EC effects while toggling between sourcing current I_c and voltage V_c results in a change $\Delta P_c^{source}(t)$ in the power drawn from the source, which is given by:

$$\Delta P_c^{source}(t) = I_c \Delta V_c (1 - \Theta(\sin(2\pi t/\mathcal{T}))) + V_c \Delta I_c \Theta(\sin(2\pi t/\mathcal{T})) \tag{5.46}$$

The total change in power consumption due to EC cycling is given by:

$$\Delta P_{source}(t) = \Delta P_h^{source}(t) + \Delta P_c^{source}(t) \tag{5.47}$$

The EC-induced change $\Delta P_{source}(t)$ in the power drawn from the source was computed for various cycle periods $\mathcal{T}$ (Fig. 5.8), and an optimal cycle period of $\mathcal{T} \sim 12$ s was found to minimize the average power consumption. Experimentally determined values of $\Delta P_{source}(t)$ for the optimized cycles are presented in Fig. 5.3f-j. The predictions of the model overestimate the experimentally observed reductions in power consumption by ~8%, most probably due to imperfect source-toggling and imperfect synchronization with EC cycling.

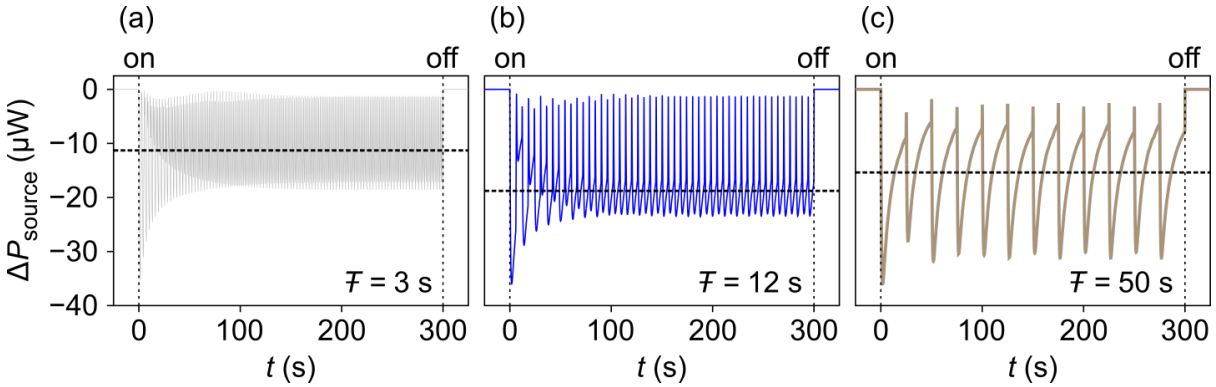

Fig. 5.8 | **Predicted power reduction for selected cycle periods.**

The power drawn from the source differs with and without EC cycling by an amount ΔP_{source} whose predicted time evolution is shown for cycles periods $\mathcal{T}$ of (a) 3 s, (b) 12 s, and (c) 50 s when operating at the lowest Peltier drive level. The time-averaged value of the EC-induced reduction in power consumption is indicated by (horizontal) dashed black lines.

5.9.7 Correction for in-series contact resistances

Consider a current or voltage source connected to a Peltier with resistance R in series with a contact resistance R_s. The relationship between the current I and the voltage V supplied by the source is given by:

$$V = I(R + R_s) + V_S \tag{5.48}$$

where V_S is the Seebeck voltage across the Peltier. A change ΔV_S in the Seebeck voltage when sourcing a fixed current I_0 produces a change in the power P_{source} drawn from the source, which is given by:

$$\Delta P_{source} = I_0 \Delta V_S \tag{5.49}$$

As the Seebeck voltage arises entirely in the Peltier itself, the resultant change in the power P_{work} consumed by the Peltier is also:

$$\Delta P_{work} = \Delta P_{source} = I_0 \Delta V_S \tag{5.50}$$

These expressions are unaltered by the value of the series resistance R_s. On the other hand, the difference between the power drawn from the source and the power consumed by the Peltier is given by:

$$P_{source} - P_{work} = I_0^2 R_s \tag{5.51}$$

In the ideal case of $R_s = 0$, the power drawn from the source equals the power consumed by the Peltiers. Experimentally determined changes in power consumption for finite R_s can be used to determine the changes in power consumption for $R_s = 0$. The fractional change in power consumption when current sourcing is corrected via the expression:

$$\frac{\Delta P_{work}}{P_{work}} = \frac{\Delta P_{source}}{P_{source} - I_0^2 R_s} \tag{5.52}$$

A change ΔV_S in the Seebeck voltage when sourcing a constant voltage V_0 produces a change in the current drawn from the voltage source, which is given by:

$$\Delta I = \frac{-\Delta V_S}{R + R_s} \tag{5.53}$$

The corresponding change in the power drawn from the source is given by:

$$\Delta P_{source} = \frac{-\Delta V_S V_0}{R + R_s} \tag{5.54}$$

Dividing by the baseline power drawn from the source yields the fractional change in power consumption:

$$\frac{\Delta P_{source}}{P_{source}} = \frac{\frac{-\Delta V_S V_0}{R + R_s}}{IV_0} = \frac{-\Delta V_S}{I(R + R_s)} = \frac{-\Delta V_S}{V_0 - V_S} \tag{5.55}$$

In the ideal case of $R_s = 0$, for which $P_{source} = P_{work}$, the same current I must be supplied to the Peltier in order to pump the same steady-state heat, albeit by sourcing a smaller voltage V_0. In this case, Eq. (5.55) simplifies to:

$$\frac{\Delta P_{work}}{P_{work}} = \frac{\frac{-\Delta V_S V_0}{R}}{IV_0} = \frac{-\Delta V_S}{IR} \tag{5.56}$$

Taking the ratio of Eq. (5.56) to Eq. (5.55) yields the correction to the fractional change in power consumption when voltage sourcing:

$$\frac{\Delta P_{work}}{P_{work}} \Big/ \frac{\Delta P_{source}}{P_{source}} = \frac{\frac{-\Delta V_S}{IR}}{\frac{-\Delta V_S}{I(R+R_s)}} = \frac{R+R_s}{R} \tag{5.57}$$

The correction for voltage sourcing given by Eq. (5.57) differs from the correction for current sourcing given by Eq. (5.52) because the Seebeck-induced change in current when sourcing voltage is sensitive to R_s [Eq. (5.53)], unlike the Seebeck-induced change in voltage when sourcing current. (Note that the baseline power consumption is inflated by series resistance whether sourcing current or voltage.)

When sourcing voltage the change in current generates a concomitant reduction in the heat pumped that is also dependent on the value of R_s. Rearranging Eq. (5.48) yields an expression for the current when sourcing voltage V_0:

$$I = \frac{V_0 - V_S}{R + R_s} \tag{5.58}$$

Dividing Eq. (5.53) by Eq. (5.58) yields the fractional change in current:

$$\frac{\Delta I}{I} = \frac{\frac{-\Delta V_S}{R + R_s}}{\frac{V_0 - V_S}{R + R_s}} = \frac{-\Delta V_S}{V_0 - V_S} = \frac{-\Delta V_S}{I(R + R_s)} \tag{5.59}$$

From the equivalence of Eqs (5.55) and (5.59), it follows that the percentage reduction in current when sourcing voltage should be corrected using Eq. (5.57), i.e. via the scale factor $\frac{R+R_s}{R}$. The heat pumped is proportional to the current (neglecting Joule heat), and thus both the percentage reduction in cooling power at zero temperature lift and the percentage reduction in the temperature lift at zero cooling power (i.e. at opposite ends of the same load line) should be corrected analogously.

5.9.8 Irrecoverable work during EC cycling

Measurements of the per-cycle charge q drawn/discharged by the MLC (Fig. 5.9a) were used to evaluate the per-cycle irrecoverable work $W_{EC} = \oint V đq \sim 2.9$ mJ. This translates to a dissipated power of $P_{EC} \sim 240$ µW that represents a substantial parasitic contribution to overall device efficiency. However, this can be minimized by geometric optimization in future, as argued below.

Thermalization of the MLC active volume with inactive thermal mass detracts from the overall device efficiency in two ways. First, it reduces the effective temperature change at the juxtaposed Peltier face and thereby reduces the efficiency gains from source-toggling. Second, it increases the irrecoverable work dissipated in the MLC. The irrecoverable work for a monopolar 100 ms triangular pulse (0 V → 600 V → 0 V) is $W_{EC} \sim 480$ µJ (Fig. 5.9b). Thus an additional ~2.4 mJ are dissipated during the 12 s cycle due to partial thermalization of the MLC active volume, which enhances the polarization prior to field removal (Fig. 5.9a). Note that dissipation caused by thermalization after fast field changes is akin to the 'triangles' that constitute the additional work required to drive a Brayton cycle versus an Ericsson cycle (Fig. 4.2).

During the 6 s half cycle, a substantial portion of the thermalization occurs between the active and inactive regions of the MLC, as corroborated by IR imaging of MLC faces after rapid changes of field (for example, Fig. 2.8b indicates that the inactive margins thermalize with the active volume ~1.5 s after rapid field application). Thermalization with the inactive region is aggravated by the additional lateral thermal conductance provided by the interdigitated metallic electrodes.

Thermalization during cycling also inevitably involves the inactive thermal mass that lies between the MLC active volume and the juxtaposed Peltier face. This includes an inactive layer of the MLC, Kapton tape, silver paint, and the plastic capping of the Peltier module. These layers also represent thermal resistance that generates delay between EC effects and the thermoelectric response of the Peltiers, with the effect of further reducing the efficiency gains from source-toggling. Geometric optimization of the Peltier-EC-Peltier device would

therefore involve minimizing inactive thermal mass that leaches EC heat and minimizing thermal resistances that slow the Peltier response to EC effects.

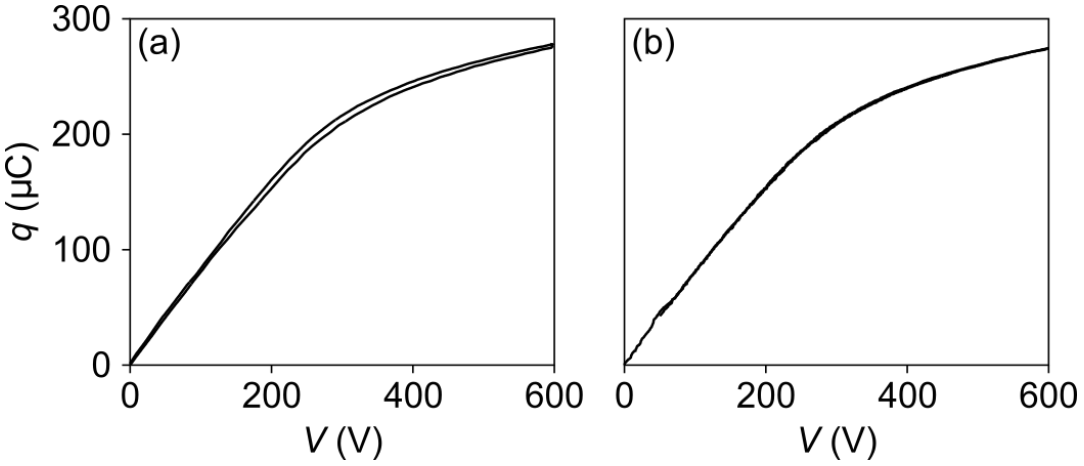

Fig. 5.9 | **Charge-voltage characteristics of the MLC for different drive forms.**

(a,b) Charge-voltage $q(V)$ characteristics of the MLC, measured for (a) square wave EC cycling between 0 V and 600 V with a period of 12 s (i.e. the drive form used when source-toggling the Peltiers) and (b) a 100 ms monopolar triangular voltage pulse with an amplitude of 600 V. The latter is taken to be sufficiently fast to render negligible the heat exchange between the MLC active volume and its surroundings.

If all the sub-optimal components are removed, then in principle heat transfer can be limited to the amount required for the juxtaposed Peltier face to thermalize with the EC working body. In the Peltier-EC-Peltier device studied here, it takes ~2 s for the juxtaposed Peltier face to thermalize with the MLC after a fast field change, as evidenced by peaks in the thermoelectric response in Fig. 5.3a-d. In these ~2 s, less than 10% of the total EC heat is conveyed to the Peltiers (EC heat is proportional to the integral of the thermoelectric response in Fig. 5.3a-d). Therefore, the bulk of the EC effect driven across all 19 active layers of the MLC was driven needlessly, and a sizeable reduction in the observed irrecoverable work could be achieved by driving the EC effect in a fewer number of active layers.

Alternatively, the cycle period can be increased to lower the power consumed in EC cycling, but this will also adversely affect the efficiency gains in the Peltiers (Section 5.9.6) as the average value of the effective temperature change at the juxtaposed Peltier surface falls. Furthermore, the active region of the MLC will further thermalize with its surrounding

thermal mass during a longer cycle, leading to increased dissipation albeit at a lower rate (i.e. lower power). Lastly, losses associated with driving a first-order transition can be minimized by avoiding the crossing of a phase boundary. This was done in this study by operating the Peltier-EC-Peltier device above the critical temperature T_{cp} ~ 330 K (Section 3.3.2). Electrical hysteresis associated with the field-driven transition was thus greatly reduced (Fig. 5.9b), but second-order materials may be preferable in future for Peltier-EC-Peltier devices.

“എന്റെ മാവും പൂക്കും.”

“My mango tree will also bloom.”

Chapter 6

Conclusions

The focus of this dissertation has been on electrocaloric (EC) measurements, working bodies and applications, and all of the work was largely based on multilayer capacitors (MLCs) of $PbSc_{0.5}Ta_{0.5}O_3$ (PST) that were supplied by Sakyo Hirose at Murata Manufacturing (Japan). The preceding five chapters are summarized below along with future perspectives.

Chapter 1 described EC effects from both phenomenological and microscopic viewpoints and provided a review of the literature on EC materials and prototypes. Since its 1930 inception [23], the field of electrocalorics has been closely aligned with the larger and more mature field of ferroelectrics, and has therefore mirrored many of its key developments. Just as the development of ferroelectric thin films produced a surge in research activity that resulted in the proliferation of applications including FeRAM [197], ferroelectric thin films of perovskite oxides [27] and polymers [54] ushered in an era of "giant" EC effects and renewed interest in electrocalorics. Recent activity has also revived interest in bulk EC materials and in particular the MLC geometry, which as identified in [69] combines the advantages of thin films (large breakdown strength permitting access to large EC effects) and the advantages of bulk (sufficient thermal mass for cooling macroscopic loads). The recent acceleration in prototype development [72-81] is an exciting development, particularly considering the vast body of work on magnetocaloric (MC) prototypes that should readily be exploited in analogous designs. Meanwhile, the search for candidate EC refrigerants is growing ever wider, as EC effects in materials systems beyond ferroelectrics have been reported, e.g. liquid crystals [85].

Chapter 2 provides a critical overview of the measurements that are employed in the study of electrocalorics. Experiments can be tailored to achieve near-adiabatic or near-isothermal EC effects, as discussed using a lumped-element thermal model for an EC capacitor that thermalizes with its environment on some timescale. There was a discussion of indirect

methods for measuring EC effects via variable-temperature electrical measurements, with emphasis on strategies to handle electrical/thermal hysteresis and artefacts of measurement. Direct measurements of temperature change can be made via contact and non-contact thermometry. A lumped-element thermal model of contact thermometry was used to ascertain the experimental requirements for near-adiabatic thermometry, away from which heat-transfer models or assumptions about thermalization can be used to scale-up other measurements of temperature change. IR imaging represents a particularly attractive form of non-contact thermometry that results in movies where temperature change is measured with spatial resolution, but spurious sources of radiation can compromise the conversion of photon counts to temperature, particularly when imaging samples with complex geometries such as MLCs. EC heat can be determined either via direct measurements, or via quasi-direct measurements that yield the field and temperature-dependent heat capacity $c(T,E)$. Direct measurements of heat are often presented as direct measurements of temperature change, but the fast changes of field that barely compromise the identification of isothermal heat are liable to compromise the calibration.

More generally, measurements of temperature change under non-adiabatic conditions, and measurements of heat under non-isothermal conditions, are likely to produce systematic errors or require unfalsifiable correction. One may likewise expect systematic errors if using the wrong Maxwell method for a given set of polarization measurements, e.g. $\left.\frac{\partial S}{\partial E}\right|_T = \left.\frac{\partial P}{\partial T}\right|_E$ with isentropic $P(E)$ data. My predecessor Sam Crossley used $\left.\frac{\partial T}{\partial E}\right|_S = -\left.\frac{\partial P}{\partial S}\right|_E$ to correct this approach for bulk PST [83] in a publication that I co-authored [2], but the discrepancy was found to be small because the EC effects are relatively small ($\Delta T << T_s$) and vary only slowly with starting temperature T_s. This ironic revelation speaks to a general truth about the current state of the field: inconsistent measurement practices can be tolerated when there is not much to measure. One can hope that as the field matures, the study of EC materials that display large EC effects compels a standardization in metrology.

In Chapter 3, EC effects in MLCs of PST were studied using the measurement techniques discussed in Chapter 2 (notably the Maxwell method and IR imaging) and Landau theory performed by Gian Guzmán-Verri [1]. PST is a well-known ferroelectric that has long been

studied for EC applications in both bulk and MLC embodiments, but the sophisticated fabrication processes overseen by Sakyo Hirose at Murata Manufacturing (Japan) yielded high B-site cation order (S_{111} ~ 0.96) in the MLC geometry for the first time. The large breakdown strength of the thin layers permitted the application of supercritical fields as large as E = 29.0 V μm^{-1}, which:

(i) drove EC effects of up to ΔT_j ~ 5.5 K in the central active area of the MLC, such that the EC effect associated with the latent heat of the transition was augmented 50% by EC effects in the transformed phase;

(ii) permitted substantial EC effects of $\Delta T_j \gtrsim 3$ K over a broad range of starting temperatures that spanned 176 K.

The magnitude and broad range of EC effects in MLCs of PST compare favourably to a relatively narrow peak of height ΔT ~ 2.5 K for the magnetocaloric (MC) refrigerant gadolinium (Gd) as used in most state-of-the-art MC prototypes with limited field ($\mu_0 H$ ~ 1.4 T applied), limited purity and finite demagnetization field [149]. This remains true even:

(i) in the unduly pessimistic limit of complete MLC thermalization prior to heat exchange with a sink/load, in which case the effective temperature change peaks at ΔT_{eff} ~ 3.3 K and exceeds ~3 K for starting temperatures that span 73 K;

(ii) for a more modest field of E = 15.8 V μm^{-1} that permits safe operation well below the breakdown field, such that the peak temperature change is ΔT_j ~ 4.3 K, which is reduced to ΔT_{eff} ~ 2.6 K if there is complete thermalization.

MLCs of PST represent the first EC working bodies that outperform Gd as used in MC prototypes, and in contrast to magnetic fields that require bulky and expensive permanent magnets, the ease with which electric fields can be applied represents a competitive advantage that may soon be exploited in state-of-the-art caloric prototypes.

It is perhaps unsurprising that developments in materials fabrication rather than the discovery of an exotic new material permitted EC working bodies to surpass the MC benchmark set by Gd. Supercritical applied fields offer a general strategy to overcome the limited magnitude of EC effects in ferroelectric materials [198]. In order to apply supercritical fields to PST, improved fabrication techniques were required to increase the breakdown field by more than

an order-of-magnitude with respect to the bulk samples of PST in which EC effects were first studied [45, 48]. However, mains voltage and/or safety concerns could limit the voltages applied in EC prototypes, just as MC effects in prototypes are limited by the strength of permanent magnets. Nevertheless, it may prove important to enhance breakdown strength via future improvements in fabrication. For example, tailoring the grain orientation of $Na_{0.5}Bi_{0.5}TiO_3$–$Sr_{0.7}Bi_{0.2}TiO_3$ in MLCs permitted access to fields as large as $E \sim 103$ V μm^{-1} to achieve state-of-the-art energy density among dielectric ceramics [199].

Chemical modifications and disorder tend to broaden first-order transitions [155] and therefore suppress the magnitude of EC effects in exchange for a broader range of starting temperatures. This strategy would not benefit the highly ordered undoped PST in the MLCs of Chapter 3, where the use of supercritical effects permitted the phase transition to be substantially broadened without compromising the peak temperature change. Uniaxial stress could conceivably sharpen the PST transition and permit access to larger EC effects over a smaller (but still large) range of starting temperatures, while pressure might have little effect on the transition given that it is associated with only a small volume change.

The challenges of imaging a complex (MLC) geometry in the infrared were discussed in Chapter 2 and led to the use of a high-emissivity paint (which happens to be black when viewed in visible light). The translucency of PST presented a serious challenge that could not be addressed with the relatively straightforward corrections that are available for reflections and transmissions. In future, IR images of bare MLC faces (Fig. 2.8) could be corrected using finite-element models that account for both complex optics and complex heat transfer. This would permit the cooling power delivered by MLCs to be maximized via geometrical optimization, as suggested previously for commercial MLCs of $BaTiO_3$ [131].

The detailed indirect EC measurements for an MLC of PST in Chapter 3 yielded polarization $P(T,E)$ and entropy $S(T,E)$ data out to 15.8 V μm^{-1} that in Chapter 4 were used to analyze the theoretical efficiency of cooling cycles based on an idealized fluid regenerator and one such MLC (many could be used together). The basis of this analysis was developed for bulk PST in my co-authored publication [2], and was used in Chapter 4 to likewise:

(i) determine the field variation along the field-on regenerator leg and thus ensure balanced regeneration, i.e. no net heat transfer between the MLC and the regenerator in each cycle;

(ii) crudely account for electrical and thermal hysteresis losses that are intrinsic to the MLC, requiring the use of both field-on and field-off polarization data when constructing cooling cycles.

Figures of merit that include the heat pumped from the load Q_c and the coefficient of performance COP were calculated for three types of cooling cycles, namely balanced Brayton cycles as used in [2], balanced Ericsson cycles, and Carnot cycles that are intrinsically balanced. Refrigerant efficiency γ was introduced here to identify the factor by which the hysteresis losses in a refrigerant reduce the COP of any given cycle. For balanced regenerative cycles with a temperature span of $T_h - T_c = 50$ K that falls within a wide range of temperatures above $T_C \sim 292$ K, MLCs of PST can achieve a refrigerant efficiency of up to ~97% if one assumes perfect energy recovery [80]. This implies that losses in an EC prototype based on MLCs of PST will primarily arise in the prototype that is built around the MLCs (engineering losses), but if one proceeds with no energy recovery, then the refrigerant efficiency is substantially lowered for all but a small range of load temperatures near T_C. The refrigerant efficiencies found here for MLCs of PST exceed the corresponding values that were also evaluated here for the bulk PST that featured in my co-authored publication [2], most probably due to the sample quality that permitted supercritical EC effects in the MLCs.

Ultimately, the efficiency of EC working bodies must be verified by experimental demonstrations in prototypes. Nevertheless, the framework for the aforementioned analysis of cooling cycles can in future be extended in two key respects:

(i) Losses due to thermal cycling can be better accounted for by constructing EC cooling cycles from both the warming and cooling branches of the zero-field heat capacity to generate two $S'(T,E)$ datasets, as briefly outlined in Chapter 2 and detailed in [119]. This is unlikely to offer any substantial improvement for the present MLCs of PST because:

- The load temperature of cycles was chosen to lie above the Curie temperature ($T_c > T_C$);

- the first-order transition in the MLCs displayed minimal thermal hysteresis;
- supercritical fields suppress thermal hysteresis completely.

(ii) The rate at which heat can be extracted from or absorbed by a working body is set by its thermal conductance, which in turn constrains the cooling power it can deliver and the temperature lift for a prototype. An updated version of refrigerant efficiency could account for the losses associated with finite thermal conductivity while assuming as little as possible (ideally nothing) about prototype design. This could be achieved using endoreversible thermodynamics [200], in which reversible subsystems exchange energy via irreversible processes.

In Chapter 5, MLCs of PST such as those described in Chapter 3 were exploited without macroscopic motion (and fluids) in a prototype that is therefore truly solid-state in the sense used to describe modern electronics. Initially, the MLC sandwiched between two Peltier elements was used to attempt Peltier-assisted Brayton cycles [186-188] in which the Peltier at the sink (load) pumps heat to (from) the sink (load) after EC field application (removal). However, operating Peltier elements as heat pumps necessarily fails to generate the heat-switch behaviour required to rectify EC heat, just as a DC voltage source cannot rectify an in-series AC source. Instead, the same device was used to demonstrate an alternative working principle that has the capacity to yield improvements in the efficiency of Peltier cooling. The two Peltiers were current sourced and voltage sourced in anti-phase to match the EC cycle. Here the Peltiers led the EC working body, and not the other way round as proposed for the Peltier-assisted Brayton cycles, such that the EC working body was used to change the surface temperature of the Peltier elements and not to pump heat. Device efficiency can only be meaningfully evaluated in future after at least some degree of optimization (e.g. minimizing the series resistance that has suppressed efficiency here), but notably any efficiency improvements may not be constrained by the thermoelectric figure of merit ZT, which is notoriously difficult to increase. Therefore, it may be possible to improve Peltier cooling for a range of thermoelectric materials via combination with EC working bodies.

The hybrid device that is described in Chapter 5 can be scaled into a multilayer Peltier(-EC-Peltier)$_n$ cascade structure in order to substantially increase the temperature lift; and

substantially greater cooling power could be achieved by placing the multilayer structures in parallel. Heat transfer between an EC working body and a Peltier element would be limited to what is required for the EC working body to thermalize with the juxtaposed Peltier surface. Any additional heat transfer generates irreversibility that reduces the recoverable work in the EC working body, and hence overall efficiency. Optimizing the hybrid device, assuming the EC working body is an MLC, would thus involve:

(i) minimizing inactive thermal mass/resistance (e.g. adhesive or plastic capping) between the active EC material and the juxtaposed Peltier face;

(ii) minimizing inactive thermal mass in the margins that lie around the active volume to minimize heat exchange and thus avoid reducing the recoverable work;

(iii) reducing the number of active EC layers because all but the outermost few layers do not thermalize with the juxtaposed Peltier surface; driving EC effects in the central layers represents wasted work.

The optimal number of active EC layers in the MLC could be identified in future via finite element analysis. The Joule heating associated with Peltier elements could be avoided if they were replaced with diode heat pipes or heat switches, but the use of Peltier elements as (active) heat pumps has the unique advantage that the cooling power is no longer limited by the low thermal conductivity of the EC working body.

References

[1] B. Nair, T. Usui, S. Crossley, S. Kurdi, G. G. Guzmán-Verri, X. Moya, S. Hirose and N. D. Mathur, "Large electrocaloric effects in oxide multilayer capacitors over a wide temperature range," *Nature,* vol. 575, p. 468, 2019.

[2] S. Crosley, B. Nair, R. W. Whatmore, X. Moya and N. D. Mathur, "Electrocaloric cooling cycles in lead scandium tantalate with true regeneration via field variation," *Phys. Rev. X,* vol. 9, p. 41002, 2019.

[3] S. Crossley, T. Usui, B. Nair, S. Kar-Narayan, X. Moya, S. Hirose, A. Ando and N. D. Mathur, "Direct electrocaloric measurement of $0.9Pb(Mg_{1/3}Nb_{2/3})O_3$-$0.1PbTiO_3$ films using scanning thermal microscopy," *Appl. Phys. Lett.,* vol. 108, p. 032902, 2016.

[4] T. Usui, S. Hirose, A. Ando, S. Crossley, B. Nair, X. Moya and N. D. Mathur, "Effect of inactive volume on thermocouple measurements of electrocaloric temperature change in multilayer capacitors of $0.9Pb(Mg_{1/3}Nb_{2/3})O_3$-$0.1PbTiO_3$," *J. Phys. D: Appl. Phys.,* vol. 50, p. 424002, 2017.

[5] S. Hirose, T. Usui, S. Crossley, B. Nair, A. Ando, X. Moya and N. D. Mathur, "Progress on electrocaloric multilayer ceramic capacitor development," *APL Mater.,* vol. 4, p. 064105, 2016.

[6] M. Ghidini, R. Mansell, R. Pellicelli, D. Pesquera, B. Nair, X. Moya, S. Farokhipoor, F. Maccherozzi, C. H. W. Barnes, R. P. Cowburn, S. S. Dhesi and N. D. Mathur, "Voltage-driven annihilation and creation of magnetic vortices in Ni discs," *Nanoscale,* vol. 12, pp. 5652-5657, 2020.

[7] M. Ghidini, R. Pellicelli, R. Mansell, D. Pesquera, B. Nair, X. Moya, S. Farokhipoor, F. Maccherozzi, C. H. W. Barnes, R. P. Cowburn, S. S. Dhesi and N. D. Mathur, "Voltage-driven displacement of magnetic vortex cores," *J. Phys. D: Appl. Phys.,* vol. 53, p. 434003, 2020.

[8] M. Ghidini, B. Zhu, R. Mansell, R. Pellicelli, A. Lesaine, X. Moya, S. Crossley, B. Nair, F. Maccherozzi, C. H. W. Barnes, R. P. Cowburn, S. S. Dhesi and N. D. Mathur, "Voltage control of magnetic single domains in Ni discs on ferroelectric $BaTiO_3$," *J. Phys. D: Appl. Phys.,* vol. 51, p. 224007, 2018.

[9] S. P. Senanayak, B. Yang, T. H. Thomas, N. Giesbrecht, W. Huang, E. Gann, B. Nair, K. Goedel, S. Guha, X. Moya, C. R. McNeill, P. Docampo, A. Sadhanala, R. H. Friend and H. Sirringhaus, "Understanding charge transport in lead iodide perovskite thin-film field-effect transistors," *Sci. Adv.,* vol. 3, p. e1601935, 2017.

[10] S. Kurdi, M. Ghidini, G. Divitini, B. Nair, A. Kursumovic, P. Tiberto, S. S. Dhesi and Z. H. and Barber, "Exchange-bias via nanosegregation in novel $Fe_{2-x}Mn_{1+x}Al$ (x = −0.25, 0, 0.25) Heusler films," *Nanoscale Adv.,* vol. 2, pp. 2602-2609, 2020.

[11] J. A. Schiemer, I. Lascu, R. J. Harrison, A. Kumar, R. S. S. D. A. Katiyar, N. Ortega, C. Salazar Mejia, W. Schnelle, H. Shinohara, A. J. F. Heap, R. Nagaratnam, S. E. Dutton, J. F. Scott, B. Nair, N. D. Mathur and M. A. Carpenter, "Elastic and anelastic relaxation behaviour of perovskite multiferroics II: $PbZr_{0.53}Ti_{0.47}O_3$(PZT)–$PbFe_{0.5}Ta_{0.5}O_3$(PFT)," *J. Mater. Sci.,* vol. 52, pp. 285-304, 207.

[12] X. Moya, S. Kar-Narayan and N. D. Mathur, "Caloric materials near ferroic phase transitions," *Nat. Mat.,* vol. 13, pp. 439-450, 2014.

[13] J. F. Scott, *Ferroelectric memories,* Berlin: Springer, 2000.

[14] W. N. Lawless and A. J. Morrow, "Specific heat and electrocaloric properties of a $SrTiO_3$ ceramic at low temperatures," *Ferroelectrics,* vol. 15, pp. 159-165, 1977.

[15] W. Känzig, "Röntgenuntersuchungen über die Seignetteelektrizität von Bariumtitanat," *Helv. Phys. Acta,* vol. 24, p. 175, 1951.

[16] G. E. Bacon and R. S. Pease, "A neutron-diffraction study of the ferroelectric transition of potassium dihydrogen phosphate," *Proc. Roy. Soc. A,* vol. 230, no. 1182, p. 359, 1955.

[17] W. Känzig, H. R. Hart Jr. and S. Roberts, "Paraelectricty and ferroelectricty due to hydroxyl ions in alkali halides; paraelectric cooling," *Phys. Rev. Lett.,* vol. 13, pp. 543-545, 1964.

[18] S. Lang, "Pyroelectricity: From ancient curiosity to modern imaging tool," *Phys. Today,* vol. 58, pp. 31-36, 2005.

[19] J. Gough, "A description of a property of caoutchouc or Indian rubber; with some reflections on the cause of the elasticity of this substance," *Mem. Lit. Phil. Soc. Manchester (second series),* vol. 1, pp. 288-295, 1805.

[20] W. Thomson, "On the thermoelastic and thermomagnetic properties of matter, Part I," *Quart. J. Pure & Appl. Math,* vol. 1, pp. 57-77, 1857.

[21] W. Thomson, "On the thermoelastic, thermomagnetic, and pyroelectric properties of matter," *Lond. Edinb. Dublin Phil. Mag. J. Sci.,* vol. 5, pp. 4-27, 1878.

[22] J. Valasek, "Piezo-electric and allied phenomena in Rochelle salt," *Phys. Rev.,* vol. 17, pp. 475-481, 1921.

[23] P. Kobeko and I. Kurtschatov, "Dielectric properties of ferroelectrics," *Z. Phys.,* vol. 66, no. 3, pp. 192-205, 1930.

[24] G. G. Wiseman and J. K. Kuebler, "Electrocaloric effect in ferroelectric Rochelle salt," *Phys. Rev.,* vol. 131, no. 5, pp. 2023-2027, 1963.

[25] G. Busch and P. Scherrer, "A new ferroelectric substance," *Naturwissenschaften,* vol. 23, no. 43, p. 737, 1935.

[26] H. Baumgartner, “Elektrische Sättigungserscheinungen und elektrokalorischer Effekt von Kaliumphosphat KH_2PO_4,” *Helv. Phys. Acta.,* vol. 23, pp. 651-696, 1950.

[27] A. S. Mischenko, Q. Zhang, J. F. Scott, R. W. Whatmore and N. D. Mathur, “Giant electrocaloric effect in thin-film $PbZr_{0.95}Ti_{0.05}O_3$,” *Science,* vol. 311, pp. 1270-1271, 2006.

[28] B. Wul, “Barium titanate: A new ferro-electric,” *Nature,* vol. 157, p. 808, 1946.

[29] A. I. Karchevskii, “Electrocaloric effect in polycrystalline barium titanate,” *Phys. Solid State,* vol. 3, pp. 2249-2254, 1962.

[30] P. D. Thacher, “Electrocaloric effects in some ferroelectric and antiferroelectric $Pb(Zr,Ti)O_3$ compounds,” *J. Appl. Phys.,* vol. 39, pp. 1996-2002, 1968.

[31] R. B. Olsen, W. F. Butler, D. A. Payne, B. A. Tuttle and P. C. Held, “Observation of a polarocaloric (electrocaloric) effect of 2 °C in lead zirconate modified with Sn4+ and Ti4+,” *Phys. Rev. Lett.,* vol. 45, pp. 1436-1438, 1980.

[32] B. A. Tuttle and D. A. Payne, “The effects of microstructure on the electrocaloric properties of $Pb(Zr, Sn, Ti)O_3$ ceramics,” *Ferroelectrics,* vol. 37, pp. 603-606, 1981.

[33] E. Birks, L. Shebanov and A. Sternberg, “Electrocaloric effects in PLZT ceramics,” *Ferroelectrics,* vol. 69 , pp. 125-129, 1986.

[34] S. G. Lu, B. Rožič, Q. M. Zhang, Z. Kutnjak, R. Pirc, M. Lin, X. Li and L. Gorny, “Comparison of directly and indirectly measured electrocaloric effect in relaxor ferroelectric polymers,” *Appl. Phys. Lett.,* vol. 97, p. 202901, 2010.

[35] W. N. Lawless, “Electrocaloric effects in antiferroelectric $PbZrO_3$,” *Ferroelectrics Lett.,* vol. 17, pp. 27-31, 1993.

[36] H. Gränicher, “Induzierte Ferroelektrizität von $SrTiO_3$ bei sehr tiefen Temperaturen und über die Kältzeerzeugung durch adiabatische Entpolarisierung,” *Helv. Phys. Acta.,* vol. 29, pp. 210-212, 1956.

[37] E. Hegenbarth, “Studies of the electrocaloric effect of ferroelectric ceramics at low temperatures,” *Cryogenics,* vol. 1, pp. 242-243, 1961.

[38] A. Kikuchi and E. Sawaguchi, “Electrocaloric effect in $SrTiO_3$,” *J. Phys. Soc. Japan,* vol. 19, pp. 1497-1498, 1964.

[39] W. N. Lawless, “Specific heat and electrocaloric properties of $KTaO_3$ at low temperatures,” *Phys. Rev. B.,* vol. 16, pp. 433-439, 1977.

[40] I. Shepherd and G. Feher, “Cooling by adiabatic depolarization of OH- molecules in KCl,” *Phys. Rev. Lett.,* vol. 15, pp. 194-198, 1965.

[41] G. Lombardo and R. O. Pohl, “Electrocaloric effect and a new type of impurity mode,” *Phys. Rev. Lett.,* vol. 15, pp. 291-293, 1965.

[42] W. N. Lawless, “Paraelectric refrigeration method and apparatus”. United States of America Patent 3436924, 1969.

[43] M. C. Robinson and M. R. Wertheimer, “Paraelectric refrigerator”. United States of America Patent 3650117, 1972.

[44] V. K. Korrovits, G. G. Liid’ya and V. T. Mikhkel’soo, “Thermostatting crystals at temperatures below 1 K,” *Cryogenics,* vol. 14, pp. 44-45, 1974.

[45] Y. V. Sinyavsky, N. D. Pashkov, Y. M. Gorovoy, G. E. Lugansky and L. Shebanov, “The optical ferroelectric ceramic as working body for electrocaloric refrigeration,” *Ferroelectrics,* vol. 90, pp. 213-217, 1989.

[46] Y. V. Sinyavsky and V. M. Brodyansky, “Experimental testing of electrocaloric cooling with transparent ferroelectric ceramic as a working body,” *Ferroelectrics,* vol. 131, pp. 321-325, 1992.

[47] Y. V. Sinyavskii, “Electrocaloric refrigerators: A promising alternative to current low-temperature apparatus,” *Chem. Petrol. Eng.,* vol. 31, pp. 295-306, 1995.

[48] L. A. Shebanov, E. H. Birks and K. J. Borman, “X-ray studies of electrocaloric lead-scandium tantalate ordered solid solutions,” *Ferroelectrics,* vol. 90, pp. 165-172, 1989.

[49] L. Shebanov and K. Borman, “On lead-scandium tantalite solid solutions with high electrocaloric effect,” *Ferroelectrics,* vol. 127, pp. 143-148, 1992.

[50] L. Shebanovs, A. Sternberg, W. N. Lawless and K. Borman, “Isomorphous ion substitutions and order-disorder phenomena in highly electrocaloric lead-scandium tantalate solid solutions,” *Ferroelectrics,* vol. 184, pp. 239-242, 1996.

[51] L. Shebanovs, K. Borman, W. N. Lawless and A. Kalvane, “Electrocaloric effect in some perovskite ferroelectric ceramics and multilayer capacitors,” *Ferroelectrics,* vol. 273, pp. 137-142, 2002.

[52] H. Kawai, “The piezoelectricity of poly (vinylidene fluoride),” *Japan. J. Appl. Phys.,* vol. 8, pp. 975-976, 1969.

[53] R. L. Ewing, “The electrocaloric effect on the pyroelectric charge in polyvinylidene fluoride,” *Ferroelectrics,* vol. 141, pp. 243-256, 1993.

[54] B. Neese, B. Chu, S. G. Lu, Y. Wang, E. Furman and Q. M. Zhang, “Large electrocaloric effect in ferroelectric polymers near room temperature,” *Science,* vol. 321, pp. 821-823, 2008.

[55] A. S. Mischenko, Q. Zhang, R. W. Whatmore, J. F. Scott and N. D. Mathur, “Giant electrocaloric effect in the thin film relaxor ferroelectric 0.9 $PbMg_{1/3}Nb_{2/3}O_3$-0.1 $PbTiO_3$ near room temperature,” *Appl. Phys. Lett.,* vol. 89, p. 242912, 2006.

[56] T. M. Correia, J. S. Young, R. W. Whatmore, J. F. Scott, N. D. Mathur and Q. Zhang, “Investigation of the electrocaloric effect in a $PbMg_{1/3}Nb_{2/3}O_3$-$PbTiO_3$ relaxor thin film,” *Appl. Phys. Lett.,* vol. 95, p. 182904, 2009.

[57] D. Saranya, A. R. Chaudhuri, J. Parui and S. B. Krupanidhi, “Electrocaloric effect of PMN-PT thin films near morphotropic phase boundary,” *Bull. Mater. Sci.,* vol. 32, pp. 259-262, 2009.

[58] T. M. Correia, S. Kar-Narayan, J. S. Young, J. F. Scott, N. D. Mathur, R. W. Whatmore and Q. Zhang, “PST thin films for electrocaloric coolers,” *J. Phys. D: Appl. Phys.,* vol. 44, p. 165407, 2011.

[59] B. Peng, H. Fan and Q. Zhang, “A giant electrocaloric effect in nanoscale antiferroelectric and ferroelectric phases coexisting in a relaxor $Pb_{0.8}Ba_{0.2}ZrO_3$ thin film at room temperature,” *Adv. Funct. Mater.,* vol. 23, pp. 2987-2992, 2013.

[60] P. F. Liu, J. L. Wang, X. J. Meng, J. Yang, B. Dkhil and J. H. Chu, “Huge electrocaloric effect in Langmuir–Blodgett ferroelectric polymer thin films,” *New J. Phys.,* vol. 12, p. 023035, 2010.

[61] X. Li, X. S. Qian, H. Gu, X. Chen, S. G. Lu, M. Lin, F. Bateman and Q. M. Zhang, “Giant electrocaloric effect in ferroelectric poly(vinylidenefluoride-trifluoroethylene) copolymers near a first-order ferroelectric transition,” *Appl. Phys. Lett.,* vol. 101, p. 132903, 2012.

[62] G. Zhang, Q. Li, H. Gu, S. Jiang, K. Han, M. R. Gadinski, M. A. Haque, Q. M. Zhang and Q. Wang, “Ferroelectric polymer nanocomposites for room-temperature electrocaloric refrigeration,” *Adv. Mater.,* vol. 27, pp. 1450-1454, 2015.

[63] S. G. Lu, B. Rožič, Q. M. Zhang, Z. Kutnjak and B. Neese, “Enhanced electrocaloric effect in ferroelectric poly(vinylidene-fluoride/trifluoroethylene) 55/45 mol% copolymer at ferroelectric–paraelectric transition,” *Appl. Phys. Lett.,* vol. 98, p. 122906, 2011.

[64] B. Rožič, M. Kosec, H. Uršič, J. Holc, B. Malič, Q. M. Zhang, R. Blinc, R. Pirc and Z. Kutnjak, “Influence of the critical point on the electrocaloric response of relaxor ferroelectrics,” *J. Appl. Phys.,* vol. 110, p. 064118, 2011.

[65] J. Peräntie, H. N. Tailor, J. Hagberg, H. Jantunen and Z. G. Ye, “Electrocaloric properties in relaxor ferroelectric $(1-x)Pb(Mg_{1/3}Nb_{2/3})O_3–xPbTiO_3$ system,” *J. Appl. Phys.,* vol. 114, p. 174105, 2013.

[66] M. Vrabelj, H. Uršič, Z. Kutnjak, B. Rožič, S. Drnovšek, A. Benčan, V. Bobnar, L. Fulanović and B. Malič, “Large electrocaloric effect in grain-size-engineered $0.9Pb(Mg_{1/3}Nb_{2/3})O_3–0.1PbTiO_3$,” *J. Eur. Ceram. Soc.,* vol. 36, no. 1, pp. 75-80, 2016.

[67] L. Fulanović, S. Drnovšek, H. Uršič, M. Vrabelj, D. Kuščer, K. Makarovič, V. Bobnar, Z. Kutnjak and B. Malič, “Multilayer $0.9Pb(Mg_{1/3}Nb_{2/3})O_3–0.1PbTiO_3$ elements for electrocaloric cooling,” *J. Eur. Ceram. Soc.,* vol. 37, p. 599, 2017.

[68] X. Q. Liu, T. T. Chen, Y. J. Wu and X. M. Chen, “Enhanced electrocaloric effects in spark plasma-sintered $Ba_{0.65}Sr_{0.35}TiO_3$-based ceramics at room temperature,” *J. Am. Ceram. Soc.,* vol. 96, pp. 1021-1023, 2013.

[69] S. Kar-Narayan and N. D. Mathur, “Predicted cooling powers for multilayer capacitors based on various electrocaloric and electrode materials,” *Appl. Phys.Lett.,* vol. 95, p. 242903, 2009.

[70] S. Crossley, J. R. McGinnigle, S. Kar-Narayan and N. D. Mathur, “Finite-element optimisation of electrocaloric multilayer capacitors,” *Appl. Phys. Lett.,* vol. 104, p. 082909, 2014.

[71] S. Kar-Narayan and N. D. Mathur, “Direct and indirect electrocaloric measurements using multilayer capacitors,” *J. Phys. D: Appl. Phys.,* vol. 43, p. 032002, 2010.

[72] H. Gu, X. Qian, X. Li, B. Craven, W. Zhu, A. Cheng, S. C. Yao and Q. M. Zhang, “A chip scale electrocaloric effect based cooling device,” *Appl. Phys. Lett.,* vol. 102, p. 122904, 2013.

[73] Y. Jia and Y. S. Ju, “A solid-state refrigerator based on the electrocaloric effect,” *Appl. Phys. Lett.,* vol. 100, p. 242901, 2012.

[74] U. Plaznik, A. Kitanovski, B. Rožič, B. Malič, H. Uršič, S. Drnovšek, J. Cilenšek, M. Vrabelj, A. Poredoš and Z. Kutnjak, “Bulk relaxor ferroelectric ceramics as a working body for an electrocaloric cooling device,” *Appl. Phys. Lett.,* vol. 106, p. 043903, 2015.

[75] Y. D. Wang, S. J. Smullin, M. J. Sheridan, Q. Wang, C. Eldershaw and D. E. Schwartz, “A heat-switch-based electrocaloric cooler,” *Appl. Phys. Lett.,* vol. 107, p. 134103, 2015.

[76] P. Blumenthal, C. Molin, S. Gebhardt and A. Raatz, “Active electrocaloric demonstrator for direct comparison of PMN-PT bulk and multilayer samples,” *Ferroelectrics,* vol. 497, pp. 1-8, 2016.

[77] D. Sette, A. Asseman, M. Gérard, H. Strozyk, R. Faye and E. Defay, “Electrocaloric cooler combining ceramic multi-layer capacitors and fluid,” *APL Mater.,* vol. 4, p. 91101, 2016.

[78] T. Zhang, X. S. Qian, H. Gu, Y. Hou and Q. M. Zhang, “An electrocaloric refrigerator with direct solid to solid regeneration,” *Appl. Phys. Lett.,* vol. 110, p. 243503, 2017.

[79] R. Ma, Z. Zhang, K. Tong, D. Huber, R. Kornbluh, Y. S. Ju and Q. Pei, “Highly efficient electrocaloric cooling with electrostatic actuation,” *Science,* vol. 357, pp. 1130-1134, 2017.

[80] E. Defay, R. Faye, G. Despesse, H. Strozyk, D. Sette, S. Crossley, X. Moya and N. D. Mathur, “Enhanced electrocaloric efficiency via energy recovery,” *Nat. Comm.,* vol. 9, p. 1827, 2018.

[81] Y. Wang, D. Schwartz, J. Kalb and J. Lee, “A self-regenerating electrocaloric cooler,” in *Proceedings of the 8th International Conference on Caloric Cooling (Thermag VIII),* Darmstadt, 2018.

[82] H. Chen, T. L. Ren, X. M. Wu, Y. Yang and L. T. Liu, “Giant electrocaloric effect in lead-free thin film of strontium bismuth tantalite,” *Appl. Phys. Lett.,* vol. 94, p. 182902, 2009.

[83] S. Crossley, “Electrocaloric materials and devices,” University of Cambridge, 2012.

[84] X. S. Qian, S. G. Lu, X. Li, H. Gu, L. C. Chien and Q. M. Zhang, “Large electrocaloric effect in a dielectric liquid possessing a large dielectric anisotropy near the isotropic–nematic transition,” *Adv. Mater.,* vol. 23, pp. 2894-2898, 2013.

[85] M. Trček, M. Lavrič, G. Cordoyiannis, B. Zalar, B. Rožič, S. Kralj, V. Tzitzios, G. Nounesisand and Z. Kutnjak, “Electrocaloric and elastocaloric effects in soft materials,” *Phil. Trans. R. Soc. A,* vol. 374, no. 2074, p. 20150301, 2016.

[86] D. Matsunami and A. Fujita, “Electrocaloric effect of metal-insulator transition in VO_2,” *Appl. Phys. Lett.,* vol. 106, p. 042901, 2015.

[87] X. Moya, E. Stern-Taulats, S. Crossley, D. González-Alonso, S. Kar-Narayan, A. Planes, L. Mañosa and N. D. Mathur, “Giant electrocaloric strength in single-crystal $BaTiO_3$,” *Adv. Mater.,* vol. 25, pp. 1360-1365, 2013.

[88] C. Cazorla, “In the search of new electrocaloric materials: Fast ion conductors,” *Results in Phys.,* vol. 5, pp. 262-263, 2015.

[89] Y. A. Çengel and A. J. Ghajar, *Heat and mass transfer: Fundamentals and applications,* McGraw-Hill, 2015.

[90] Y. Suemune, “Thermal conductivity of $BaTiO_3$ and $SrTiO_3$ from 4.5° to 300°K,” *J. Phys. Soc. Jpn.,* vol. 20, p. 174, 1965.

[91] H. Uršič, M. Vrabelj, L. Fulanovič, A. Bradeško, S. Drnovšek and B. Malič, “Specific heat capacity and thermal conductivity ofthe electrocaloric $(1-x)Pb(Mg_{1/3}Nb_{2/3})O_3–xPbTiO_3$ ceramics between room temperature and 300°C,” *J. Microelectron. Electron. Components Mater.,* vol. 45, pp. 260-265, 2015.

[92] C. Y. Iguchi, W. N. dos Santos and R. Gregorio, “Determination of thermal properties of pyroelectric polymers, copolymers and blends by the laser flash technique,” *Polym. Test.,* vol. 26, pp. 788-792, 2007.

[93] T. J. Kelly, “On the general solution to RC circuits: Green’s function in prose form,” *Eur. J. Phys.,* vol. 39, p. 025802, 2018.

[94] Y. S. Koshkid'ko, J. Ćwik, T. I. Ivanova, S. A. Nikitin, M. Miller and K. Rogacki, “Magnetocaloric properties of Gd in fields up to 14 T,” *J. Magn. Magn. Mater.,* vol. 433, pp. 234-238, 2017.

[95] D. Viehland, J. F. Li, S. J. Jang, L. E. Cross and M. Wuttig, “Glassy polarization behavior of relaxor ferroelectrics,” *Phys. Rev. B,* vol. 46, p. 8013, 1992.

[96] F. Le Goupil, A. Berenov, A. -K. Axelsson, M. Valant and N. M. Alfrod, “Direct and indirect electrocaloric measurements on <001>-$PbMg_{1/3}Nb_{2/3}O_3$-$30PbTiO_3$ single crystals,” *J. Appl. Phys.,* vol. 111, p. 124109, 2012.

[97] T. Tong, J. Karthik, R. V. K. Mangalam, L. W. Martin and D. G. Cahill, “Reduction of the electrocaloric entropy change of ferroelectric $PbZr_{1-x}Ti_xO_3$ epitaxial layers due to an elastocaloric effect,” *Phys. Rev. B,* vol. 90, p. 094116, 2014.

[98] M. E. Lines and A. M. Glass, *Principles and applications of ferroelectrics and related materials*, Oxford: Clarendon Press, 1977.

[99] W. J. Merz, “Double Hysteresis Loop of $BaTiO_3$ at the Curie Point,” *Phys. Rev.*, vol. 91, no. 3, p. 513, 1953.

[100] Y. H. Kim and J. J. Kim, “Scaling behavior of an antiferroelectric hysteresis loop,” *Phys. Rev. B,* vol. 55, p. 933, 1997.

[101] S. M. Yang, J. Y. Jo, T. H. Kim, J. Yoon, T. K. Song, H. N. Lee, Z. Marton, S. Park, Y. Jo and T. W. Noh, “AC dynamics of ferroelectric domains from an investigation of the frequency dependence of hysteresis loops,” *Phys. Rev. B,* vol. 82, p. 174125, 2010.

[102] S. Hoshino, T. Mitsui, F. Jona and R. Pepinsky, “Dielectric and thermal study of tri-glycine sulfate and tri-glycine fluoberyllate,” *Phys. Rev.*, vol. 107, p. 1255, 1957.

[103] P. Chandra and P. Littlewood, “A Landau primer for ferroelectrics,” in *Physics of ferroelectrics: A modern perspective,* K. M. Rabe, C. H. Ahn and J. M. Triscone, Eds., Berlin, Springer, 2007, p. 80.

[104] L. Caron, Z. Q. Ou, T. T. Nguyen, D. T. Cam Thanh, O. Tegus and E. Brück, “On the determination of the magnetic entropy change in materials with first-order transitions,” *J. Magn. Magn. Mater.*, vol. 321, pp. 3559-3566, 2009.

[105] C. B. Sawyer and C. H. Tower, “Rochelle salt as a dielectric,” *Phys. Rev.*, vol. 35, p. 269, 1930.

[106] A. M. Glazer, P. Groves and D. T. Smith, “Automatic sampling circuit for ferroelectric hysteresis loops,” *J. Phys. E Sci. Instrum.*, vol. 17, no. 2, pp. 95-97, 1984.

[107] M. Stewart, M. G. Cain and P. Weaver, “Electrical measurement of ferroelectric properties,” in *Characterisation of ferroelectric bulk materials and thin films,* M. G. Cain, Ed., Springer Netherlands, 2014, pp. 1-14.

[108] J. F. Scott, “Ferroelectrics go bananas,” *J. Phys. Cond. Matter,* vol. 20, p. 021001, 2008.

[109] J. Park, B. Kim, J. Park, I. Kim, H. Je, Y. Kim, S. J. Park, B. Kim, J. Park and I. Kim, “Dielectric hysteresis measurement in lossy ferroelectrics,” *Ferroelectrics,* vol. 230, p. 151, 1999.

[110] L. Pintilie and M. Alexe, “Ferroelectric-like hysteresis loop in nonferroelectric systems,” *Appl. Phys. Lett.*, vol. 87, p. 112903, 2005.

[111] J. F. Scott and J. Gardner, “Ferroelectrics, multiferroics and artifacts: Lozenge-shaped hysteresis and things that go bump in the night,” *Mater. Today,* vol. 21, p. 553, 2018.

[112] V. Koval, G. Viola and Y. Tan, “Biasing effects in ferroic materials,” in *Ferroelectric materials: Synthesis and characterization*, A. Peláiz-Barranco, Ed., InTechOpen, 2015.

[113] Y. Q. Tan, J. L. Zhang and C. L. Wang, “Aging behaviours of CuO modified $BaTiO_3$ ceramics,” *Adv. Appl. Ceram.*, vol. 113, p. 223, 2014.

[114] N. Balke, D. C. Lupascu, T. Granzow and J. Rödel, “Fatigue of lead zirconate titanate ceramics. I: Unipolar and DC loading,” *J. Am. Ceram. Soc.*, vol. 90, no. 4, pp. 1081-1087, 2007.

[115] G. E. Pike, W. L. Warren, D. Dimos, B. A. Tuttle, R. Ramesh, J. Lee, G. Keramidas and J. T. Evans, “Voltage offsets in (Pb,La)(Zr,Ti)O_3 thin films,” *Appl. Phys. Lett.*, vol. 66, p. 484, 1995.

[116] K. Abe, N. Yanase, T. Yasumoto and T. Kawabuko, “Voltage shift phenomena in a heteroepitaxial $BaTiO_3$,” *J. Appl. Phys.*, vol. 91, p. 323, 2002.

[117] S. P. Alpay, I. B. Misirlioglu, V. Nagarajan and R. Ramesh, “Can interface dislocations degrade ferroelectric properties?,” *Appl. Phys. Lett.*, vol. 85, p. 2044, 2004.

[118] B. Asbani, J. -L. Dellis, Y. Gagou, H. Kaddoussi, A. Lahmar, M. Amjoud, D. Mezzane, Z. Kutnjak and M. E. Marssi, “Electrocaloric effect in $Ba_{0.2}Ca_{0.8}Ti_{0.95}Ge_{0.05}O_3$ determined by a new pyroelectric method,” *EPL*, vol. 111, p. 57008, 2015.

[119] E. Stern-Taulats, B. Nair, A. A. Avramenko, S. Crossley, R. W. Whatmore, N. D. Mathur and X. Moya, “Large reversible electrocaloric performance in $PbSc_{0.5}Ta_{0.5}O_3$ ceramics,” *Manuscript in preparation*, 2020.

[120] R. Z. Levitin, V. V. Snegirev, A. V. Kopylov, A. S. Lagutin and A. Gerber, “Magnetic method of magnetocaloric effect determination in high pulsed magnetic fields,” *J. Magn. Magn. Mater.*, vol. 170, p. 223, 1997.

[121] S. Crossley, R. W. Whatmore, N. D. Mathur and X. Moya, “Quasi-indirect measurement of electrocaloric temperature change in $Pb_{0.5}Sc_{0.5}TaO_3$ via comparison of adiabatic and isothermal electrical polarization data,” *Manuscript in preparation*, 2020.

[122] Y. Jia and Y. Sungtaek Ju, “Direct characterization of the electrocaloric effects in thin films supported on substrates,” *Appl. Phys. Lett.*, vol. 103, p. 042903, 2013.

[123] S. Pandya, G. Velarde, L. Zhang and L. W. Martin, “Pyroelectric and electrocaloric effects in ferroelectric silicon-doped hafnium oxide thin films,” *Phys. Rev. Mater.*, vol. 2, p. 124405, 2018.

[124] C. R. H. Bahl and K. K. Nielsen, “The effect of demagnetization on the magnetocaloric properties of gadolinium,” *J. Appl. Phys.*, vol. 105, p. 013916, 2009.

[125] B. Rožič, B. Malič, H. Uršič, J. Holc, M. Kosec, B. Neese, Q. M. Zhang and Z. Kutnjak "Direct measurements of the giant electrocaloric effect in soft and solid ferroelectric materials," *Ferroelectrics,* vol. 405, p. 26, 2010.

[126] V. S. Bondarev, E. A. Mikhaleva, I. N. Flerov and M. V. Gorev, "Electrocaloric effect in triglycine sulfate under equilibrium and nonequilibrium thermodynamic conditions," *Phys. Solid State,* vol. 59, pp. 1118-1126, 2017.

[127] M. Sanliap, V. V. Shvartsman, R. Faye, M. O. Karabasov, C. Molin, S. Gebhardt, E. Defay and D. C. Lupascu, "Quasi-adiabatic calorimeter for direct electrocaloric measurements," *Rev. Sci. Instrum.,* vol. 89, p. 034903, 2018.

[128] S. G. Lu, B. Rožič, Q. M. Zhang, Z. Kutnjak, X. Li, E. Furman, L. J. Gorny, M. Lin, B. Malič, M. Kosec, R. Blinc and R. Pirc, "Organic and inorganic relaxor ferroelectrics with giant electrocaloric effect," *Appl. Phys. Lett.,* vol. 97, p. 162904, 2010.

[129] G. Sebald, L. Seveyrat, J. Capsal, P. Cottinet and D. Guyomar, "Differential scanning calorimeter and infrared imaging for electrocaloric characterization of poly(vinylidene fluoride-trifluoroethylene-chlorofluoroethylene) terpolymer," *Appl. Phys. Lett.,* vol. 101, p. 022907, 2012.

[130] S. Kar-Narayan, S. Crossley, X. Moya, V. Kovacova, J. Abergel, A. Bontempi, N. Baier, E. Defay and N. D. Mathur, "Direct electrocaloric measurements of a multilayer capacitor using scanning thermal microscopy and infra-red imaging," *Appl. Phys. Lett.,* vol. 102, p. 032903, 2013.

[131] Y. Liu, H. Strozyk, B. Dkhil and E. Defay, "Insight into electrocaloric cooling power in multilayer capacitors using infra-red camera," *Appl. Phys. Lett.,* vol. 109, p. 212902, 2016.

[132] M. Vollmer and K. -P. Möllmann, *Infrared thermal imaging: Fundamentals, research and applications*, Weinheim: Wiley-VCH, 2010.

[133] F. Sakuma and S. Hattori, "Establishing a practical temperature standard by using a narrow-band radiation thermometer with a silicon detector," in *Temperature: Its measurement and control in science and industry,* vol. 5, J. F. Schooley, Ed., New York, AIP, 1982, pp. 421-427.

[134] F. Sakuma and M. Kobayashi, "Interpolation equations of scales of radiation thermometers," in *Proceedings of TEMPMEKO '96,* Torino, 1996.

[135] M. Ochs, T. Horbach, A. Schulz, R. Koch and H.-J. Bauer, "A novel calibration method for an infrared thermography system applied toheat transfer experiments," *Meas. Sci. Tech.,* vol. 20, p. 075103, 2009.

[136] G. Sebald, L. Seveyrat, D. Guyomar, L. Lebrun, B. Guiffard and S. Pruvost, "Electrocaloric and pyroelectric properties of $0.75Pb(Mg_{1/3}Nb_{2/3})O_3–0.25PbTiO_3$," *J. Appl. Phys.,* vol. 100, p. 124112, 2006.

[137] E. D. West and E. F. Westrum Jr., “Adiabatic calorimetry from 300 to 800°K,” in *Calorimetry of non-reacting systems*, J. P. McCullough and D. W. Scott, Eds., London, Butterworth & Co., 1968, pp. 333-367.

[138] N. Novak, R. Pirc and Z. Kutnjak, “Impact of critical point on piezoelectric and electrocaloric response in barium titanate,” *Phys. Rev. B* , vol. 87, p. 104102, 2013.

[139] T. S. Komatsu, N. Nakagawa, S. Sasa and H. Tasaki, “Exact equalities and thermodynamic relations for nonequilibrium steady states,” *J. Stat. Phys.*, vol. 159, p. 1237, 2015.

[140] V. Basso, F. Russo, J. F. Gerard and S. Pruvost, “Direct measurement of the electrocaloric effect in poly(vinylidene fluoride-trifluoroethylene-chlorotrifluoroethylene) terpolymer films,” *Appl. Phys. Lett.*, vol. 103, p. 202904, 2013.

[141] M. Sanlialp, V. V. Shvartsman, M. Acosta, B. Dkhil and D. C. Lupascu, “Strong electrocaloric effect in lead-free $0.65Ba(Zr_{0.2}Ti_{0.8})O_3$-$0.35(Ba_{0.7}Ca_{0.3})TiO_3$ ceramics obtained by direct measurements,” *Appl. Phys. Lett.*, vol. 106, p. 062901, 2015.

[142] X. Li, X. S. Qian, S. G. Lu, J. Cheng, Z. Fang and Q. M. Zhang, “Tunable temperature dependence of electrocaloric effect in ferroelectric relaxor poly(vinylidene fluoride-trifluoroethylene-chlorofluoroethylene terpolymer,” *Appl. Phys. Lett.*, vol. 99, p. 052907, 2011.

[143] Y. Bai, G. Zheng and S. Shi, “Direct measurement of giant electrocaloric effect in $BaTiO_3$,” *Appl. Phys. Lett.*, vol. 96, p. 192902, 2010.

[144] K. N. Marsh, J. B. Ott, C. J. Wormald, H. Yao, I. Hatta, P. M. Claudy and S. Van Herwaarden, “Calorimetry,” in *Measurement of the Thermodynamic Properties of Single Phases*, A. R. H. Goodwin, K. N. Marsh and W. A. Wakeham, Eds., Amsterdam, Elsevier Science B. V., 2003, p. 336.

[145] M. J. O'Neill, “Measurement of specific heat functions by differential scanning calorimetry,” *Anal. Chem.*, vol. 38, p. 1331, 1966.

[146] Y. Liu, J. F. Scott and B. Dkhil, “Direct and indirect measurements on electrocaloric effect: Recent developments and perspectives,” *App. Phys. Rev.*, vol. 3, p. 031102, 2016.

[147] G. V. Brown, “Magnetic heat pumping near room temperature,” *J. Appl. Phys.*, vol. 47, pp. 3673-3680, 1976.

[148] B. Yu, M. Liu, P. W. Egolf and A. Kitanovski, “A review of magnetic refrigerator and heat pump prototypes built before the year 2010,” *Int. J. Refrig.*, vol. 33, pp. 1029-1060, 2010.

[149] R. Bjørk, C. R. H. Bahl and K. K. Nielsen, “The lifetime cost of a magnetic refrigerator,” *Int. J. Refrig.*, vol. 63, pp. 48-62, 2016.

[150] A. Tura and A. Rowe, “Concentric Halbach cylinder magnetic refrigerator cost optimization,” *Int. J. Refrig.,* vol. 37, pp. 106-116, 2014.

[151] S. Qian, A. Abdullah, J. Ling, J. Muehlbauer, Y. Hwang, R. Radermacher and I. Takeuchi, “Performance enhancement of a compressive thermoelastic cooling system using multi-objective optimization and novel designs,” *Int. J. Refrig.,* vol. 57, p. 62-76, 2015.

[152] P. Lloveras, A. Aznar, M. Barrio, P. Negrier, C. Popescu, A. Planes, L. Mañosa, E. Stern-Taulats, A. Avramenko, N. D. Mathur, X. Moya and J. -Ll. Tamarit, “Colossal barocaloric effects near room temperature in plastic crystals of neopentylglycol,” *Nat. Commun.,* vol. 10, p. 1803, 2019.

[153] C. G. F. Stenger and A. J. Burggraaf, “Order–disorder reactions in the ferroelectric perovskites $Pb(Sc_{1/2}Nb_{1/2})O_3$ and $Pb(Sc_{1/2}Ta_{1/2})O_3$,” *Phys. Status Solidi A,* vol. 61, p. 653-664, 1980.

[154] N. Setter and L. E. Cross, “The contribution of structural disorder to diffuse phase transitions in ferroelectrics.,” *J. Mater. Sci.,* vol. 15, pp. 2478-2482, 1980.

[155] Y. Imry and M. Wortis, “Influence of quenched impurities on first-order phase transitions,” *Phys. Rev. B,* vol. 19, pp. 3580-3585, 1979.

[156] X. Moya, E. Defay, V. Heine and N. D. Mathur, “Too cool to work,” *Nat. Phys.,* vol. 11, pp. 202-205, 2015.

[157] P. Lloveras, E. Stern-Taulats, M. Barrio, J. -L. Tamarit, S. Crossley, W. Li, V. Pomjakushin, A. Planes, L. Mañosa, N. D. Mathur and X. Moya, “Giant barocaloric effects at low pressure in ferrielectric ammonium sulphate.,” *Nat. Commun.,* vol. 6, p. 8801, 2015.

[158] J. Liu, T. Gottschall, K. P. Skokov, J. D. Moore and O. Gutfleisch, “Giant magnetocaloric effect driven by structural transitions,” *Nat. Mater.,* vol. 11, p. 620-626, 2012.

[159] R. W. Whatmore, N. W. Shorrocks, P. C. Osbond, S. B. Stringfellow, C. F. Carter and R. Watton, “Modified lead scandium tantalate for uncooled LWIR detection and thermal imaging.,” in *Proc. 8th IEEE International Symposium on Applications of Ferroelectrics (ISAF)*, 1992.

[160] G. W. H. Höhne, W. F. Hemminger and H. -J. Flammersheim, *Differential scanning calorimetry*, Springer, 2003, pp. 121-126.

[161] D. V. Christensen, K. K. Nielsen, C. R. H. Bahl and A. Smith, “Demagnetizing effects in stacked rectangular prisms,” *J. Phys. D: Appl. Phys.,* vol. 44, p. 215004, 2011.

[162] S. Y. Dan’kov, A. M. Tishin, V. Pecharsky and K. Gschneidner, “Magnetic phase transitions and the magnetothermal properties of gadolinium,” *Phys. Rev B,* vol. 57, p. 3478, 1998.

[163] Y. Hou, L. Yang, X. Qian, T. Zhang and Q. M. Zhang, "Electrocaloric response near room temperature in Zr- and Sn-doped $BaTiO_3$ systems," *Phil. Trans. R. Soc. A,* vol. 374, p. 20160055, 2016.

[164] X. S. Qian, H. J. Ye, Y. T. Zhang, H. Gu, X. Li, C. A. Randall and Q. M. Zhang, "Giant electrocaloric response over a broad temperature range in modified $BaTiO_3$ ceramics," *Adv. Funct. Mater.,* vol. 24, p. 1300, 2014.

[165] H. Wang and W. A. Schulze, "Order-disorder phenomenon in lead scandium tantalate," *J. Am. Ceram. Soc.,* vol. 73, p. 1228, 1990.

[166] N. Novak, Z. Kutnjak and R. Pirc, "High-resolution electrocaloric and heat capacity measurements in barium titanate," *EPL,* vol. 103, p. 47001, 2013.

[167] S. Candel, M. Juniper, G. Singla, P. Scouflaire and C. Rolon, "Structure and dynamics of cryogenic flames at supercritical pressure," *Combus. Sci. and Tech.,* vol. 178, pp. 161-192, 2007.

[168] W. A. Steyert, "Stirling-cycle rotating magnetic refrigerators and heat engines for use near room temperature," *J. Appl. Phys.,* vol. 49, pp. 1216-1226, 1978.

[169] J. A. Barclay, "The theory of an active magnetic regenerative refrigerator," in *NASA Conference Publication 2287: Refrigeration for Cryogenic Sensors,* Greenbelt, Maryland, 1982.

[170] A. Greco, C. Aprea, A. Maiorino and C. Masselli, "A review of the state of the art of solid-state caloric cooling processes at room-temperature before 2019," *Int. J. Refrig.,* vol. 106, pp. 66-88, 2019.

[171] R. Radermacher and Y. Hwang, *Vapor compression heat pumps with refrigerant mixtures,* Taylor & Francis, 2005.

[172] E. Defay, S. Crossley, S. Kar-Narayan, X. Moya and N. D. Mathur, "The electrocaloric efficiency of ceramic and polymer films," *Adv. Mater.,* vol. 25, pp. 3337-3342, 2013.

[173] J. Chui, Y. Wu, J. Muehlbauer, Y. Hwang, R. Radermacher, S. Fackler, M. Wuttig and I. Takeuchi, "Demonstration of high efficiency elastocaloric cooling with large ΔT using NiTi wires," *Appl. Phys. Lett.,* vol. 101, p. 073904, 2012.

[174] J. He, J. Chen, J. T. Wang and B. Hua, "Inherent regenerative losses of a ferroelectric Ericsson refrigeration cycle," *Int. J. Therm. Sci.,* vol. 42, no. 2, pp. 169-175, 2003.

[175] H. Gu, B. Craven, X. Qian, X. Li, A. Cheng and Q. M. Zhang, "Simulation of chip-size electrocaloric refrigerator with high cooling-power density," *Appl. Phys. Lett.,* vol. 102, p. 112901, 2013.

[176] H. Gu and X. -S. Qian, H. -J. Ye and Q. M. Zhang, "An electrocaloric refrigerator without external regenerator," *Appl. Phys. Lett.,* vol. 105, p. 162905, 2014.

[177] U. Plaznik, M. Vrabelj, Z. Kutnjak, B. Malič, A. Poredoš and A. Kitanovski, "Electrocaloric cooling: The importance of electric-energy recovery and heat regeneration," *EPL,* vol. 111, no. 5, p. 57009, 2015.

[178] M. P. Annaorazova, S. A. Nikitin, A. L. Tyurin, S. A. Akopyan and R. W. Myndyev, "Heat pump cycles based on the AF–F transition in Fe–Rh alloys induced by tensile stress," *Int. J. Refrig.,* vol. 25, no. 8, pp. 1034-1042, 2002.

[179] F. C. Chen, R. W. Murphy, V. C. Mei and G. L. Chen, "Thermodynamic analysis of four magnetic heat-pump cycles," *J. Eng. Gas Turbines Power,* vol. 114, no. 4, pp. 715-720, 1992.

[180] G. Diguet, G. Lin and J. Chen, "Performance characteristics of magnetic Brayton refrigeration cycles using Gd, $Gd_{0.74}Tb_{0.26}$ and $(Gd_{3.5}Tb_{1.5})Si_4$ as the working substance," *Int. J. Refrig.,* vol. 35, no. 4, pp. 1035-1042, 2012.

[181] G. Diguet, G. Lin and J. Chen, "Performance characteristics of a magnetic Ericsson refrigeration cycle using Gd_xDy_{1-x} as the working substance," *J. Mag. Mag. Mater.,* vol. 350, pp. 50-54, 2014.

[182] A. Smaïli and R. Chahine, "Composite materials for Ericsson-like magnetic refrigeration cycle," *J. Appl. Phys.,* vol. 81, p. 824, 1997.

[183] W. Dai, "Regenerative balance in magnetic Ericsson refrigeration cycles," *J. Appl. Phys.,* vol. 71, p. 5272, 1992.

[184] G. Lin, O. Tegus, L. Zhang and E. Brück, "General performance characteristics of an irreversible ferromagnetic Stirling refrigeration cycle," *Phys. B: Cond. Mat.,* vol. 344, pp. 147-156, 2004.

[185] A. Kitanovski and P. W. Egolf, "Innovative ideas for future research on magnetocaloric technologies," *Int. J. Refrig.,* vol. 33, pp. 449-464, 2010.

[186] U. Tomc, J. Tušek, A. Kitanovski and A. Poredos, "A new magnetocaloric refrigeration principle with solid-state thermoelectric thermal diodes," *Appl. Therm. Eng.,* vol. 58, pp. 1-10, 2013.

[187] P. W. Egolf, L. Gravier, T. Francfort, A. -G. Pawlowski, G. Courret and M. Croc, "High-frequency magnetocaloric modules with heat gates operating with the Peltier effect," *Int. J. Refrig.,* vol. 37, pp. 176-184, 2014.

[188] A. Kitanovski, J. Tušek, U. Tomc, U. Plaznik, M. Ozbolt and A. Poredoš, "Special heat transfer mechanisms: Active and passive thermal diodes," in *Magnetocaloric energy conversion: From theory to applications.,* Springer, 2015, pp. 211-267.

[189] R. I. Epstein and K. J. Malloy, "Electrocaloric devices based on thin-film heat switches," *J. Appl. Phys.,* vol. 106, p. 064509, 2009.

[190] A. Basilius and R. Berry, "Solid-state electrocaloric cooling system and method". United States of America Patent 4757688, 1988.

[191] G. Wehmeyer, T. Yabuki, C. Monachon, J. Wu and C. Dames, “Thermal diodes, regulators, and switches: Physical mechanisms and potential applications,” *Appl. Phys. Rev.*, vol. 4, p. 041304, 2017.

[192] G. S. Nolas, J. Sharp and H. J. Goldsmid, *Thermoelectrics: Basic principles and new materials development*, Springer, 2001, p. 105.

[193] W. de Vries and T. H. van der Meer, “Application of Peltier thermal diodes in a magnetocaloric heat pump,” *Appl. Therm. Eng.*, vol. 111, pp. 377-386, 2017.

[194] A. Schilling, X. Zhang and O. Bossen, “Heat flowing from cold to hot without external intervention by using a 'thermal inductor',” *Sci. Adv.*, vol. 5, p. eaat9953, 2019.

[195] C. Goupil, “Thermodynamics of thermoelectricity,” in *Thermodynamics*, T. Mizutani, Ed., InTech, 2011, p. 284.

[196] H. J. Goldsmid, “The thermoelectric figure of merit,” in *The physics of thermoelectric energy conversion*, Morgan & Claypool, 2017.

[197] J. F. Scott, “Applications of modern ferroelectrics,” *Science*, vol. 315, no. 5814, pp. 954-959, 2007.

[198] G. G. Guzmán-Verri and P. B. Littlewood, “Why is the electrocaloric effect so small in ferroelectrics?,” *APL Mater.*, vol. 4, p. 064106, 2016.

[199] J. Li, Z. Shen, X. Chen, S. Yang, W. Zhou, M. Wang, L. Wang, Q. Kou, Y. Liu, Q. Li, Z. Xu, Y. Chang, S. Zhang and F. Li, “Grain-orientation-engineered multilayer ceramic capacitors for energy storage applications,” *Nat. Mater.*, 2020.

[200] K. H. Hoffman, J. M. Burzler and S. Schubert, “Endoreversible Thermodynamics,” *J. Non-Equilib. Thermodyn.*, vol. 22, no. 4, pp. 311-355, 1997.